Departament de Física Atòmica, Molecular i Nuclear
Institut de Física Corpuscular

Doctorat en Física

Low energy calibration, continuous monitoring, and background studies for the NEXT-White detector at the LSC

Brais Palmeiro Pazos

Supervisors:

Michel Sorel	Jose Ángel Hernando Morata
Unidad experimental	Departamento de Física de Partículas
Institut de Física Corpuscular (UV-CSIC)	Universidade de Santiago de Compostela

Tutora:

Nuria Rius Dionis
Departament de Física Teòrica
Universitat de València

Desembre de 2021

The work in this thesis has been carried out at the Instituto de Física Corpuscular (IFIC), affiliated with the Universitat de València and CSIC. It has been partially funded by the Consellería d'Educació, Investigació, Cultura i Esport de la Comunitat Valenciana under the scholarship Ajudes per a la Contratació de Personal Investigador en Formació de Caràcter Predoctoral (ACIF16/2016/097).

Informe de los directores

Michel Sorel, Científico titular del Consejo Superior de Investigaciones Científicas,

Jose Ángel Hernando Morata, Profesor titular del departamento de Física de Partículas de la Universidad de Santiago de Compostela,

como directores de tesis y

Nuria Rius Dionis, Catedrática del departamento de Física Teórica de la Universidad de Valencia,

como tutora,

Certifican:

Que la presente memoria titulada, **Low energy calibration, continuous monitoring, and background studies for the NEXT-White detector at the LSC** ha sido realizada bajo su dirección y tutela en el Instituto de Física Corpuscular, centro mixto de la Universidad de Valencia y del CSIC, por **Brais Palmeiro Pazos**, y constituye su Tesis para optar al grado de Doctor por la Universitat de València una vez cursados los estudios en el Doctorado en Física.

Valencia, a 21 de Diciembre de 2021,

Michel Sorel   Jose Ángel Hernando Morata

Nuria Rius Dionis

In time, mutations occurred, and an odd subset of humans began roaming the land. They were arrogant. They were not content to enjoy the magnificence of the universe. They asked "How?" How was the universe created? How can the "stuff" of the universe be responsible for the incredible variety in our world: stars, planets, sea otters, oceans, coral, sunlight, the human brain? The mutants had posed a question that could be answered — but only with the labor of millennia and with a dedication handed down from master to student for a hundred generations. The question also inspired a great number of wrong and embarrassing answers. Fortunately, these mutants were born without a sense of embarrassment. They were called physicists.

Leon M. Lederman
The God Particle:
If the Universe Is the Answer, What Is the Question?

Resumen

El estudio de los neutrinos ha supuesto varias revoluciones en el pensamiento sobre el funcionamiento de la naturaleza. De hecho, la confirmación en la primera década del siglo XXI de que los neutrinos son partículas con masa da cuenta de que aún juegan un papel importante en los paradigmas actuales. La observación de su masa implica que el modelo actual de la física de partículas (SM) falla en una de sus asunciones principales. La manera de incorporar esta masa en una extensión del SM abre dos posibilidades: que sean fermiones de Dirac o de Majorana.

La primera se basa en introducir un término de masas análogo al de los demás fermiones del SM. Este añadido tiene la indudable ventaja de continuar el esquema ya trazado dentro del modelo. Sin embargo, pese a que esta postura sería la más directa, presenta el inconveniente de tener que incluir los campos de dextrógiros para los neutrinos. Dichos estados no tendrían ninguna interacción dentro del SM, ergo, a priori, serían estados inobservables.

La otra posibilidad sería que fueran neutrinos de Majorana. El mecanismo, propuesto a principios del siglo XX, proporciona un término de masas alternativo, solo posible para fermiones neutros. Así mismo, como consecuencia, implica que dicho fermión sería su propia antipartícula. El principal inconveniente es que dicha naturaleza no ha sido aún observada en partículas elementales al ser solo accesible a los neutrinos. Por otro lado, las ventajas son bastante interesantes. En primer lugar, no necesita de la incorporación *ad hoc* de los dos campos quirales que sí precisa el otro método. Además, esta hipótesis abre la puerta a una serie de mecanismos de adquisición de masas (*seesaw* o balancín) que de manera natural explicarían la gran diferencia de escala que tienen las masas de los neutrinos con respecto a los demás fermiones. A mayores, el término de masas introduce una violación en la conservación del número leptónico, lo que encajaría con los requisitos para la *leptogénesis*, que intenta explicar la asimetría entre materia y antimateria presente en el universo actual.

La hipótesis de Majorana traería consigo una nueva y rica fenomenología que se puede explotar para tratar de dilucidar la naturaleza última de los neutrinos. Entre ellas, la más madura experimentalmente, y en la actualidad más prometedora, es la desintegración doble beta sin neutrinos. Siguiendo el teorema de la caja negra,

de observarse dicha interacción, se probaría inequívocamente que los neutrinos son fermiones de Majorana.

Desintegraciones doble beta

La desintegración doble beta con emisión de neutrinos ($2\nu\beta\beta$) es un proceso nuclear posible y observable, aunque muy lento. Tiene lugar cuando dos de los nucleones de un determinado isótopo se desintegran en un proceso beta simultáneamente, emitiendo dos partículas beta y dos neutrinos. Es decir, en el caso de una doble transición β^- se tendría un isótopo de número atómico Z y número másico A transformándose en su isóbaro con $Z+2$ y la emisión de dos electrones y dos antineutrinos:

$$ {}^A_Z X \rightarrow^A_{Z+2} Y + 2e^- + 2\overline{\nu}_e. $$

Aunque se puede dar en cualquier núcleo, su presencia es despreciable frente a la desintegración beta simple. Es decir, solo es observable en aquellos isótopos cuya desintegración beta simple está prohibida o altamente suprimida.

En el caso de que los neutrinos fuesen fermiones de Majorana, se abre la posibilidad de que un antineutrino procedente de una de las desintegraciones podría introducirse como neutrino en la otra y hacer una beta inversa, con lo que el resultado del proceso sería el mismo que el anterior, pero sin la emisión de los dos neutrinos. Este proceso, conocido como desintegración doble beta sin emisión de neutrinos ($0\nu\beta\beta$), estaría aún más suprimido que el caso estándar, dado el cambio de helicidad del neutrino, y, hasta la fecha, no ha habido ningún indicio experimental de su existencia.

En el caso más simple del proceso de un intercambio de neutrinos ligeros, la semivida del mismo vendría dado por

$$ \left(T^{0\nu}_{1/2}\right)^{-1} = G^{0\nu}|M^{0\nu}|^2 \left(\frac{m_{\beta\beta}}{m_e}\right)^2, $$

donde $G^{0\nu}(Q,Z)$ es un factor del espacio de fases que depende del *Q-value* de la transición y de la carga; $M^{0\nu}$ es el elemento de matriz nuclear, que se calcula de manera teórica y es bastante dependiente del modelo elegido para su evaluación y $m_{\beta\beta}$ es la llamada masa de Majorana efectiva, que define como

$$ m_{\beta\beta} = |U^2_{ei} m_i|, $$

donde U es la matriz de Pontecorvo-Maki-Nakagawa-Sakata, que da cuenta de la relación entre los autoestados de masa y de sabor de los neutrinos, m las masas de los neutrinos e i recorre los índices de los autoestados de masa.

Desde el punto de vista experimental, la observación del proceso es un todo un reto. Debido a su carácter monoenergético, la primera señal que se debería buscar es la suma de las energías de los electrones emitidos. Sin embargo, la radiación natural, varios órdenes de magnitud más abundante, dificultan enormemente la tarea. Es por eso que tecnologías que sean capaces de aportar más información que la simple calorimetría ayudan enormemente a discriminar la señal del fondo.

En la tarea de elegir el isótopo de interés para la desintegración, no existe un candidato privilegiado. Hay que tener en cuenta muchos parámetros interrelacionados, como son la abundancia natural, su precio de enriquecimiento, el *Q-value* del proceso y la tasa de desintegración del modo con neutrinos del isótopo. En cuanto a la abundancia y enriquecimiento, son un claro limitante en la tendencia de acumular la mayor cantidad del elemento de interés para aumentar la exposición. Un alto *Q-value* tiene dos efectos positivos. El primero es que la semivida de la desintegración depende en última instancia de la quinta potencia de este. El segundo es que a mayor *Q-value*, menor es el peligro que la radioactividad natural. Por último, el modo con dos neutrinos es un ruido irreducible y, por tanto, cuanta mayor sea la diferencia entre los dos procesos, peor efecto tendrá en la búsqueda.

Otro factor fundamental a tener en cuenta a la hora de diseñar este tipo de proyectos es la influencia que otras interacciones pueden tener en el detector, el llamado ruido, fondo o *background*. La principal fuente de ruido a nivel del mar es la radiación cósmica y sus efectos (como las activaciones por captura de neutrones). Para evitarla al mayor grado posible, los experimentos se construyen y operan en laboratorios subterráneos ya que la roca por encima reduce varios órdenes de magnitud la influencia de dicha radiación. Otra preocupación es la radiación natural, proveniente de isótopos radiactivos presentes en cualquier material. Por tanto, durante el diseño y construcción, los materiales han de ser cuidadosamente analizados para seleccionar las opciones más radiopuras y evaluar su impacto en las medidas que se lleven a cabo. Por último, el radon es un gas noble radiactivo con una gran difusión que también puede afectar a las medidas, aunque pueden ser reducidos con el uso de filtros de radón. Los sistemas de blindaje pasivos y activos son también usados para controlar los posibles fondos residuales remanentes.

Desde principios del s. XXI ha habido un interés creciente en la $0\nu\beta\beta$, que ha motivado una profunda actividad que ha paulatinamente acotado más los límites para la semivida en diversas propuestas experimentales. Actualmente, el liderazgo está ejercido por GERDA usando $^{76}\mathrm{Ge}$ y Kamland-Zen y EXO-200 usando $^{136}\mathrm{Xe}$. Además, el campo se encuentra a las puertas del salto a los detectores con una tonelada de masa del isotopo de interés. El límite actual en la semivida, marcado por Kamland-Zen, es de $T^{0\nu}_{1/2} > 10.7 \cdot 10^{25}$ yr (90% CL), que se traduce en una masa de Majorana efectiva de $m_{\beta\beta} >$ 61–165 meV (90% CL) (donde el rango depende de la incertidumbre en el elemento de matriz nuclear).

NEXT

NEXT (Neutrino Experiment with a Xenon TPC) es uno de los experimentos de nueva generación encaminados a la detección de la $0\nu\beta\beta$ en $^{136}\mathrm{Xe}$. El experimento emplea una cámara de proyección temporal (TPC) con xenon gaseoso a alta presión, con gas enriquecido al 91 % en $^{136}\mathrm{Xe}$ a 15 bar. El detector presenta una técnica de detección novedosa (SOFT) que se basa en la separación de la adquisición de la información de la energía y la topología del evento. La cámara tiene forma cilíndrica y uno de los planos (EP) está instrumentado con PMTs (tubos fotomultiplicadores), que son excelentes midiendo la energía, mientras que el plano opuesto (TP) está instrumentado con SiPMs (fotomultiplicadores de silicio) con una alta densidad, lo que permite una buena determinación de la información espacial del evento. Los objetivos del experimento son una resolución energética en el Q-value del $^{136}\mathrm{Xe}$ mejor del 1 % FWHM y una buena discriminación de la señal y el fondo mediante el uso de la información topológica.

Cuando una partícula cargada se propaga en el gas, es capaz de arrancar electrones secundarios del Xe. Este proceso crea un leve centelleo (S_1) que es recogido en el EP y actúa como trigger. El campo eléctrico presente dentro de la cámara evita que estos electrones secundarios se recombinen y comiencen a desplazarse hacia el ánodo. Justo antes de llegar a este atraviesan una región, llamada gate, donde el campo es mucho más intenso. Este campo los acelera fuertemente contra el TP, haciendo que por el camino exciten el gas, que en el proceso de desexcitación liberan una gran cantidad de luz (S_2). Parte de esa luz se recoge en el EP, dando lugar a la medida energética, y otra parte se recoge en el TP, dando lugar a la caracterización de las coordenadas xy del evento. El tiempo entre el S_1 y el S_2 da cuenta de la coordenada z.

La elección de la fase gaseosa se debe a la mejor resolución energética intrínseca que esta presenta ($\sim$ 0.3 % FWHM en la $Q_{\beta\beta}$). El uso de la electroluminiscencia también sigue criterios de mejorar la resolución, siendo que este método tiene significativamente menos fluctuaciones que la recolección de carga. De hecho, en condiciones óptimas, los detectores han demostrado resoluciones cercanas a la intrínseca.

El otro buque insignia del proyecto es la capacidad que ofrece el xenon gaseoso de producir trazas para los electrones. Esto permite reconstruir los eventos y desarrollar técnicas que permiten la discriminación de eventos que presenten un solo electrón a otros que presenten dos.

La fase inicial de la colaboración (2009-2014) se centró en demostrar las capacidades del método en términos de resolución energética y reconstrucción de trazas con detectores con $\sim$ 1 kg de gas. Los resultados concernientes a la mejor resolución energética en ambos prototipos fueron de 1 % FWHM (0.5 % FWHM) a 662 keV y 1.62 % FWHM (0.74 % FWHM) a 511 keV (y su extrapolación naíf a la energía de la $Q_{\beta\beta}$), para NEXT-DBDM y NEXT-DEMO respectivamente. Así mismo, NEXT-DEMO demostró un buen comportamiento del poder de selección topológica con una reducción del fondo del $\sim$76 % frente a una eficiencia para la señal del $\sim$66 %.

El siguiente paso fue la construcción y puesta en funcionamiento de NEXT-White (2016-2021). Este detector es una versión a escala 1:2 de NEXT-100, con $\sim$ 5 Kg of Xe, e implementa la mayoría de las soluciones técnicas y materiales proyectados para este. Además, fue el primer prototipo construido con el objetivo de ser radiopuro, así como el primero en desarrollarse en un laboratorio subterráneo, el LSC. Los principales objetivos del detector fueron la validación del concepto de diseño en una máquina de grandes dimensiones, la evaluación de las predicciones sobre el fondo esperado y la medida de la semivida de la $2\nu\beta\beta$. Todos ellos han resultado un rotundo éxito del detector.

Actualmente, la colaboración está centrada en el siguiente paso del programa, empezando la construcción y puesta en marcha de NEXT-100 en 2021. NEXT-100 contendrá hasta $\sim$ 100 Kg y será capaz de poner un límite a la semivida de la $0\nu\beta\beta$ competitivo con los mejores de hoy en día. El salto a los detectores con una tonelada de masa de isótopo está también en consideración y es un campo activo de investigación, tratando de proyectar las lecciones aprendidas en el proceso, así como de incorporar nuevas ideas como las mezclas de gases de baja difusión o el *barium tagging*.

Calibración de baja energía y monitoreo continuo en NEXT-White

La desintegración por conversión interna del isómero $^{83m}\mathrm{Kr}$ produce una señal monoenergética de 41.5 keV. Además, como es un gas, y su vida media lo permite, es capaz de difundirse por todo el volumen activo y generar eventos por toda la cámara. Esto es especialmente útil a la hora de realizar la calibración del detector.

Los sensores de medida sufren ajustes regulares derivados de datos tomados durante la operación del detector, con LEDs situados en el plano opuesto. Esto, no obstante, no es suficiente, ya que no es capaz de tener en cuenta los efectos que se producen en la zona de electroluminiscencia, debido a imperfecciones en los planos, ni los derivados de la captación de electrones secundarios durante su desplazamiento, debido a impurezas en el gas. Es por ello que la presencia de eventos de $^{83m}\mathrm{Kr}$ es tan útil, ya que permite conocer la respuesta a datos dentro de la cámara, fáciles de identificar y con una energía característica, que da cuenta de los efectos de distorsión que suceden y permite ecualizar la respuesta en todo el detector.

La herramienta para las correcciones son los llamados *mapas* de energía (o de geometría) y *lifetime*. Esta última se extrae mediante un ajuste a una exponencial en el eje z (efecto esperado de la captación de los electrones secundarios) en función de x e y. Las correcciones energéticas dependen igualmente de las coordenadas transversales y se obtienen como la energía en $z = 0$, también del ajuste exponencial. Estos mapas han permitido la obtención de excelentes resoluciones no solo en las bajas energías, sino un funcionamiento correcto en todo el rango de interés para la colaboración (aunque para trazas extensas, algunas correcciones adicionales han de ser tomadas en cuenta para refinar la medida).

A mayores, también se ha estudiado la estabilidad de dichos mapas a lo largo de toda la toma de datos, comprendiendo largos períodos con diversas configuraciones de los campos eléctricos y presión. En cuanto a los mapas geométricos, se ha observado una gran estabilidad en la totalidad del tiempo estudiado, con el único cambio de la escala de energía de todo el mapa, pero la forma del mapa es compatible entre distintos runes y períodos. Esto indica que las condiciones del campo eléctrico y de propagación y reflexión de luz apenas varían con el tiempo. Además, abre la puerta a estrategias de cara a las futuras generaciones en las que el mayor tamaño de los detectores supondrá un reto de cara a la toma continua de datos de Kr, por la excesiva cantidad de eventos para producir los mapas. En cambio, todo indica que se podría hacer una campaña dedicada a la obtención del mapa geométrico y asumir que es constante, con las debidas comprobaciones y calibraciones intermedias.

En cambio, los mapas de *lifetime* sí han presentado una notable variación en el tiempo, muy posiblemente relacionados con las variaciones de los patrones de flujo del gas en el detector, lo cual ha sido tenido en cuenta generando un mapa cada día de toma de datos, para hacer la corrección lo más pormenorizada, y aún significativa, posible. Un entendimiento más profundo y pormenorizado del comportamiento del gas en la cámara permitiría entender mejor esta relación y, pensando en las limitaciones de las futuras generaciones, disminuir la necesidad del gran volumen de datos para corregir los efectos de *lifetime*.

Por otra parte, la posibilidad de una doble adquisición de datos, con una parte dedicada a los eventos de interés en la región de alta energía y otra a los eventos de calibración de baja energía, no solo ha permitido la elaboración de mapas en un esquema diario sin necesidad de interrumpir las campañas de física, sino que también ha abierto la puerta a usar los datos del $^{83m}\mathrm{Kr}$ como una herramienta para el monitoreo casi continuo de las condiciones del detector. La cámara muestra un buen comportamiento, estabilidad razonable y una adecuada recuperación de los diferentes inconvenientes sufridos, como cambios de temperatura en el laboratorio y chispas dentro del sistema de alto voltaje del aparato. Además, también se ha constatado la mejora ininterrumpida de la *lifetime*, pasando de unos pocos cientos de microsegundos al comienzo de las operaciones a más de trece milisegundos al terminar la toma de datos del detector. Así mismo, se ha puesto de manifiesto como un mejor control sobre las condiciones externas del detector (concretamente el sistema de aire limpio de radón y el castillo interno, que aislaban el sistema de los cambios del laboratorio y proporcionaban condiciones constantes) repercute directamente en una mayor estabilidad de la *lifetime* registrada.

Impacto del radon interno en el programa de NEXT

El gas radón es un problema típico en los experimentos en la búsqueda de eventos extraordinariamente raros. Su habilidad de emanar de cualquier material y difundirse por todo el detector lo convierten en un potencial peligro. Además, dado que es un gas y su vida media lo permite, alcanza una distribución homogénea en el volumen activo. Los núcleos descendientes pueden ser conducidos por los campos eléctricos hacia el cátodo, donde se acumulan. De entre todos los isótopos presentes en la naturaleza, se ha encontrado que el único problemático en el caso de NEXT-White es el $^{222}\mathrm{Rn}$, dado que es el único que se ha medido a un nivel significativo.

Después de una caracterización completa de las desintegraciones alfa en NEXT-White, con varias tomas de datos específicas, la tasa del $^{222}\mathrm{Rn}$ durante el período de baja actividad del radon hallada es (38.1 ± 2.2 (stat) ± 5.9 (sys)) mBq/m^3. A mayores, se ha demostrado que esta tasa es suficiente para explicar la presencia y tasa de electrones en el cátodo, que se asumen estar dominados por la progenie del radon. Con estos resultados, se concluye que la contaminación debida al $^{222}\mathrm{Rn}$ en NEXT-White está muy por debajo de lo esperado de otras fuentes, por tanto despreciable, y que la actividad observada puede ser empleada para hacer predicciones sobre el impacto de este en el programa de NEXT-100.

Con esa finalidad, se han llevado a cabo una serie de simulaciones de Monte-Carlo (MC) y posterior reconstrucción de eventos y análisis, tanto para NEXT-White, con la finalidad entender la comparativa entre datos y simulación y prever la incidencia en la medida de la desintegración $2\nu\beta\beta$, como para NEXT-100, para evaluar la predicción de los efectos en la búsqueda de la desintegración $0\nu\beta\beta$. Los resultados se han calculado teniendo en cuenta dos posibles extrapolaciones de las medidas: un escenario pesimista y otro optimista. El escenario pesimista asume el peor caso posible donde las contribuciones del radon provienen de las emanaciones de los componentes internos del detector, haciendo que escalen con el área interna expuesta al gas del mismo (seis veces mayor en el caso de NEXT-100 con respecto NEXT-White) y que la eficiencia de selección de señal se comporta de manera conservativa, obteniéndose una tasa de (0.07 ± 0.03) cuentas/a. En cambio, el caso optimista considera que la emisión del radón dominante proviene del sistema de gas, siendo por tanto el mismo (o muy similar) que en el caso de NEXT-White y que la reconstrucción se comporta de manera favorable, resultando en un ratio de $(3.9 \pm 2.1) \cdot 10^{-3}$ cuentas/a. Cuando se comparan estas predicciones con las demás fuentes de ruido esperadas para el detector, incluso en el escenario más pesimista, la contribución se encuentra un orden de magnitud más bajo que la fuente dominante. Posiblemente será aún más depreciable si se cumplen las condiciones favorables.

Se puede concluir, por tanto, que los fondos debidos al radón en el detector NEXT-100 tendrán lugar a un nivel más que tolerable para sus propósitos y que no serán necesarias mayores acciones en ese aspecto.

Fondo de radioactividad natural en NEXT-White

Las impurezas radioactivas contenidas en todo tipo de materiales representa un ruido dominante para muchos experimentos de muy bajo fondo. Se ha realizado un estudio sobre la selección de datos, el modelo de fondo en MonteCarlo y su comparación con los datos medidos, así como una discusión sobre la extrapolación de estos resultados en la campaña de medida de las doble betas. El análisis se basa en una intensa y dedicada campaña de simulaciones de MC, los datos de bajo fondo del Run IV (de $\sim$ 40 días de duración a caballo entre 2018 y 2019), y datos de calibraciones de alta energía tomados durante el período del citado Run IV.

Los isótopos identificados como potenciales problemas para las distintas campañas de NEXT son cuatro. En primer lugar, el ^{40}K y ^{60}Co son dominantes en la región de energías medias (hasta $\sim$1.5 keV). Por lo tanto, son de especial relevancia en el estudio de la desintegración $2\nu\beta\beta$. Por otro lado, el ^{208}Tl y ^{212}Bi tienen fotopicos cercanos a la región de interés de la desintegración $0\nu\beta\beta$, así como una presencia notable en las medias-altas energías consideradas en el experimento, con lo que también tienen relevancia en el estudio de la $2\nu\beta\beta$.

El diseño del detector incluye una primera fase de selección meticulosa de todos los materiales presentes, así como una campaña exhaustiva de simulaciones para evaluar el impacto de la actividad de los distintos materiales, debido a su lugar con respecto al volumen activo, lo que conlleva la consideración de un modelo para las expectativas del fondo. La tasa de eventos predicha por el modelo, para eventos con $E >$1 MeV es de (0.489 $\pm$ 0.002 (stat) $\pm$ 0.0042 (sys)) mHz, mientras que la tasa medida en el experimento fue de (0.84 $\pm$ 0.02) mHz.

Posteriormente, y tras una selección fiducial de datos, un ajuste a las distribuciones de energía y z de los datos de fondo con respecto a las predicciones del modelo suponen una manera de inferir la contribución por isótopo a la tasa total medida, así como la distribución espacial del mismo. Los isótopos de interés son cuatro: ^{40}K y ^{60}Co, especialmente dominantes en la región de interés para la $2\nu\beta\beta$, y ^{208}Tl y ^{214}Bi, con emisiones gamma muy cerca de la región de interés para la $0\nu\beta\beta$. Las contribuciones halladas para cada isótopo considerado serían: $R_{^{40}\mathrm{K}} =$ 0.13 $\pm$ 0.02, $R_{^{60}\mathrm{Co}} =$ 0.23 $\pm$ 0.02, $R_{^{208}\mathrm{Tl}} =$ 0.27 $\pm$ 0.02 y $R_{^{214}\mathrm{Bi}} =$ 0.23 $\pm$ 0.02. En cuanto a la información espacial, el exceso más significativo parece provenir de la región del ánodo.

Con la finalidad de emplear estos resultados para estimar el impacto del fondo en las búsquedas de $\beta\beta$, se han considerado una serie de cortes adicionales: los eventos deben presentar una sola traza y sus trazas han de presentar las características topológicas de una traza de dos electrones (esto es, presentar dos picos de Bragg en los extremos de la traza, llamados *blobs*). La tasa del fondo tras la selección topológica es (0.248 $\pm$ 0.010) mHz en el caso de los datos y de (0.246 $\pm$ 0.001 (stat) $\pm$ 0.008 (sys)) mHz para las predicciones del MC. Los datos del mejor ajuste al fondo se han usado para estimar la sensitividad de NEXT-White a la medida de la $2\nu\beta\beta$, que resulta ser (3.5 $\pm$ 0.6) σ y (5.1 $\pm$ 0.4) σ para el caso de la selección estándar y mejorada, respectivamente, para un año de toma de datos. Respecto a la $0\nu\beta\beta$, el fondo esperado en una amplia ventana de 200 keV alrededor de la $Q_{\beta\beta}$ es (0.75 ± 0.12 (stat) ± 0.02 (sys)) eventos en 37.9 días, mientras que se ha observado 1 evento en los datos. Por ende, el modelo del fondo definido para datos con $E > 1\,$MeV se valida incluso en el rango de alta energía de la $0\nu\beta\beta$.

Conclusiones

La naturaleza de los neutrinos es una de las grandes cuestiones pendientes en la física actual y su respuesta abre las puertas a un rico camino para el futuro del campo. Hoy en día, las mayores esperanzas para hallar la respuesta están centradas en la búsqueda de la desintegración $0\nu\beta\beta$. NEXT es uno de los experimentos diseñados para tal fin, que intenta encontrar el proceso en $^{136}\mathrm{Xe}$, con una cámara de proyección temporal de gas a alta presión. Los prototipos han mostrado un gran desempeño en el camino final de llegar a la siguiente generación de detectores. Entre ellos se encuentra el más reciente, NEXT-White, el primer detector de grandes dimensiones de la colaboración.

La calibración del detector es un tema central en el experimento. Se ha visto que los datos de baja energía de la transición interna del $^{83m}\mathrm{Kr}$ son de extrema utilidad para desarrollar los mecanismos de corrección geométrica y de *lifetime*. Así mismo, la continua toma de este tipo de datos ha supuesto la posibilidad de llevar a cabo un profundo monitoreo de las condiciones de la cámara en tiempo real.

Además, siendo uno de los propósitos fundamentales del prototipo, se han estudiado y determinado las influencias de dos fondos de especial interés. En el primer caso, el causado por el $^{222}\mathrm{Rn}$ ha sido medido y demostrado que no presenta un riesgo real ni para la física de NEXT-White ni para el futuro programa de NEXT-100. En cuanto a los fondos radiogénicos, si bien exceden las primeras proyecciones de los estudios previos, han sido medidos y comprendidos con un nivel más que suficiente para los objetivos del detector y sus futuros acometidos.

Preface

Neutrinos' nature is one of the most important open questions in the current paradigm of Particle Physics, and its answer promises a bright future for the field. Among all the possible ways to discern neutrinos' true nature, neutrinoless double beta decay is currently the most promising and developed technique. Double beta decay with neutrino emission is a standard process allowed within the SM and has been observed for several nuclei. Notwithstanding, the neutrinoless mode is only possible if neutrinos present a Majorana nature.

NEXT is an experiment that seeks to find such an interaction in $^{136}\mathrm{Xe}$, using a high-pressure gas time projection chamber. It proposes a novel technique for the detection, the SOFT concept, that consists of the separation of the energy and spatial information in two independent measurement planes. The project is founded on a solid R&D program that has already proven some of the relevant challenges concerning the proof of concept, the excellent energy resolution, the background model, and the topological potentials. The most recent prototype, NEXT-White, is the first large-scale detector operated by the collaboration.

This work is focused on two crucial aspects of the NEXT-White operation and its objectives: low energy calibration and background studies.

Detector calibration is a key consideration for the experiment. $^{83m}\mathrm{Kr}$ internal transition has shown to be an extremely useful tool in order to develop not only the geometric and lifetime corrections but also the continuous screening of the NEXT-White chamber conditions during 2017-2021.

Finally, following the goals of the detector, two significant sources of background have been studied and their impact on the physics program assessed. First, the $^{222}\mathrm{Rn}$ related one has been measured and shown that it does not represent any concern for the objectives for either NEXT-White or NEXT-100. Second, regarding the radiogenic contaminations, although the measured rates exceeded the initial prospects, they have been determined and understood to a comfortable level for the remaining detector's goals.

⁂

This thesis is arranged into ten chapters, subdivided into several parts.

Chapter 1 covers the basics of Particle Physics related to the phenomenology of massive neutrinos. Additionally, Chapter 2 focuses on the main aspects of the neutrinoless double-beta decay, both theoretical and experimental. Also, it presents the state of the art of the field.

The following three chapters present the NEXT experiment's main features and the road map (Chapter 3), NEXT-White design description and performance (Chapter 4), and the central elements concerning the collaboration reconstruction and simulation tools (Chapter 5).

Chapter 6 describes the low-energy calibration procedure developed for the detector and the possibility of using that kind of data to monitor the chamber conditions continuously. The correction procedure is based on the publication.

- NEXT Collaboration, G. Martínez-Lema, J.A. Hernando Morata, **B. Palmeiro** et al., *Calibration of the NEXT-White detector using* $^{83m}\mathrm{Kr}$ *decays*, Journal of Instrumentation 13, P10014 (2018), [arXiv:1804.01780].

of which I am one of the principal authors.

The last part of the work reports the studies performed to evaluate the impact of the background in the NEXT program. After a brief characterization of the potential backgrounds (Chapter 7), the particular cases for the $^{222}\mathrm{Rn}$ (Chapter 8) and radiogenic (Chapter 9) backgrounds are presented. Those chapters are based on the publications.

- NEXT Collaboration, P. Novella, **B. Palmeiro** , A. Simón, M. Sorel et al., *Measurement of radon-induced backgrounds in the NEXT double beta decay experiment*, JHEP 10, 112 (2018), [arXiv:1804.00471]
- NEXT Collaboration, P. Novella, **B. Palmeiro** , M. Sorel, A. Usón et al., *Radiogenic Backgrounds in the NEXT Double Beta Decay Experiment*, JHEP 10, 051 (2019), [arXiv:1905.13625]

respectively, of which I am one of the main authors.

Finally, Chapter 10 concludes the thesis.

Afterward, four appendices gather some supplemental material for the report. First, Appendix A provides a more detailed evolution of the maps within the operation time. Then, Appendix B exemplifies the data selection for the alpha analysis.

Appendix C displays the actual parameters involved in the background model construction. To conclude, Appendix D presents additional material to evaluate the background fits.

Acknowledgements

This dissertation represents the end of a long epoch and an indispensable step on the just starting journey. Countless people have supported the work here presented one way or another, converting it into a sort of collective effort. To all of them, my deepest gratitude, I am very thankful for having encountered you along the route.

Now (it might be the only reason you even open the book), let me do a *little* name-dropping trying to cover everyone (in the hope that you, my dearest reader, can find yourself).

I must first express my appreciation to my supervisors, **José Ángel** and **Michel**. José Ángel, thank you very much for guiding my initial steps in research and introducing me to the exciting field of Neutrino Physics, particularly to the NEXT experiment and all the crew. Michel, I owe you my transition into a fully developed scientist. Thank you both for your (incommensurable) patience and guidance throughout this –sometimes rocky– journey.

I would like to extend my gratitude to our great spokesperson, **JJ**; the tons of hours discussing with you have broadened my understanding of Physics and life. Additionally, it is fair to acknowledge all the support and company I've found within the NEXT collaboration, particularly the Spanish team's people. Thanks for welcoming me as part of the family and helping on uncountable occasions.

Vull agrair també a tota la gent que vaig conèixer a València, la meua terreta d'adopció.

Primer de tot, a tots els companys de l'IFIC amb els que vaig compartir tants moments. Gràcies a **Paola** i a **Andrew**, els millors amfitrions que es pot demanar, tant ajudant amb les preguntes contínues com en un sopar descobrint la ciutat. Gràcies als nexters més veterans per la seua disposició a donar un cop de mà i discutir qualsevol problema: **Pau**, **Neus**, **Francesc**, **Josh** i **Justo**. També als infatigables habitants del despatx: **Alberto**, **Miryam**, **Carmen**, **Marija**, **Ander**, **Jose María**, **Ryan**, **Javi M.**, **Javi P.**, **Miquel** i **Ale**; les penúries del doctorat semblen innocents amb gent com vosaltres al costat. No seria just oblidar tampoc els veïns del zulo, que sempre són un plaer visitar: **Vicente**, **Sara**, **Javi**, **Marc** i **Alberto**. Menció especial per **José**, per salvar-me del caos burocràtic en tantes ocasions.

En segon lloc, cal reconèixer el fantàstic equip que estic joiós d'haver descobert, el meu seny de la pandèmia, postpandèmia i tot el que queda per venir: **Miguel**, **Pablo**, **Inma**, **Lydia** i **Juan**. A **Cristian**, moltes gràcies per obrir-li la teua llar a aquest nòmada. A **Txema** per les passejades quan la saturació creixia.

Gràcies als companys d'aventures per Amèrica: Miguel G., **Miguel E.**, **José** i **Cristoph**. Així mateix, a **Pilar**, per moltes empanadas improvisades més. Molt agraït a més a **Olga** i Michel, així dóna gust anar d'estada! Many thanks too to **Adam**, not only a great host but also a person to learn how to understand the fundamentals of any problem.

Tampouco me esquezo de toda a xente de Santiago, a de toda a vida e aos máis recentes.

Non podo evitar empezar por **Gonzalo**; sen a túa dedicación, traballo, paciencia e axuda prestada no meu devagar polo mundo da investigación e da programación seguramente non habería nin unha soa verba neste traballo. Aos compañeiros de fatigas en Condesa, que axudan a non perderse: **Alicia**, **Jorge**, **Miguel**, **Sofía**, **Miriam**, **Antonela**, **Cris**, **Fran** e **Xuan**; todo se ve máis doado diante dun café. A **Martín**, **Sandra** e **Dani** por terme aturado todo este tempo. Aos compañeiros da OUSC que fixeron enormemente interesantes estes anos, en especial: **Laura**, **Manuchelo**, **Carmen J.**, **Carmen E.**, **Clara**, **Gonzalo**, **Sabela**, **Ana**, **Julia**, **Maritza** e **Mario**. Nos lindeiros da música, unha aperta tamén aos antigos compañeiros de andanzas no conser **Sabela**, **Tania**, **Ana**, **Paula**, **Roberto** e **Marta**. Non podería escapar tampouco sen mencionar **Antía**, compañeira de mil viaxes e aínda máis *escapes*.

Por último, e non para nada menos importante, aos principais actores da miña vida. Grazas a **meus pais**, **miña irmá** e familia en xeral por estar sempre aí, ser o soporte en tempos duros e partícipes dos momentos doces. En resumo, por facerme ser quen cheguei a ser hoxe en día. Mil grazas a **Sergio** tamén, que chegou para poñer un broche de ouro a esta etapa. Xa levas demostrada moita paciencia... e a que che queda!

A todos os que estades e aos que non estades, e ata dos que me esquecín de nomear (xa o sinto), grazas de corazón!

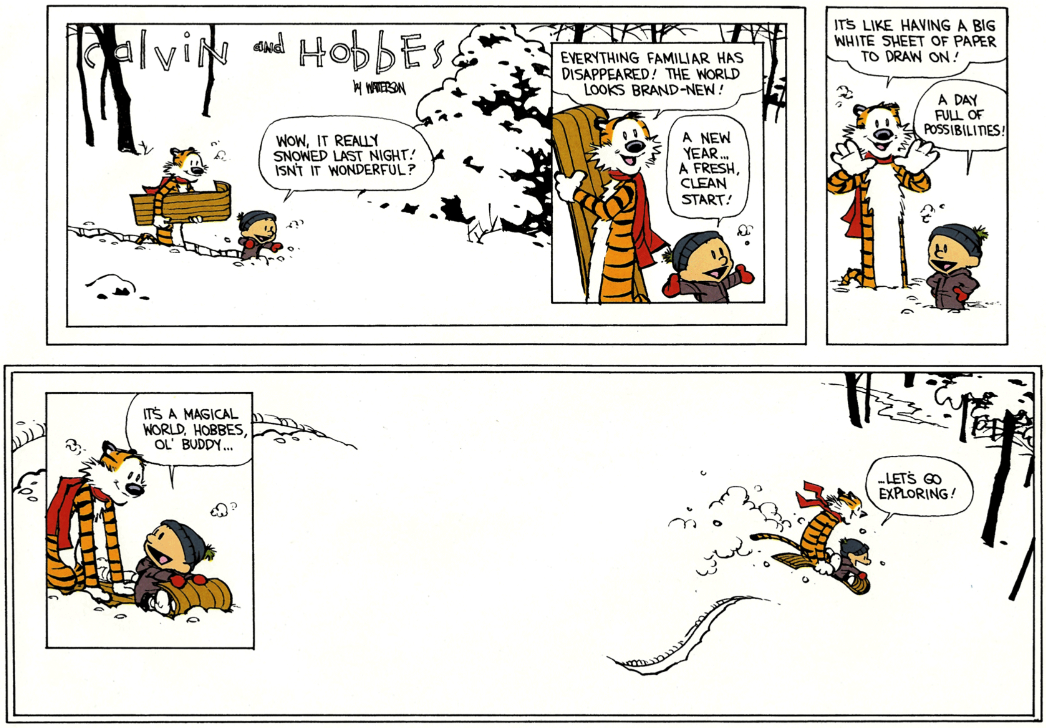
calvin and HoBBES
by WATTERSON
WOW, IT REALLY SNOWED LAST NIGHT! ISN'T IT WONDERFUL?
EVERYTHING FAMILIAR HAS DISAPPEARED! THE WORLD LOOKS BRAND-NEW!
A NEW YEAR... A FRESH, CLEAN START!
IT'S LIKE HAVING A BIG WHITE SHEET OF PAPER TO DRAW ON!
A DAY FULL OF POSSIBILITIES!
IT'S A MAGICAL WORLD, HOBBES, OL' BUDDY...
...LET'S GO EXPLORING!

Contents

List of Figures

List of Tables

Acronyms

$\beta\beta$	Double Beta decay.
$0\nu\beta\beta$	Neutrinoless Double Beta decay.
$2\nu\beta\beta$	Two Neutrino Double Beta decay.
BAO	**B**aryon **A**coustic **O**scillation.
BEGe	**B**road-**E**nergy **Ge**rmanium.
BFS	**B**readth **F**irst **S**earch.
BLR	**B**ase **L**ine **R**estauration.
BOLD	**B**arium i**O**n textbfLight **D**etection.
BSM	**B**eyond **S**tandard **M**odel.
Cν**B**	**C**osmic **N**eutrino **B**ackground.
CERN	European Organization for Nuclear Research.
CKM	**C**abibbo-**K**obayashi-**M**askawa.
CMB	**C**osmic **M**icrowave **B**ackground.
CP	**C**harge Conjugation and **P**arity.
CUORE	**C**ryogenic **U**nderground **O**bservatory for **R**are **E**vents.
DAQ	**D**ata **acq**uisition.
DBDM	**D**ouble **B**eta and **D**ark **M**atter.
detsim	**Det**ector **Sim**ulation.
DNN	**D**eep **N**eural **N**etwork.
DONUT	**D**irect **O**bservation of the **Nu** **T**au.

DST	**D**ata **S**ummary **T**ape.
DUNE	**D**eep **U**nderground **N**eutrino **E**xperiment.
ECC	**E**mulsion **C**loud **C**hamber.
EL	**E**lectro**l**uminescence.
EP	**E**nergy **P**lane.
EXO	**E**nriched **X**enon **O**bservatory.
FANAL	**F**ast **Ana**lysis.
FC	**F**ield **C**age.
FEC	**F**ront-**E**end **C**oncentrator.
FWHM	**F**ull **W**idth at **H**alf **M**aximum.
GERDA	**Ger**manium **D**etector **A**rray.
GUT	**G**rand **U**nified **T**heory.
GWS	**G**lashow-**W**einberg-**S**alam.
HD	**H**igh **D**efinition.
HDPE	**H**igh-**d**ensity **P**oly**e**thilene.
HM	**H**eidelberg-**M**oscow.
HPXe	**H**igh-**P**ressure gas-**Xe**.
IC	**I**nvisible **C**ities.
ICS	**I**nner **C**opper **S**hielding.
ICS	**I**nner textbfLead-**C**astle.
IO	**I**nverted **O**rdering.
ITO	**I**ndium **t**inl **o**xide.
KamLAND-Zen	**Kam**ioka **L**iquid Scintillator **A**ni**n**eutrino **D**etector - **Ze**ro **N**eutrino.
KATRIN	**Ka**rlsruhe **Tri**tium **N**eutrino Experiment.

LAr	**L**iquid **Ar**gon.
LBL	**L**ong **B**ase **L**ine.
LC	**L**ead-**C**astle.
LFV	**L**epton **F**lavor **V**iolation.
LNGS	**L**aboratori **N**azionali del **G**ran **S**asso.
LNV	**L**epton **N**umber **V**iolation.
LS	**L**iquid **S**cintillator.
LSC	**L**aboratorio **S**ubterráneo de **C**anfranc.
LXe	**L**iquid **Xe**non.
MBL	**M**edium **B**ase **L**ine.
MC	**M**onte **C**arlo.
MIP	**M**inimum **I**onizating **P**article.
MS	**M**ultiple **S**cattering / **M**ulti-**S**ite.
NEMO	**N**eutrino **E**ttore **M**ajorana **O**bservatory.
NEW	**NE**XT-**W**hite.
NEXT	**N**eutrino **E**xperiment with a **X**enon **T**PC.
Nexus	**NEX**T **U**tility for **S**imulation.
NME	**N**uclear **M**atrix **E**lement.
NO	**N**ormal **O**rdering.
OPERA	**O**scillation **P**roject with **E**mulsion-T**r**acking **A**pparatus.
PEDOT	**P**oly **e**thylene**d**i**o**xy**t**hiophene.
PMNS	**P**ontecorvo-**M**aki-**N**akagawa-**S**akata.
PMT	**P**hoto-**M**ultiplier **T**ube.
PP	**P**hoto**p**eak.
PSF	**P**oint **S**pread **F**unction.

PTFE	**P**oly**t**etra**fl**uor**e**thylene.
PTOLEMY	**P**rinceton **T**ritium **O**bservatory for **L**ight, **E**arly-Universe, **M**assive-Neutrino **Y**ield.
R&D	**R**esearch **and** **D**evelopment.
RAS	**R**adon **A**batement **S**ystem.
RMS	**R**esidual **M**ean **S**quare.
ROI	**R**egion **o**f **I**nterest.
SBL	**S**hort **B**ase **L**ine.
SC	**S**low **C**ontrol.
SHiP	**S**earch for **Hi**dden **P**articles.
SiPM	**Si**licon **P**hoto**M**ultiplier.
SM	**S**tandard **M**odel.
SMFI	**S**ingle-**M**olecule **F**luorescence **I**maging.
SNO	**S**udbury **N**eutrino **O**bservatory.
SOFT	**S**eparated-**O**ptimized **F**unctions **T**PC.
SS	**S**ingle-**S**ite.
TP	**T**racking **P**lane.
TPB	**T**etra**p**henyl **b**utadiene.
TPC	**T**ime **P**rojection **C**hamber.
UV	**U**ltra**v**iolet.
VEV	**V**acuum **E**xpectation **V**alue.
VUV	**V**acuum **U**ltra**v**iolet.

1

The physics of massive neutrinos

Neutrinos have been a gateway to discoveries and paradigm changes in the way physicists understand elementary particles and their interactions, primarily related to the weak force, starting with their first proposal, and the resulting Fermi theory for beta decays, the discovery of neutral currents, and, more recently, the so-called solar neutrino problem and its main implication: neutrinos are massive particles.

1.1 A journey through neutrino discovery

Back at the beginning of the 20th century, alpha, beta, and gamma radiations were found to be helium nuclei, electrons, and photons, respectively. Both alpha and gamma were monoenergetic emissions, where its energy depends on the particular nucleus. However, beta emissions were not, as Chadwick pointed out in 1914 [1]. This continuous spectrum contradicted what was then known about beta decays since a nucleus emitting one electron must have fixed kinetic energy, given by the Q-value of the reaction.[1] One of the most accepted explanations to solve this problem was the energy loss of the electrons in the target but shown not to be the case by Ellis and Wooster in 1927 [2]. At this point, some attempts suggested that maybe energy was not conserved in these type of decays.

In these *desperate* circumstances, Pauli proposed a *desperate remedy* in his famous letter in 1930 [3]. The only way for the energy conservation principle to be maintained was assuming there was a neutral particle playing a role, one he named *neutron*, and was supposed to be very light (same order of magnitude as the electron mass), spin 1/2, and should be another product of the beta decay. Consequently, the process becomes a three-body decay where the electron and the neutrino share the energy. Therefore, although the electron has a continuous spectrum, the electron and neutrino kinetic energies would add to the total energy released, given that the much more massive daughter nucleus carries negligible kinetic energy. Pauli

---

[1] In the case of a β^- decay: $Q_\beta = M_{\text{parent}} - M_{\text{daughter}}$, where M refers to atomic mass.

did not really like this proposal as it implied a new particle he thought was almost undetectable.

Despite Pauli's reluctance, the approach was taken seriously by E. Fermi. By 1934, he had built the first beta decay theory [4] that unified Dirac's positron (proposed in 1928 and discovered in 1932), Chadwick's heavy neutron (found in 1932), Pauli's neutrino (renamed by Fermi due to Chadwick's finding), and Heisenberg's atomic model (where the nucleus is constituted by neutrons and protons). Fermi's theory is based on a 4-particle vertex where a neutron decays into a proton, an electron, and a neutrino with strength G_F, the so-called Fermi constant. The resulting process would look like:

$$n \rightarrow p + e^{-} + \overline{\nu}. \tag{1.1}$$

Using Fermi's proposal, it is possible to compute some spectra and half-lives, yielding results that are consistent with experimental data. Nevertheless, he got a rejection from Nature for the submission of the paper "*because it contained speculations too remote from reality to be of interest to the reader*" [5] and he ended up publishing his work in Italian and German journals. Later, Gamov and Teller made a significant contribution to Fermi's interaction model, adding the forbidden beta decays, those involving parity violation [6], in order to match discrepancies with experimental data in the thorium chain.

As a consequence of Fermi's interpretation of neutron decay, it would be conceivable the existence of processes with the same participants and interaction, but rather a different configuration. For instance, this is the case of inverse beta decay, where an incoming neutrino scatters a neutron resulting in a proton and electron, as in:

$$\nu + n \rightarrow p + e^{-}. \tag{1.2}$$

Nonetheless, this four-particle vertex implies that Fermi's theory is not renormalizable, being then an effective theory. It is very accurate when the energy of the process is much lower than the W boson mass ($\sim$80 GeV). However, for comparable energies or higher, the theory is not valid as the coss-section grows with the square of the energy of the event, $\sigma \propto G_F^2 E^2$. Glashow [7], Weinberg [8], and Salam [9], among many others, showed later in the 60's that the Fermi interaction was better represented as an exchange of a W boson and came across with the idea of the unification of the weak and electromagnetic forces, the so-called GWS theory, the fundamental base of the Standard Model.

Considering the inverse beta decay depicted in Eq. 1.2, the detection of the neutrino becomes feasible. Bethe and Peierls [10] computed in 1934 the amplitude for a given input energy of 2 MeV yielding a cross-section: $\sigma < 10^{-44}$ cm^2, that implies a mean free path in solid matter greater than 10^{16} km. If no other interaction involves the neutrino, "*one can conclude that there is no practically way of observing neutrino*.".

Pontecorvo was the first pointing out that the detection was not that hopeless. It is, in fact, possible to get a few events per day in ton scale detectors if a sufficiently bright source of neutrinos is available, for instance, neutrino flux coming from the sun, reactors or radioactive materials from the reactor [11]. Later, in 1946, he suggested a new radiochemical method for making the detection feasible [12], recovering an old idea already used by Crane in 1939 in one of the early attempts to measure neutrinos [13]. The technique consists of the use of reactions of the kind:

$$\nu + {}^{A}_{Z}\mathrm{X} \rightarrow e^- + {}^{A}_{Z+1}\mathrm{Y}, \tag{1.3}$$

where the key is that the Y nucleus is not stable, but with a relatively long half-live. This way, the detector can be left accumulating events for a certain amount of time, not longer than Y's half-life, and then count how many Y decays happen. The one he considered the most promising, later named the Pontecorvo-Davis reaction, was:

$$\nu + {}^{37}_{17}\mathrm{Cl} \rightarrow e^- + {}^{37}_{18}\mathrm{Ar}. \tag{1.4}$$

The main advantage is twofold. On the one hand, the Cl isotope can be easily found in nature, and substances such as CCl_4 and C_2Cl_4 are inexpensive and straightforward to deal with. On the other hand, Ar is a noble gas, which makes it simple to extract and measure its radioactivity in a counter. The half-life ($\sim$35 days) is also adequate for the purpose of the experiment since a much shorter one may have decayed completely before extracting it, while a much longer one may complicate the measurement in the counter.

Pontecorvo's radiochemical method became an essential technique for future experiments, such as Davis' first solar neutrino detection,[2] also known as the Homestake experiment [14], and the GNO [15] and SAGE [16] experiments. Davis used the aforementioned isotope, whereas the latter cases both used ^{71}Ga as a target (with a lower threshold), producing ^{71}Ge upon a solar neutrino interaction.

---

[2] Davis was awarded the Nobel Prize in Physics for the discovery in 2002

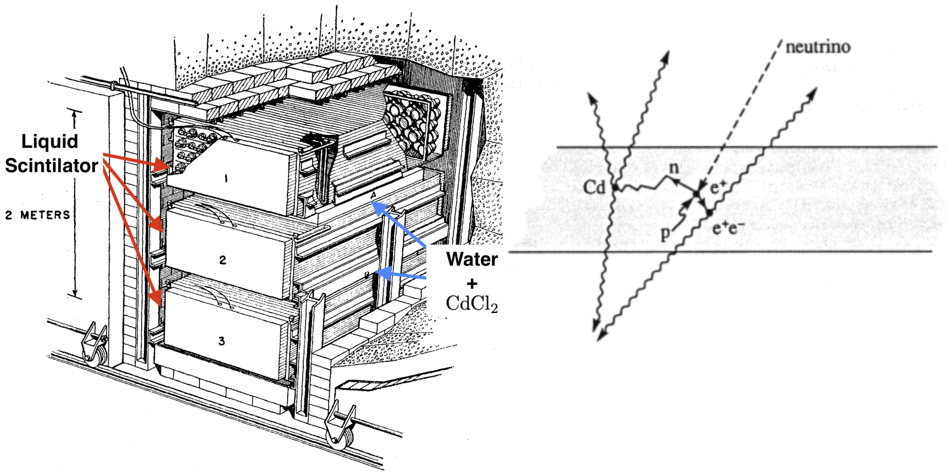

Figure 1.1.: The left figure shows the David-Reines experiment scheme, located close to the Savannah River Nuclear Reactor, South Carolina. This device was able to perform the first detection ever of a neutrino event. Picture taken from [18] and adapted. On the other hand, the right picture shows the detection technique they used, yielding a characteristic and unambiguous signature of two annihilation gammas at 511 keV and one retarded gamma from the neutron capture. Diagram extracted from [19].

It was not until 1956 that Cowan and Reines found the first evidence ever of the existence of neutrinos [17]. The reaction they used for the discovery is analogous to the one in Eq. 1.2:

$$\overline{\nu} + p \rightarrow e^{+} + n. \tag{1.5}$$

This process has a unique and distinctive signature, as shown in Fig. 1.1 right. When a neutrino enters and induces an inverse beta decay, a proton is converted to a positron and a neutron. The positron is quickly annihilated, resulting in two gamma rays at 511 keV. Then the neutron, once thermalized, is captured and another gamma is emitted in the absorption process. Both annihilation gammas and the delayed one in coincidence make the signal distinctive from possible backgrounds. The proton targets were the hydrogen nuclei in water molecules. The water contained dissolved $CdCl_2$, where the Cd has a high cross-section for neutron capture. The detector had two tanks of this doped water surrounded by three containers filled with liquid scintillator in order to detect the gammas from the events. Concerning the cosmic rays, the detector was 12 m deep, as well as fully shielded. The experimental setup is presented in the Fig. 1.1 left.

The neutrino flux was coming from a nuclear plant nearby, the Savannah River one, in South Carolina, with a flux high enough to get $\sim$3 events per hour, producing an unambiguous signal for the discovery, $\sim$20 times greater than the expected background [17].[3]

Reines and Cowan's experience established a new detection technique widely implemented nowadays in many neutrino experiments.

Making use of the very same reactor, Davis tried to take the Pontecorvo-Davis reaction (Eq. 1.4) but found no evidence of argon atoms [20]. This absence was interpreted to be due to the inability of the neutrinos coming from the reactor to undergo the proposed reaction. That led to the assumption that neutrinos may be two different particles, in analogy to the rest of the known fermions. Hence, there could be a new conserved quantity, the lepton number, positive unit for leptons and negative for antileptons, zero for other particles. Thus, the β^- particle emission in the reactor concurred with an *antineutrino* while the above-mentioned reaction would require *neutrinos* to happen; therefore, the SM (see Sec. 1.2) considered them to be different particles. Notwithstanding, the approach where neutrinos and antineutrinos are of different nature is known to be somewhat arbitrary since this discrepancy in the behavior can be explained due to the $V - A$ structure of the electroweak interaction and the tiny mass of the neutrinos [21].

Now that the neutrino had been discovered, a question remained: are the neutrinos involved in electron interactions the same as those in muon and pion decays? At that time, it was believed to be so. However, voices like Feinberg's pointed out that it was not the case [22]. If so, muon decay $\mu^\pm \rightarrow e^\pm + \gamma$ is allowed and should happen with a specific ratio compared with the standard one, $\mu^\pm \rightarrow e^\pm + \overline{\nu} + \nu$. Unfortunately, experiments found no evidence so far of such events (and still have not found any nowadays [23]).

Therefore, Pontecorvo proposed in 1959 several processes that can disentangle the situation [24]. The reactions he suggested implied a source of the presumably muon-partnered neutrinos and proposed a method to get a highly pure beam of this kind of flavored neutrino through pion decays:

$$\pi^\mp \rightarrow \mu^\mp + \overline{\nu}_\mu/\nu_\mu. \tag{1.6}$$

It took three years, in 1962, for Lederman, Schwartz and Steinberger to finally set up a neutrino beam and probe the existence of muon neutrinos [25], in the

---

[3] Reines was awarded the Nobel in Physics prize in 1995 (as Cowan passed away in 1974).

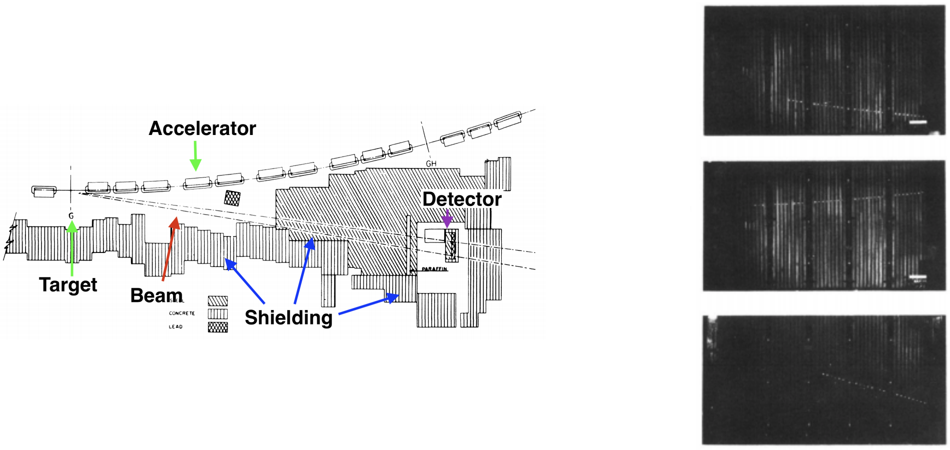

Figure 1.2.: The left image presents a Brookhaven experiment scheme, where protons coming from the accelerators produced a pion beam. Neutrinos come from the pion decay and are filtered by the shielding before the detector, where remaining pions and muons are absorbed. The right figure shows three actual muon events detected from neutrinos reacting by the spark chamber. Both are taken from [25] and adapted.

so-called Brookhaven experiment,[4] depicted in Fig. 1.2. The pions were produced by protons in a Be target and then decayed in-flight as Eq. 1.6 shows, resulting in a collimated muon and neutrino beam. This beam hits the 13 m shielding wall, where all the particles are stopped, except for the neutrinos. After that, neutrinos reach a 10-ton spark chamber, divided into ten modules, each with nine aluminum plates. As a result, in the detector, only muons were identified, while if the neutrino were a single particle, a similar amount of electrons and muons should have been seen.

The technique they used to produce high-energy neutrino beams led to several later discoveries, such as neutral currents in the GARGAMELLE bubble chamber, at CERN, a great support for the electroweak theory, and is a standard method used extensively in modern neutrino experiments. Obtaining a pure $\overline{\nu}_\mu/\nu_\mu$ beam is straightforward by selecting just π^-/π^+, respectively, with a magnet.

The Brookhaven experiment showed that there was a family number that is conserved through all weak processes, known as flavor lepton number, L_ℓ. It also confirmed that the leptons were arranged in pairs (ν_ℓ, ℓ).

Within this framework, after the τ discovery in 1975, it was clear that a third type of neutrino must be present in nature. Eventually, it was found by the DONUT collaboration, in Fermilab, in 2000 [26]. Charmed meson decays were used in order to create a ν_τ beam. Then, in an *Emulsion Cloud Chamber* (ECC), an unambiguous

---

[4] Lederman, Schwartz and Steinberger were awarded the Nobel prize in Physics in 1988

tau appearance signal was recorded. In addition to the discovery, the collaboration also validated a new concept, the ECC, which is being used in very recent experiments and becoming a standard technique, for instance, in the OPERA experiment at Gran Sasso.

These observations, among others, were taken into consideration in the construction of the Standard Model of particle physics, introduced in the next section.

1.2 Standard Model

The Standard Model of particle physics (SM) is the realization of our best understanding of how elementary particles behave and interact, offering its current most complete description. It explains the quantization of three of the four fundamental forces, electromagnetic, nuclear strong and nuclear weak, via the exchange of gauge bosons (force carriers) among the particles affected by each force.

The particle content is summarized in Fig.1.3. It consists of three generations of matter (heavy copies of the first one) for fermions, divided mainly into quarks (those that feel strong interactions) and leptons (those that do not). The quark sector contains six elements, the only ones that can interact via all the possible forces. There are also six leptons, three charged ones (e, μ, and τ) and three neutral, the neutrinos. The last one joining the group is the Higgs boson, coming from the Electroweak symmetry breaking and responsible for the mass for all the other particles. All the ordinary matter of the Universe is comprised of the first generation constituents: up and down quarks make protons and neutrons, and by adding electrons, one gets neutral atoms.

Neutrinos in the standard model are the top component of the left-handed lepton doublets.[5] As already mentioned, neutrinos are electrically neutral and have no color, i.e., they only feel the Weak Force both in Charged Currents (interactions between neutrinos and their charged lepton via $W^{\pm}$ exchange) and Neutral Currents (interactions among themselves via Z^0 exchange). Additionally, neutrinos are massless for the SM.

Whereas the SM has been a source for outstanding predictions, and has been matching data with a formidable accuracy, even further than the original range of application, it is known to be incomplete. Major concerns requesting for an extension are:

---

[5] Also known as active neutrinos, since the right components, within the SM's gauge structure, can not interact in any way. Those are the so-called sterile neutrinos.

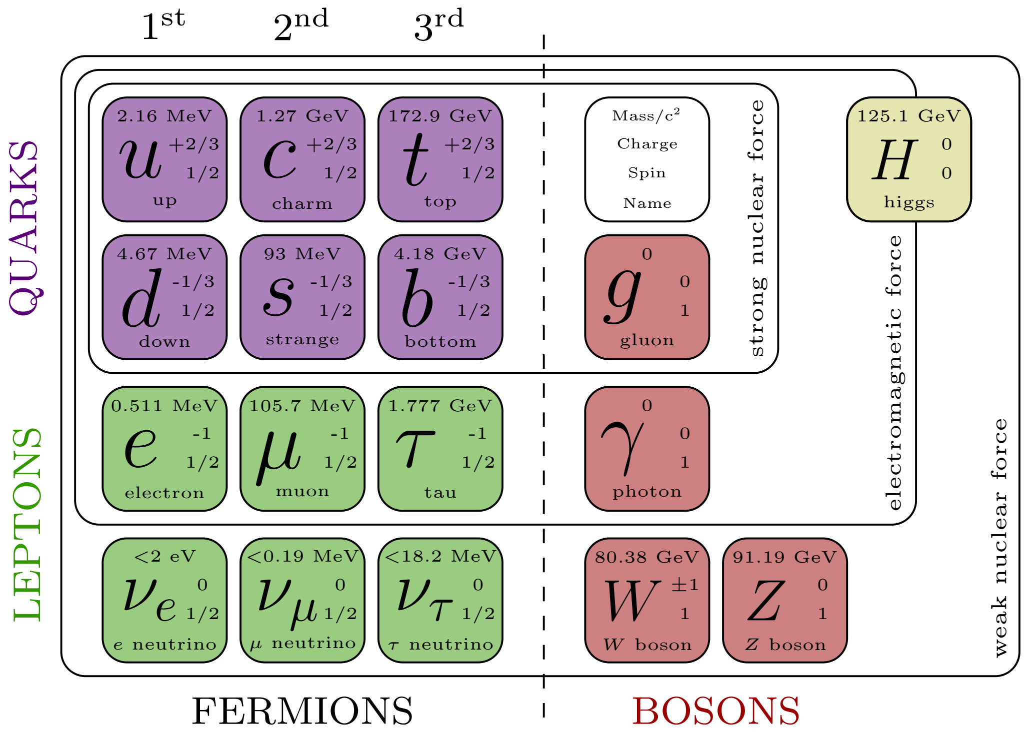

Figure 1.3.: Chart showing the elementary particles constituting the SM and the interactions among them. Each particle is characterized by its mass, charge, and spin. Figure recreated from [27].

The lack of a quantization procedure for the gravity force. So far, no theory has been able to describe gravitational phenomena in the quantum regime being compatible with General Relativity [28].

The great matter-antimatter asymmetry in the Universe The SM predicts an almost symmetric production for matter and antimatter; therefore, an equal amount of them should have been created in the Big Bang, and, consequently, after eons of evolution, both species should have annihilated each other. However, astronomic observations show a small fraction of matter managed to survive, and nowadays, all the known Universe is matter dominated [29]. This implies there is a certain mechanism generating the matter-antimatter symmetry [30]. Although there are some sources that can contribute to this imbalance already built-in in the weak interaction part of the SM, they are not enough to explain it [31, 32].

The evidence of the existence of the Dark Matter and Dark Energy. Dark Matter comes from observation of gravitational effects at the galactic level, as galaxy rotation curve anomalies; galaxy clusters mass and lensing; large scale structure formation; etc. that suggest the presence of a new kind of matter that, so far, can only interact via the gravitational force and maybe the weak one. Dark energy comes from the observation of the expansion of the Universe, which is accelerating. None of them can be explained within the SM [32].

The hierarchy problem. There is a concern among the theoretical community for some constants of the SM to be spread over a vast range (e.g., the masses of the particles, displayed in Fig. 1.6). This goes against the so-called *naturalness* concept [33], which postulates that when such an extended parameter's space occurs, there is an underlying mechanism that accounts for it. Historically, it has been a successful tool predicting new physical phenomena, such as the difference in the strengths of the weak and electromagnetic interactions (that is explained due to the fact that the bosons mediating the former are massive while the photon is massless). One typical example concerning the SM is the Higgs mass that, according to quantum corrections, should be much higher, of the order of the grand unification energy [34]. One promising solution proposed for explaining this issue would be supersymmetry [35].

The evidence for neutrino mass. Recent experiments show neutrinos change their flavor when propagating (see Sec. 1.3.1); this is only possible if neutrinos have mass. The way neutrino mass generation could be added to a SM extension is not yet unambiguous and two main approaches have been suggested, as discussed in Sec. 1.4.

1.3 Massive neutrinos

1.3.1 Neutrino oscillations

Recent experiments have shown neutrinos change their flavor as they propagate [36,37].[6] These oscillations puzzle out the *solar neutrino problem*, solving a forty years old conundrum started when the expected rate of neutrinos coming from the Sun, computed using the standard solar model, did not match the experimental outcome, that resulted in yielding around one third of the predicted number of events [14]. Later experiments also confirm the discrepancy, although they also showed that the deficit depends on the energy of the neutrinos, and may depend also on the distance they have traveled from the emission point [38,39,40].

---

[6] T. Kajita and A.B. McDonald were awarded the Nobel Prize in Physics for the discovery in 2015.

It was first proposed by Pontecorvo back in 1957 in analogy with neutral kaon mixing [41, 42] and later formalized by Maki, Nakagawa, and Sakata in 1962 [43]. This effect arises from the fact that the neutrino flavor eigenstates (those feeling the weak force) are a combination of three mass eigenstates:

$$|\nu_\alpha\rangle = U^*_{\alpha i}|\nu_i\rangle, \tag{1.7}$$

where $\alpha = (e, \mu, \tau)$ takes the flavor index, $i = (1, 2, 3)$ the mass eigenstates, both $|\nu_\alpha\rangle$ and $|\nu_i\rangle$ are orthogonal bases, and U is a 3x3 unitary matrix, the so-called neutrino mixing matrix or the Pontecorvo-Maki-Nakagawa-Sakata (PMNS) matrix. This matrix is similar to rotation ones; therefore, within the Dirac paradigm (see Sec. 1.4.1), it is usually parametrized by 3 Euler angles and 1 phase:

$$U = \begin{pmatrix} c_{13}c_{12} & c_{13}c_{12} & e^{-i\delta}s_{13} \\ -e^{i\delta}s_{13}s_{23}c_{12} - c_{23}s_{12} & -e^{i\delta}s_{13}s_{23}s_{12} + c_{23}c_{12} & s_{23}c_{13} \\ -e^{i\delta}s_{13}c_{23}c_{12} + s_{23}s_{12} & -e^{i\delta}s_{13}c_{23}s_{12} - s_{23}c_{12} & c_{23}c_{13} \end{pmatrix}, \tag{1.8}$$

where $s_{ij} = \sin(\theta_{ij})$, $c_{ij} = \cos(\theta_{ij})$, θ_{ij} are the mixing angles between i and j masses and δ is the Dirac phase. Angles can be taken, without loss of generality, to fall in the first quadrant, $\theta_{ij} \in [0, \pi/2]$, and the phase can take any value $\delta \in [0, 2\pi]$ [32]. This matrix is completely homologous to CKM one for the quark physics. On the other hand, suppose neutrinos are Majorana fermions (see Sec. 1.4.2). In that case, there are two emerging phases from the fact that neutrino fields are not invariant under U(1) any longer, so they cannot be absorbed as in the Dirac case and the neutrino mixing matrix now reads:

$$U^M = U\,\mathrm{diag}(e^{i\widetilde{\alpha}_1}, e^{i\widetilde{\alpha}_2}, 1), \tag{1.9}$$

where U is given by Eq. 1.8 and the new Majorana phases, $\widetilde{\alpha}_{1,2}$, as well as the Dirac one, can take any value. If not null, the three phases are sources of CP violation, even though Majorana ones are not observable with oscillation experiments.

In the case of oscillations in vacuum for ultra-relativistic neutrinos, the oscillation probability, i.e., the possibility that a neutrino created with a flavor α is detected as the flavor β after traveling a distance L and an energy E is [44]:

$$\begin{aligned}P_{\alpha\beta} = |\langle\nu_\beta|\nu_\alpha\rangle|^2 = \delta_{\alpha\beta} &- 2\sum_{i>j}\mathfrak{Re}\left(U_{\beta i}U^*_{\beta j}U^*_{\alpha i}U_{\alpha j}\right)\left[1-\cos\left(\frac{\Delta m^2_{ji}}{2E}L\right)\right] \\ &+ 2\sum_{i>j}\mathfrak{Im}\left(U_{\beta i}U^*_{\beta j}U^*_{\alpha i}U_{\alpha j}\right)\sin\left(\frac{\Delta m^2_{ji}}{2E}L\right).\end{aligned} \tag{1.10}$$

Eq. 1.10 shows the dependencies in neutrino oscillations that depend not only on the mixing angles but also on the mass differences ($\Delta m^2_{ji} = m^2_j - m^2_i$). In particular, $P_{\alpha\beta} = \delta_{\alpha\beta}$ if $\Delta m^2_{ji} = 0 \forall i, j$. Therefore, in order to happen, neutrinos must have a non-vanishing mixing and different masses. Furthermore, from Eq. 1.10, one can see that the oscillating length goes as $4\pi E/|\Delta m^2_{ji}|$ and the amplitude is proportional to the product of the PMNS matrix elements involved in the transition. It is also clear that when dealing with oscillations in vacuum, the result is not sensitive to the sign of the Δm^2_{ji} but just to the absolute value. To solve this degeneracy, it is necessary to measure oscillations in matter via the Mikheyev-Smirnov-Wolfenstein effect [45, 46].

Oscillation experiments can be classified according to the way the neutrinos detected are produced:

- Solar neutrinos: The source is the pp and CNO thermonuclear reactions occurring in the Sun, yielding an initial flux containing just electron flavor, although they are subject to matter effects. They are sensitive to Δm^2_{21} (also called solar mass difference, Δm^2_{sun}), θ_{12}, and θ_{13}.

- Atmospheric neutrinos: The source is the decay of pions and kaons produced when cosmic rays interact with the atmosphere's nucleons. The initial flux is composed of ν_μ and ν_e in a relation of 2:1. They are sensitive to θ_{23}, $|\Delta m^2_{31,32}|$ (also known as atmospheric mass difference, Δm^2_{atm}), θ_{13}, and δ.

- Reactor neutrinos: The source is the different fissions and beta decays coming from the fission of heavy elements. They provide a very intense flux of $\overline{\nu}_e$. Depending on the distance to the reactor, the experiments can be subdivided into long baseline (LBL), at ~100 km from the reactor, and medium baseline (MBL), at ~1 km. However, recent results demanded the construction of detectors closer to the source, ~10 m. They are sensitive to Δm^2_{21}, θ_{12}, and θ_{13} for LBN and $|\Delta m^2_{31,32}|$ and θ_{13} for MBL.

- Accelerator neutrinos: The source is the pion and kaon decays, as in atmospheric ones, but produced by high energy protons from a human-made particle accelerator colliding a target. The main advantage is that the beam

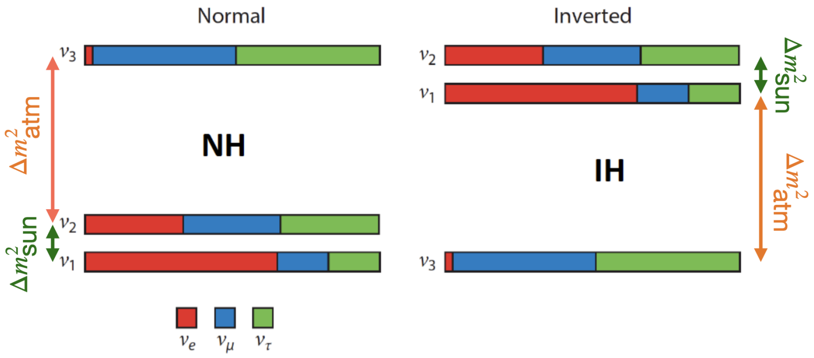

Figure 1.4.: Diagram summarizing all oscillation parameters ly and showing the two potential mass orderings, depending on the Δm^2_{atm} sign, normal ordering on the left and inverted on the right. It also shows the contribution each flavor has in each mass eigenstate. The masses increase from bottom to top and the differences are not in scale. Figure adapted from [47].

can be selected, so the flux is neutrino or antineutrino dominated. Although the predominant flavor is μ, there are contaminations on e neutrinos from kaon and muon decays. As well as reactor neutrinos, they can be subdivided according to the distance to the accelerator, which is chosen to match the L/E to the oscillation effect of interest. They are sensitive to $|\Delta m^2_{31,32}|$ and θ_{23} for LBL ν_μ disappearance and δ, θ_{13}, and θ_{23} for LBL ν_e appearance.

It is remarkable that while the sign of Δm^2_{sun} is known, it is not the case for Δm^2_{atm} (and also that $|\Delta m^2_{\text{sun}}| \ll |\Delta m^2_{\text{atm}}|$). That opens two possible scenarios, whether m_3 is the heaviest among the three neutrino mass eigenstates, the so-called normal ordering (NO), or m_3 is the lightest mass eigenstate, noted as inverted ordering (IO). This mass ordering problem is more than just a convention issue, as it affects oscillation parameters and other neutrino-related phenomena, such as double beta decay. This is displayed in Fig. 1.4.

The current best knowledge about the parameters affecting the oscillations is summarized in Table 1.1. All the parameters are determined with a σ uncertainty equal or better than a 3 % but for the δ that, although still have significant uncertainties, shows a little preference towards CP violation (however, CP conservation —$\delta \sim 180°$— still allowed within a $\sim \sigma$ range). Regarding the mass ordering, the fit to oscillation data yields a 2.0σ preference towards the NO, which can be raised to 2.7σ if $0\nu\beta\beta$ and cosmological constraints are considered [48]. Future experiments as DUNE will yield some light [49] on this.

Parameter	Normal Ordering	Inverted Ordering
Δm^2_{12} (10^{-5}eV^2)	$7.50^{+0.22}_{-0.20}$	
$\lvert\Delta m^2_{31}\rvert$ (10^{-3}eV^2)	$2.55^{+0.02}_{-0.03}$	-
$\lvert\Delta m^2_{32}\rvert$ (10^{-3}eV^2)	-	$2.45^{+0.02}_{-0.03}$
$\theta_{12}(^\circ)$	34.3 ± 1.0	
$\theta_{23}(^\circ)$	49.26 ± 0.79	$49.46^{+0.60}_{-0.97}$
$\theta_{13}(^\circ)$	$8.53^{+0.13}_{-0.12}$	$8.58^{+0.13}_{-0.14}$
$\delta(^\circ)$	194^{+24}_{-22}	284^{+26}_{-28}

Table 1.1.: Neutrino mixing parameters and their 1σ range for the 3ν paradigm according to the most recent global fit [48]. In order to extract these parameters, all relevant experimental contributions are considered and fitted to a model considering all the parameters entering the oscillations, both for NO and IO.

1.3.2 Absolute neutrino mass determination

Neutrino oscillation studies are a great source of understanding about the fundamental properties of neutrinos, but, among other limitations, they are not sensitive to the absolute mass scale of the neutrinos. There are three main approaches to explore them: direct mass measurements, cosmological bounds and neutrinoless double beta decays (extensively covered in Sec. 2.1).

Direct measurements

The main technique for direct mass determination aims to study the kinematic end-point of beta interactions carefully. They offer the most model-independent method to determine the absolute mass scale as the only assumption used is energy conservation. When a beta decay occurs, the total kinetic energy available for the products ($e^-\overline{\nu}_e$ or $e^+\nu_e$ for β^- and β^+ cases, respectively), is the total energy, Q_β. Thus, studying the limit when the electron gets all the kinetic energy (i.e., the end of the spectrum) gives information about the effective electron neutrino mass:

$$m_\beta^2 = \Sigma_i |U_{ei}|^2 m_i^2. \tag{1.11}$$

One graphical example of the mass effect on the spectrum is displayed in Fig. 1.5.

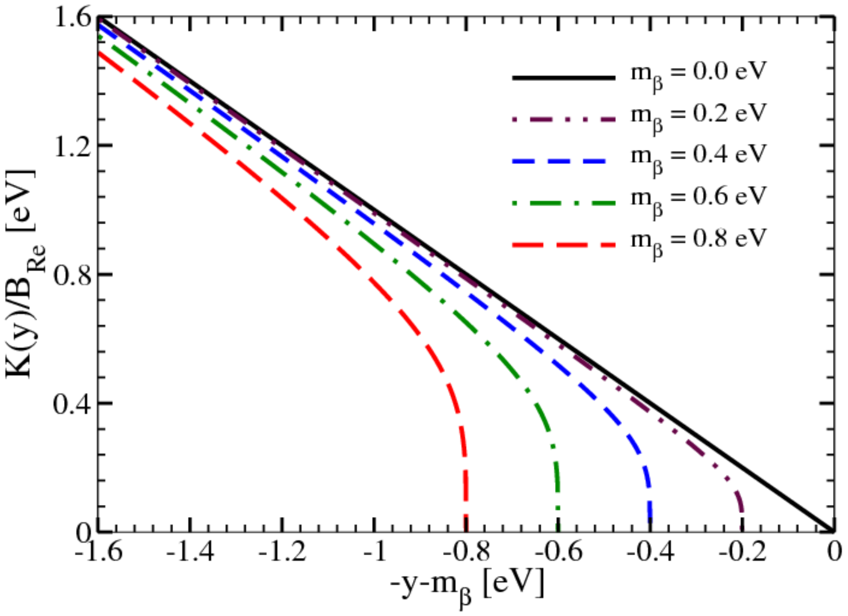

Figure 1.5.: Example of a Kurie plot (a sort of convenient linearization of the beta spectrum) normalized by the matrix element, B, versus $-y - m_\beta = E_e - Q_\beta$, for different effective neutrino masses for the case of ^{187}Re. In the null mass hypothesis (solid black), the electron gets all the available energy (Q_β) and the spectrum presents a linear behavior. In contrast, as the neutrino mass increases, the shape diverges more in form from that limit. Plot extracted from [50].

The main feature for source selection is the Q_β. For this kind of measurement, the lower, the better, as this increases the number of counts at the end of the spectrum and helps handle other β of no interest in the experiment [51]. However, this enters into conflict with the outstanding energy resolution required to resolve the spectrum distortion. The current limit corresponds to the KATRIN experiment, which works with tritium, ^{3}H [52]:

$$m_\beta < 0.8\,\text{eV (90 \% CL)}. \tag{1.12}$$

Tritium is relatively stable, has a low Q_β, presents a super allowed transition, and has a straightforward electron structure. Other possible nuclei are ^{187}Re [53] and ^{163}Ho [54].

Besides these beta shape studies, there is also the possibility of measuring the mass directly from the time of flight. The main disadvantage of the approach is the need for really powerful sources, as supernovas. Supernovas are rare and are not fully theoretically understood, so the method relies on the model and the chance to observe a SN explosion during the lifetime of the experiment. The 1987 supernova in the Large Magellanic Cloud (SN1987a) yielded a limit of <5.7 eV (95 % CL) [55] or <5.8 eV (95% CL) [56], depending on the model.

Cosmological bounds

Massive neutrinos have a noticeable impact on cosmological observations, so they can be used to constrain neutrino properties. Those effects are sensitive to the sum of neutrino masses:

$$\Sigma m_\nu = m_1 + m_2 + m_3. \tag{1.13}$$

This mass affects the Cosmic Microwave Background (CMB), the matter spectrum, large structure formation, rate of expansion, and so on. That, combined with other phenomena such as Baryon Acoustic Oscillation (BAO), led to the setting of the latest Planck collaboration limit [57]:

$$\Sigma m_\nu < 0.12\,\text{eV (95 \% CL, Planck, TT,TE,EE+lowE+lensing+BAO)}. \tag{1.14}$$

Notwithstanding, the limits depend dramatically on the cosmological model assumptions and the data combination recipe.

It is remarkable to mention that, following the results from Table 1.1, one gets a naive $\Sigma m_\nu \sim 0.06$ eV and $\Sigma m_\nu \sim 0.1$ eV, for NO and IO, respectively, depending on the mass ordering considered. This implies that in the near future cosmological observations should also be able to measure the neutrino mass ordering.

1.4 Extending the SM

The solar neutrino problem solution comes with another problem: how to incorporate the neutrino masses into the SM. In principle, one could assume it is just mimics the quark sector procedure, where both weak duplet integrants get mass through the Higgs mechanism. The main problem with this approach is that it implies the contribution from the right-handed neutrino sector, not present in the SM particle content. However, as already mentioned, they behave as a singlet for all the SM interactions, so there is no feasible Yukawa term involving them. Another option could be generating them via loop interactions. Nevertheless, all the potential terms violate the lepton number conservation by two units. Therefore, no mechanism within the SM allows building neutrino mass terms; one has to go beyond SM options. We will consider two of them, whose aim is to preserve SM gauge invariance and add an arbitrary number of sterile neutrinos in order to build the mass terms.

1.4.1 Dirac mass term

It is the simplest way to proceed, apply the same scheme as for the up-like quarks, incorporating an ad-hoc Yukawa term to the already exiting ones (those that give mass to the charged leptons) in the Higgs part of the lagrangian:

$$-\mathscr{L}_H = Y'^{\ell}_{\alpha\beta}\overline{L_{\alpha L}}\Phi\ell'_{\beta R} + Y'^{\nu}_{\alpha\beta}\overline{L_{\alpha L}}\tilde{\Phi}\nu'_{\beta R} + h.c., \tag{1.15}$$

where α and β run over the three flavors, Y'^{ℓ} and Y'^{ν} are the 3x3 Yukawa coupling complex matrices for charged leptons and neutrinos, respectively, Φ is the standard Higgs doublet, $\tilde{\Phi}$ is the conjugated Higgs doublet ($\tilde{\Phi} = -\sigma_2\Phi$), $L_{\alpha L}$ are the left-handed lepton doublets, and $\ell'_{\beta R}$ and $\nu'_{\beta R}$ are the lepton right-handed singlets, for charged leptons and neutrinos, respectively. Applying the spontaneous electroweak symmetry breaking and the vacuum expectation value (VEV) for the Higgs field,[7] and diagonalizing, the Eq. 1.15 results in:

$$-\mathscr{L}_H = \frac{v+H}{\sqrt{2}}\left(y^{\ell}_{\alpha}\overline{\ell_{\alpha L}}\ell_{\alpha R} + y^{\nu}_{k}\overline{\nu_{kL}}\nu_{kR}\right) + h.c., \tag{1.16}$$

where y^{ℓ} and y^{ν}_k are the Yukawa couplings, v is the VEV, and H is the Higgs field. The couplings with the Higgs field and the mass terms for both the charged leptons and the neutrinos are now explicit. Reading form 1.16, the masses are:

$$m_{\ell_\alpha} = \frac{v\cdot y^{\ell}_{\alpha}}{\sqrt{2}} \quad \text{and} \quad m_{\nu_k} = \frac{v\cdot y^{\nu}_{k}}{\sqrt{2}} = m_{D_k}. \tag{1.17}$$

Then, focusing just on the mass term for neutrinos and using that $\nu = \nu_L + \nu_R \Rightarrow \overline{\nu}\nu = (\overline{\nu}_L\nu_R + \overline{\nu}_R\nu_L)$, we get to the so-call Dirac mass term:

$$-\mathscr{L}^D_m = m_{D_k}(\overline{\nu_{kL}}\nu_{kR} + \overline{\nu_{kR}}\nu_{kL}) = m_{D_k}\overline{\nu_k}\nu_k. \tag{1.18}$$

---

[7] I.e.,

$$\Phi = \frac{1}{\sqrt{2}}\begin{pmatrix} 0 \\ v+H \end{pmatrix}$$

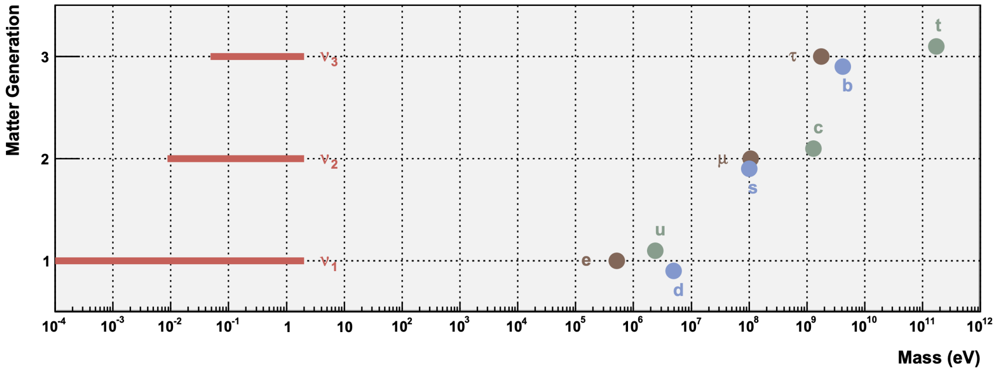

Figure 1.6.: Mass scale for all the fermions in the SM. The neutrino sector is plotted assuming NO. Figure extracted from [59].

Digging on the symmetries of the expression 1.18, it is straightforward to see that the term is invariant over global phase transitions. This U(1) invariance is, in fact, the lepton number conservation. However, it is not possible to find a transformation acting on each flavor individually; therefore, the family lepton number is not conserved any longer [58]. Actually, this is consistent with neutrino oscillations.

Despite introducing a valid term for neutrino masses, the Dirac approach has two main disadvantages. First, it implies the ad-hoc addition of the right-handed neutrinos, which cannot interact within any SM part other than the Higgs field. On the other hand, there is a concern among theoreticians about theories that require unnatural adjustments for some of the theory parameters. For the case of neutrinos, the Yukawa couplings have to be much smaller than for the other particles, given their very low mass scale (at least six orders of magnitude lighter than the electron) as displayed in Fig.1.6. Still, this can well be just a prejudice about a beauty concept with no translation in nature.

1.4.2 Majorana mass term

When dealing with massless neutrinos, they can be described as single chiral fields with two components, called Weyl spinors. For the Dirac prescription, however, in analogy with the other particles, spinors have four components. These extra degrees of freedom are reflected in the appearance of the sterile neutrinos. In 1937, Ettore Majorana realized that this was not the only option [60]: there is a way to keep using a two-component Weyl spinor for massive neutrinos. In order to do so, it is necessary to assume that chiral fields are not independent but linked via a relationship known as the Majorana condition:

$$\nu_R = \nu_L^C \Longleftrightarrow \nu_L = \nu_R^C, \tag{1.19}$$

where $\nu^C = C\overline{\nu}^T$ (and C is the charge conjugation operator), known as charge conjugated field. The condition also admits an arbitrary phase; nonetheless, it can be absorbed in the neutrino field. Remarkably, the Eq. 1.19, using that $\nu = \nu_L + \nu_R = \nu_L + \nu_L^C$ and $\nu^C = \nu_L^C + \nu_R^C = \nu_L^C + \nu_L$, gives:

$$\nu = \nu^C. \tag{1.20}$$

Eq. 1.20 implies that any Majorana fermion has to be electrically neutral, as the particle is identical to its antiparticle. Consequently, within the particle content of the SM, only neutrinos are candidates for such nature.

Consequently, substituting Eq. 1.19 in 1.18, we obtain the Majorana mass term:

$$-\mathscr{L}_m^M = \frac{1}{2} m_k (\overline{\nu}_{kL} \nu_{kL}^C + \overline{\nu_{kL}^C} \nu_{kL}), \tag{1.21}$$

where the $1/2$ factor accounts for the double-counting since the fields are not independent.

Regarding symmetries, as the starting expression does not conserve the lepton family number, this one is not expected to do so. In fact, it is not invariant under global phase transformations. Thus, this violation of U(1) implies that also the total lepton number is not conserved. The non-validity of the lepton number as a conserved charge could be read, as well, from the fact that particle and antiparticle are the same, then, they cannot have different quantum numbers. Majorana mass term interactions have $\Delta L = \pm 2$ transitions.

Given that the rest of the lagrangian does preserve the lepton number and the smallness of the neutrino masses, for most of the processes involving neutrinos, the effect is negligible. Hence, it is possible to define an effective total lepton number that is conserved in every process not sensitive to Majorana mass terms.

The Majorana mass term cannot be built within the SM since it yields non-renormalizable lagrangians. One potential approach would be building an effective lagrangian that leads to the right mass term. The lowest dimensional term generating a Majorana term built with SM particle content is the so-called Weinberg operator or lepton number violating term [61]:

$$\mathscr{L}_5 = \frac{g_{\alpha\beta}}{\mathcal{M}}(L_{\alpha L}^T \sigma_2 \Phi) C^\dagger (\Phi^T \sigma_2 L_{\beta L}) + h.c., \tag{1.22}$$

where $g_{\alpha\beta}$ is a 3x3 dimensionless coupling constants matrix, and $\mathcal{M}$ is a constant with mass dimensions. Analogously to the procedure applied to Eq. 1.15, by the electroweak symmetry breaking and diagonalization, we get:

$$-\mathscr{L}_5^m = \frac{v^2}{2\mathcal{M}} g_{\alpha\beta} \overline{\nu_{\alpha L}^C} \nu_{\beta L}, \tag{1.23}$$

where the pre-factors are usually defined as the Majorana matrix:

$$M_{\alpha\beta}^L = \frac{v^2}{2\mathcal{M}} g_{\alpha\beta}, \tag{1.24}$$

where M^L has mass dimensions inherited from the fact that also v and $\mathcal{M}$ both have them as well.

Thus, reading from Eqs. 1.17 and 1.24:

$$m_M \propto \frac{m_D^2}{\mathcal{M}}. \tag{1.25}$$

Therefore, taking expression 1.25 and plugging the typical numbers, i.e., $m_D \sim 10^2\,\mathrm{GeV}$ ($m_D \sim v$) and $\mathcal{M} \sim 10^{15}\,\mathrm{GeV}$ (the scale of the grand unification theories), one obtains a $m_M \sim 10^{-2}\,\mathrm{eV}$ that is perfectly fitting the expected neutrino mass scale.

About the origin and suitability of the $\mathscr{L}_5$, even though it is true that the lagrangian is not renormalizable, it is not hard to argue that, as SM is not the final theory, a more general framework that embraces that kind of effective terms could be renormalizable. This is precisely the case for the Fermi theory for beta decays, where the interaction first proposed was not renormalizable, and it was not until the GWS theory that a well-behaved and more general theory took place.

It should be noted that, although the discussion about the Majorana mass term was explicitly performed using the left-handed fields, an analogous derivation can be made using the right-handed ones.

1.4.3 Dirac and Majorana mass term

Combining all the possible mass terms, one can build the most general case as:

$$\mathscr{L}_m^{DM} = \mathscr{L}_m^{M,L} + \mathscr{L}_m^{D} + \mathscr{L}_m^{M,R}, \tag{1.26}$$

that can be rewritten in a more condensed way as:

$$\mathscr{L}_m^{DM} = \frac{1}{2}\boldsymbol{N}_L^{\prime T} C^{\dagger} M^{DM} \boldsymbol{N}_L^{\prime} + h.c., \tag{1.27}$$

where:

$$\boldsymbol{N}_L^{\prime} = \begin{pmatrix} \boldsymbol{\nu}_L^{\prime} \\ \boldsymbol{\nu}_R^{C} \end{pmatrix}, \boldsymbol{\nu}_L^{\prime} = \begin{pmatrix} \nu_{eL}^{\prime} \\ \nu_{\mu L}^{\prime} \\ \nu_{\tau L}^{\prime} \end{pmatrix}, \boldsymbol{\nu}_R^{C} = \begin{pmatrix} \nu_{s_1 R}^{C} \\ \dots \\ \nu_{s_{N_s} R}^{C} \end{pmatrix},$$

N_s is an arbitrary number of right-handed sterile neutrinos added,and M^{DM} is a square matrix as:

$$M^{MD} = \begin{pmatrix} M_L^M & M^D \\ \left(M^D\right)^T & M_R^M \end{pmatrix}, \tag{1.28}$$

where M^D, M_R^M, and M_L^M are complex matrices. M_L^M is 3×3, M_R^M is $N_s \times N_s$ and M^D is $N_s \times 3$.

One can again diagonalize Eq. 1.27, yielding:

$$\mathscr{L}_m^{DM} = -\frac{1}{2} m_k \overline{\nu_k^C} \nu_k. \tag{1.29}$$

From Eq. 1.29, it is remarkable to realize the complete analogy with 1.21 one. Thus, this fact implies that the combination of Dirac and Majorana mass terms implies that massive neutrinos are Majorana fermions.

Seesaw mechanism

There are three main ways to get to the Weinberg operator displayed in Eq. 1.22, using only renormalizable interactions at tree level (again, analogously to Fermi's

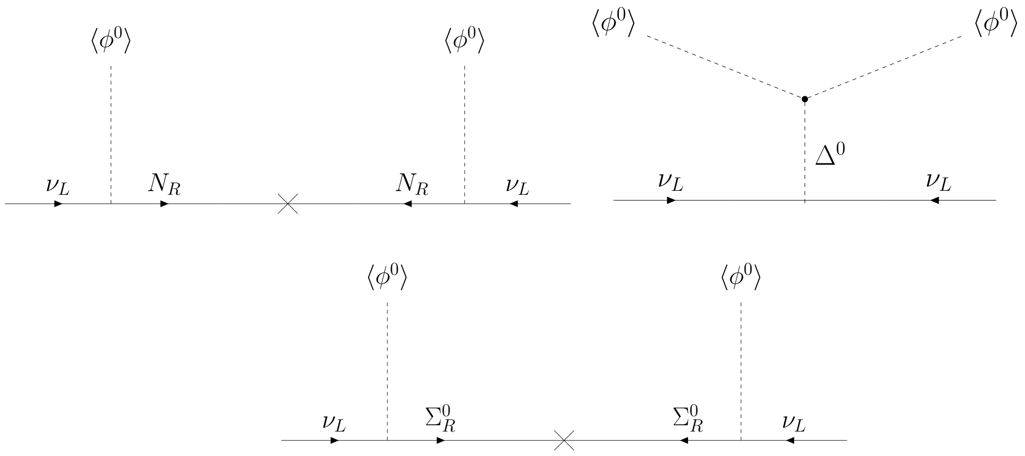

Figure 1.7.: Feynman diagrams showing seesaw type I, II, and III, respectively. N_R accounts for the singlet, Δ^0 for the scalar triplet, and Σ_R^0 for the fermion triplet. Diagrams extracted from [63].

theory historical development) [62], the well-known seesaw types. Each type is characterized by the extra particle content needed:

- Type I: Heavy fermion singlet,
- Type II: Heavy scalar triplet,
- Type III: Heavy fermion triplet.

Fig. 1.7 shows the different tree level realizations for each seesaw type.

As an example, one can focus on the type I realization since it is the simplest case of the seesaw model, only needing a Dirac mass term and a right-handed Majorana term. For that, starting from Eq. 1.28 and taking $M_L^M = 0$ (that is not an arbitrary choice since this contribution is forbidden within SM symmetries):

$$M^{MD} = \begin{pmatrix} 0 & M^D \\ \left(M^D\right)^T & M_R^M \end{pmatrix}, \tag{1.30}$$

where both M_R^M and M^D are 3×3 matrices. Then, diagonalizing the expression and assuming M_R^M eigenvalues are much greater than M^D ones:

$$m \approx \begin{pmatrix} -M_D M_R^{-1} M_D^T & 0 \\ 0 & M_R \end{pmatrix} = \begin{pmatrix} M_{light} & 0 \\ 0 & M_{heavy} \end{pmatrix}. \tag{1.31}$$

The heavy neutrinos' masses are given by M_R^M eigenvalues, whereas the light ones are determined by $M_{light} \approx -M_D M_R^{-1} M_D^T$ (that happens to be diagonalizable by the U, defined in Eq. 1.7). The bigger M_R^M is, the lighter those neutrinos become, explaining the seesaw denomination. Another thing to remark is the similarity between the behavior of M_{light} and the expected from Eq. 1.25.

The other types of seesaw introduce different particles and interactions, and other more sophisticated mechanisms work with loops. However, the outcome is quite similar: by letting those new products run into large mass scales, one can obtain reasonable small masses for the light neutrino sector in agreement with experimental results.

It is significant to stress that if seesaw mechanism exists, that would imply that:

- Neutrinos are unambiguously Majorana particles.
- Neutrino mass scale is naturally much smaller than lepton and quark one, solving the discrepancy shown in Fig. 1.6.
- Heavy Majorana particles, the ones involved in the seesaw mechanism, must exist. Those Majorana particles could lead to leptogenesis through CP-violating decays in the early Universe [64].

1.4.4 Experimental determination of the Majorana nature of neutrinos

The determination of the neutrinos' final nature from the experimental side is an open issue, and there have been multiple fronts trying to solve it.

First of all, the most extensively explored and promising phenomena are the Lepton Number Violation (LNV) processes [65]. As described in Sec. 1.4.2, Majorana interactions induce a $|\Delta L| = 2$ transitions, and all of them follow the diagram depicted in Fig. 1.8, i.e., events mediated by:

$$W^{\pm}W^{\pm} \to l_{\alpha}^{\pm} l_{\beta}^{\pm} \tag{1.32}$$

This mechanism allows the systematic categorization observing the final lepton flavors, (α, β), involved. In the case where the process is mediated only by light

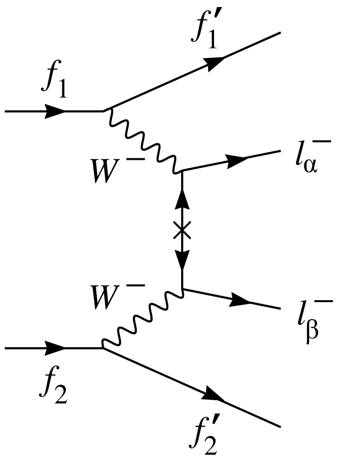

Figure 1.8.: General Feynman diagram for the $|\Delta L| = 2$ LNV processes. Diagrams extracted from [66].

Majorana neutrino exchanges, the matrix element for the event is proportional to the (α, β) element of the *effective neutrino mass matrix* [66]:

$$\langle m_\nu \rangle_{\alpha\beta} = U^*_{\alpha i} U^*_{\beta i} m_i \tag{1.33}$$

where $m_\nu = M_{light}$ defined in Eq. 1.31, U is the PMNS matrix defined in Eq. 1.7 and m_i are the three light neutrino masses. The neutrino mass matrix elements are a useful and quantitive method to compare the possible realizations of the process and the experimental techniques adopted. The phenomenology and, consequently, the techniques used in order to study such interactions are diverse [67] and have been summarized in Table 1.2. On the other hand, the most competitive constraints on the LNV interactions are summarized in Table 1.3.

Reading from Table 1.3, it is clear that the determination of m_{ee} is several orders of magnitude better than the best of the others. This is directly linked to the experimental technique ability to gather an enormous amount of $\beta\beta$ emitters (as described in Sec. 2.4), while the others have to rely on the occurrence of the events in an accelerator-based experiment. Therefore, the number of events expected from an accelerator is highly outperformed by Avogadro's number. However, it may well be that the (e, e) element of the matrix is disfavoured due to phase cancellations. Thus, it is essential to keep pushing the boundaries for the processes involving other than only electron flavor.

Another interesting approach is the search for low-energy (non-relativistic) neutrino absorption on neutrons, as described in Eq. 1.2. For such low energy, rates

Type	Subtype	Process	Matrix element
Rare decays	$0\nu\beta\beta$	${}^{A}_{Z}\mathrm{X} \rightarrow^{A}_{Z+2} \mathrm{Y} + 2e^-$	(e,e)
	Meson decay (mainly K, D, and B types)	$M_1 \rightarrow M_2\ l^\pm_\alpha\ l^\pm_\beta$	(α,β)
	Baryon decay (mainly Λ^+_C and Ξ^- types)	$B_1 \rightarrow B_2\ l^\pm_\alpha\ l^\pm_\beta$	(α,β)
	τ decay	$\tau^\pm \rightarrow M_1\ M_2\ l^\mp_{\alpha\neq\tau}$	$(\tau,\alpha\neq\tau)$
Scattering	$\mu - e$ conversion	$\mu^\pm +^{A}_{Z} \mathrm{X} \rightarrow e^\mp +^{A}_{Z\mp2} \mathrm{Y}$	(e,μ)
	ep collider	$e^\pm\ p \rightarrow \overset{(-)}{\nu}_e\ l^\pm_\alpha l^\pm_\beta\ X$	(α,β)
	ν beam	$\overset{(-)}{\nu}_\mu\ N \rightarrow \mu^\mp\ l^\pm_\alpha l^\pm_\beta + X$	(α,β)

Table 1.2.: Categorization of the main studied or proposed $|\Delta L| = 2$ LNV proceses. Some of the decays may involve extra mesons in the final state. Note that, technically, the $0\nu\beta\beta$ is a particular case of the barion decay class, but it is taken as a different category for historical, experimental, and maturity reasons.

of interaction for the Majorana case are twice as large as in Dirac's scenario [70]. The only known source of that kind of neutrinos is the Cosmic Neutrino Background (CνB) and the target must have no threshold for the reaction, so candidates as the ones for direct searches (see Sec. 1.3.2) are suitable for the task. Future experiments as PTOLEMY [71] may shed some light and give some constraints. However, given the very low rate expected, prospects are quite pessimistic [72].

Besides, other possible way would be searching for strange decays in accelerators via lepton flavor violating (LFV) processes. Those processes, such as $\mu \rightarrow e\gamma$ and $\mu \rightarrow eee$ [73], although not directly related to the Majorana nature of neutrinos, are extremely suppressed in the SM and can be enhanced by the presence of heavy Majorana neutrinos [74].

Finally, accelerator experiments might perform direct searches for heavy Majorana neutrinos [75]. Such particles could be produced as an intermediate state whose decay can be detected, where the most promising channels are the three lepton final states [76] and $W\gamma$ fusion [77]. Future detectors as SHiP [73] and DUNE [78] will explore wider regions for the parameter space. However, nowadays, given the very low rates and abundant backgrounds, current discovery potential is quite hopeless.

Flavors	Leading exp. bound	90% CL bound	$\langle m \rangle_{\alpha\beta}$ (eV)
(e, e)	$T_{1/2}(^{136}\mathrm{Xe} \rightarrow ^{136}\mathrm{Ba} + 2e^-)$	$> 1.07 \cdot 10^{26}\,\mathrm{yr}$	$< 1.65 \cdot 10^{-1}$
(e, μ)	$\Gamma(\mathrm{Ti} + \mu^- \rightarrow e^+ + \mathrm{Ca}_{\mathrm{gs}})$ / $\Gamma(\mathrm{Ti} + \mu^-\text{capture})$	$< 1.7 \cdot 10^{-12}$	$< 1.7 \cdot 10^{7}$
(e, τ)	$\Gamma(\tau^- \rightarrow e^+\pi^-\pi^-)/\Gamma_{\mathrm{tot}}$	$< 2.0 \cdot 10^{-8}$	$< 1.2 \cdot 10^{12}$
(μ, μ)	$\Gamma(K^+ \rightarrow \pi^-\mu^+\mu^+)/\Gamma_{\mathrm{tot}}$	$< 4.2 \cdot 10^{-11}$	$< 5.7 \cdot 10^{10}$
(μ, τ)	$\Gamma(\tau^- \rightarrow \mu^+\pi^-\pi^-)/\Gamma_{\mathrm{tot}}$	$< 3.9 \cdot 10^{-8}$	$< 2.1 \cdot 10^{12}$
(τ, τ)	$\sigma(e^+p \rightarrow \overline{\nu}_e\tau^+\tau^+ + X)$	-	$< 2.0 \cdot 10^{16}$

Table 1.3.: Current limits on effective neutrino masses from LNV processes for each flavor combination in the neutrino mass matrix . The procedure for the computation in decays is taken from [66], data taken from [32, 67, 68, 69].

Hence, $0\nu\beta\beta$ is the main feasible, popular, and mature technique that is able to probe Majorana nature for neutrinos with high sensitivity. In fact, it the current limits for this effective Majorana matrix element are 10^8 better that the next most competitive one. This interaction, implications, and experimental efforts are further explained in Chapter 2.

2

Neutrinoless double beta decay

Whether neutrinos are Majorana fermions or not has become a key question for the foundations of Physics. The affirmative answer could open new horizons for other remaining open questions such as what is the dark matter [79] and where did all the antimatter of the Universe go after the Big Bang [64]. As explained in Sec. 1.4.4, several approaches are proposed for solving the enigma, although, nowadays, it is widely accepted that the most competitive technique is the neutrinoless double beta decay.

2.1 Double beta decay

Double beta decay ($\beta\beta$ or $2\nu\beta\beta$) is a very rare nuclear decay, first proposed by Goeppert-Mayert back in 1935 [80], where a nucleus undergoes two simultaneous beta decays, either β^-, β^+ or ε (electron capture). For instance, for a double β^-transition,[1] one expects:

$$^{A}_{Z}X \rightarrow ^{A}_{Z+2} Y + 2e^- + 2\overline{\nu}_e. \tag{2.1}$$

In 1950 there was the first indirect evidence for the decay by geochemical methods in ^{130}Te [81]. However, it was not until 1987 that the first laboratory detection was performed in ^{82}Se [82]. As presented in Table 2.1, and following theoretical expectations (as they are second-order Feynman diagrams), the lifetime for this kind of processes is $\gtrsim 10 \cdot 10^{19}\,\mathrm{yr}$. Hence, although the initial condition for it to happen ($M_X > M_Y$) is fullfilled by several nuclei, in reality, due to the competition with ordinary β decays, this process is only visible when the single β is forbidden (due to mass differences) or highly suppressed (due to large spin changes). This scenario is well illustrated in Fig. 2.1.

---

[1] Hereafter, if not specified, $\beta\beta$ will be referred to $\beta\beta^-$, defined in Eq. 2.1.

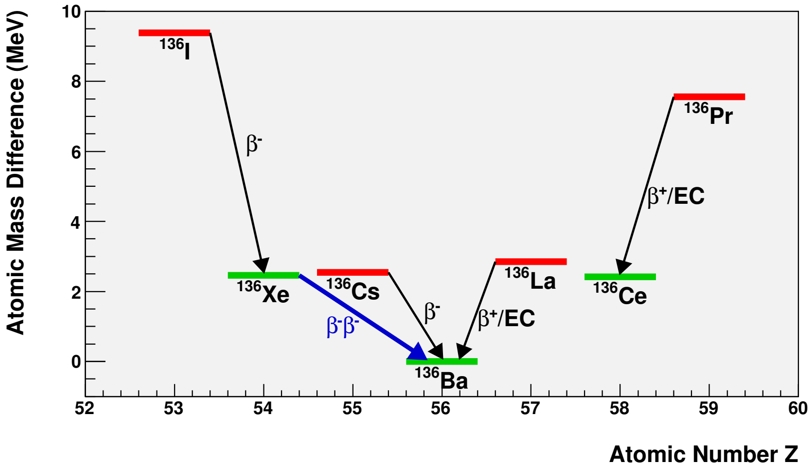

Figure 2.1.: Mass parabola case for $A = 136$ isotopes. Green is for even-even nuclei while red is for odd-odd ones. The left branch shows the double beta scenario for $^{136}\mathrm{Xe}$: as $^{136}\mathrm{Cs}$ mass is greater, single β is forbidden and the only process to get to $^{136}\mathrm{Ba}$ is $\beta\beta$. On the other hand, the right branch shows the same scenario but with β^+/ε for the $^{136}\mathrm{Ce}$ case. Diagram extracted from [59]

There are 35 isotopes that match that requirement [58] (thanks to the double mass parabola effect emerging for even-even to odd-odd decay chains), although it has been observed for only 14 of them, listed in Table 2.1.

From a kinematic point of view, initial neutrons are considered to be uncorrelated, as suggested in the diagram in Fig. 2.2a. Thus, neglecting the nucleus recoil, leptons take all the available energy. Then, if adding electron energies, one expects a continuous spectrum, analogous to the single β case, extending from 0 to $Q_{\beta\beta}$ and peaking below $Q_{\beta\beta}/2$ (see Fig. 2.2b). The $Q_{\beta\beta}$ is defined as the energy released from the decay, i.e.:

$$Q_{\beta\beta} = M_X - M_Y, \tag{2.2}$$

M refers to the atomic mass for each element and neutrino masses are neglected.

As already mentioned, other flavours of $\beta\beta$ are possible, as double electron captures, double β^+ decay, and simultaneous electron capture and β^+ decay. However, the latter are disfavoured by the smaller phase space. On the other hand, $\varepsilon\varepsilon$ has been recently developed, in particular via the observation of $^{124}\mathrm{Xe}$ double electron capture by XENON1T [85].

Isotope	Process	$T^{2\nu}_{1/2}$ $(10^{20}\mathrm{yr})$	Experiments
^{48}Ca	$\beta\beta^-$	$0.53^{+0.12}_{-0.08}$ [83]	NEMO-3, IrvineTPC, TGV,
^{76}Ge	$\beta\beta^-$	18.8 ± 0.8 [83]	PNL-USC-ITEP-YPI , IGEX, H-M, GERDA
^{78}Kr	$\varepsilon\varepsilon$	190^{+130}_{-80} [84]	BAKSAN
^{82}Se	$\beta\beta^-$	$0.87^{+0.02}_{-0.01}$ [83]	NEMO-2, NEMO-3, CUPID-0, IrvineTPC
^{96}Zr	$\beta\beta^-$	0.23 ± 0.02 [83]	NEMO-2, NEMO-3
^{100}Mo	$\beta\beta^-$	$0.0706^{+0.0015}_{-0.0013}$ [83]	NEMO-2, NEMO-3, ELEGANT, Irvine TPC, CUPID-Mo
^{116}Cd	$\beta\beta^-$	0.269 ± 0.009 [83]	NEMO-2, NEMO-3, ELEGANT, Aurora
^{124}Xe	$\varepsilon\varepsilon$	180 ± 51 [85]	XENON1T
^{128}Te	$\beta\beta^-$	22500 ± 900 [83]	geochemical method
^{130}Ba	$\varepsilon\varepsilon$	22 ± 5 [86]	geochemical method
^{130}Te	$\beta\beta^-$	7.91 ± 0.21 [83]	NEMO-3, CUORE, CUORE-0
^{136}Xe	$\beta\beta^-$	21.8 ± 0.5 [83]	EXO, Kamland-Zen
^{150}Nd	$\beta\beta^-$	0.0934 ± 0.0065 [83]	NEMO-3, Irvine TPC, ITEP TPC
^{238}U	$\beta\beta^-$	20 ± 6 [87]	radiochemical

Table 2.1.: Lifetime for the 14 observed $2\nu\beta\beta$ decays (ground state to ground state only) and the experiments that contributed to the half-life determination for each isotope.

2.2 Neutrinoless double beta decay

In addition to the allowed and measured $2\nu\beta\beta$ decay, there is another option, first suggested by W.H.Furry [88] as a potential test for the Majorana theory, the neutrinoless double beta decay $0\nu\beta\beta$:

$$^{A}_{Z}X \rightarrow ^{A}_{Z+2} Y + 2e^-. \tag{2.3}$$

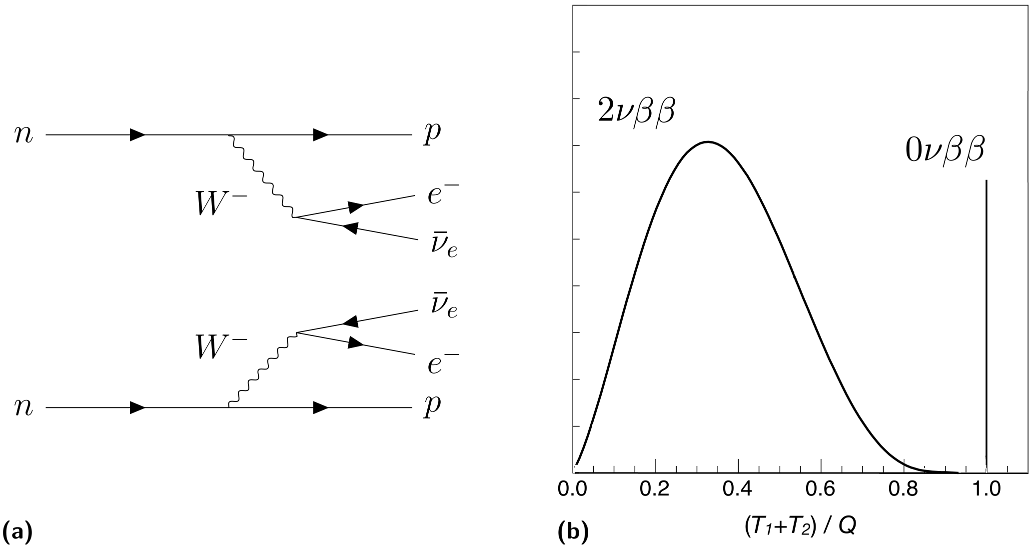

(a) **(b)**

Figure 2.2.: a: Feynman diagrams for a $2\nu\beta\beta$ decay. b: $\beta\beta$ energy spectra for two neutrino and neutrinoless cases. Rates are not to scale. Plot adapted from [59].

The initial neutrons, in contrast to the two neutrino mode, are correlated. Also, neglecting nuclear recoils, now, the sum of the kinetic energy for the outcoming electrons is a mono-energetic line laying on the $Q_{\beta\beta}$-value (defined in Eq. 2.2) as displayed in Fig. 2.2b.

Regarding phase-space arguments, $0\nu\beta\beta$ should be favored over two neutrino mode. Nevertheless, as Majorana effects go with m/E and given the low neutrino masses, the process is highly suppressed in the case of Majorana neutrinos, and cannot occur for Dirac neutrinos.

2.2.1 The black box theorem

Neutrinoless double beta decay is a typical prediction for LNV theories. Schechter and Valle showed in 1982 [89] that, regardless of the mechanism that leads to this process, it would imply that the neutrinos are Majorana particles since any of them would contribute to the $(m_\nu)_{ee}$ matrix element (Eq. 1.24). This is the so-called black box theorem. Fig. 2.3 shows a $\overline{\nu} \rightarrow \nu$ transition induced by an LNV operator, implying the non-zero value for $(m_\nu)_{ee}$.

However, the diagram considered in Fig. 2.3 is a four-loop process. Therefore, masses generated should be rather small and could not account for the mass differences coming from oscillation observations [90]. This implies that other Dirac or Majorana mass sources must exist. Moreover, the black box theorem cannot explain

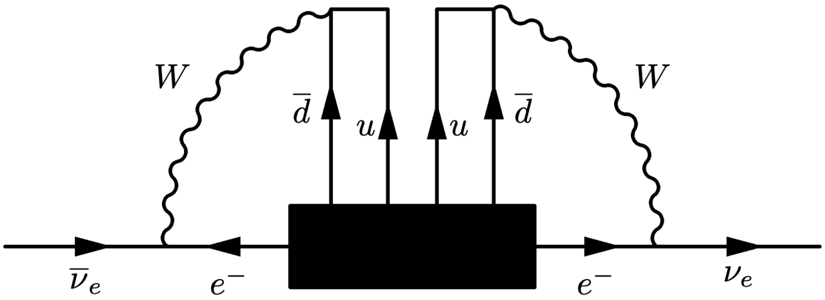

Figure 2.3.: Feynman diagram for the black box theorem case for a transition from $\overline{\nu}$ to ν, contributing to an effective Majorana mass term. Figure from [90].

anything about the dominant mechanisms contributing to make $0\nu\beta\beta$ measurable. Neither is able to tell if such a mechanism is related or not to neutrino oscillations. The standard case, covered in Sec. 2.2.2, is an example of a direct connection.

2.2.2 The standard mechanism for neutrinoless double beta decays

The simplest scenario for the neutrinoless double beta decay would be the exchange of a light Majorana neutrino, as displayed in Fig. 2.4. The neutrino created in one vertex as right-handed acts as a left-handed one in the vertex where it is absorbed. Given this chirality flip, the process is suppressed by a m/E factor.

The amplitude for the process should be proportional to the sum over the three light neutrino mass eigenstates and U_{ei}^2. Hence, the modulus of the amplitude must be proportional to the so-called effective neutrino Majorana mass:

$$m_{\beta\beta} = |U_{ei}^2 m_i|. \tag{2.4}$$

Where $m_{\beta\beta}$ happens to be the modulus of the $(e$,$e)$ neutrino mass matrix element, $m_{\beta\beta} = |(m_\nu)_{ee}|$ (see Sec. 1.4.4).

For the scenario where light neutrino exchange is the dominant contribution, the half-life for the $0\nu\beta\beta$ can be written as:

$$\left(T_{1/2}^{0\nu}\right)^{-1} = G^{0\nu}|M^{0\nu}|^2 \left(\frac{m_{\beta\beta}}{m_e}\right)^2, \tag{2.5}$$

where $G^{0\nu}(Q,Z)$ is a phase-space and $M^{0\nu}$ is the nuclear matrix element (NME) for the process. The first factor takes into account the kinematics of the transition and can be precisely computed ($\sim 0.1\%$ accuracy) [91, 92]. On the other hand,

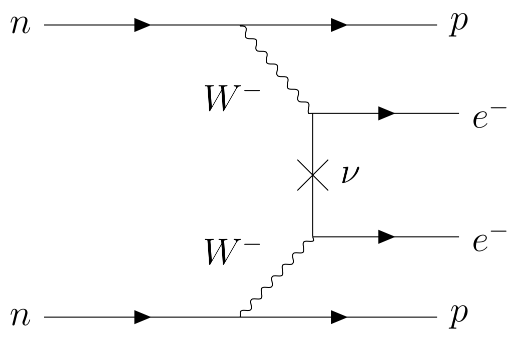

Figure 2.4.: Feynman diagram for a $0\nu\beta\beta$ decay.

the NME has to be estimated using a given nuclear model, relying on complicated calculations, resulting in discrepancies among different models.[2] Furthermore, the Eq. 2.5 links the effective Majorana mass to a non-zero rate for the neutrinoless double beta decay. Thus, even a non-positive detection of this process can lead to tighter constraints to $m_{\beta\beta}$ via an upper bound.

Additionally, if this happens to be the dominant contributor to $0\nu\beta\beta$ decay, from Eq. 2.4, it reads that then, the process is entirely related to the oscillation phenomenology, providing information about the absolute mass scale. This extra information may complement the one obtained through cosmological bounds and β decay, as explained in Sec. 1.3.2. However, the actual relation is affected by the uncertainties of the oscillation parameters, the neutrino masses' final ordering, and the mass matrix's remaining unknown phases. Despite this, the relation between $m_{\beta\beta}$ and the neutrino masses can be parametrized up to a certain accuracy as displayed in Fig. 2.5, where the $m_{\beta\beta}$ is represented in function of the m_{lightest}.[3] Each band represents the case for normal ordering (red) and inverted ordering (green) with some width due to the mixing angles' uncertainties and the unknown Dirac/Majorana phases. A lower bound in the process half-life implies an upper one for $m_{\beta\beta}$ (see Eq. 2.5), that, due to NME uncertainties, is translated into a horizontal exclusion band. This horizontal band, in turn, as it rules out regions of the allowed parameter space, implies a constraint for m_{lightest}. In addition, cosmological data impose direct upper limits for m_{lightest}.

The current generation of $0\nu\beta\beta$ experiments (see Sec. 2.4) has explored right next to the IO region, territory left for the next generation to come, the tonne-scale

---

[2] New experiments like NUMEN are trying to shed some light on the NME problem from an experimental perspective, using a specific nuclear reaction type (double charge exchange reactions) to extract information [93, 94].

[3] $m_{\text{lightest}} = m_1(m_3)$ for NO(IO)

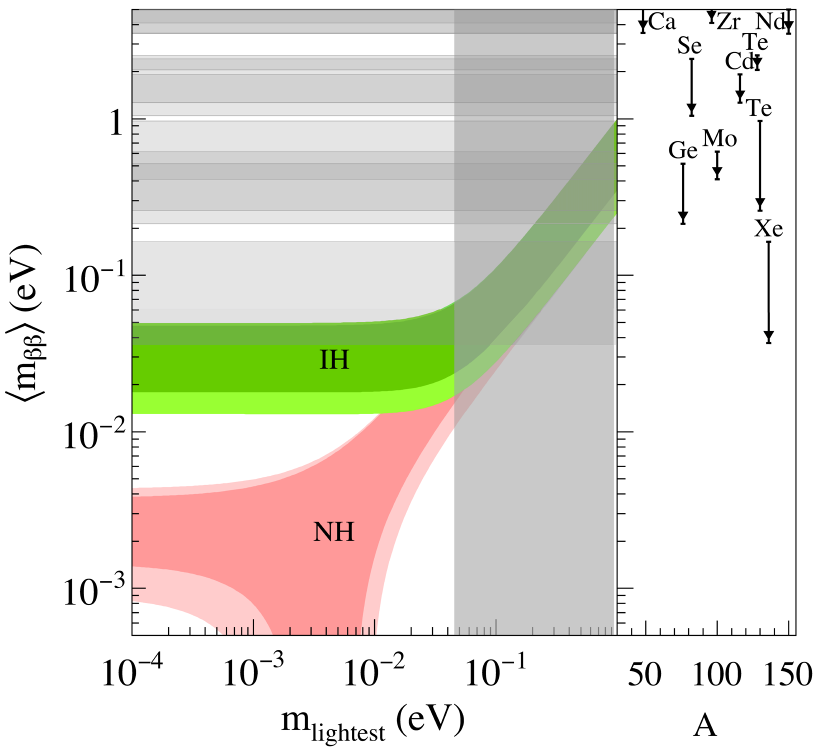

Figure 2.5.: The effective Majorana mass $\langle m_{\beta\beta}\rangle$ as a function of the lightest neutrino mass (m_{lightest}). Dark bands represent the 1σ region for the NO (red) and IO (green), while lighter ones take the 3σ variation. In the vertical axis, horizontal-band constraints come from double beta experiments. In fact, for each isotope, there is a grey band showing the excluded region, and isotopes are displayed in the right part. On the other hand, the horizontal axis is constrained by cosmological observations. The actual value displayed comes from [95] and is $m_{\text{lightest}} < 0.042\,\text{eV}$ (IO). This type of representation was first proposed by F.Vissani [96]. Plot from [68] and adapted.

experiments (Sec. 2.5). Nevertheless, oscillation phenomenology (see Sec. 1.3.1) and cosmology bounds (see Sec. 1.3.2) show some preference towards the NO. That would imply that the experimental requirements may need to be further improved to even larger scales than next-generation ones. This would finally depend on the final values for the parameters involved as it may well be that they happen to fall in the upper-right region with a $m_{\beta\beta}$ high enough to be detected without increasing the sensitivity. In fact, the probability of observing the $0\nu\beta\beta$, even in the NO scenario, could be up to 50 % (within assumptions) [97]. Therefore, despite the chances for the parameters to be conveniently arranged, in order to ensure the observation, future improvements are vital.

The results from the determination of the actual absolute mass scale for neutrinos can open new ways to study neutrino properties. One example could be that joint information from m_β (defined as in Eq. 1.11) and Σm_ν (defined as in Eq. 1.13) can be essential to determine the Majorana phases $\widetilde{\alpha}_i$ in Eq. 1.9 [91]. On the other hand, the determination of m_β and Σm_ν may constrain m_{lightest} in a way inconsistent with $m_{\beta\beta}$ determinations. If so, a null observation for $0\nu\beta\beta$ would imply that neutrinos are Dirac particles. Ultimately, even with a non-zero $m_{\beta\beta}$ determination may imply additional sources of LNV, other than light Majorana neutrino exchanges.

2.2.3 Alternative mechanisms for neutrinoless double beta decay

Different authors have proposed a variety of non-standard mechanisms for the $0\nu\beta\beta$ decay [98]. The main features for these alternatives can be summarized by the considered aspect to change from the standard process:

- The Lorenz structure of the currents. Left-right symmetric theories predict positive-chirality currents mediated by a W_R. One example of this interaction is displayed in fig 2.6a, where a massive right-handed Majorana neutrino is exchanged. Experiments able to detect each electron tracks could potentially prove this mechanism by measuring the energy and angular correlation.
- The mass scale of the exchanged virtual particles. Maybe heavy left-handed Majorana neutrinos can take the place of light ones in the standard process. Another possibility is the exchange of heavy supersymmetric neutral particles, as the neutralino, χ, in R-parity violating theories, as displayed in fig 2.6b.
- Additional particles in the final state. One common example of this would be the emission of a light (or even massless) Majoron, a theoretical particle that can couple to neutrinos, as shown in Fig. 2.6c. In this case, the spectrum is no longer mono-energetic but continuous.

2.3 Experimental aspects of double beta decay searches

Neutrinoless double beta decay detection would imply a profound impact in particle physics's foundations, confirming that neutrinos are Majorana fermions (as explained

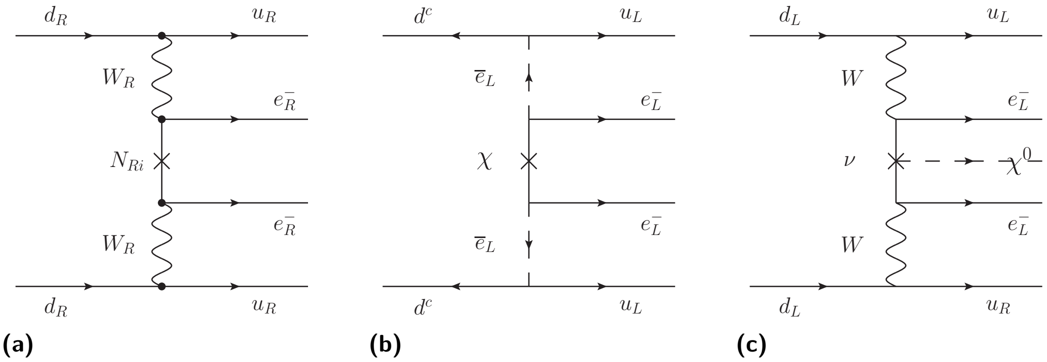

Figure 2.6.: Feynman diagrams for three examples of non-standard mechanisms for $0\nu\beta\beta$: (a) Massive right-handed neutrino exchange with positive chirality currents [99]; (b) Neutralino exchange [100]; (c) Majoron emission [101].

in Sec. 2.2). However, from an experimental perspective, the $0\nu\beta\beta$ decay search is a technological challenge. The first problem one faces is the very long half-life of the process ($\gtrsim 10^{26}$ yr, several orders of magnitude greater than the age of the Universe). Phenomena with such extreme lifetimes have never been observed, which implies that the experimental techniques must be pushed to the limit.

Considering the exponential decay behavior for the process, one can estimate the expected number of events, $N_{0\nu}$, for a given observation time, $t \ll T^{0\nu}_{1/2}$, as:

$$N_{0\nu} = \log 2 \cdot \frac{N_A}{W_{\beta\beta}} \cdot \epsilon \cdot M_{\beta\beta} \cdot t \frac{1}{T^{0\nu}_{1/2}}, \tag{2.6}$$

where N_A is the Avogadro constant, $W_{\beta\beta}$ is the molar mass of the $\beta\beta$ isotope, $M_{\beta\beta}$ is the total mass of $\beta\beta$ isotope accumulated for the experiment, and ϵ is the detection efficiency. When comparing different experiments with diverse active masses and observation times, a useful variable is the exposure, defined as $M_{\beta\beta} \cdot t$. Plugging some numbers, assuming no background, perfect efficiency, and a $T \sim 10^{26}$ yr ($m_{\beta\beta}$ ~50 meV), Eq. 2.6 shows that the required isotope masses are of the order of 100 kg.

However, the experimental conditions are far from ideal. The detectors are designed, ideally, as calorimeters focused around the $Q_{\beta\beta}$ region, as the event's energy is expected to be mono-energetic at $Q_{\beta\beta}$. Nevertheless, finite resolution cause this ideal line to be a Gaussian distribution, with a certain spread. There is a possible contribution from background events falling in this region of interest (ROI), which worsens the sensitivity.

2.3.1 Sensitivity to $m_{\beta\beta}$

Sensitivity, defined *à la* Feldman and Cousins, is the average upper limit one would get from an ensemble of experiments with the expected background and no true signal [102]. I.e., when quoting the sensitivity of an experiment, the worst scenario is considered, when no signal is found, and what upper bound yields for the *negative* result. For the $0\nu\beta\beta$ ideal case of no backgrounds, the sensitivity for $m_{\beta\beta}$ can be extracted from combining Eqs. 2.5 and 2.6 as:

$$S(m_{\beta\beta}) = K_1 \sqrt{\frac{\overline{N}}{\epsilon M_{\beta\beta} t}}, \tag{2.7}$$

where

$$K_1 = \sqrt{\frac{W_{\beta\beta}}{\log 2\; N_A} \frac{m_e^2}{G^{0\nu}|M^{0\nu}|^2}} \tag{2.8}$$

is a constant that only depends on the isotope and $\overline{N}$ is the averaged upper limit of events in the absence of signal.

When considering an ideal case, i.e., an experiment with no background, the observed number of events is always zero, without fluctuations. Therefore, the sensitivity results depend only on the inverse square root of the exposure, $(Mt)^{-1/2}$.

Unfortunately, for a realistic case, background level, b, plays a role. For this scenario, $\overline{N}$ can be taken, approximately, as [103]

$$\overline{N} = k\sqrt{b}. \tag{2.9}$$

The background level is usually parametrized as proportional to the exposure, Mt and the energy window width considered, ΔE, which would be defined according to the resolution of the detector:

$$b = c \cdot M_{\beta\beta} t \cdot \Delta E, \tag{2.10}$$

where c is known as the background rate, typically measured in counts/(keV · kg ·yr). Consequently, Eq. 2.7 becomes:

$$S(m_{\beta\beta}) = K_2\; \epsilon^{-1/2} \sqrt[4]{\frac{c \cdot \Delta E}{M_{\beta\beta} t}}, \tag{2.11}$$

where $K_2 = \sqrt{k} K_1$.

Therefore, comparing Eq. 2.7 and 2.11, one realizes that the presence of background reduces the sensitivity drastically, as the inverse square root dependence with the exposure changes to a fourth root one. Moreover, any experiment should aim to reduce the background rate per unit energy, mass and time, improve the resolution (allowing smaller energy windows, ΔE), and increase exposure, $M\ t$. All those strategies depend on the chosen isotope and the experimental technique, and both considerations are highly entangled since the isotope selection narrows the options for the technique to be applied.

2.3.2 Detection efficiency

Given the extremely long half-life, the detection efficiency is a crucial requirement. Reading from Eq. 2.11, a factor r of efficiency improvement would require a factor r^2 in background reduction to match the sensitivity gain in the same conditions. Thus, experiments should try to focus on maximizing efficiency.

Homogeneous detectors, those capable of using the isotope of interest as the detection medium, are more efficient than a separate source-detection scheme. However, homogeneous detectors may use a fraction of the mass close to the boundaries to self-shield against external backgrounds.

In general, the simpler the detection method, the higher the efficiency. In the case of germanium diodes or bolometers, pure calorimeters, have efficiencies over 80 %, whereas tracking-based detectors have a more modest one, close to 30-40 % [104].

2.3.3 Isotope

The isotope taken to be the $\beta\beta$-emitter is a delicate choice, as its properties dictate the real possibilities of the experiment and determine the technology to be applied. There are several points to be taken into account for the final consideration.

First of all, Eq. 2.5 makes clear that any isotope's goal would be to maximize $G^{0\nu}$ and $|M^{0\nu}|$. On the one hand, for the phase-space factor, it is essential to notice that it depends on $Q_{\beta\beta}^5$, to a first approximation [92]. Thus, only the higher values for the $Q_{\beta\beta}$ are preferable. In fact, only the eleven candidates with $Q_{\beta\beta} > 2\,\mathrm{MeV}$ have been historically considered. On the other hand, the NME situation is not that clear. As already pointed out in Sec. 2.2.2, there are various methods for computing the NME, each one yielding a different estimation, although the values

Isotope	I.A. (%)	$W_{\beta\beta}$ (g mol^{-1})	$Q_{\beta\beta}$ (keV)	$G^{0\nu}$ (10^{-15}yr^{-1})	$\lvert M^{0\nu}\rvert$
^{48}Ca	0.187	47.95	4263	24.81	0.541 - 2.23
^{76}Ge	7.75	95.92	2039	2.36	2.81 - 5.55
^{82}Se	8.82	81.92	2998	10.16	2.64 - 4.67
^{96}Zn	2.80	95.91	3346	20.58	2.53 - 6.50
^{100}Mo	9.74	99.91	3034	15.92	3.73 - 6.59
^{110}Pd	11.72	109.91	2018	4.82	3.62 - 5.726
^{116}Cd	7.51	115.90	2814	16.70	2.78 - 5.35
^{124}Sn	5.79	123.91	2287	9.04	2.558 - 5.79
^{130}Te	34.08	129.91	2528	14.22	2.65 - 6.41
^{136}Xe	8.86	135.91	2458	14.58	2.117 - 4.77
^{150}Nd	5.64	149.92	3371	63.03	2.19 - 3.32

Table 2.2.: Summary of the main properties for the $\beta\beta$-isotope candidates for those with $Q_{\beta\beta} > 2\text{MeV}$: natural isotopic abundance (I.A.) [105], atomic weight ($W_{\beta\beta}$) [106], $Q_{\beta\beta}$, the phase-space factor ($G^{0\nu}$) [92], and the range for the nuclear matrix elements (NME). For the latter, several models were considered, taking the minimum and maximum for each isotope: ISM [107], QRPA Jy [108], QRPA Tü [109], IBM-2 [110], and EDF [111].

for the different isotopes are contained in a factor of five of each other. Consequently, despite the fact that NME computation is affected by uncertainties from the nuclear models used, this variation does not drastically affect the final determination and no isotope is preferred in this regard. Both $G^{0\nu}$ and $|M^{0\nu}|$ contributions can be summarized in the K_1 factor defined in Eq. 2.8. K_1 for all the $\beta\beta$-isotopes with a $Q_{\beta\beta} > 2\,\text{MeV}$. is shown in Fig. 2.7. Additionally, the main parameters describing K_1 for each source are displayed in Table 2.2. The main conclusion from it is that no isotope is particularly praised in terms of K_1, as the decay rate per unit mass is comprised within a factor of 2.

The preference towards high $Q_{\beta\beta}$ has another positive side effect: the background reduction. Natural radioactive background tends to concentrate on the low energy region, mostly under 3 MeV. Hence, the greater the $Q_{\beta\beta}$, the more background is left below the ROI. Sec. 2.3.5 will briefly focus on that and Chapter 7 will cover the NEXT experiment case study.

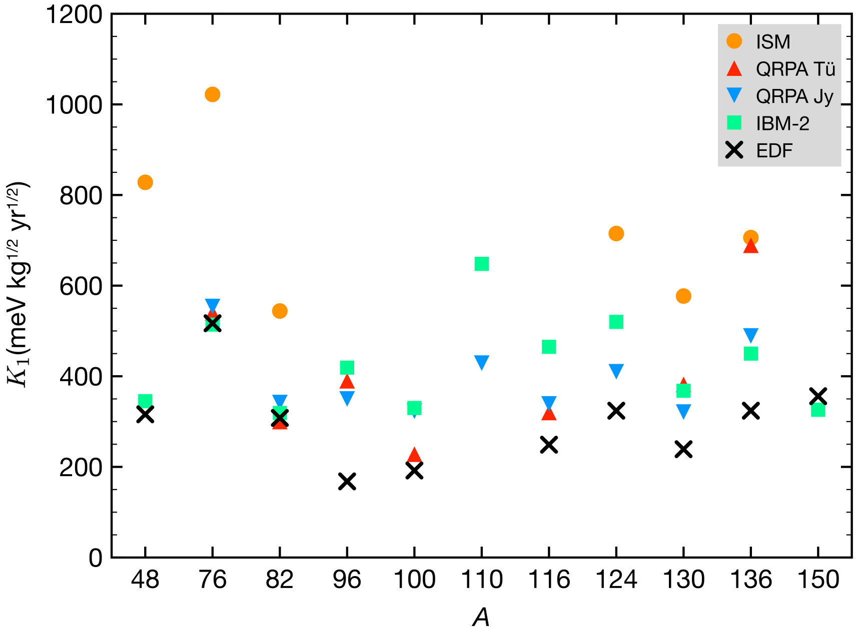

Figure 2.7.: K_1 value for the main $\beta\beta$-isotopes, those with $Q_{\beta\beta} > 2\text{MeV}$, represented by their atomic mass (A). Each marker style symbolizes a nuclear model for $|M^{0\nu}|$. Figure from [104].

Another issue to focus on is $2\nu\beta\beta$ rate. The two neutrino mode is an irreducible background for any $\beta\beta$ experiment. Hence, decays with a relatively slow rate are preferable, especially for those experiments with a modest resolution (Table 2.1 shows the half-lives for all the experimentally known $\beta\beta$-emitters).

Exposure

The current generation of detectors is of the order of 100 kg in double beta isotope mass. However, that is not enough to cover the inverse ordering region (see Fig. 2.5) in a reasonable amount of time. The next generation's goal is to go for a tonne-scale detector, as most collaborations are attempting. Nevertheless, the experimental method is crucial since the scalability depends dramatically on it since the economic and logistical feasibility is diverse for the various candidate isotopes.

Most of the natural abundances for the $\beta\beta$-emitters are below 10 % (see Table 2.2). The only exception to this is $^{130}\mathrm{Te}$, representing more than a third of natural Te, whereas, in the other extreme, $^{48}\mathrm{Ca}$ only constitutes a tiny 0.2 % of natural Ca. Therefore, enrichment becomes necessary in order to accumulate the large amount needed, which elevates the cost significantly in the acquisition of the isotopes. On the one hand, centrifugal separation is available for the elements with a stable gas compound, being the most cost-effective technique [112]. Xe treatment is simpler, and therefore cheaper, than other elements under the centrifugation method.[4] From this point of view, $^{136}\mathrm{Xe}$ turns out to be a good candidate for the tonne-scale generation, balancing a usual isotopic abundance and the relatively low cost of enrichment.

In conclusion, isotope properties show that there is no ideal choice. Several candidates seem to be equally favored and the final decision relies on the actual cost of acquisition and the desired experimental technology for the detector.

2.3.4 Energy resolution

Going back to Eq. 2.11, it is clear that energy resolution plays an essential role in background reduction and, consequently, in the ultimate sensitivity for a $\beta\beta$ experiment. As pointed out in the previous section, even an ideal background-free detector would have to face the unavoidable $2\nu\beta\beta$ mode contribution. Hence, an excellent energy resolution is crucial.

An example of this is sketched in Fig 2.8. It displays three toy Monte Carlo simulations for a hypothetical signal (Gaussian) with the same number of counts but different resolutions and background (flat). Both the signal strength (50 counts) and the background rate (1 count/keV) are typical values for a tonne-scale generation experiment after a typical exposure of $\sim$100 kg · yr and a $m_{\beta\beta}$ $\sim$100 meV. The peak is crystal clear in the most promising scenario (1 %FHWM), whereas it is barely distinguishable for the intermediate case (3.5 %FWHM), and it has disappeared for the last situation (10 %FWHM).

Consequently, the resolution is a fundamental parameter when designing a $\beta\beta$ experiment. The better resolution, the greater the sensitivity, and it is even more critical for the experiments aiming to cover the normal ordering, as they will require background-free conditions. For the current generation, experiments with a moderate resolution have to compensate for it by increasing the exposure and lowering the background rate per unit energy.

---

[4] Since Xe is already a gas, then it can be separated directly. On the other hand, elements like $^{76}\mathrm{Ge}$, $^{82}\mathrm{Se}$, $^{100}\mathrm{Mo}$, and $^{130}\mathrm{Te}$ have to be embedded in a organic molecule, fluorides typically.

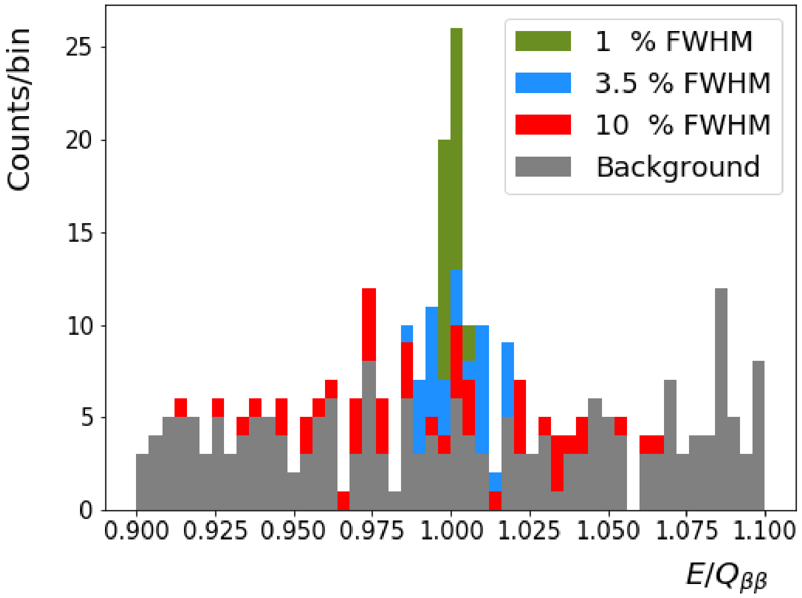

Figure 2.8.: Signal and background (color and grey histograms, respectively) in the ROI around the $Q_{\beta\beta}$. Each signal histogram is stacked with the same background. The signal strength is taken as the same for the three (50 counts) but with a different energy resolution (green for the 1 %FWHM case, blue for the 3.5 %FWHM, and red for the 10 %FWHM) Gaussianly smeared around the $Q_{\beta\beta}$. The background is considered to be flat with a rate of 1 count/keV.

2.3.5 Background reduction

As discussed in the Sec. 2.3.1, the existence of background in the ROI for the $Q_{\beta\beta}$ reduces the trend of the exposure from an inverse square root to an inverse fourth root. This is even more dramatic as the sensitivity aim approaches the NO region. Hence, a complete background-free detector is an ultimate goal for any experiment.

Excluding the aforementioned intrinsic and irreducible $2\nu\beta\beta$ contribution, the background sources are diverse. They include the radioactive isotopes from the natural decay channels as impurities in the detector materials and surroundings. Therefore, a must for any single piece within the detector is a complete screening looking for the most radiopure materials. Usually, the radioactive impurities' inside the detector components represents the main contribution to the total background rate. In this regard, the typical harmful isotopes are ^{208}Tl and ^{214}Bi, present in the Thorium (4n) and Uranium (4n+2) chains respectively.

Another common concern is Radon, mainly $^{220}\mathrm{Rn}$ and $^{222}\mathrm{Rn}$. Since it is a noble gas, it is very chemically stable and can easily diffuse through detector materials entering the active volume. Radon decay subproducts are radioactive as well and, as they tend to be charged, adhere to surfaces or dust. This background interference can be mitigated by installing radon-free environments (using radon traps) or flushing the detector location and components with pure nitrogen.

Apart from the materials constituting the detector, their whole surroundings are also radioactive. This represents a considerable flux of gammas and neutrons entering the active volume and reacting. A usual way of getting rid of this contribution is shielding the detector, for example with dense and radiopure materials as Roman lead and cooper, or even placing the experiment inside a water tank.

Finally, the last typical backgrounds to deal with are those related to cosmic rays, generally the main external contribution. The method to mitigate them is going underground, as those underground laboratories have a muon and neutron flux that is several orders of magnitude less than on Earths's surface. However, since detectors are growing towards large scales, cosmogenic sources will become an issue again, mainly from neutron captures due cosmic ray muons and solar neutrino interactions. There are, nonetheless, ongoing efforts in order to reduce those effects for the next-generation experiments [113].

In addition to all of those *passive*, background reduction approaches, most experiments are developing mechanisms for *active* signal and background discrimination, such as pulse-shape discrimination [114, 115], topology reconstruction (either single-site versus multi-site events or track reconstruction) [116, 117, 118, 119] and even the attempt to detect the daughter ion produced in $\beta\beta$ events [120, 121].

Further discussion about the background's contribution in the context of the NEXT experiment can be found in Chapter 7.

2.4 State of the art and main experiments

Furry's theoretical proposal arouse some interest, and the first attempts to measure the $0\nu\beta\beta$ were performed. Unfortunately, after the confirmation of the parity violation and the $V-A$ structure of weak interaction in 1957 [122], it became clear that the rates for the neutrinoless mode were significantly suppressed with respect to the two neutrino mode. This reduced the interest in this search. However, in the early 1980s, there was a resurgence among the community, mainly due to an experimental claim concerning neutrino masses of ~30 eV [123] (later rejected by other experiments), the consideration of the neutrino as a potential dark matter constituent, and the explosion of GUT theories development. This new enthusiasm crystalized in the aftermentioned black box theorem in 1982, instigating a more severe experimental development.

The principal experiment of the early stages of the field is the Heidelberg-Moscow (HM) one [124]. It consisted of high-purity germanium diodes enriched with $^{76}\mathrm{Ge}$, which accumulated a total exposure o 71.7 kg · yr and was located in the Laboratori Nazionali del Gran Sasso (LNGS), Italy. HM provided the best limit for many years using the pulse shape discrimination: $T^{0\nu}_{1/2} > 1.9 \cdot 10^{25}$ yr (90% CL) [125].

A cleavage within the HM, after re-analyzing data independently, claimed the discovery of the $0\nu\beta\beta$ in 2001 [126]. This observation happened to be quite controversial and was received with skepticism by the community [127,128]. Several later experiments, even with the same isotope, have ruled out the discovery since then [129, 130].

Other remarkable initial attempts are Cuoricino experiment [131], which was based on Te bolometric crystals,[5] and NEMO-3 experiment [132], the only experiment able to use different emitters, as the source material was displayed in thin layers in between tracking calorimeters.

Currently, no unambiguous evidence for $0\nu\beta\beta$ exists in any nucleus. The present best estimations for the $0\nu\beta\beta$ in the main isotopes can be found in Table 2.3.

Additionally, Table C.1 summarizes the main features for the main recent detectors. The rest of the section will focus on a subset of those: GERDA, CUORE, KamLAND-Zen, and EXO, each representing, also, a different technology approach.

2.4.1 Bolometers: CUORE

Bolometers are cryogenic calorimeters that work at quite low temperatures ($\sim$ 10 mK, 7 mK for CUORE's case), and the experimental technique is based on detecting small temperature changes in the crystals ($\sim$ 0.1 mK). A weak thermal link connects an absorber and a low-temperature bath, and a thermometer monitors the temperature. When an event happens in the detector, the energy deposited induces some heat and a slight increase in the temperature. Concerning the materials, they can be

---

[5] Cuoricino reached a sensitivity comparable to HM's, but due to NME uncertainties could not disprove the result.

Isotope	$T_{1/2}^{0\nu}(\mathrm{yr})$	$m_{\beta\beta}(\mathrm{eV})$	Experiment
^{48}Ca	$> 5.8 \cdot 10^{22}$	$<$ 3.5 - 22	ELEGANT-IV [133]
^{76}Ge	$> 1.8 \cdot 10^{26}$	$<$ 0.079 - 0.180	GERDA [129]
^{82}Se	$> 3.5 \cdot 10^{24}$	$<$ 0.311 - 0.638	CUPID-0 [134]
^{96}Zn	$> 9.2 \cdot 10^{21}$	$<$ 7.2 - 19.5	NEMO-3 [135]
^{100}Mo	$> 1.5 \cdot 10^{24}$	$<$ 0.31 - 0.54	CUPID-Mo [136]
^{116}Cd	$> 1.0 \cdot 10^{23}$	$<$ 1.4 - 2.5	NEMO-3 [137]
^{130}Te	$> 2.2 \cdot 10^{25}$	$<$ 0.090 - 0.305	CUORE [138]
^{136}Xe	$> 2.3 \cdot 10^{26}$	$<$ 0.036 - 0.156	KamLAND-Zen [139]
^{150}Nd	$> 2.0 \cdot 10^{22}$	$<$ 1.6 - 5.3	NEMO-3 [140]

Table 2.3.: Best limits (90% CL) for the $0\nu\beta\beta$ process only considering transitions from the ground state to the ground state. The $m_{\beta\beta}$ limits are shown as quoted by the source reference.

composed of multiple materials and several of them happen to have $\beta\beta$-isotopes, letting detectors be homogeneous.

On the one hand, their main advantage is the excellent energy resolution they provide, and the growth technique allows the possibility of intrinsically low radioactive impurities. However, they present some drawbacks. First, the low temperatures required to operate the detector increase the technical difficulties and are a handicap for the scalability. Another issue is that the detectors consist of independent crystal arrays, so they are considerably affected by the volume to area ratio for background shielding. As detectors scale-up, in principle, the volume grows as $\sim r^3$ while the outer surface grows as $\sim r^2$. This trend is beneficial for the external background suppression since one can use a proportionally smaller detector's active volume for that shielding. However, when the detector is highly segmented, they consist, naively, of small stacked subdetectors. Hence, the surface and the volume scale with the same ratio. For further information about bolometers and their usage in $\beta\beta$ searches, see [158].

Experiments	Technology	Features		
		Homogeneous	High energy resolution	Tracking/topology
GERDA, MJD, LEGEND	HPGe	✓	✓	×
CUORE, LUCIFER, AMoRE, CROSS	Bolometers	✓	✓	×
Kamland-Zen, SNO+, ZICOS	Liquid Scintillators	✓	×	×
CANDLES	Inorganic Scintillators	✓	×	×
EXO	LXe-TPC	✓	×	✓
NEXT, PandaX-III, AXEL	HPXe-TPC	✓	✓	✓
NEMO	Tracking Calorimeters	×	×	✓

Table 2.4.: Technology and main features for the principal $0\nu\beta\beta$ experiments. The acronyms in the technologies stand for: High-Purity Germanium (HPGe), Liquid Xenon Time Projection Chamber (LXe-TPC), and High-Pressure gas-Xe Time Projection Chamber (HPXe-TPC). Data extracted from [141, 142, 143, 144, 145, 146, 147, 148, 149, 150, 151, 152, 153, 154, 155, 156, 157].

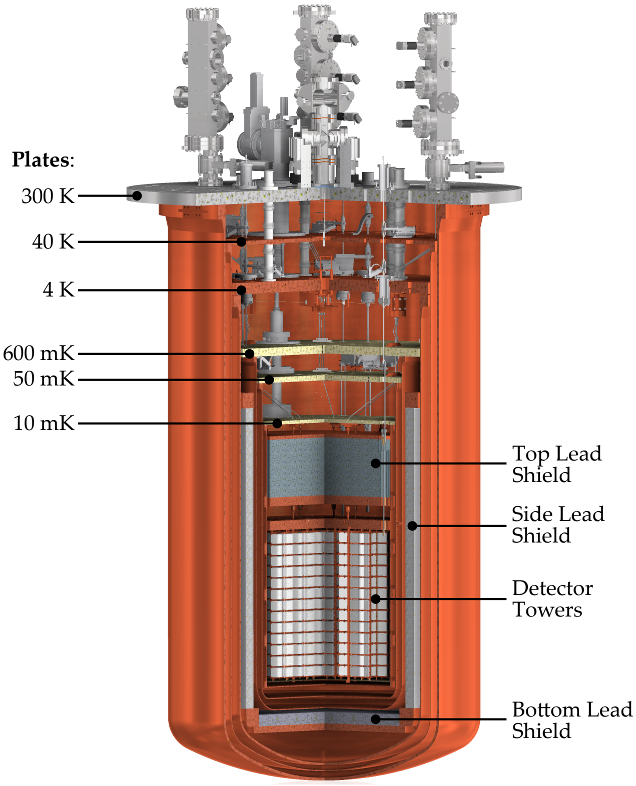

Figure 2.9.: Illustration of the design of the CUORE detector. Figure from [160].

CUORE

The Cryogenic Underground Observatory for Rare Events (CUORE) [159] is an experiment located in LNGS consisting of 988 TeO_2 unenriched[6] bolometer crystals, each with 750 g and 5x5x5 cm. Individual crystals are mounted in 19 towers, held inside a cryostat, to keep the desired working temperature. Several layers of Roman lead shield external backgrounds. In addition, an extra screening region made of lead, borated polyethylene, and boric acid surrounds the cryostat for further γ and neutron suppression. Fig. 2.9 sketches the main features of the design of the CUORE detector.

After a more than two years long run and total exposure of a 103.6 kg· yr of $^{130}\mathrm{Te}$ [161]. First of all, the energy resolution reported is (7.0 ± 0.4) keV FWHM (which translates to (0.28 ± 0.02) %FWHM), competitive with the ones obtained using Ge detectors. Regarding the limits for the $0\nu\beta\beta$, they are the leading experiment for the isotope, and the translation to $m_{\beta\beta}$ is competitive with the current best

---

[6] Given the fair amount of the isotope of interest in natural Te, the experiment does not need enrichment.

(check Table 2.3). On the other hand, the accounted background rate in the ROI is $(1.38 \pm 0.07) \cdot 10^{-2}$ counts / (keV· kg· yr). In this regard, the comparison with Ge experiments is not that successful, being one order of magnitude above GERDA's.

The experiment projects to reach a sensitivity of $9 \cdot 10^{25}$ yr (5 times better than the current bound) after running a total of five years [162].

2.4.2 Semiconductors: GERDA

Semiconductor detectors have a bias voltage applied across them, so an electric field is present inside the material. When a charged particle interacts, it produces electron-hole pairs drifted in opposite directions, inducing a current on the electrodes, the signal. For further information about semiconductors in the $\beta\beta$ searches, see [163].

Germanium detectors are the most mature technology used for $0\nu\beta\beta$ searches, as it is broadly used in commercial applications.[7] Another fundamental advantage of this approach is the excellent energy resolution accomplished. In addition, the crystal growing process lowers the level of impurities. On the contrary, the elevated cost of enrichment and the fact that they are constituted of many identical sub-detectors (hence, suffering from the volume to area ratio scaling problem, as bolometers) are the major handicaps for the strategy.

GERDA

The GERmanium Detector Array (GERDA) [143] was an experiment also located in LNGS consisting of 41 $^{76}\mathrm{Ge}$-enriched high-purity germanium diodes, immersed in a liquid-argon (LAr) cryostat in order to cool the detector and shield it against external backgrounds. The diodes are organized in seven strings, and each one is mounted by a low-mass support and suspended inside the cryostat, which is vacuum-insulated. A 6 cm copper covering layer is located in the inner face of the cryostat, and outside it, there is a water tank. Both the water tank and the LAr volumes are instrumented as a veto for external backgrounds entering the detector. A schematic view of the detector is displayed in Fig. 2.10.

---

[7] That affirmation is only valid for Ge case. In contrast, other semiconductor technologies are in an early stage, thus not feasible for the next-generation detectors. Examples of those new ideas are CdZnTe [164] and CMOS pixel array [165]

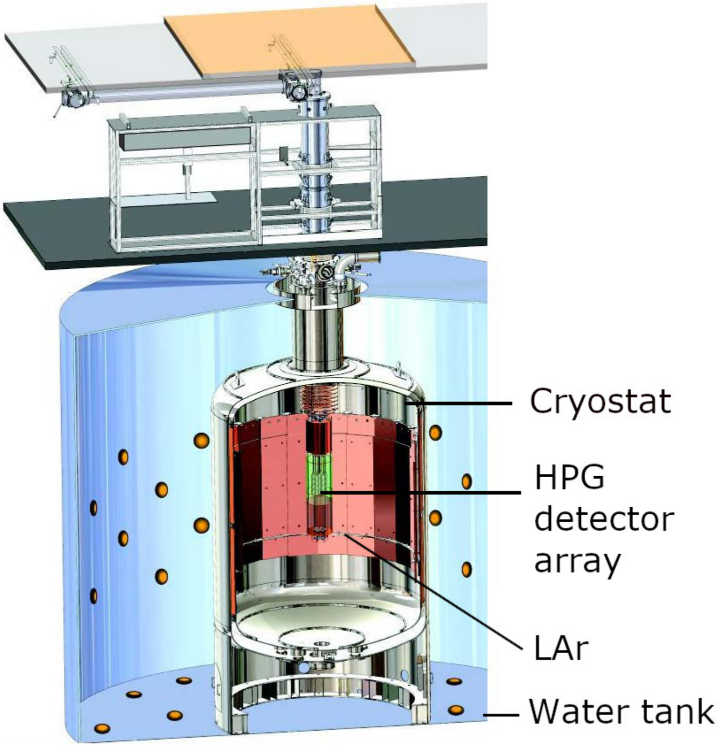

Figure 2.10.: Illustration of the design of the GERDA detector. Figure from [166].

The experiment's initial stage (Phase I) ran one year and a half, with the first set of reprocessed semi-coaxial detectors from the preceding H-M and Igex experiments and a new set of *broad-energy germanium* diodes (BEGe), summing a total of 7 and 30 units, respectively, and a final exposure of (16.34 ± 0.58) kg· yr of $^{76}\mathrm{Ge}$ and a background rate of $1 \cdot 10^{-2}$ count/(keV· kg· yr) [167] after the pulse-shape discrimination.[8]

For the Phase II, several updates were performed. For instance, adding the remaining detectors, the first bunch of 20 kg of BEGe diodes [166] in late-2015, and later in mid-2018 another 9.6 kg of *inverted coaxial point-contact* (ICPC) detectors [169], and instrumenting the LAr volume. Those changes improved background reduction and exposure. In fact, the final results from GERDA yielded a background of $5.2^{+1.6}_{-1.3} \cdot 10^{-4}$ count/(keV· kg· yr) [168]. Both phases can be combined for a total upper limit for the $0\nu\beta\beta$ $T^{0\nu}_{1/2} > 1.8 \cdot 10 \cdot 10^{26}$ yr (see Table 2.3) using a total exposure of (97.9 ± 1.4) kg· yr and the resolution is (4.9 ± 1.4) keV FWHM, (0.240 ± 0.067) %FWHM, for the coaxial case, and (2.6 ± 0.2) keV FWHM, (0.1275 ± 0.0098) %FWHM, for the BEGe one. Taking into account the back-

---

[8] Pulse-shape discrimination helps to discriminate signal, which is expected to be single-site (SS), from background, usually detected as multi-site (MS) events.

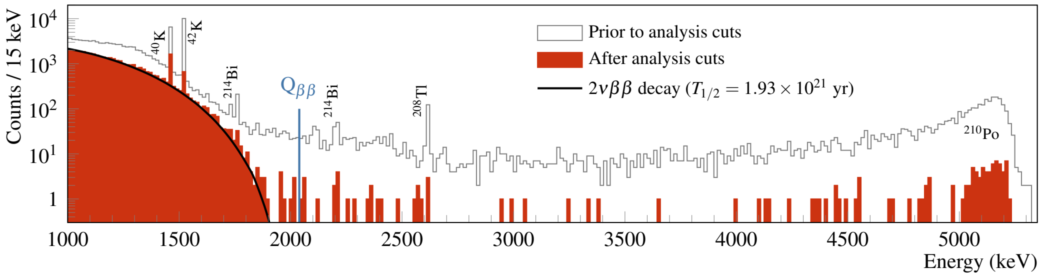

Figure 2.11.: GERDA's energy spectrum before and after selection for Phase II events. The prominent γ lines are labeled, as well as the α region due to $^{210}\mathrm{Po}$. Figure from [168].

ground rate, energy resolution, and exposure, GERDA can be considered to be in a background-free regime.

2.4.3 Liquid Scintillators: KamLAND-Zen

R. Raghavan first proposed the xenon-loaded LS technique for neutrinoless double beta decay searches in 1994 [171]. It offers a new opportunity to reuse detectors whose main objective has been fulfilled, as it is the case of KamLAND-Zen and SNO+, recycling KamLAND and SNO detectors, respectively. The main advantage of the approach is the simplicity and possibility of employing notable amounts of the desired isotope. The most significant limitation is the fairly poor energy resolution and the enormous efforts required for purification. Another typical concern for large-LS experiments is the background arising from neutrino-electron elastic scattering of ^{8}B solar neutrinos, although it can be mitigated using the directionality of those events in a Cherenkov tank [172, 173].

KamLAND-Zen

The KAMioka Liquid scintillator AniNeutrino Detector - ZEro Neutrino (KamLAND-Zen) [68] is an experiment located in the Kamioka Observatory, Japan. It consists of two concentric and transparent balloons. The inner balloon (IB) contains a mixture of Xe and liquid scintillator (LS), whereas the outer one (OB) contains pure liquid scintillator. A buffer oil separates the OB and a stainless-steel tank that shields the detector from the external background. The containment tank is instrumented with 1879 PMTs and surrounded by a water-Cherenkov detector. The mixture in the IB is a 13 ton Xe-loaded liquid scintillator, containing ~680 kg of $^{136}\mathrm{Xe}$. The OB has

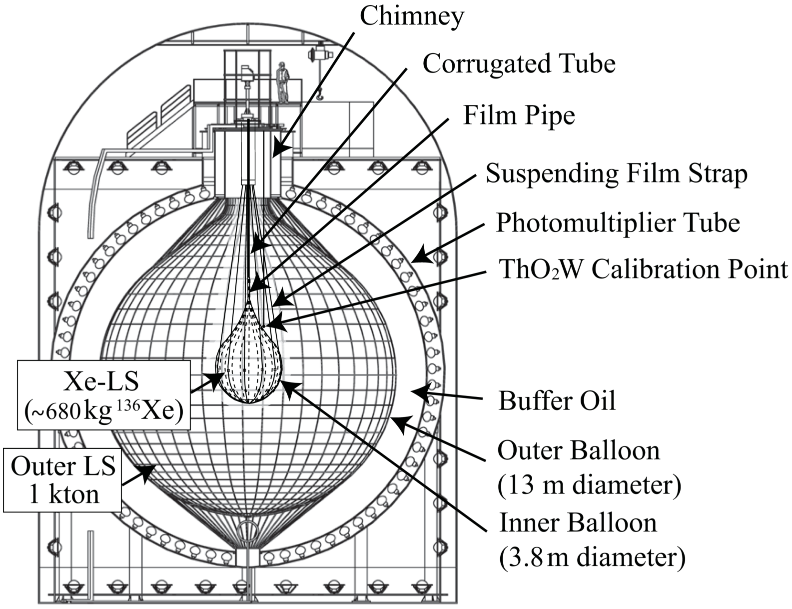

Figure 2.12.: Illustration of the design of the KamLAND-Zen detector with the current KamLAND-Zen 800 numbers. Figure from [170].

two purposes, shielding the IB from incoming radiation and detecting the outgoing one. Fig. 2.12 displays a scheme of the detector with the most important features labeled.

The first phase, Period1, of the KamLAND-Zen detector, with 320 kg of enriched Xe ($\sim$90 % purity), suffered dramatically from a $^{110\mathrm{m}}\mathrm{Ag}$ background contamination, most probably coming from the Fukushima incident [130]. The background rate was $\sim 3.8 \cdot 10^{-3}$ count/(keV · kg · yr) [174].

After a purification campaign, Period2 began, with 380 kg of enriched Xe. The background rate improved significantly down to $4 \cdot 10^{-4}$ count/(keV· kg· yr) [174] for the cleanest data subset. The resolution is the main counterpart of the experiment, as resulted in being $\sim$ 11 % FWHM. However, results for this stage regarding the $0\nu\beta\beta$ half-life are still competitive for the isotope, $T^{0\nu}_{1/2} >$10.7 · 10^{25} yr, with a total exposure of 504 kg· yr of $^{136}\mathrm{Xe}$. Fig. 2.13 shows the fit and data that lead to those results.

Nowadays, the detector operations are KamLAND-Zen800 [175], with 750 kg of enriched Xe, currently running since the beginning of 2019 and planning to reach a $T^{0\nu}_{1/2}$ sensitivity of $\sim 2 \cdot 10^{27}$ yr after running for five years. A recent initial look into this phase data reported the the current best limit for the isotope: $T^{0\nu}_{1/2} >$2.3 · 10^{26} yr (see Table 2.3), corresponding to an exposure of 970 kg· yr of $^{136}\mathrm{Xe}$.

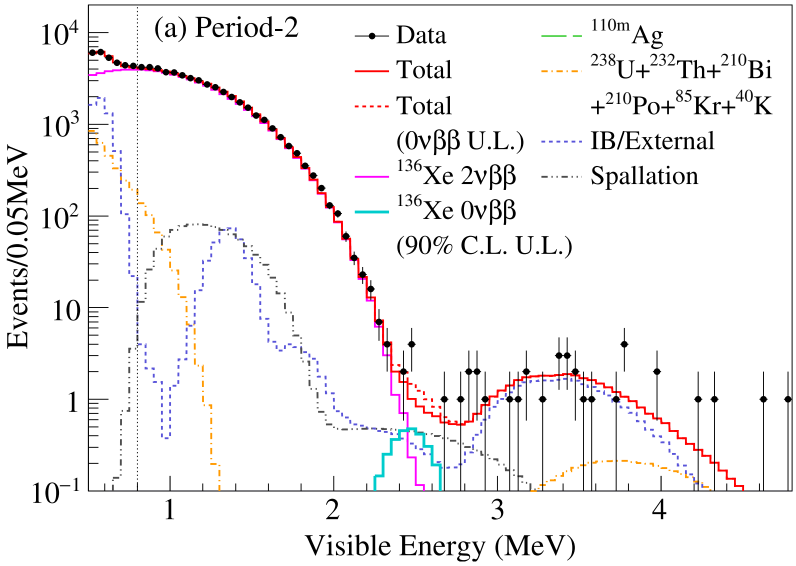

Figure 2.13.: KamLAND-Zen's energy spectrum of $\beta\beta$ candidates within a 1m-radius sphere fidutial volume for Period-2 data (dots), fit results (red solid line for the total and dashed for each individual component), and the upper limit for $0\nu\beta\beta$. Figure from [68].

2.4.4 TPCs: EXO-200

Time Projection Chambers (TPCs) are detectors that combine scintillation light and ionization electrons drift in order to be able to reconstruct 3D events,[9] first proposed by D. Nygren in the early 1970s [176]. Thus, they have access to topological information, and that is powerful information for background and signal discrimination. In addition, they are good calorimeters since they are homogeneous detectors and generate lots of ionization electrons (see Sec. 3.1.2). There are two possibilities, either gaseous or liquid Xe.

On the one hand, high-pressure gas-phase detectors allow getting an excellent energy resolution, ideally better than 0.5 % FWHM [177], and the reconstruction of full tracks since the low density of the gas allows the ∼MeV events to travel distances of the order of a few cm (whereas in the liquid case, they are of the order of mm at most). See Chapter 3 for a detail review of HPXe TPCs.

On the other hand, liquid-phase ones, although they have a lower resolution, they are denser, optimizing the volume needed for the emitter mass and the self-shielding. They can not resolve tracks, but point-like events, whereas still handle

---

[9] Techincally speaking, scintillation light is not mandatory for a 3D reconstruction. For instance, an external trigger can be used or even just the ionization electrons by themselves (paying the price of losing the absolute z coordinate determination but the relative one).

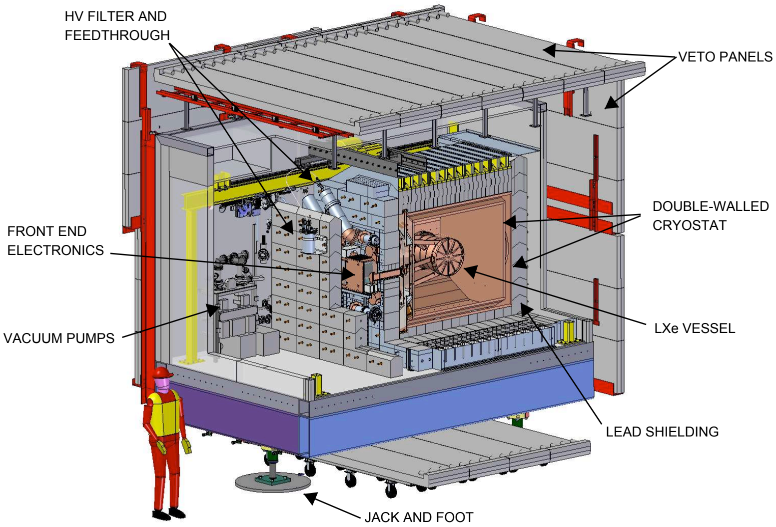

Figure 2.14.: Illustration of the design of the EXO detector. Figure from [183].

the spatial information to distinguish signal and background, primarily through single-site (SS) events, most likely signal, and multi-site (MS) ones, background.

A bridging solution would be the dual-phase detectors. They consist of a liquid active volume where the interactions occur and a gaseous region where the ionization electrons' collection occurs. This way, it combines the high density of liquid detectors with an EL readout, only possible in the gaseous phase (see Sec. 3.1.3). However, since the ionization takes place in the liquid region, the resolution is affected by the worse performance of the medium (see Sec. 3.1.2). Another disadvantage is the technical difficulty of the stability of the phase transition area. This kind of detector is a popular choice for dark matter detection as it maximizes the potential targets and allows lower energy thresholds [178, 179]. In fact, the DARWIN experiment claims to have the capability to perform a competitive $0\nu\beta\beta$ search, a $T^{0\nu}_{1/2}$ sensitivity of $8.5 \cdot 10^{27}$ yr (90% CL) for a exposure of 140 $\text{t} \cdot \text{yr}$ of natural xenon [180].

Finally, a significant advantage of TPCs is the potential detection of the daughter ion produced in the double beta decay. In the case of $^{136}\mathrm{Xe}$ it would be $^{136}\mathrm{Ba}$ (see Sec. 2.3.5).

For a more detailed review, see [181, 182].

EXO-200

The Enriched Xenon Observatory (EXO) [183] was an experiment located in the Waste Pilot Plant (WIPP), New Mexico, USA. It consisted of a symmetrical single-phase TPC full of liquid xenon (LXe). The 44-cm TPC was divided into two drift regions by a transparent cathode, photodetectors at both ends, and crossed wires for event spatial reconstruction. It was held inside a copper vessel, surrounded by a cooling and shielding liquid inside a cryostat, with an inner layer of lead with an active muon veto, for further shielding. A schematic view of the detector is displayed in Fig. 2.14.

EXO Phase I ran from 2011 to 2014 with enriched Xe, demonstrating the experimental technique potential [184]. For the following stage, a radon abatement system was installed, and improvement to the electronic noise was performed. Phase II ran for two years, from 2016 to 2018, yielding great results [185]. The half-life limit was set at $T^{0\nu}_{1/2} > 3.5 \cdot 10^{25}$ yr at 90 %CL, combining both phases with a total exposure of 234.1 kg· yr. Concerning the resolution, the measured value for Phase II is (2.708 ± 0.047) %FWHM. This energy resolution is not that great compared to semiconductors, bolometers, or HPXe, although much better than the one achieved by liquid scintillators. Finally, the background rate for Phase II resulted in $(1.9 \pm 0.2) \cdot 10^{-3}$ count/(keV· kg· yr). The best fit to low background data results can be found in Fig. 2.15.

2.5 Next-generation plans

Most of the experiments are moving towards the next stage of their development, mainly focused on scanning the IO parameter space, an endeavor that implies masses of the order of the tonne scale.

CUPID The Cuore Upgrade with Particle IDentification (CUPID) is an upgrade of CUORE detector which attempts to improve the bolometer performance by adding active particle identification, for example, through the Cherenkov light in the crystals. Although the final technology is not decided yet, waiting for the results of the initial R&D developments, the goal of the collaboration is $T^{0\nu}_{1/2} \sim 10^{27}$ yr and a ideal background rate of 0.02 count/(keV· t· yr) [186].

LEGEND After the enormous success of the Ge based detectors, the two main collaborations in the field (GERDA and Majorana Demonstrator) decided to join their efforts in the Large Enriched Germanium Experiment for Neutrinoless

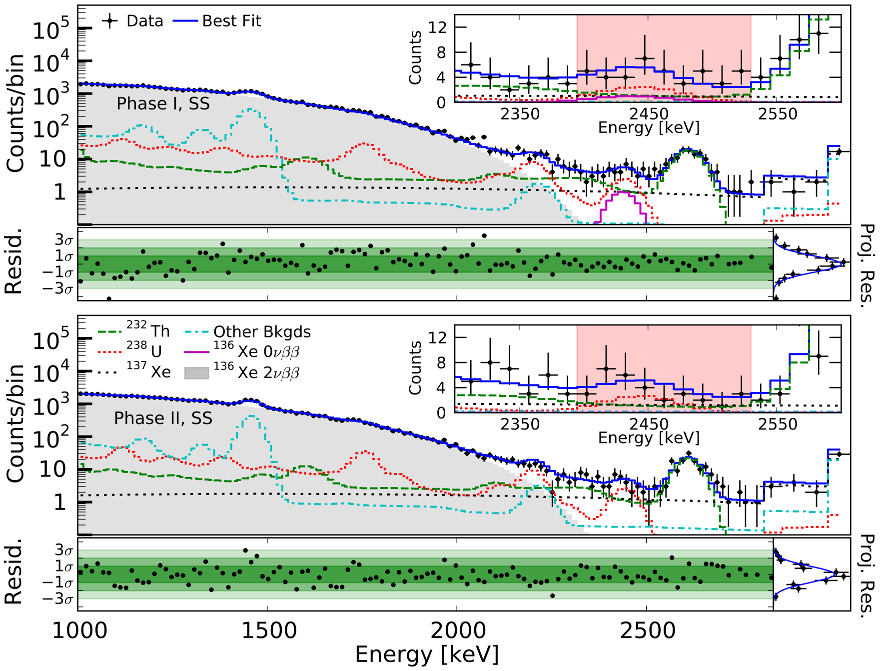

Figure 2.15.: Best fit to low background data for SS for Phase I (top) and Phase II (bottom) for EXO-200. The inset shows a zoomed in view around the $Q_{\beta\beta}$-value. Figure from [185].

double-beta Decay (LEGEND). The projected sensitivity is $T^{0\nu}_{1/2} \sim 10^{28}$ yr with a background of 0.1 count/(keV· t· yr) in a phased program: LEGEND-200 (scheduled for 2021) and LEGEND-1000 [187, 188].

KamLAND2-Zen It is the long term plan for the detector, aiming to reach the tonne of Xe and reduce the $2\nu\beta\beta$ background in the ROI, mainly improving the resolution by a factor of two. The main upgrades are a new and cleaner scintillation balloon, high light yield LS, light collecting mirror (Winston cone), and high quantum efficiency PMTs. The attempted sensitivity is $T^{0\nu}_{1/2} \sim 10^{27}$ yr after five years of running [189].

SNO+ Analogously to KamLAND-Zen, SNO+ is the follow-up of the Sudbury Neutrino Observatory (SNO), placed in SNOLAB, Ontario, Canada. It also consists of a $\beta\beta$-isotope dissolved in a LS, but, in this case, using ^{130}Te, up to $\sim$ 1t for the first stage. As its partner experiment, the external backgrounds must be carefully controlled, and the low resolution of the method makes $2\nu\beta\beta$ an issue, although ^{130}Te is among the ones with longer lifetimes for the process. The projected sensitivity for the initial phase is $T^{0\nu}_{1/2} \sim 1.9 \cdot 10^{26}$ yr for five years of data-taking [190].

nEXO It is the continuation of the EXO-200 collaboration, planning to use up to 5 tonnes of enriched Xe. nEXO is the detector in this list that actually enhances the most when scaling, as it is highly favored by the volume to area ratio. It represents a robust competitor with a reasonable resolution, background discrimination, and the construction seems feasible, as demonstrated by current experiments. The aimed sensitivity for the experiment is $T^{0\nu}_{1/2} \sim 10^{28}$ yr with a background rate of 0.15 count/(keV· t· yr) [191].

Notwithstanding, as already pointed out in Sec. 1.3.1, preliminary data from oscillation experiments hint at a slight preference for the NO. If that turns out to be the case, the experimental scope may be beyond current developments (see discussion in Sec. 2.2.2). Even though it is already essential, scalability will become a central issue. Additionally, background-free will be a must, and resolution, playing a role in $2\nu\beta\beta$ reduction, also needs to be as good as possible. Finally, the cost of enrichment (or even just acquisition of natural materials) will imply a considerable limitation for most of the isotopes (see Sec. 2.3.3).

3

NEXT: Technological approach and roadmap

The Neutrino Experiment with a Xenon TPC (NEXT) is an experimental program aiming to observe the neutrinoless double beta decay of $^{136}\mathrm{Xe}$ using an electroluminescent high-pressure gas-xenon Time Projection Chamber. As pointed out in the previous chapter, a serious proposal for a $\beta\beta$ experiment has to rely on several aspects: low background, relatively good energy resolution, and scalability towards further exploring the parameter space. Throughout this chapter and the following chapters, those items will be addressed, showing that the NEXT proposal goes even beyond those requirements, providing topological information for additional background discrimination. The collaboration comprises around 100 people (physicists and engineers) from 20 institutions and universities in Spain, the USA, Portugal, Israel, and Colombia. In this chapter, there will be a review of the main features of the experimental technique, the detector program, and the current stage of the experiment.

3.1 NEXT detection technique

3.1.1 The SOFT concept

The Separated-Optimized Functions TPC (SOFT) concept is based on a separation of the energy and tracking detection systems. The energy resolution requirement demands large photon collection areas with a single-photon sensitivity, whereas the spatial resolution forces to have a fine and dense distribution of small sensors. Therefore, the idea is to separate both detections and build a detector with different detection areas with different techniques, optimizing each one as much as possible, given the common environment [193, 194].[1]

---

[1] When implementing the SOFT idea, there are two possibilities: either a symmetric TPC with the tracking detectors at both ends and calorimeters along the barrel or an asymmetric TPC with tracking detectors in one end and energy detectors in the other one. Both implementations have their advantages and disadvantages. However, the former option represents a technological challenge and has not been seriously considered for the NEXT physics program. The interested

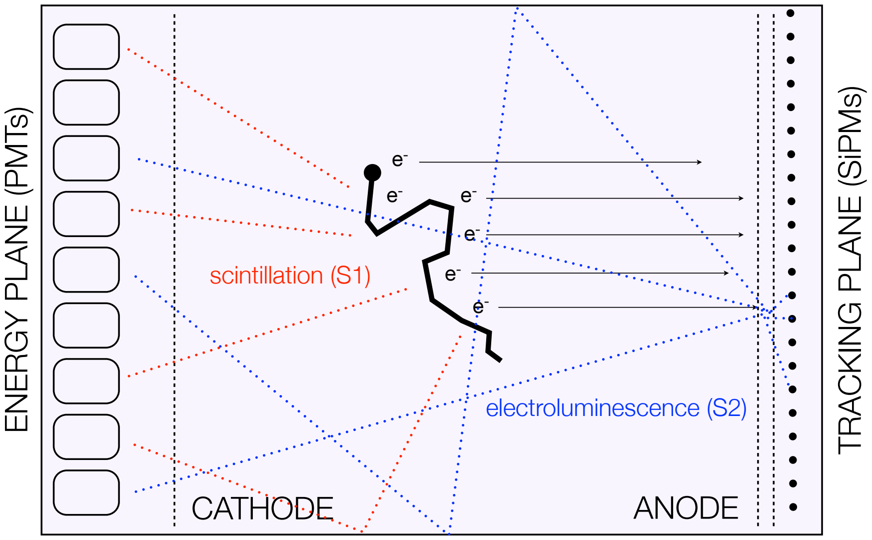

Figure 3.1.: SOFT concept scheme in the final implementation adopted for the NEXT experiment. The primary electron (bold black line) producing secondary electrons while emitting scintillation light (dashed red), noted as S1. An electric field pushes those secondary electrons towards the anode (thin black arrows), where another field highly accelerates them, forcing the emission of electroluminescence light (dashed blue), noted as S2. The S1 is only read by PTMs and provides the start of the time of the event. On the other hand, S2 is detected for both planes, providing a calorimetry measurement (PMTs) and an x, y estimation. The time difference between S1 and S2 provides the z coordinate information. See the text for more details. Figure from [192].

The detector consists of a cylindric asymmetric TPC with one of the extremes devoted to energy determination (the *energy plane*), instrumented with photomultiplier tubes (PMTs), whereas the other side is dedicated to the tracking information determination (the *tracking plane*), instrumented with an array of silicon photomultipliers (SiPMs).

Fig. 3.1 summarizes the detection process within this paradigm. When the primary electron is created inside the active volume, the process emits a scintillation light (S1) in the UV range ($\sim$178 cm). As this primary electron propagates through the gas, it loses energy while producing secondary ionization electrons (ie). In order to prevent recombination, there is a moderate electric field (0.3–0.5 kV /cm) that also drifts them towards the anode. Once the cloud of secondary electrons reaches the end of the drift region, they enter a section where a stronger field (2–3 kV /(cm · bar)). The accelerated electrons collide with Xe atoms generating

---

reader is advised to reach a discussion about this in [194]. The one adopted so far, and will be referred to hereafter, is the asymmetric option.

further VUV photons (S2) isotropically by a process known as electroluminescence (see Sec. 3.1.3). The S1 is only measured by the energy plane, and it establishes the start of the event, t_0. The S2, on the other hand, is detected by both planes. The energy plane collects most of the light, either directly or reflected, and acts as a signal integrator, i.e., the event energy is proportional to the number of photons detected by the PMTs. In contrast, the tracking plane is a few millimeters away from the electroluminescence (EL) region, which means the light is highly focused in a small area of the detection surface and measured by a regular array of SiPMs, acting as x-y pixels. The charge measured by each individual pixel is inversely proportional to the distance to the square emission point. The z coordinate is estimated using the time difference between S1 and S2 signals, once determined the drift velocity. This way, a set of three-dimensional reconstructions is possible with an accurate determination of the event's energy.

Finally, in order to increase the light collected by the energy plane, the surface of the barrel and the space between SiPMs are covered with a highly reflective material (Polytetrafluoroethylene, PTFE, in this case). Moreover, as the sensors are not usually sensible to UV light, all the available surfaces are additionally coated with a wavelength shifter (commonly tetraphenyl butadiene, TPB) to convert the light to the optimal regime of efficiency of the PMTs, usually around the blue light ($\sim$ 430 nm).

3.1.2 The resolution in Xe detectors

In Sec. 2.3.4, the resolution is a fundamental requirement for any serious $0\nu\beta\beta$ observation attempt. Therefore, it is essential to carefully determine the possibilities of the method.

When dealing with gaseous detectors, the energy can be well established using the ionization signal since W_i (the average energy required to create an electron-ion pair) can be considered independent of the type and energy of the ionizing radiation. Therefore, naively, the limiting aspect for the resolution is the stochastic fluctuations in the number of pairs produced. The process would be entirely Poissonian if all the ionizations are independent of each other, expecting, in this case, a variance following the Poissonian distribution: $\sigma_i^2 = N_i$, where N_i is the mean number of pairs generated for a given deposited energy. Nevertheless, it is not the case, and the fluctuations are not independent [195]. In this scenario, they can be described by:

$$\sigma_i^2 = F\ N_i, \tag{3.1}$$

where F is the so-called Fano factor[2] and depends on the medium.

In an ideal case, this would be the only effect limiting the resolution, establishing a limit for the best resolution achievable, known as intrinsic resolution (FWHM) or Fano limit, given by:

$$\frac{\delta E}{E} = \frac{\delta N_i}{N_i} = 2.355\frac{W_i\sigma_i}{E} = 2.355\sqrt{\frac{FW_i}{E}}, \tag{3.2}$$

where the 2.355 factor is the translation between σ and FWHM for the Gaussian distribution and the energy is given by

$$E = N_i W_i. \tag{3.3}$$

The Fano factor for gaseous Xe has been extensively studied, and the results are in a range of 0.12–0.29 [196, 197, 198], in good agreement with the Monte Carlo simulations [197, 199, 200]. In contrast, the Fano factor extracted from the liquid phase case's energy resolution [201,202] is on the order of $F < 20$, which overpasses the theoretical estimations [203], predicting it to be at least 3.5 better than the gaseous detector scenario. The origin of the large discrepancy is not clear [204,205], even though a reasonable explanation would be that, at a high-density regime, the fluctuations due to recombination become more important than the fluctuations in the electron-ion pair creation [193, 205]. The recombination process yields most of the energy in the form of scintillation light, although not all. This creates an anticorrelation between ionization and scintillation that must be taken into account in order to improve the resolution (see Fig. 3.2) [201], despite the fact that the large fluctuations remain.

Bolotnikov and Ramsey [207] measured the dependence of the resolution of the ionization signal, generated by a 662 keV gamma from $^{137}\mathrm{Cs}$, with the Xe density. From their results (see Fig. 3.3), it is clear that for the density range below $\rho \sim 0.55\,\mathrm{g/cm}^3$, the resolution is almost constant and around 0.6 %FWHM at the experiment energy, close to the Fano resolution expectations. Nevertheless, for densities above that, the resolution deteriorates quickly and gets to match the observed values for LXe. The worsening may be due to the formation of liquid xenon glubs coexisting with the gas as density increases. Those glubs would impact the resolution due to the higher recombination for the liquid phase, and, as the density increments, so would do the fraction of the liquid phase. Fortunately, the glubs'

---

[2] Named after Ugo Fano, the first showing the variance of the process back in 1947 [195].

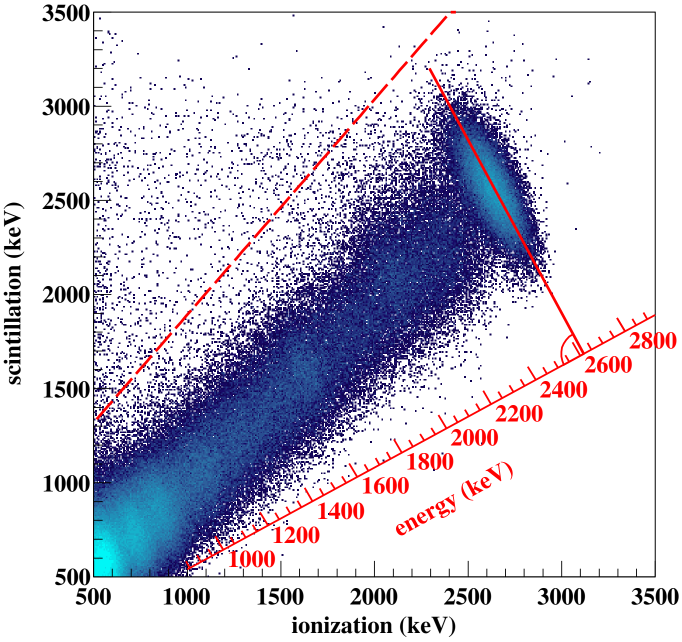

Figure 3.2.: Anticorrelation for scintillation and ionization in LXe light measured by EXO-200 experiment using a $^{229}\mathrm{Th}$ calibration source. The red axis shows the improvement in the energy resolution when both signals are tanking into consideration. Figure from [206].

effect seems negligible for the densities below the threshold mentioned above (and within the NEXT experiment range).

Scintillation

The scintillation light is the radiation some materials emit when a charged particle leaves energy in them due to the electrons' excitation inside the material's atoms [208]. As discussed in Sec. 3.1.1, the scintillation signal is the trigger for the event's initial time, t_0, and, ultimately, the z coordinate estimation. The average energy required to produce a scintillation photon, W_{SC}, measured for the NEXT experiment conditions [209] is:

$$W_{SC} = (39.2 \pm 3.2)\,\mathrm{eV}. \tag{3.4}$$

And the translation of this result for the number of scintillation photons at $Q_{\beta\beta}$ energy yields:

$$N_{SC} = (32\,300 \pm 2500)\ \text{photons}. \tag{3.5}$$

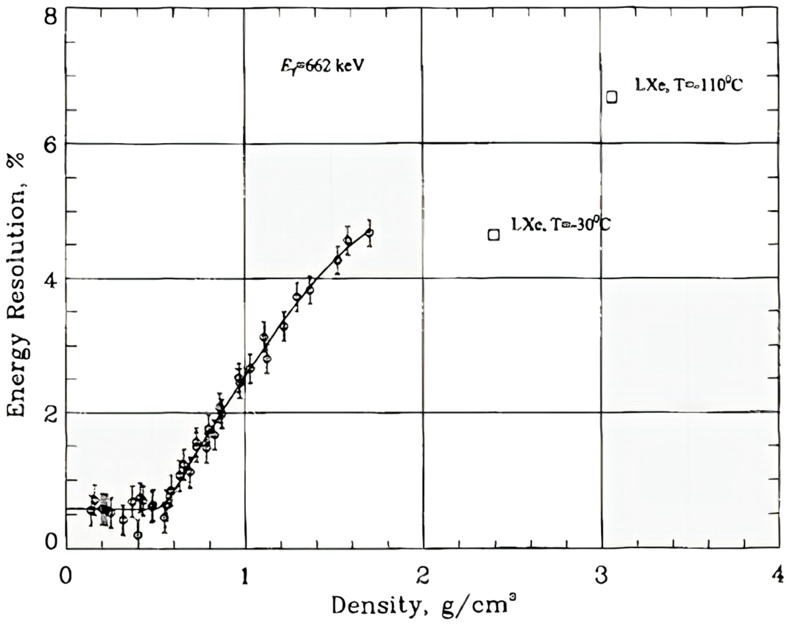

Figure 3.3.: Density dependence of the energy resolution in Xe using the ionization signal from the $^{137}\mathrm{Cs}$ gamma. Figure from [207].

Those photons are emitted isotropically and require a sensible device to be detected, able to count single photoelectrons. Furthermore, fortunately, xenon is transparent to its own scintillation light (although it has to be shifted in order to be detected), but other elements dissolved in the gas, such as hydrogen, nitrogen, methane, or carbon dioxide, may quench the signal [210, 211, 212].

Ionization

It is the complementary process of scintillation. In this case, the electron is quicked off the atom, and thus an electron-ion pair is created. As aforementioned, the ionization mechanism is an excellent signal to measure the energy in gas detectors and even to extract the topology information. The average energy required to produce an electron-ion pair measured for the NEXT experiment conditions is [213]:

$$W_i \simeq 22.4\,\mathrm{eV}. \tag{3.6}$$

Then, translating it to the number of pairs produced at $Q_{\beta\beta}$ energy:

$$N_i \simeq 10^5 \text{ photons}. \tag{3.7}$$

Final experimental resolution

The intrinsic resolution described by Eq. 3.2 is only achievable in ideal conditions. However, in real life detectors, there are several instrumental effects inherent to the measurement process that can damage the resolution:

1. During the drifting of secondary electrons, electronegative impurities may trap them, preventing them from reaching the anode and being measured. This is the so-called attachment and can be mitigated by continuous xenon purification. On top of that, other effects can have residual contributions to the loss of electrons in their way to the anode, as recombination,[3] non-perfect transparency of the detector components, and so on. As the fluctuations are relatively smaller, the more electrons detected, the better. Those fluctuations for N_i number of electrons produced by ionization due to electron losses can be parametrized as $L = 1 - \varepsilon$, where ε is the overall electron collection efficiency.

2. Once the electrons reach the anode, they must be amplified. The various options for the multiplication lead to very different scales in the fluctuation. It can be parametrized by G for a given m signal augmentation.

3. The calorimeters have an intrinsic electronic noise, affecting the fluctuations. In the PMTs case, the noise is Gaussian and hence described by the standard deviation n, in electron units.

4. Other effects can damage the resolution, such as Bremsstrahlung losses, the miscalibration of the detectors, non-linearities, etc. Nevertheless, they are considered smaller than those mentioned above and thus not considered a significant source of fluctuations to be addressed.

If all the aforementioned issues are assumed to be uncorrelated and Gaussianly distributed, the Eq. 3.1 can be updated, and the total variance would be:

$$\sigma_i^2 = (F + L + G)N_i + \frac{n^2}{m}, \tag{3.8}$$

and so the energy resolution:

$$\frac{\delta E}{E} = 2.355\sqrt{\frac{F + L + G + \frac{n^2}{mN_i}}{N_i \varepsilon^2}}. \tag{3.9}$$

---

[3] Although it was shown that recombination does play a role in liquid xenon, for the gas-phase case is almost negligible. However, this is only true when the ionization electron density is not too large, as it is in the alpha interactions [214].

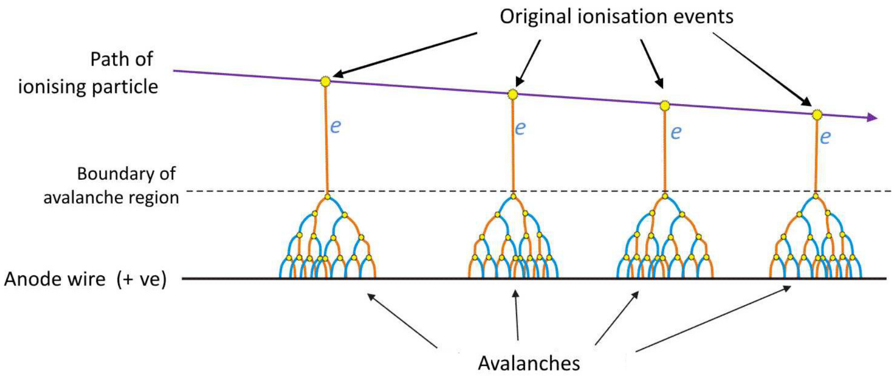

Figure 3.4.: Scheme of the functioning of a proportional counter, through Townsend avalanches. Figure from [215].

As discussed already, the Fano factor, F, is irreducible and intrinsic to the detection medium. However, the typical values for G are usually greater than F when using avalanche multiplication but seem to be of the order of F for electroluminescence amplification (see Sec. 3.1.3). The contribution of L can be reduced by cleaning the gas and also by improving ε, which will also minimize the total fluctuation. Last, the typical values for the noise at the range of $Q_{\beta\beta}$ are negligible and only an issue when dealing with low energy events. Therefore, at high energies and perfect efficiency, the Eq. 3.9 can be reduced to:

$$\frac{\delta E}{E} = 2.355\sqrt{\frac{F+G}{N_i}}. \tag{3.10}$$

3.1.3 Electroluminescence

Once drifted to the anode, the ionization electrons need to be amplified to be properly measured. It is clear from Eq. 3.9 and later discussion that G is one of the fundamental parameters to keep under control and should drive the amplification process's selection. typical way for the multiplication in TPCs is the charge-avalanche. For this kind of device, the electrons are forced into a large electric field in a thin anode wire's surroundings. This leads to massive ionization of the gas that causes an avalanche multiplication gain, collected by the wire (see Fig. 3.4). The amplification obtained by the technique is $m \sim 10^3$–10^4 . In the regime where M is not large enough, space charge effects can be ignored, and the number of electrons out of the multiplication, $N_a = MN_i$, is approximately proportional to the energy.

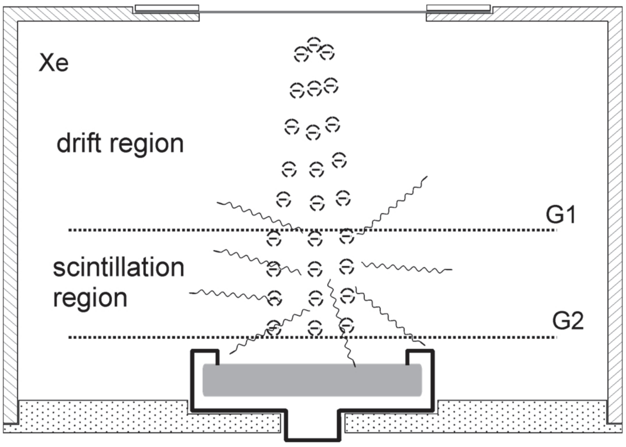

Figure 3.5.: Scheme of the functioning of a scintillation counter. Figure from [219].

Unfortunately, for the avalanche-based multiplication detectors (often known as proportional counters), the amplification magnitude, M, is subject to not negligible fluctuations. In fact, the $G_a = (\sigma_M/M)^2$ factor is of the order of the Fano contribution, with values in the range of 0.2–0.9 [208,216,217]. Experiences with such a technique showed a resolution $>$1 % FWHM [218]. Although that is fine for most of their purposes in tracking detectors and counters, it is not optimal for the $0\nu\beta\beta$ program.

Another option, born in the late 1970s, is the scintillation drift chamber [220] where, instead of avalanches, the multiplication would be due to electroluminescence. The electrons reaching the anode are accelerated as well, but not too much to provoke the gas's ionization, just enough to excite the atoms. When atoms de-excite emit VUV light that can be collected by photo-sensible detectors, such as PMTs (see Fig. 3.5). The amplification gain (EL yield), Y, can be parameterized as [221]:

$$\frac{Y}{P\Delta x} = \left((136 \pm 1)\,\frac{E}{P} - (99 \pm 4)\right) \text{photons/(electron} \cdot \text{cm} \cdot \text{bar)}, \tag{3.11}$$

where P is the pressure, E/P is the reduced EL field, and Δx is the EL region's width.

Regarding the fluctuations in the process, it can be described by the Conde-Policarpo factor, J_{CP}, as $\sigma_Y^2 = J_{CP}Y$. Hence, for a total of N_i initial electrons:

$$\sigma_{\text{EL}}^2 = J_{\text{CP}} N_i Y, \tag{3.12}$$

where $N_i Y = n_{\text{EL}}$ is the number of photons generated in the multiplication process. Fig. 3.6 displays the behavior of the factor as a function of the reduced field, and it

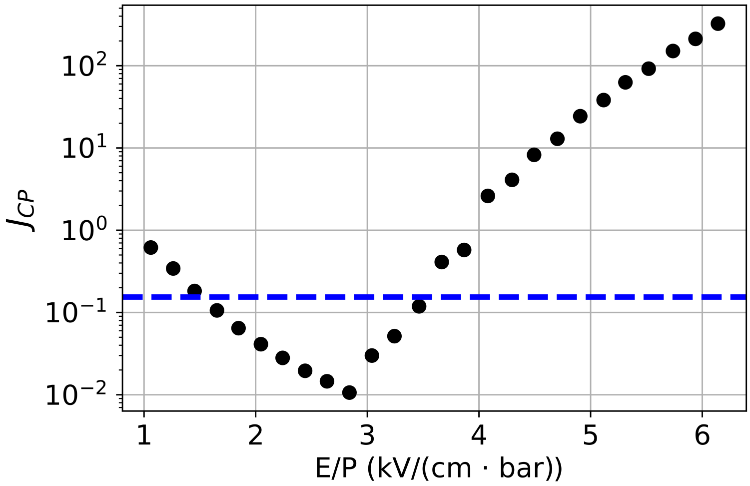

Figure 3.6.: Conde-Policarpo factor, J_{CP} as a function of the reduced field, E/P, for gaseous xenon (black dots). The blue dashed line shows the Fano factor under the same conditions.

is remarkable that in the region of E/P ~1.5–3.5 kV /(cm · bar) the fluctuations of the method are well below the Fano factor contribution.

Nonetheless, despite the promising performance in terms of fluctuation, the EL method counterpart is the detected light's efficiency, η, that is typically $\lesssim 1\%$. This effect takes into account the detector's intrinsic and unavoidable features both in the light propagation, such as the photosensor coverage and non-ideal reflectivity in the detector materials, causing absorption loss, and photosensors' intrinsic efficiency. The process is known to follow a binomial distribution with mean μ_{pe}, thus a variance

$$\sigma^2_{\text{pe}} = \eta(1-\eta)N_iY. \tag{3.13}$$

The final contribution to the process dispersion is the photon detection itself. The usual technique for the photosensor's performance is the multiplication of a single electron (ripped from the active surface of the apparatus via a photoelectric interaction) based on an avalanche paradigm, analogous to the one discussed earlier. Hence, the contribution to the signal fluctuation can be characterized by the charge resolution of the sensor $\sigma_{\text{M}} = \frac{\sigma_q}{q}$, where q is the total charge produced in the avalanche. Thus, for a total of $\eta N_i Y = n_{\text{det}}$ photons detected by the sensor:

$$\sigma^2_{\text{ps}} = \eta N_i Y \sigma^2_{\text{M}}. \tag{3.14}$$

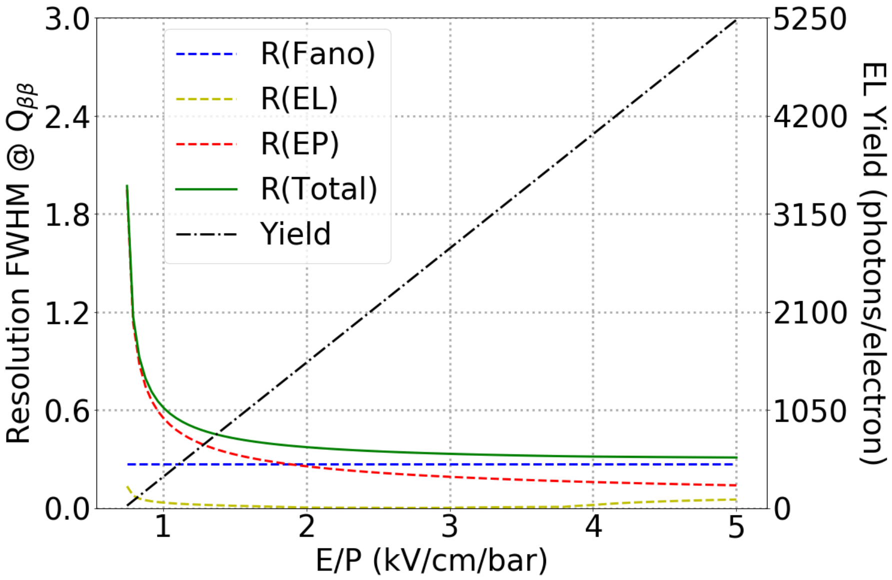

Figure 3.7.: Energy resolution contributions and EL yield versus the reduced field, E/P, conditions. R(Fano) stands for the contribution coming from the first term in Eq. 3.15, R(EL) for the first term in Eq. 3.16, and R(EP) for the last one in Eq. 3.16. The contributions are computed for a pressure $P = 15\,\mathrm{bar}$ (the nominal NEXT-White pressure), a photon collection efficiency $\eta = 0.006$, and a EL region width of 6mm. Figure extracted from [222].

Consequently, for the EL technique scenario, implementing the Eqs. 3.8, 3.12, 3.13, and 3.14 in the general resolution in Eq. 3.10 yields

$$\begin{aligned}\left(\frac{1}{\xi}\frac{\delta E}{E}\right)^2 &= \left(\frac{\sigma_i}{N_i}\right)^2 + \left(\frac{\sigma_{\mathrm{EL}}}{n_{\mathrm{EL}}}\right)^2 + \left(\frac{\sigma_{\mathrm{pe}}}{n_{\mathrm{det}}}\right)^2 + \left(\frac{\sigma_{\mathrm{ps}}}{n_{\mathrm{det}}}\right)^2 \\ &= \frac{F}{N_i} + \frac{J_{\mathrm{CP}}}{N_i Y} + \frac{(1-\eta)}{\eta N_i Y} + \frac{(\sigma_q/q)^2}{\eta N_i Y},\end{aligned} \tag{3.15}$$

where $\xi = 2.355$ is the abovementioned translation between gaussian σ and the FWHM. Finally, the G term can be expressed as

$$G = \frac{J_{\mathrm{CP}} - 1}{Y} + \frac{(\sigma_q/q)^2 + 1}{\eta Y}. \tag{3.16}$$

As far as the pursuit for the closest-to-the-intrinsic resolution is concerned, following the discussion from Sec 3.1.2, G must be smaller than the Fano factor, that for gaseous Xe is F=0.15. This can be reinterpreted as an argument about the total amount of photoelectrons generated in the EL multiplication per ionization electron, ηN_i. Regarding the Conde-Policarpo factor, it is clear from Fig. 3.6 that, within the detector's range of operation, it is well below the Fano factor, which makes it negligible. Even if the Conde-Policarpo factor were of the same order or slightly greater than the fano factor, it would still be negligible given the gain dividing the former (see Eq. 3.15), which manifestsin Fig. 3.7, where the EL contribution, yellowish dashed line, is visibly smaller than all the others. On the other hand, for the second term of the Eq. 3.16, the PMT related piece depends on $(\sigma_q/q)^2$ that, in the current generation of detectors, can be of the order of 0.5 or less. Thus, the higher the gain (and finally, looking to Eq. 3.11, the higher the reduced field), the lower the contribution. This last statement is patent in Fig 3.7, where the overall contribution is displayed in red. For small values of the reduced field, the resolution worsens dramatically, whereas, above $\sim 2\,\mathrm{kV}\,/(\mathrm{cm}\cdot\,\mathrm{bar})$ it is below the Fano factor input. In fact, the total resolution, full green line, tends towards the constant Fano contribution for the reduced field's high values.

3.1.4 Topology of the electron tracks

Following the discussion about the TPC features in Sec. 2.4, the potential recording of the topological information of the track is one of the main advantages of this technology and enables a powerful tool in background discrimination. As already described in the aforementioned section, liquid-phase detectors are not able to record tracks but point-like energy depositions. This is enough to develop a single-site versus multi-site events distinction. However, this section will focus on the tracking characteristics for the gas phase.

The general behavior of electrons through matter is well understood and described. An electron will lose energy while ionizing and exciting the atoms of the medium, or even processes such as emitting bremsstrahlung photons (relevant for MeV events). The energy loss probability for each step is described by the Landau distribution [223]. On the other hand, the average energy loss of charged particles, the so-called stopping power ($S = -dE/dx$), is characterized by the Bethe formula (also known as Bethe-Barkas-Bloch) [224]. However, for the scenario that concerns the present work, the main aspects of the behavior of an electron propagating through matter can be summarized in two regimes. First, for high energy ranges, the electron would perform as a Minimum Ionization Particle (MIP), where S is close to its minimum, being, in the case of Xe, $S_{\mathrm{MIP}} \sim 1.3\,\mathrm{MeV}\cdot\mathrm{cm}^2\,/\,\mathrm{g}$ [32]. Moreover, for small energies, the track evolution is dominated by multiple scattering (MS). MS can be described via the angle of deflection for the track, having an RMS following $\theta_0 \propto E^{-1}$ [225].

Therefore, for a near-$Q_{\beta\beta}$-energy electron, one expects an initial section of the track where the deflection is almost negligible while it losses gradually the energy and, eventually, the scattering angle gets bigger and enters in a regime where it losses the energy rapidly and the path curls more and more and a final deposition of energy (corresponding to Bragg peak) occurs at the end of the tortuous track, the so-called *blob*. In contrast, a $0\nu\beta\beta$ consists of two-electron tracks emerging from the same vertex and a $Q_{\beta\beta}$ energy shared. Thus, those kinds of tracks would present a central MIP region and two blobs at both terminal sections. That implies that being able to resolve precisely enough to distinguish the different trajectory sectors faithfully is a handful tool for the signal and background characterization. Notwithstanding, the previously mentioned delta ray and bremsstrahlung emission and the diffusion of the secondary-electrons cloud in its way to the EL region make the pursuit of a perfect spatial resolution quite hopeless. Both emissions blur the track itself and, as well, they can mimic the appearance of a $0\nu\beta\beta$ one, as they might produce an additional low energy electron close to the beginning of the track. Both conceivable scenarios are depicted in Fig. 3.8 a pair of MonteCarlo (MC) generated tracks illustrating the expected topology of a single and double electron, respectively.

Consequently, even without considering other physical effects that can mimic the $\beta\beta$ expected features, diffusion plays a key role. The secondary electron cloud, in its way to the EL region, spreads both transversally and longitudinally. This causes the track's clean appearance to blur, and, eventually, the peculiarities cannot be resolved any longer. For pure xenon and the typical NEXT experiment conditions (20 °C, 9.1 bar), the diffusion has been measured to be $318.9 \pm 1.8(stat) \pm 20.1(sys)$ μm/ $\sqrt{\text{cm}}$ for the longitudinal value and $1276 \pm 3(stat) \pm 34(sys)\,\mu$m / $\sqrt{\text{cm}}$ [226] in very well agreement with the a priori expectations. Hence, a sensor separation below 1 cm is unnecessary and only adds to the total bill. In fact, MonteCarlo simulation studies have shown that the 1 cm pitch in a square arrangement of sensors is a fair compromise between a convenient two-blob characterization and an adequate number of electronic channels [194]. Fortunately, recently developed techniques such as the Richarson-Lucy deconvolution point to the possibility of reversing, to some extent, the effects of the diffusion [227].

Additionally, several studies were performed in order to decrease diffusion through small amounts of gasses diluted in the xenon, such as Co_2, CF_4 and He [212, 228, 229, 230]. Unfortunately, none of those dopings seem to fulfill the overall requirements as they deteriorate the light yield, or PMTs cannot operate in their presence. Thus, no gas mixture is foreseen for the near future detectors, relying on PMTs for the energy measurement. Notwithstanding, for the tonne-scale prototypes,

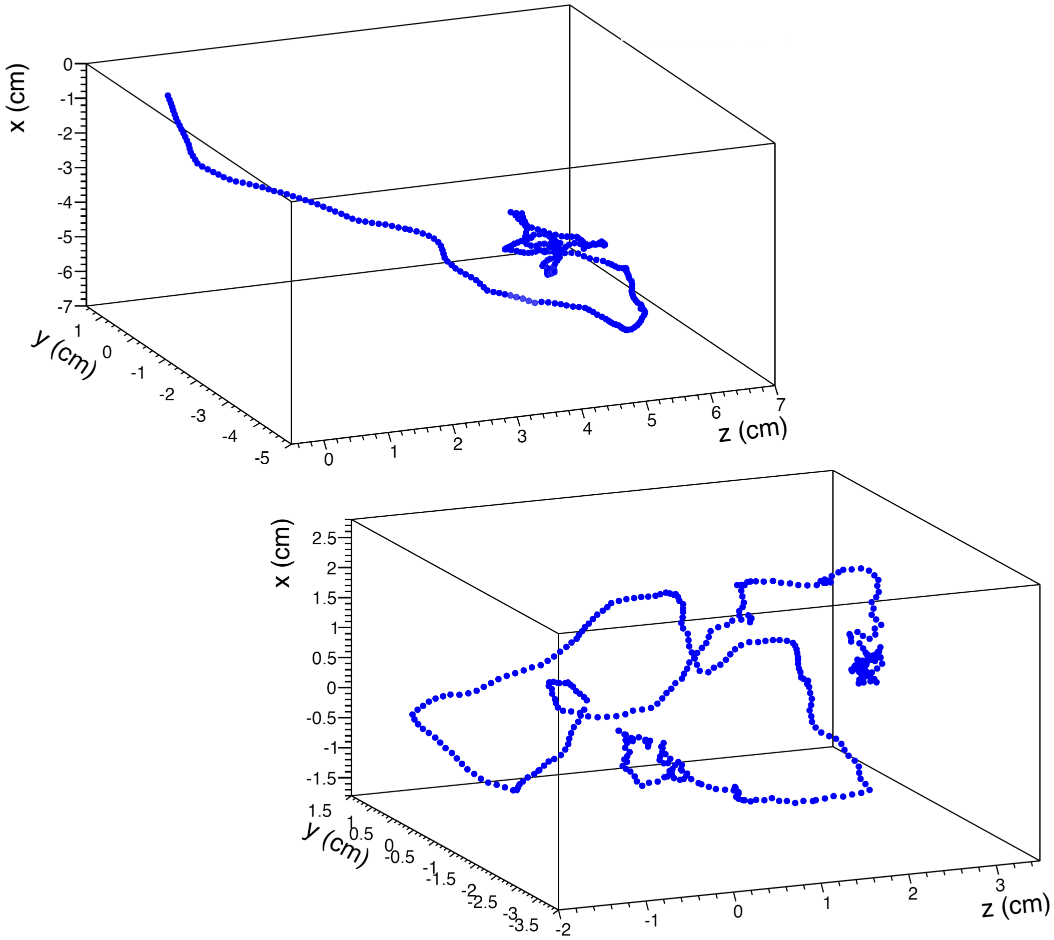

Figure 3.8.: Example of a single electron track (top) and a double electron track (bottom) produced using the NEXT Monte Carlo simulation at 15 bar. It is patent how the single electron shows a first section where the propagation is smooth and a final section, the blob, when the Bragg peak happens, and a huge energy deposit takes place in a small region. In contrast, for the double electron track, the situation is noticeably different as both ends manifest a blob nature while the central zone of the track presents the MIP behavior.

the radioactive budget makes such sensors intolerable, which opens the possibility of incorporating Xe-He mixtures [229].

3.2 NEXT road map

The previous section describes a novel technique the NEXT experiment proposes in the quest for the $0\nu\beta\beta$ and, as has been discussed, that carries a bunch of challenges. Since the starting proposal in 2009 [231], an intensive R&D program has been

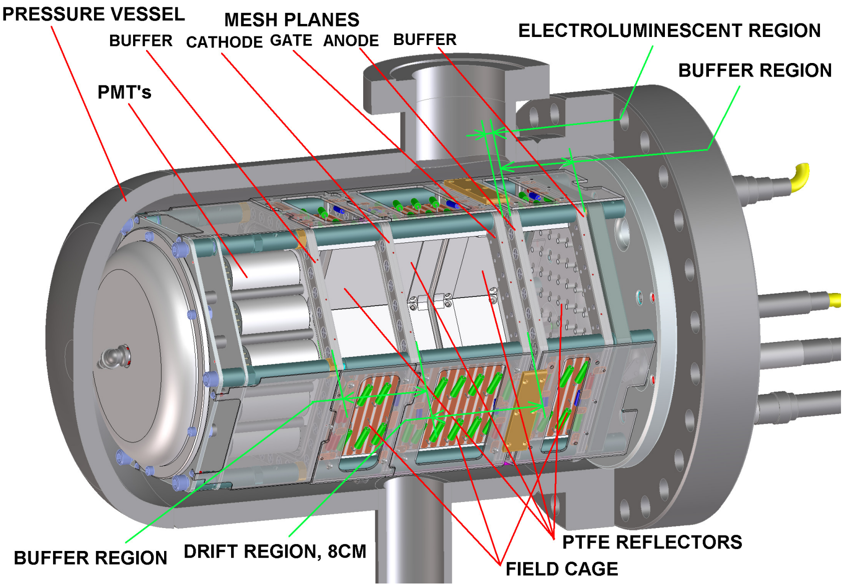

Figure 3.9.: Cutaway view of the NEXT-DBDM detector with the main features labeled. In contrast to the TPC described in Sec. 3.1.1, one thing to notice is the absence of a tranking plane, replaced by a reflective surface. Figure extracted from [177].

developed by the Collaboration in order to prove the feasibility of the technology and demonstrate its potential capabilities. This program includes two small early stages of around 1kg, a recently decommissioned detector containing 5kg, an in-construction machine of 100kg, and a future development plan towards the tonne scale.

3.2.1 NEXT-DBDM

The NEXT-DBDM (Double Beta and Dark Matter) prototype aimed to demonstrate the near-intrinsic resolution in high-pressure gas with an EL scheme. It was built and operated in the Lawrence Berkeley National Laboratory (USA) from 2009 to 2014. The detector hosted $\sim$1 kg of natural Xe and consisted of a hexagonal field cage divided in a 8 cm long drift length and a 5 mm EL region embedded in a cylindrical pressure vessel of length 33.5 cm and radius 20 cm. For most of the operative time, it only comprised an energy plane with 19 PMTs arranged in an hexagonal pattern, whereas the tracking plane was replaced by a reflective plate in order to improve the light collection efficiency. The main characteristics of the detector are depicted in Fig. 3.9.

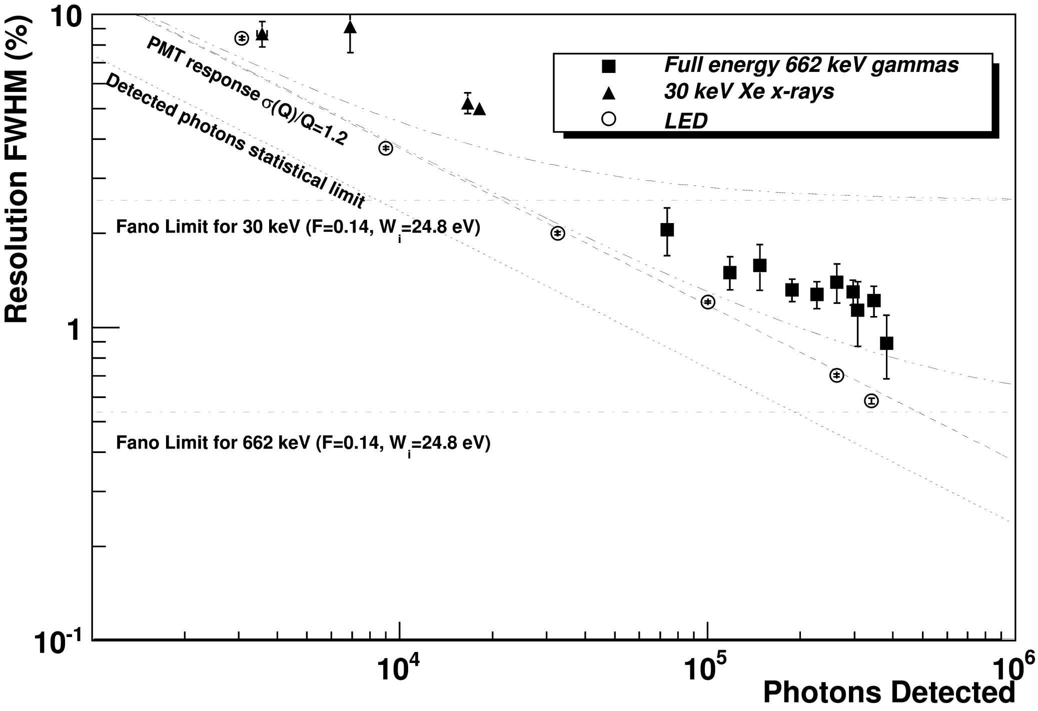

Figure 3.10.: Energy resolution results in NEXT-DBDM as a function of the number of photons detected. See text for more details. Figure from [177].

The principal study carried out in the prototype was the characterization of the energy resolution of an EL-based HPXe TPC. That was achieved through the analysis of a ^{137}Cs gamma-ray source (662 keV) and, secondarily, the intrinsic xenon X-rays ($\sim$30 keV) at two pressures (10 and 15 bar) and different gain values (i.e. varing the EL field, see Eq. 3.11). The results obtained, after a fiducial selection and a correction to account lifetime effects, were around the 1 %FWHM at ^{137}Cs photopeak (PP), that, naively extrapolating as $\propto E^{-1/2}$, translates to 0.5 %FWHM at the $Q_{\beta\beta}$-value.[4]

Fig.3.10 summarizes the measurements from the prototype and condenses much information. It shows the energy resolution as a function of the number of detected photons. Data points comprise the X-ray (triangles), Cs PP (squares), and a LED (circles). The first two come for direct measurement of the resolution of the respective peaks; the latter comes from a dedicated LED varying the light intensity

---

[4] Hereafter, the resolution values are going to be presented with their correspondent naive extrapolation, following the $E^{-1/2}$ expected behavior, at the $Q_{\beta\beta}$-value. Note that this is not a statement of the resolution for each detector in this energy scale, as additional effects can affect the assumed trend, but rather a way of better comparing resolutions obtained at different energy regimes.

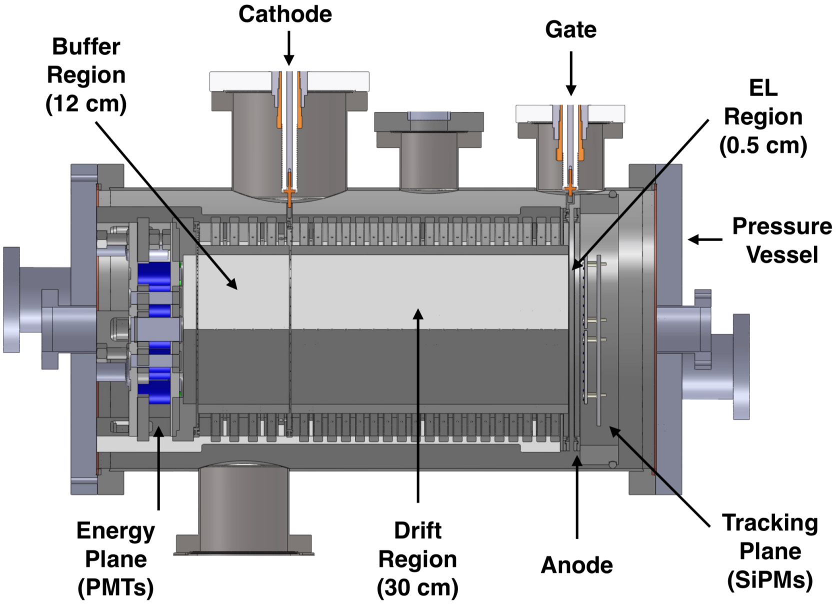

Figure 3.11.: Cutaway view of the NEXT-DBDM detector with the main features labeled. Figure from [232].

per pulse). Diagonal dashed lines represent two expected resolution limits: the resolution due to the Poisson statistical limit (lower one) for a certain number of detected photons and the effect of the PMT noise effect on the former (upper one). The horizontal lines stand for the Fano limits, thus the intrinsic resolution of xenon gas, the top one for the X-rays regime, the bottom one for the PP case. Lastly, the two remaining curves represent the expected resolution combining the number of photons detected, PMT-related effects, and the Fano limit. The general remark is that the data points fit the expected behavior, although the match is not perfect. The ~20-30% disagreement can be attributed to the non-uniformity response of the $x - y$ plane.

For further description and details of the analysis and results, check [177].

3.2.2 NEXT-DEMO

The NEXT-DEMO prototype was designed as a proof-of-concept of the SOFT proposal, with the aim to prove the energy resolution and the potential of the background rejection using the topological information, and, additionally, as a suitable testbench for potential studies in pursuance of improving the detector performance towards larger scales, such as understanding the gas circulation and purification, high voltages, wavelength shifters, and long drift lengths. The detector operated from

2009 to 2014 installed at Instituto de Física Corpuscular (IFIC) in València, Spain. In contrast with NEXT-DBDM, in this case, the SOFT scheme was fully materialized in an asymmetric EL TPC of 30 cm drift length tube, with a 16 cm-diameter hexagonal shape, and a 5 mm El region, contained in a vessel 60 cm long and 30 cm wide capable of hold up to 15 bar. Concerning the measurement planes, the EP consisted of 19 PMTs, whereas the TP contained 256 SiPMs of $1 \times 1\,\mathrm{mm}^2$ each arranged in a square distribution of 1 cm pitch. The detector hosted $\sim$1.5 kg of natural Xe. Fig. 3.11 illustrates the principal components of the detector. The apparatus was not made taking care of its components' radiopurity, nor had any shielding from external backgrounds, and was placed in a surface laboratory (background studies are beyond the goals for the prototype), although the location was a semi-clean room.

For an early stage of the detector, instead of the SiPM tracking plane, there was one with 19 PMTs (therefore, both planes consisted of the same number of PMTs). Thus, no track information could be reconstructed, but an averaged position for the event. This arrangement was applied to study the importance of the light wavelength in the energy resolution by exploring two different configurations, one using the xenon scintillation ultraviolet light straight for the PMT recollection and the other one coating the surfaces of the detector with a wavelength shifter to blue spectral region. The resolution was estimated analyzing a $^{22}\mathrm{Na}$ gamma at 511 keV (coming from the β^+ annihilation). After a careful correction for the geometrical effects, the energy resolutions for the gamma PP were 2.86 %FWHM (without TPB) and 1.75 %FWHM (with TPB) [192]. The major improvement is attributed to the significant difference in the light collection efficiency in the PMTs, enhanced by a factor of 3 between the UV and blue radiation.

In the next phase of the detector, the SiPM plane was in place, allowing a more detailed track characterization [233]. The resolution has been characterized for this configuration using $^{22}\mathrm{Na}$ and $^{137}\mathrm{Cs}$ calibration sources, yielding a result of 1.62 %FWHM (translated to 0.74 %FWHM for the $Q_{\beta\beta}$-value) and 1.56 %FWHM (extrapolated to 0.83 %FWHM for the $Q_{\beta\beta}$), respectively [234] (see Figs. 3.12a and 3.12b).

On top of that, some dedicated studies for the topological reconstruction were performed. The technique divided the track into 4 μs slices along the z coordinate (the drift direction), whereas the x, y information was recovered by applying the barycenter algorithm. Therefore, for each slice, just one point, and its associated energy deposit, was reconstructed. Figs. 3.12c, 3.12d, and 3.12e show three distinct tracks for different sources. A more refined analysis taking care of the blob info was able to evaluate the capabilities for the technique's background rejection [116].

The results show a background rejection of (75.7 ± 1.4) %, with a signal acceptance of (66.0 ± 1.0) %, in good agreement with the MC simulation prospects (see Fig. 3.12f).

DEMO++

It is a new resurrection of the apparatus devoted to several pending studies supporting the physics program of NEW and NEXT-100 started in mid-2019. The overall design is similar to the previous version but presents some minor changes, including having only 3 PMTs.[5] The current research topics going on include the decision of whether to use metal meshes for both the cathode and the anode (as the original DEMO did) or a quartz plate replacing the anode one (as NEW does), helium mixtures to reduce diffusion, the viability and effects of changing the SiPM pitch to 15 mm, and technical solutions on the design and construction of NEXT-100, currently ongoing.

3.2.3 NEXT-WHITE

The NEXT-White[6] (NEW) detector is the most recently completed phase of the R&D program of the NEXT collaboration, started back in 2016, finished in 2021, and the first apparatus located underground, specifically, in the Laboratorio Subterráneo de Canfranc (LSC). It was designed to be a 1:2 scale model of the NEXT-100, holding around 5 kg of xenon at 10 bar. The apparatus was conceived as an intermediate step towards the 100 kg stage, with the aim to solve several technical and physics issues hanging in the Technical Desing Report [235] and not solved by the previous stages. Concerning the physics objectives, the principal ones were:

- Design and refine the calibration techniques for such big gaseous chambers, both at low and high energies.
- Validation of the background model and complete estimation of all the contributions that may not affect the NEW physics case dramatically but will be critical for future detectors.
- Measurement of the $2\nu\beta\beta$ mode and its half-life, as well as perform a rough first limit on the $0\nu\beta\beta$ one.

---

[5] Since the PMT for DEMO++ are the ones employed in NEXT-White and NEXT-100, significantly bigger in size, the number of PMTs has to be reduced in comparison with the original DEMO design.

[6] Named after Prof. James T. White.

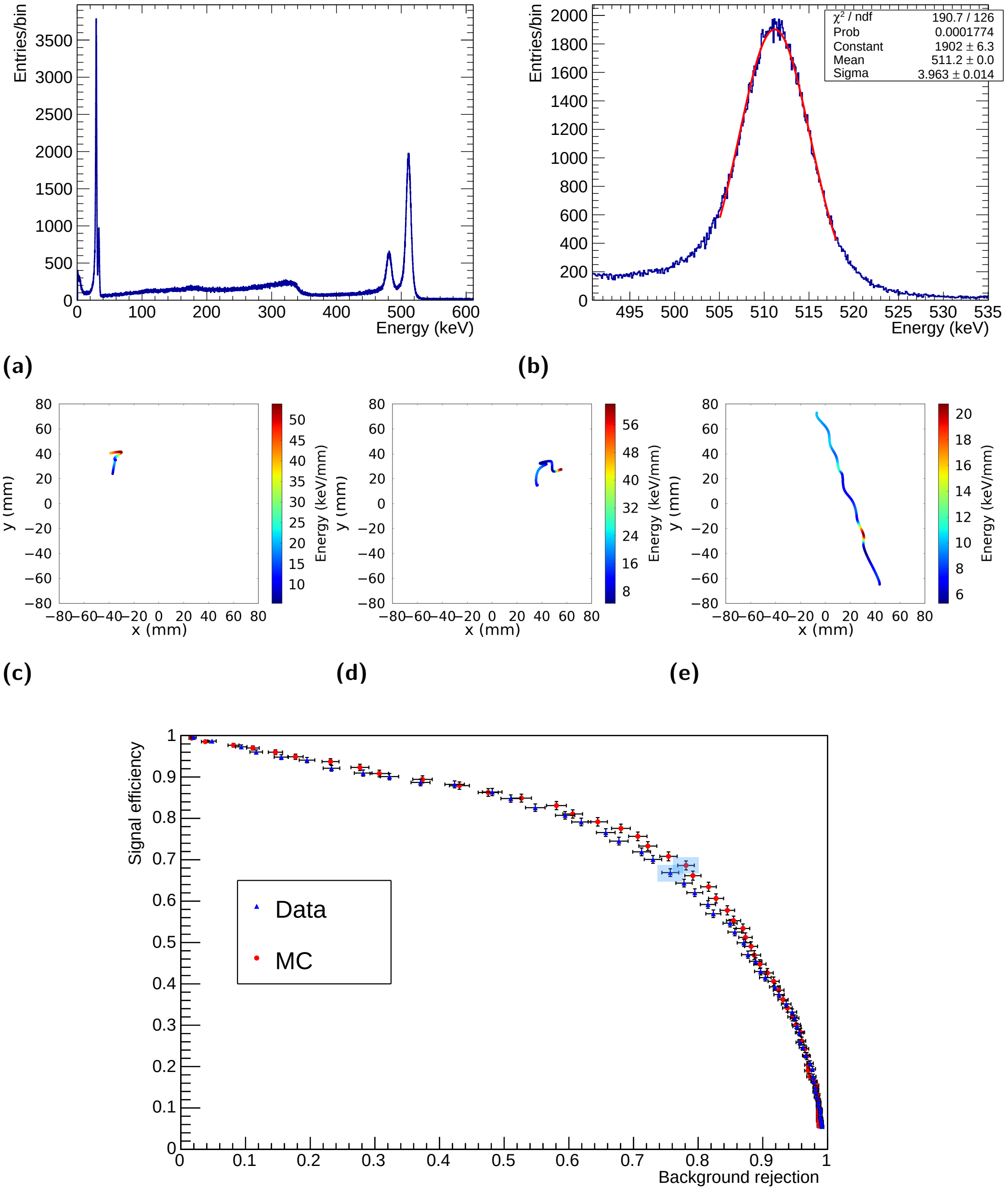

(a)

(b)

(c)

(d)

(e)

(f)

Figure 3.12.: Results from NEXT-DEMO concerning resolution, tracks, and background rejection. The top row comprises the resolution for the PMT + SiPM configuration at the $^{22}\mathrm{Na}$, general spectrum, a, and photopeak zoom, b. The central row shows tracks reconstructed with the algorithm described in the text, with a cubic spline line to interconnect the points, and the color representing the energy collected in each point, corresponding to $^{22}\mathrm{Na}$, c; $^{137}\mathrm{Cs}$, d; and muon case, e. The last row, f, presents the signal acceptance efficiency vs. the background rejection when modifying the lower energetic blob candidate's minimum energy required to be considered a true blob, showing the MC and data scenarios. The blue squares represent the best compromise quoted for each case (see text). Figures a, b, c, d, and e are extracted from [233], figure f is from [116].

- Determination of the energy resolution close to the $Q_{\beta\beta}$-value.
- Improvement and further understanding of the track characterization and background rejection. As NEW was the first detector able to fully contain tracks of energies close to the $0\nu\beta\beta$ ROI, it was worthwhile to polish the reconstruction, the accurate characterization of two-electron tracks (both $\beta\beta$ and from calibration sources), and, consequently, the background rejection techniques.

The detector will be subject to a more detailed and dedicated review concerning the design and achievements in Sec. 4.

3.2.4 NEXT-100

NEXT-100 represents the collaboration's most significant ongoing efforts, devoted both to the final design undecided aspects and the detector's actual construction, scheduled for 2021-2022, whereas the data taking is expected to be started by the end of 2022. Although NEW was planned as a scaled version, several aspects have been revisited, and minor details are pending on the final verdict.

It is a radiopure detector containing about 100 kg of xenon gas at 15 bar. The chamber is a cylinder of drift length 130 cm and radius 107 cm and the EL gap is 1 cm. The energy plane will comprise 60 PMTs, while the tracking plane will be made up of 3584 SiPMs with a 1.55 cm pitch (mainly for the technical inviability of arranging the number of cables needed for keeping the NEW solution). A 12 cm copper structure houses the active region while providing an important shielding against incoming radiation, and it is held in a stainless-steel pressure vessel with an additional layer of 20 cm lead bricks placed in a stainless-steel castle. Fig 3.13 summarizes the principal elements of the NEXT-100 detector. It is planned to be placed in the LSC, in the same location where NEW operated.

There is a collection of minor design changes with respect to NEW, in general, motivated for the bigger size or the pursuit of reducing the amount of troublesome material (radioactively speaking), such as the reduction of the amount of kapton on the SiPM dice boards (keeping it to only one side of them) and the changes on the PMT base circuits (to count with fewer capacitors). The only significant difference concerns the gas system, even though, for the most part, it can be conserved in the upgrade. One notorious change is the new emergency tank, as the volume increases notably. In addition, and following the NEW experience, the gas system has been upgraded, incorporating a new mechanism to reverse the gas flow inside

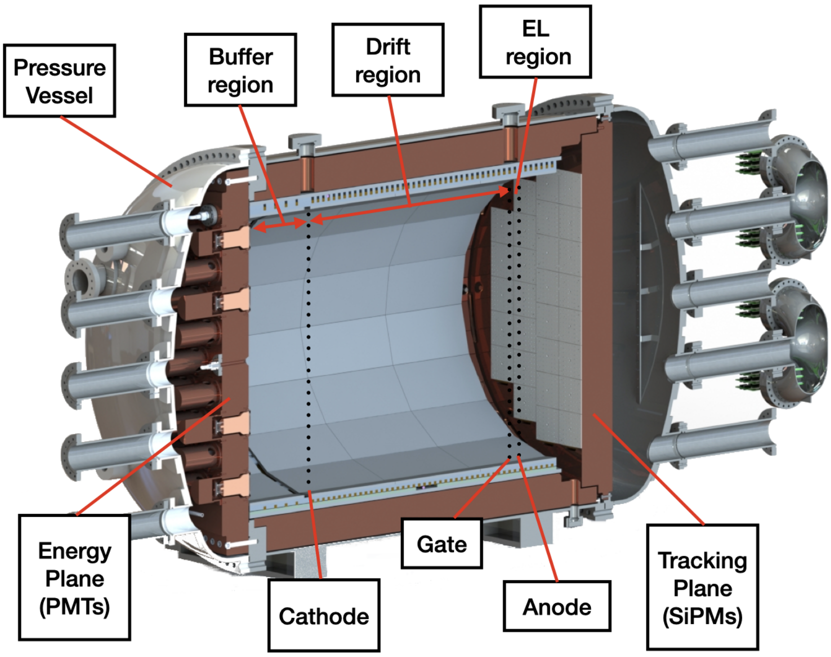

Figure 3.13.: Cutaway view of the NEXT-100 detector with the main features labeled. Figure adapted from [236].

the chamber, and the gas input pipes are moved to the back of the energy plane. Both modifications aim is improving the gas purity inside the chamber. Besides, auxiliary pipes are included to enhance the gas's recovery time inside the detector, and the krypton-controlling valve is replaced from a manual to a precise metering one.

NEXT-100 has a projected sensitivity of $6 \cdot 10^{25}$ yr after 3 effective years of data taking (see Fig. 3.14). The combined good resolution, topological rejection habilities, and low-radioactive budget yield an expected background index of, at most, $4 \cdot 10^{-4}$ count / keV · kg · yr.

3.2.5 NEXT-Tonne

Parallel to the efforts devoted to NEXT-100 construction, simulation, and later data taking and analysis, the collaboration is additionally pushing the needed scaling in order to cover the IO region entirely (see Sec. 2.2.2). The current program projects a two-phased approach, the first one with a more conservative approach and the second incorporating several innovative paradigms.

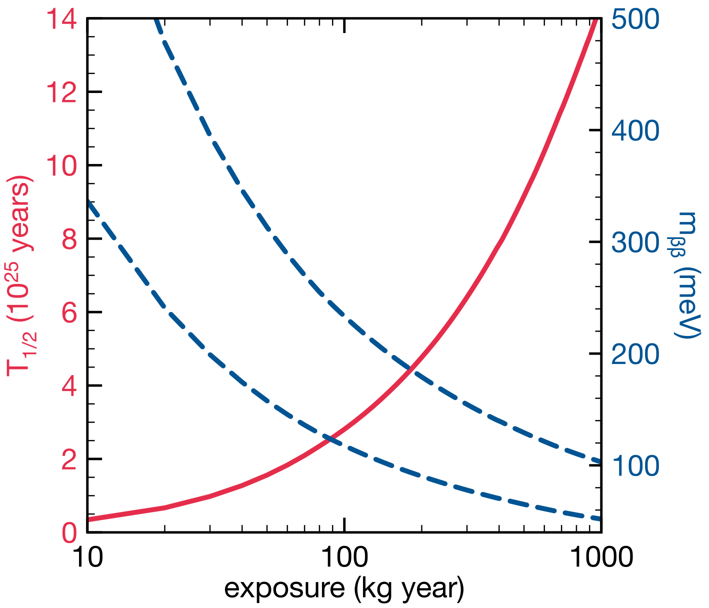

Figure 3.14.: Prospects for the sensitivity to the $0\nu\beta\beta$ half-life for the NEXT-100 detector and its translation to the $m_{\beta\beta}$. Figure from [237].

NEXT-HD

The first phase, called NEXT-HD (High Definition), is based on a careful scaling up of the NEXT-100 detector. However, it presents many notable differences with respect to the previous prototypes [238].

Given the exigent background budget and taking into consideration that they are the leading contributors, this stage would get rid of the PMTs for the energy determination. Instead of them, large area SiPMs are the optimal technological solution. Notwithstanding, this substitution carries some concerns that should be addressed, although it brings some benefits inherently. The most significant gain is that the detector's mechanical complexity decreases notably, as the PMTs cannot handle electric fields and high pressures; hence they must be encapsulated in individual receptacles with a neutral atmosphere and a sapphire window towards the active volume (see Sec. 4.1.2). On the contrary, SiPMs can operate exposed to high-pressure gas and have no problem dealing with electric fields. The drawback of the replacement, the primary concern is related to the S1 and low energy events (such as krypton) measurement. The dark count rate of the SiPMs (several others of magnitude higher than PMTs' at room temperature) makes those kinds of signal detection a challenge that can be potentially mitigated. The R&D solutions under study are twofold: on the one hand, exploring the large-area photo collectors

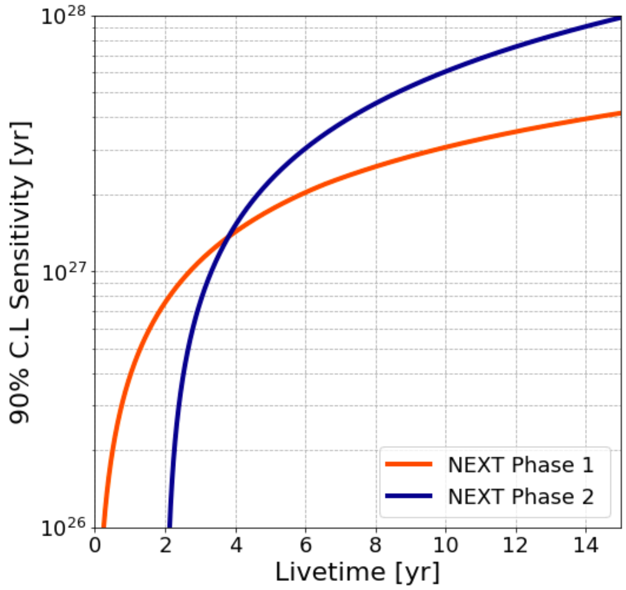

Figure 3.15.: Prospects for the sensitivity for the each phase of the tonne scale detector, where Phase 1 and Phase 2 stand for HD and BOLD, respectively. Note the two years gap between the starting of each phase. Figure from [239].

to improve the signal-to-noise ratio; on the other hand, moderately reducing the gas temperature produces a notable dark noise drop (30 degrees of diminishment implies an order of magnitude less noise). Besides, the Kapton circuit boards will be replaced by ultra-low-background quartz circuits to reduce the background estimates further.

Another significant change is the adoption of a symmetrical scheme for the TPC with a central cathode. In this scenario, the energy can be recollected either by the SiPM planes at both ends of the detector or by extracting the signal from the barrel via optical fibers to external sensors (PMTs or SiPMs).

Moreover, the detector will incorporate other enhancements such as low-diffusion gas mixtures [229] and, conceivably, other gas mixtures to reduce cosmogenic neutrons' impact [113].

The expected sensitivity of the experiment is depicted in Fig. 3.15.

NEXT-BOLD

NEXT-BOLD (Barium iOn Light Detection) represents a more radical approach, implementing barium tagging's groundbreaking idea. As discussed back in Sec.

2.3.5, the possibility of detecting the daughter ion produced in the $\beta\beta$ decay is a powerful tool in the pursuit of a background-free experiment.

The summarized idea of the process is that once the Xe has decayed, the electric field drifts the secondary electron cloud towards the anode (see Sec. 3.1.1) and, additionally, would drift the Ba^{2+} ion towards the cathode, where it should be identified. Therefore, the detection would occur in coincidence, although very delayed, as the ion propagation is 1000 times slower[7]). The first concern is whether the ion is able to reach the detection area, although preliminary studies seem to point out that this might be the case [240, 241]. Nevertheless, in this scenario, the central challenge is ion detection using the so-called *single-molecule fluorescence imaging* (SMFI). The goal of the method, proposed back in 2016 [242], is to find a molecule that, when exposed to Ba^{2+} ion, traps it and starts fluorescing, while when no ion is trapped, the molecule does not emit any light. The first proof of concept came out shortly after the proposal, being able to detect individual ions [120]. A profound multidisciplinary research line inside the collaboration is entirely devoted to fully integrating the design in an HPXe TPC, with several achievements yet [243,244,245], even though there is still a long way to go. This method implies a large improvement in the reduction of background, as represented in Fig. 3.15, where it is clear that, despite the delay in the commissioning of the detector, the solution with barium tagging is competitive and beats the previous design.

---

[7] $\sim$1 m/s for ions compared to $\sim$1 mm/μs for electrons

4

NEXT-White

NEXT-White (NEW) represented the largest radiopure HPXe-EL apparatus functioning in the world. As discussed in the preceding chapter, it is the most recent operational detector, which started the commissioning in October 2016 and data taking shortly after, in March 2017, at LSC, and finished operations in mid-2021, as an immediate previous step towards NEXT-100. This chapter will comprise a general description of the subcomponents, performance, data taking, and significant results achieved so far.

4.1 Design

The outline of the design was sort to speak, an upgraded version of NEXT-DEMO. However, there were several technical challenges when facing such big volumes that had to be carefully understood, characterized, and solved. The detector nominal mass was 5 Kg at 15 bar, in a cylindrical chamber of 530.3 mm of drift length and 208 mm of radius of active volume. The EL gap was 6 mm wide. The energy plane contained 12 PMTs (31% coverage), and it was separated from the cathode by a 13 cm long buffer region, whereas the tracking plane consisted of 1792 SiPM distributed in a squared distribution of 10 mm pitch. The present section aims to provide a brief overview of the main constituents of the detector. Fig 4.1 summarizes the principal elements of the NEW detector. For a more detailed review, check [246].

4.1.1 TPC

Field Cage

NEW's Field Fage (FC) was a cylindrical high-density polyethylene (HDPE) tube of 454 mm outer diameter, 664.5 mm length, and 21 mm of thickness, and can be segmented in three sections: drift (from the cathode to the gate), buffer (from the

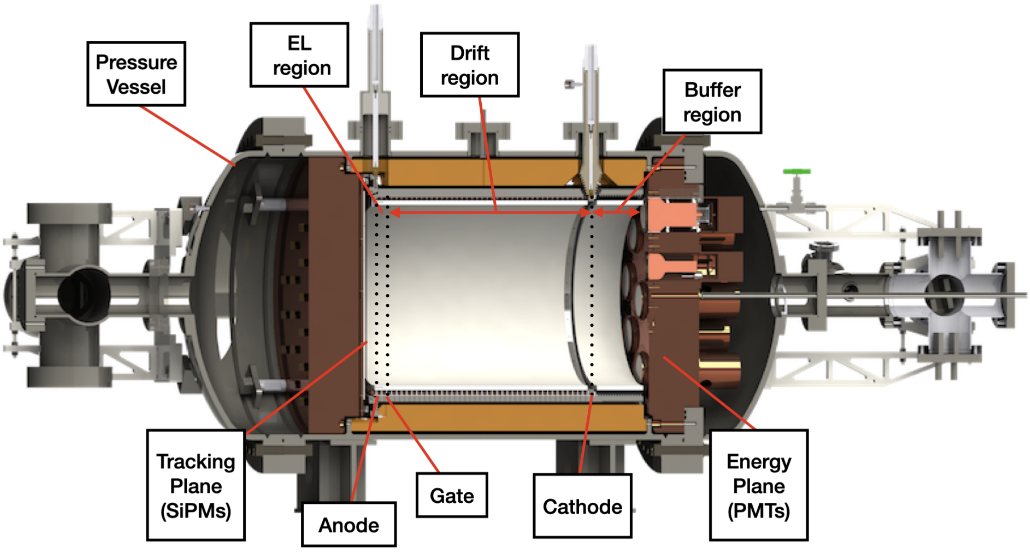

Figure 4.1.: Cutaway view of the NEXT-White detector with the main features labeled. Figure adapted from [246].

cathode to the energy plane) and EL (from the gate to the anode) regions (see Fig. 4.1).

Field Cage's function was to provide an electric field, capable of carrying the secondary electrons towards the anode, inside the detector's active volume. The field requirements in order to ensure the minimum charge loss were that it had to be highly uniform, homogeneous, and strong enough to prevent recombination during the drifting. Therefore, the whole FC outer part length of the drift volume (530.3 mm long) was covered with copper rings, uniformly distributed along the inner side of the FC, connected by copper clamps to a resistor chain. The purpose of the resistor chain was twofold: on the one hand, it attached both sides of the rings, and, on the other hand, it connected the rings by resistors. As a result, it created a voltage divider, and the electric field was uniformly degraded. The grooves for the rings to lie on were deep enough to allow some space between the copper and the light tube, held inside the FC.

In contrast, the buffer region was needed to guarantee that the giant electric field smoothly degraded from the cathode to the energy plane, where the PMTs are. There was no need for homogeneity, so no rings are required. It was 129.5 mm long.

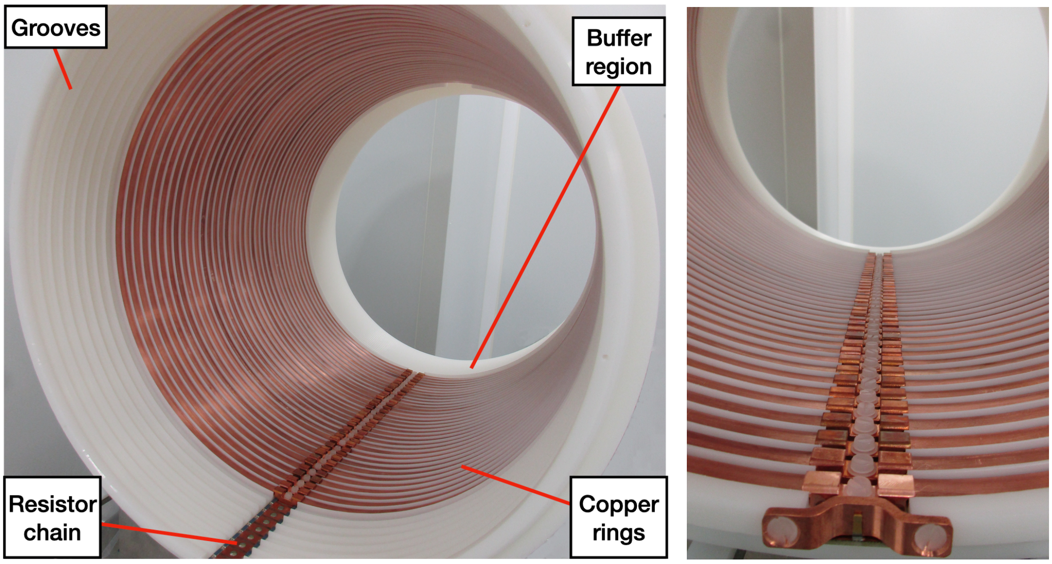

Figure 4.2.: NEXT-White field cage during assembly. Left: The copper rings being installed; thus, all the components are visible (and labeled). Right: Detailed view of the bottom part of the FC where the rings are attached to the resistor chain.

The last and more delicate component of the FC was the EL region. The electric field was very high (27 kV/cm at 15 bar), and uniformity and homogeneity are mandatory in order to avoid deteriorating the energy resolution.

Figure 4.2 depictes the FC and its most relevant constituents.

Cathode

It was a transparent steel grid delimiting the drift region towards the buffer (see Figs. 4.1 and 4.3a). It was made of 0.15 mm diameter wires with a 10 mm pitch, with a total of 95.5 % optical transparency.

One of the most delicate technical challenges of the design was how to provide the voltage to the planes inside the chamber since xenon is a poor insulator and the typical commercial solutions make use of non-radiopure materials. Based on the ideas of [247], the cathode feedthrough (Fig. 4.3b) aim was to hold the very high voltages, up to a nominal −41 kV at 15 bar, avoiding sparks. It was made of HDPE and fitted in a stainless steel external piece.

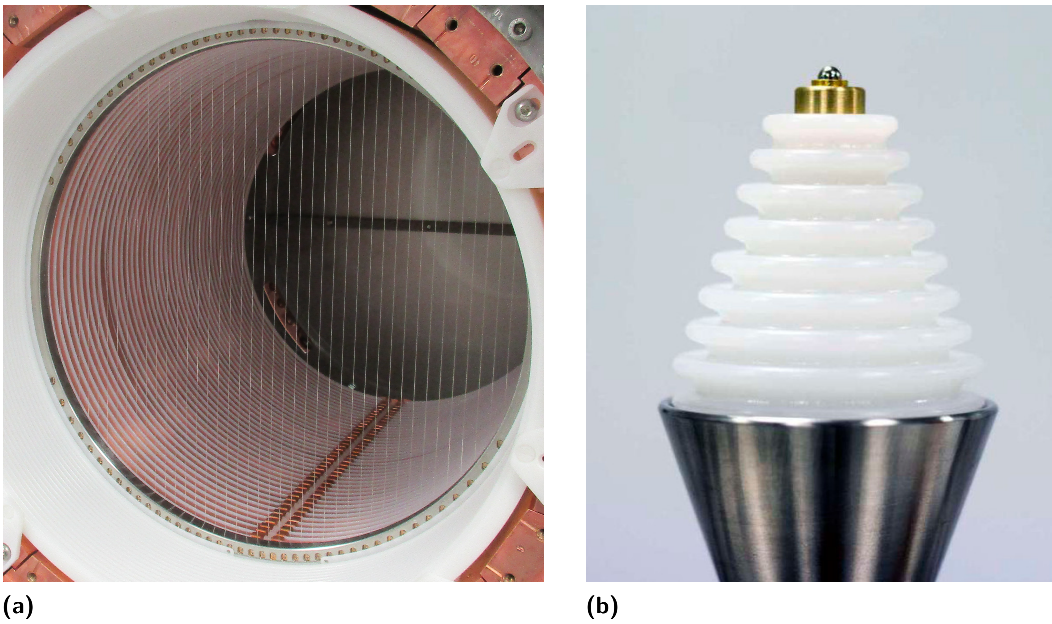
(a) (b)

Figure 4.3.: Left: Cathode during the assembly in its final placement, between the buffer and the drift regions. Right: detail of the cathode feedthrough tip.

Gate

It consisted of a woven steel mesh delimiting the drift region towards the EL region (see Figs. 4.1 and 4.4a). The mesh was made of 40 μm diameter wires with a 0.5 mm pitch, with a total of 90 % open area and a 100 % electron transparency under normal conditions.

In contrast with the cathode case, the gate feedthrough design was much simpler (Fig. 4.4c). The intended voltage was to hold up to a nominal -15 kV at 15 bar. It was, as well, made of HDPE and fitted in a stainless steel external piece.

Anode

The anode represented the end of the field cage towards the SiPM plane (see Fig. 4.1).By contrast to the other two high voltage planes, its implementation was a quartz plate (Fig. 4.4b). The plate was made of fused silica, of 522 mm diameter and 3 mm thickness coated with a thin layer of indium tin oxide (ITO). The ITO layer, of $\sim$15 nm, was a conductor film connected to the ground through a steel frame contacting the ITO via a 1 mm indium wire surrounding the plate. An extra coating of TPB allowed for shifting the light wavelength from the VUV xenon typical

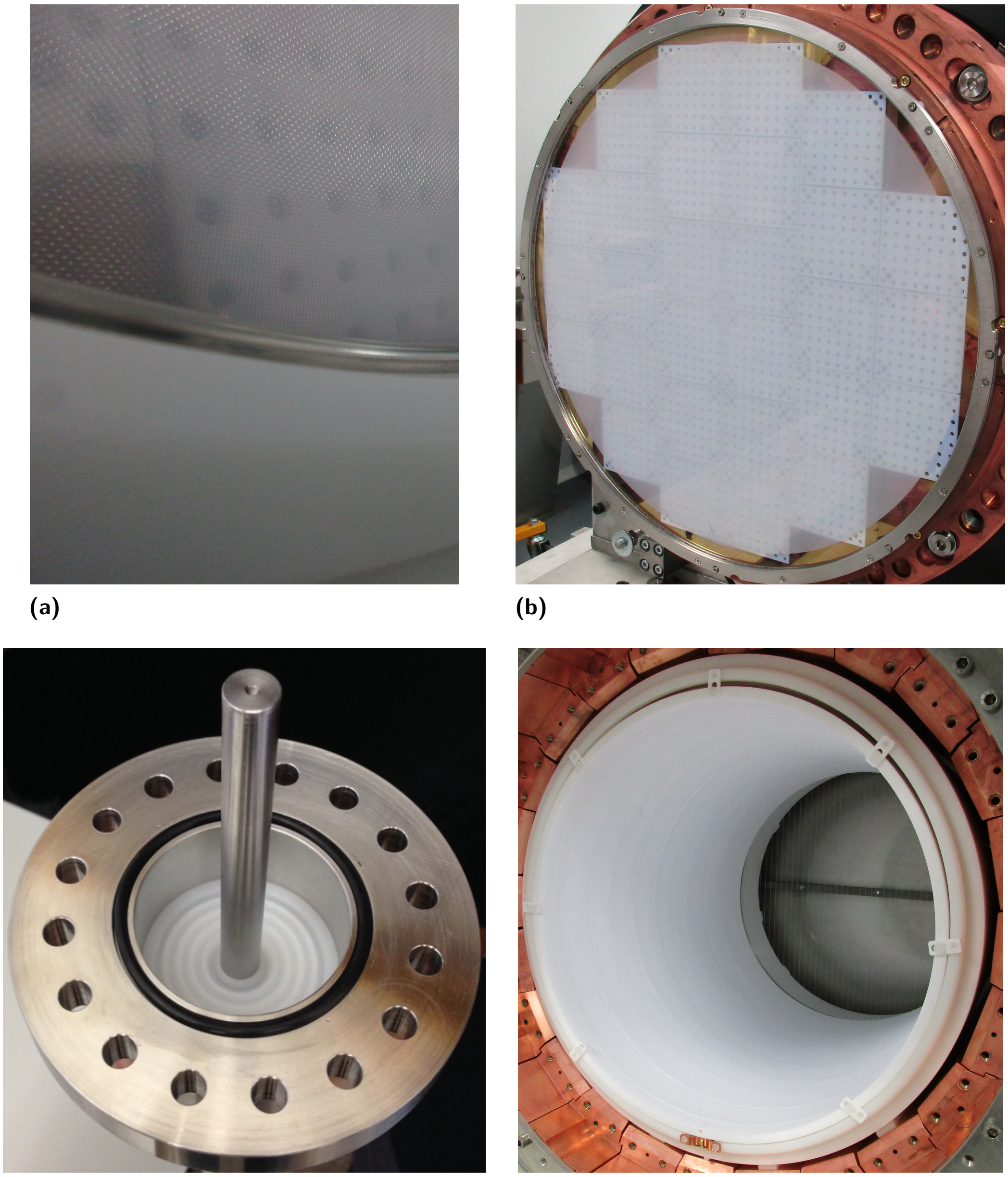

(a) (b) (c) (d)

Figure 4.4.: Close-up view of the NEXT-White gate mesh (a), anode plate installed in front of the TP (b), gate feedthrough (c), and light tube placed inside the field cage (d).

emission to a blue (400–450 nm) spectrum needed for the SiPM detection. The ITO layer was arranged for a total transmission of 93 % for the TPB emitted light.

The anode implementation had several advantages. First, the production of the quartz plate is simpler and cheaper than the mesh case. Second, the installation is also more straightforward since it does not need any mechanical tension: a small ring surrounding the plate is able to prevent sharp edges of the conductive layer. Additionally, it represents a physical protection for the TP against sparks and avoids having to coat the SiPM with TPB. However, it also presents some disadvantages. One is that it obstructs enormously the gas flow and prevents it from being laminar since it only can pass through small windows on the sides of the plate. Another problem is some charge-up effects observed with the quartz plate implementation.

Both the gate and the anode were mounted on top of the TP, so the three planes were parallel, and the EL distance (therefore, the distance between the gate and the anode) could be carefully tuned between 4 and 6 mm.

Light Tube

It was the innermost component of the detector, right in contact with the gas (see Fig. 4.4d). Its primary purpose was to increase the light collection. In order to do so, it consisted of a PTFE cylinder of 416 mm of inner diameter and a width of 10 mm coated with TPB, reaching an excellent reflectivity, $\sim$ 98 %.

4.1.2 Energy Plane

The energy plane of the detector consisted of 12 PMTs arranged in a two-concentrical circles configuration (see Fig. 4.5). The chosen PMTs are the Hamamatsu R11410-10, a typical election for low background experiments, given its low radioactivity and adequate performance. The EP was mounted in an 120 mm thick radiopure copper plate that shielded the detectors from the gas volume and provided a shield against external radiation. An individual aperture in the plate holded each PMT, and a sapphire window separated and protected each apparatus from high pressure. The window was welded to its corresponding radiopure copper frame that sealed against the copper plate and coupled to the PMT bulb with an optical gel. Additionally, the windows were coated with TPB for wavelength shifting and poly ethylenedioxythiophene (PEDOT), a resistive layer whose purpose was to define a uniform ground across the window's surface. The PMTs were stored inside individual copper vessels that provided each detector with further shielding (see Fig. 4.5) and prevented the background from entering through the PMT windows.

The copper plate granted insulation against the gas inside the active volume and createed an independent volume with the endcap.[1] That allowed operating the PMTs in a low-pressure regime, vacuum, or a neutral atmosphere (e.g., with N_2).

Concerning the light collection, the PEDOT coating is up to a $\sim$95 % pf transparency, and the total photocathode coverage was 31 %.

The PMTs work in a high voltage regime. In order to supply it and also to extract the signal, the bases were connected to a feedthrough at the endcap via a Kapton twisted pair cable. The PMT bases provided the individual voltage supply and signal extraction. The bases' circuit was also made from Kapton (fairly radiopure), covered with a copper cap, and filled with radiopure epoxy. The bases were connected to the copper plate in order to allow the dissipation of the heat generated during operation, even under vacuum conditions.

Regarding the front-end electronics for the EP [248], the main design parameter to optimize was the energy resolution outcome (matching the critical requirement for any $0\nu\beta\beta$ experiment). Therefore, careful control over the lineality of the whole system was performed. Other crucial motivations behind the implementation were to improve the radioactive budget and to cope with long signals (corresponding to the most extended tracks) without distortion.

4.1.3 Tracking plane

It consisted of a matrix of 1792 individual SiPMs arranged in a square configuration of 10 mm pitch (see Fig. 4.6). The detectors were subdivided into 28 Kapton boards (known as DICEboards), having each an 8x8 array of sensors.[2] The selected SiPMs were the model MicroFC-10035-SMT-GP, from SensL, C series, having an active area of $1 \times 1\,\text{mm}^2$, presenting a good performance (low dark count and good efficiency for the TPB emitted light) and quite a fair radiopurity [250]. The DICEboards themselves had long tails in order to drive the signal from the TP to the feedthrough and also included a temperature sensor and a blue led to calibrate the EP [251]. A 120 mm thick copper plate holded the DICEboards and provided extra shielding against external backgrounds.

---

[1] Endcap denotes each torispherical head of the pressure vessel (see Fig 4.1 and Sec. 4.1.4).

[2] For practical reasons, every DICEboard shared the same bias voltage for each sensor. In order to improve the performance and get closer to an ideal individual supply for every SiPM, they were carefully selected to have similar gains [249].

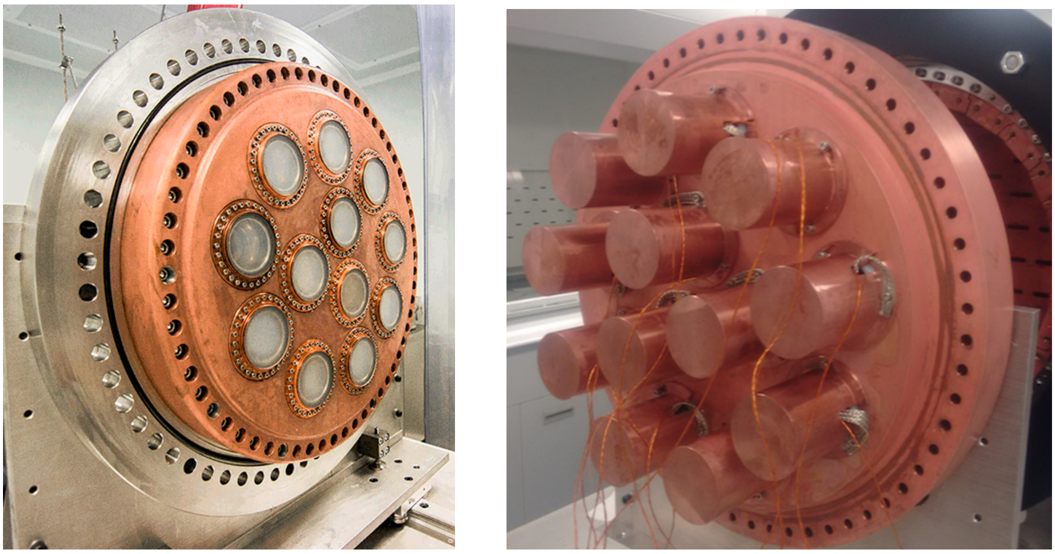

Figure 4.5.: NEXT-White Energy Plane during assembly. The left image shows the PMT arrangement in a two-corona scheme and the individual sapphire windows to protect the detectors. On the other hand, the right picture shows the back part of the EP, where individual copper hats store each PMT, and a pair of twisted cables connect every sensor.

Additionally, the DICEboards were covered by PTFE masks (see Fig. 4.6) to reflect more EL light to the EP, improving the collection efficiency.

Regarding the front-end electronics [252], the sampling requirements were slower than for the EP case (1 μs for the TP in contrast to the 25 ns for the EP). Hence, this allowed for more straightforward and more conventional solutions while dealing with an enormous number of channels.

4.1.4 Vessel

The NEW pressure vessel was the outermost component of the detector. It was made out of radiopure stainless steel alloy (^{316}Ti). It consisted of three sections: the cylindrical central volume and the two torispherical endcaps (see Figs. 4.1 and 4.7). The middle piece had an inner diameter of 64 cm, a length of 950 cm, and a thickness of 2.4 cm whereas the endcaps were 30 cm long and 1.26 cm wide. Concerning the pressure, although the vessel was designed to hold up to 50 bar, it was only certified for 20 bar.

The vessel presented several openings in order to circulate the gas in and out of the detector, the high voltage feedthroughs, signal extraction, and some calibration ports.

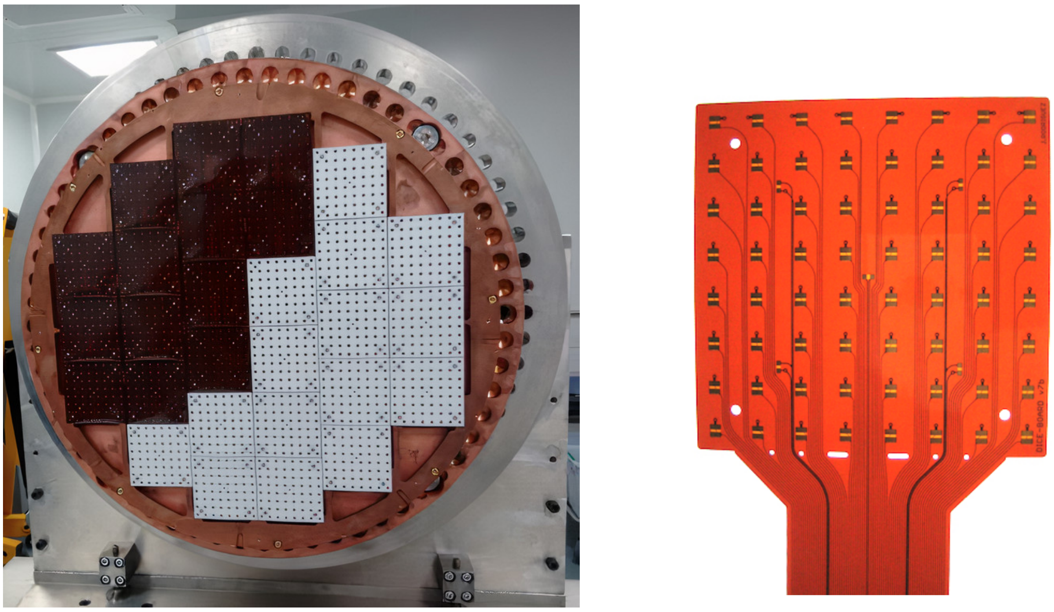

Figure 4.6.: The left picture shows the NEXT-White plane during assembly. The 28 DICE-boards (dark red) are held by the copper plate behind. Half of the dices are covered (the final configuration has all masked) with the PTFE layer (white) to improve reflectivity. The right image presents a detailed look at the custom-made Kapton boards containing an 8x8 SiPM array.

Concerning the NEXT-100 design, its vessel follows the same approach and materials described here but scaled up and adapted.

4.1.5 Gas system

The fundamental purpose of the gas system (Fig. 4.8a) was to circulate de gas in and out of the detector, removing the impurities that affect the electron collection. Following the discussion in the first item in Sec. 3.1.2, those impurities may trap the secondary electrons in their propagation towards the anode. The cleaning was achieved by circulating the gas through chemical purifiers (getters).

In addition, the gas system was in charge of maintaining and monitoring the conditions inside the chamber. The pressure must be kept at the nominal values all the time, reacting automatically to any inconvenience that may damage the detector or imply a gas loss, and, if the conditions worsen enough, enter in a safe mode.

Therefore, the duties of the gas system can be summarized in three main tasks: the pressurization (and depressurization) of the system, the recirculation and cleaning of the gas, and the eventual evacuation of the detector. All of them should

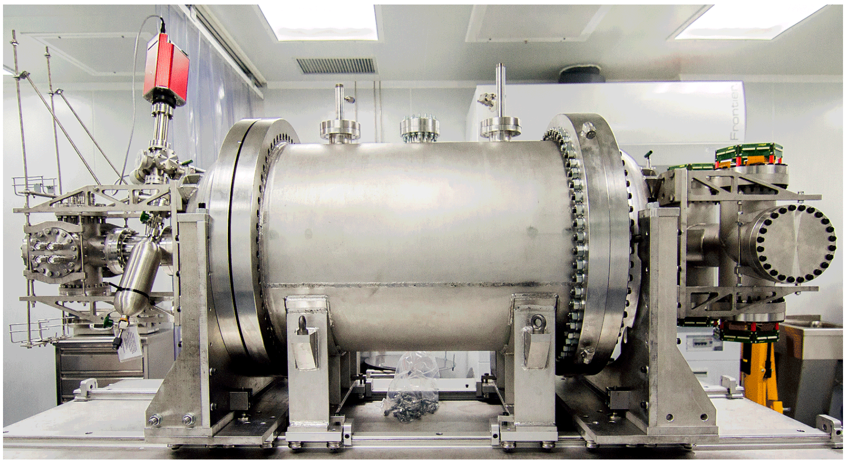

Figure 4.7.: NEXT-White pressure vessel during assembly, in the clean room of the LSC.

be performed safely and without any risk, implying the need for active decision-making based on the system's parameters. The component in the control of that was the Compact RIO (Fig. 4.8c), which ran a real-time LabVIEW version, connected to the several monitoring gauges of the system and behaved correspondingly, opening or closing the appropriated valves.

The first operational phase of the detector, prior to the gas filling, is creating a vacuum level of 10^{-5} bar, in order to eliminate gaseous impurities. The various materials inside the detector, when exposed to the atmosphere, can trap small amounts of gas inside. Thus, by pumping out the gas (and also warming the non-heat sensible parts), it is possible to significantly induce the outgassing to prevent it from happening when the Xe gas is already filled. The whole process was supervised via two Residual Gas Analyzers (RGAs).

By the time the level of contaminants is below the desired level for filling, the Xe is loaded inside the vessel directly from the bottles. Now, the circulation can begin, passing the gas through the getters for further and continuous cleaning for the impurities that can still be present or outgassed [253]. There are two kinds of getters installed in the system, the cold getter (specialized in trapping O_2, H_2O, CO, and H_2) and the hot getter (devoted to O_2, H_2O, CO, CO_2, H_2, N_2, and CH_4 removal).

Finally, for the gas evacuation, when the operation time is over, the procedure consists of liquefying the gas present in the gas system using a cryorecovery bottle (Fig 4.8d): a recovery bottle embedded in a liquid nitrogen bath, creating a temperature drop on the system, thus a pressure gradient towards the bottle.

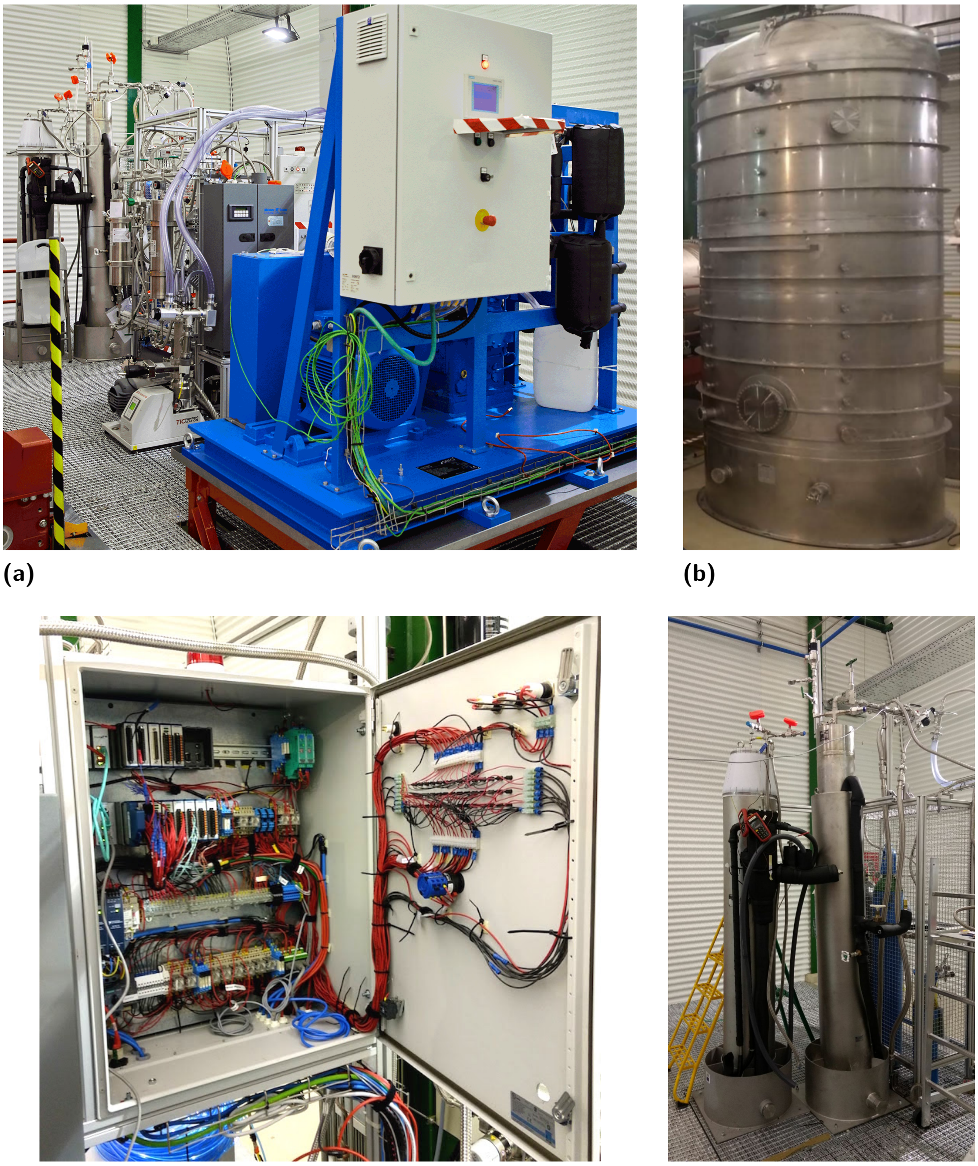

(a) (b) (c) (d)

Figure 4.8.: Different components of the NEXT-White gas system. a: Overview of the gas system installation with the compressor in the foreground, the area where the getters are installed in the middle ground, and the cryorecovery station in the background. b: Emergency recovery tank before the installation. c: Detail of the cabinet of the Compact RIO. d: Cryorecovery bottle.

However, the standard recovery is lengthy. Hence, an emergency protocol must be set up. An emergency tank (Fig. 4.8b), with a volume large enough to hold the gas in the system to ∼1 bar, is kept at a moderate vacuum. In case of an irregularity where the gas might be compromised is detected, a Carten valve would open, so it can flow into the emergency vessel, quickly reducing the pressure in the system.

The design of the gas system of NEXT-100 is, in principle, straightforward since most of the system can be reused as it is.

4.1.6 Shielding

Shielding the detector is the fundamental strategy to deal with natural sources of external background as a passive approach (see Sec. 2.3.5)). In order to block against high-energy gammas, the material selection has to be carried out carefully, fulfilling two essential requirements: having a high atomic number (since the interaction of gamma rays with atoms increases with the atomic number[3]) and density and being extremely radiopure (to prevent it from being a background source). Among the typical materials used for low background experiments, the chosen for the experiment were copper, stainless steel, and lead.

In the case of NEW, there were three main structures insulating the active area:

Lead Castle

The lead castle (LC) was the outermost shielding structure (Fig. 4.9a). It is a stainless steel frame 265 cm high, 195 cm wide, and 293 cm divided sagittally in two halves. The frame holded a layer of staggered roman-lead bricks (200 mm^3 × 100 mm^3 × 50 mm^3, for a total wall with of 20 cm) with an activity lower than 0.4 mBq /kg. It was designed to hold both NEW and NEXT-100.

The divided sections are movable, mounted on a wheels system that can alternate between the two possible states: open and closed. The former was helpful for the installation and service of the pressure vessel, e.g., when placing and removing the high energy sources for the calibration of the chamber. The latter was the desired

---

[3] The gammas can interact, essentially, via three processes, having each a different dependence on Z: photoelectric (the strength goes as $\sim Z^{4-5}$), Compton scattering (its magnitude runs approximately lineal with Z), and the pair production (that depends as $\sim Z^2$) [208]

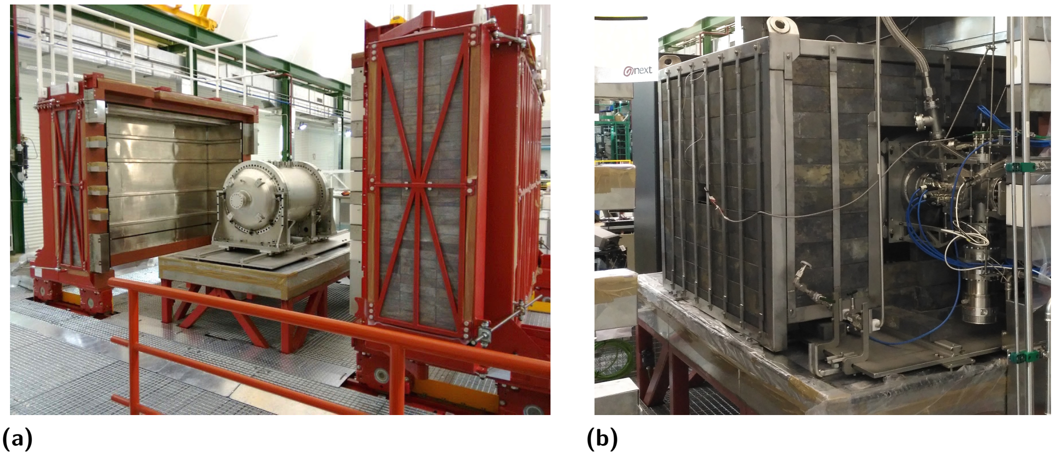
(a) (b)

Figure 4.9.: NEXT-White Lead Castles. Left: outer lead castle in the open configuration. The vessel is placed in the final location prior to any piping and cabling connection. Righ: inner lead castle installed around the detector.

configuration for normal operation, especially when focused on low background data.

For the support of the LC and the pressure vessel, considering the mild seismic activity of the Pyrenees region where the LSC is located, a seismic structure had been built. Therefore, the LC is independent of the working platform, and all the connections between the seismic structure and the working platform are flexible.

Inner Lead Castle

The Inner Lead Castle (ILC) was a shielding component installed right on top and around the pressure vessel (Fig. 4.9b). Set in place in December 2018, the ILC aimed to provide an extra rejection against incoming radiation. As well as the LC, it consisted of a stainless steel frame of 115 cm high, 145 cm wide, 150 cm deep holding a layer of staggered roman lead bricks (same size) for a total 50 mm of thickness. The ILC incorporated some removable bricks around the calibration ports in order to perform small operations like installing and removing the high-energy calibration sources.

Inner Copper Shielding

The Inner Copper Shielding (ICS) is the innermost piece of shielding present in the detector, thus the last barrier against the background produced by the various materials inside the inner castle. It is located inside the pressure vessel surrounding

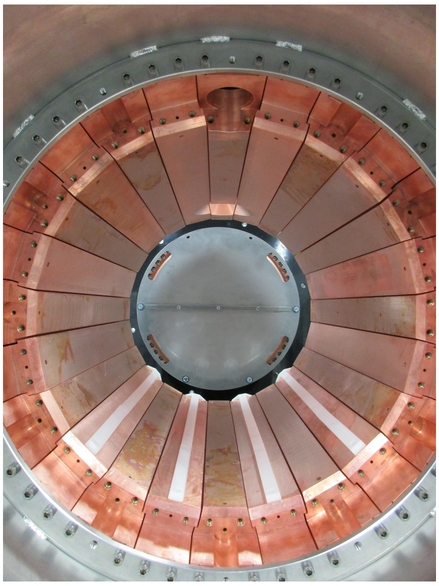

Figure 4.10.: NEXT-White Inner Copper Shielding during assembly. Note the HDPE strips to hold the field cage in place.

the field cage. It consists of three different sections: the aforementioned plates holding both the Energy (Fig. 4.5) and Tracking plates (Fig. 4.6) and the barrel portion (Fig. 4.10). The latter constituent consists of ultrapure copper bars, 60 mm thick situated inside the vessel surrounding and holding the field cage.

4.1.7 DAQ and trigger

The Data Acquisition System (DAQ) for NEXT-White was based on the modular architecture Scalable Readout System developed jointly with the CERN-PH in the RD51 collaboration framework [254, 255], specifically on a second version based on ATCA. The aim of the scheme was scalability and compatibility among the various stages of the project. Actually, the implementations in NEW were, in a large portion, an enhancement of those in use for NEXT-DEMO.

Both the EP and TP had custom design front-ends [248, 251]. The front-ends were connected with the DAQ modules via the so-called Front-End Concentrator (FEC) cards [256]. The DAQ was designed for a maximum operation rate of 10 Hz and divided into three sections, each with a dedicated FEC: the energy plane (12 PMTs), the tracking plane (28 boards with a total of 1792 channels), and the trigger.

Once the signal got to the DAQ module, it was split into a two-level server farm, where the DATE software [254] was running. The FECs transmited the sub-events to Local Data Concentrators, which performed the first stage of the process. The LCDs passed them into the next step, the Global Data Concentrators. They packaged all the data together and saved the entire event to disk, ready for offline analysis. A comprehensive, complete, and detailed description of the DAQ implemented in NEW can be found in [236].

The trigger [257] was also an evolution of the one developed for NEXT-DEMO [258], improving flexibility and event selection. The additions were motivated by the wide range of energy and orientation of the electrons, causing a diverse S2 behavior.[4]

NEW had implemented a circular buffer of 3.2 ms length (that corresponds to around six times the detector size). In addition, it had been developed a system of double trigger (trg1 and trg2) in order to minimize the death time. Typically, they worked on a configuration of priority for the events of interest, meaning signal-like ones. Thus, this allowed taking a continuous set of data for the detector low-energy calibration (associated with trg1) while recording with no losses the high energy events (linked to tgr2) happening much less frequently. Therefore, the double trigger paradigm allowed reducing the chances of missing important events while continually monitoring the chamber (see Chapter 6).

Besides, another convenient feature was zero suppression. This procedure ignored those SiPM buffer sections away from the signal (thus, below a certain threshold in the DAQ). Therefore, the amount of data handled was significantly reduced, as well as the time for full detector readout (see Fig. 5.3). When this mode was switched on, even at high rates of 1 Hz, the death time was below 0.1 % [246].

4.1.8 Slow Control

Thereby, the NEXT-White detector involved very diverse and delicate components that must be carefully managed, necessitating an advanced control system, the so-called slow control (SC). The SC got direct information from the detector components, kept the system safe and running, and performed the programmed duties, problem-prevention, problem-solving, and hardware control. The various SC elements ran in different industrial computers, connected among them via an internal network.

---

[4] Even though it is possible to set the trigger based on detecting S1, the typical choice, for simplicity, is to do so based on S2 signals. In addition, it is the right strategy when dealing with small signals, like Kr, whose S1 are, sometimes, delicate to find, as depicted in Fig. 5.4.

Figure 4.11.: NEXT-White Slow Control displays inside the LSC lab.

Each major constituent system had a dedicated SC program, for a total of six of them (see Fig. 4.11):

High Voltage (HHV) It was in charge of controlling and monitoring the cathode and gate's voltages. It managed the correct rising and dropping of the feature. One of its principal duties was the detection of sparks and the subsequent auto-recovery protocol, ensuring there was no damage in the system.

Gas System (GAS) It took care of all the parameters related to the gas system, like valves, pressure gauges, vacuum pumps, compressor, chiller, and RGA, and reacted to any abnormal value. The monitoring activities include the eventual emergency recovery if the detector was in danger or the gas may be compromised. In addition, it allowed for manual activation of the emergency stop.

Power Supplies (PWR) It controled the power supplies that fed the electronics in the detector: SiPM DICE-boards, SiPM and PMTS front-ends, and even the fan for cooling the rack.

PMT High Voltage (PMT) It managed the PMTs power supply and the vacuum pump in charge of the EP endcap region.

Sensors (SNS) It was responsible for monitoring essential parameters, such as the temperature, of the electronics and DAQ computers.

Main Slow Control (MSC) It was the central piece, receiving the principal information from the other SCs. It summarized and presented it to the shifter, so one SC displayed the relevant parameters for the whole system. Besides, it gathered the info and reported the relevant one to the LSC. It also had an emergency switch that stopped everything to prevent any damage and was able to switch off and on the other SC computers remotely.

All the SC components were intercommunicated since the decisions or anomalies not only affected the subsystem they were supervising. They also generated reports compiling the incidents and principal parameters. Moreover, they had a complete alert mechanism sending emails and different messages with the eventual warnings or alarms that may be triggered, so the shifters and the experts were aware of them and could intervene straight away.

4.2 Detector Performance

The first gas filling was performed back in October 2016. It was a short period devoted to several tests and checks, for instance, the demonstration of the recovery scheme.

In fact, the main commissioning run was Run II, which started at the beginning of March 2017. This run period was dedicated to further understanding of the detector, sensor calibration, energy calibration, technical tests, and some relevant data taking.

With regard to the gas system, the operation was very successful. Although gas entered the gas in a non-perfectly clean state and the presence of outgassing, the pre-filling pumping and purifying process showed to work nicely. In addition, the chamber ran up to eight months with the initial filling conditions accounting for slight losses of gas, around 1 μbar per day for a total of 130 g during the whole Run II period, which quite an exceptional achievement (and kept the gas waste under an acceptable range). The high voltage also behaved correctly throughout the different run periods, the voltages were really stable, and their values were adapted to the pressure to keep the same gain and drift velocity. However, even not being a severe issue, during Run II, sparks had occurred quite often: six of them in the gate along the first eight months (at 7.2 bar), a ratio that increased during the last month (at 9.1 bar). Notwithstanding, all of them were recovered automatically without any damage to the detector or the light response.

Concerning the detector response, no significant concerns were raised neither. Periodic sensor calibrations show a smooth trend both for the EP and TP. Some SiPMs were a bit noisier, and, from time to time, one of them may be masked because of that or even stopped responding. Yet, it was perfectly fitting and within the expected

Run	Sub-run	Duration	Purpose	Pressure (bar)	Gas
II	IIa	8 month	Commisioning	7.2	Depleted
	IIb	1 month	and calibration	9.1	
IV	IVa	41 day	Low background	10.25	Depleted
	IVb	27 day			
	IVc	40 day			
V	Va	80 day	$2\nu\beta\beta$	10.20	Enriched
	Vb	48 day		10.15	
	Vc	150 day		10.05	
VI	-	230 day	Low background	10.30	Depleted

Table 4.1.: NEXT-White data-taking summary. Note that duration refers to the approximate time span of the operation, not to the actual exposure. Also, pressure tends to slightly decreases along with runs; an indicative level is reported.

behavior. From the low and high energy calibration, no trouble was noticed (further detail in Chapter 6).

4.2.1 Data Taking

Apart from Runs I and III, whose only purpose was testing and checking, NEW has accomplished four remarkable data-taking periods, each having a different aim and conditions, even during the same stage. Now, some highlights about the runs are presented, as well as a brief summary of relevant parameters in Table 4.1.

Run II First long-term run and, as already mentioned, devoted to calibration, testing, and data-taking. This phase data did not serve a sole intention but to understand different features of the detector better. The first objective was getting to the bottom of the low and high calibration, using $^{83m}\mathrm{Kr}$ for the former and $^{22}\mathrm{Na}$, $^{137}\mathrm{Cs}$, and $^{232}\mathrm{Th}$ for the latter. The high-energy calibration also helped to refine the track reconstruction and selection. Another one was the characterization of the radon-induced backgrounds and a first look into the other sources. Also, there were several dedicated runs with different gate and cathode configurations to study the behavior of secondary electrons while drifting towards the anode. Finally, there was a small gas refilling up to 9 bars for the last sub-run and further testing. It operated only with depleted Xe (the residual of $^{136}\mathrm{Xe}$ enrichment, i.e., natural Xe without the isotope of interest).

Run IV First physics run, dedicated almost entirely to the radiogenic background characterization. Thus, the operations were performed, as well as in the previous period, with depleted gas. Prior to the data-taking, there were some changes regarding the radioactivity, for instance, substituting the field cage resistor chain for a more radiopure one. This stage is further divided into three main sub-runs as a function of two additional improvements affecting the background reduction. The initial one was the starting of the Radon Abatement System (RAS), a radon-free air supply inside the castle, and the last one was the installation of the inner lead castle.

Run V Fist run using $^{136}\mathrm{Xe}$, wholly dedicated to the measurement of the $2\nu\beta\beta$ signal. In this case, the chamber conditions were intended to be kept as close as possible to RunIVc, for better result comparison. This term is divided into three sub-runs, but, on this occasion, the classification is just driven by operational ranges, not for chamber conditions.

Run VI Final run, going back to depleted Xe data. The purpose of this last period was to collect more depleted data for complementing and enhancing the $2\nu\beta\beta$ characterization. Hence, the conditions were kept, again, as similar as possible to the previous runs.

4.2.2 Results

The various data-taking periods in NEW were very prolific. The different results cover a wide range of topics, from performance and calibration to background characterizations. This section will present a brief overlook of the publications resulting from the detector data.

TPC properties

Using several drift fields and the two pressure regimes from Run II, this study evaluates the drift velocity and longitudinal and transverse diffusions of the secondary electrons (from $^{83m}\mathrm{Kr}$ events) towards the anode. Those effects have been compared with *Magboltz* simulations, getting a pretty good agreement (within 5 %) and other measurements found in the literature. That helps to understand the detector and shows the possibilities and good behavior of the NEXT concept and experimental program. The complete analysis may be found here [226].

Low energy calibration

This work describes the low energy calibration studies performed using Kr dissolved in the gas (see Chapter 6) for a more detailed description). Those kinds of events are monoenergetic and, under the detector conditions, pointlike. Thus, they are a handy tool for parametrizing the difference in response as a function of the event's position inside the chamber. Therefore, the geometrical effects (caused by the variations in coverage (solid angle), both for direct and reflected light, and edge effects) and the attachment (caused by the secondary electron trapping by impurities during the drift) can be corrected. In addition, Kr events can be used for energy resolution studies, projecting (naively with the square root) to a performance well within the 1 % target. The complete analysis may be found here [222].

High energy calibration

On the high energy regime, energy depositions are no longer pointlike but extended tracks. Hence, their behavior must be well scrutinized, especially those around the $Q_{\beta\beta}$ energy and those that imitate the signal (double escape peaks). An initial analysis based on Run II data already showed a resolution (naively extrapolated) around 1 % and a consistent performance throughout all the considered energy range (from $\sim$ 30 keV of Xe X-rays to $\sim$ 1.6 MeV from ^{208}Tl double escape peak). Later, now using data from calibration tasks during Run IV, the resolution had improved and the energy range broadened (up to$\sim$ 2.6 MeV from ^{208}Tl photopeak), as shown in Fig 4.12. The complete analysis may be found here [259] for the first attempt and here [154] for the more mature one.

Event identification and background rejection

With regards to the background rejection, two principal approaches were conducted. Both are based on the study of the ^{208}Tl double escape peak. This kind of event consists of a pair production where both gammas from the positron annihilation leave the detector without interacting. Thus, the resulting track is only an electron and positron pair, mimicking the $\beta\beta$ features. This is really useful in order to

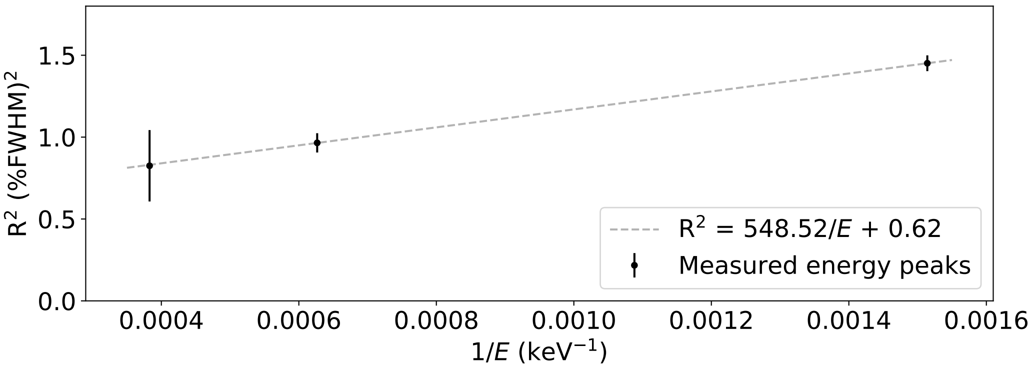

Figure 4.12.: Peak resolution form high energy calibration (corresponding to ^{208}Tl photopeak and double escape peak and ^{137}Cs photopeak, respectively) as a function of the inverse of the energy. Figure extracted from [154].

identify the features of the signal and improve the reconstruction and background rejection.

On the one hand, there was the *classical* analysis based on the blob characterization, i.e., selecting $\beta\beta$ candidates based on the energy deposited at the ends of the track. This has the advantage of being a more controlled, mature, and physics-driven method.The results show that double escape peak events have a good performance of the topological reconstruction and blob characterization, improving the performance with respect to NEXT-DEMO. Regarding the event selection, the signal efficiency reached is (71.6 ± 1.5) % for a background acceptance of (20.6 ± 0.4) %, as depicted in Fig. 4.13. More detail here [117].

On the other hand, another interesting strategy, that is quite a fashion, is the Deep Neural Networks (DNNs). DNNs are a machine learning technique that tries to extract information from a training data set with different aims, such as regression, classification, pattern recognition, and clustering. In this case, the DNN subtype, known as convolutional neural networks, is used for classification goals in two categories: signal and background. The outcome was a 10 % background acceptance while maintaining around a 65 % of the signal, as displayed in Fig. 4.13. Hence, the method has proven its potential and viability for the NEXT physics case. Complete analysis in [260].

Reconstruction improvement

The efforts attempting to enhance the reconstruction had led to the successful implementation of the Richarson-Lucy deconvolution algorithm. The method helps to

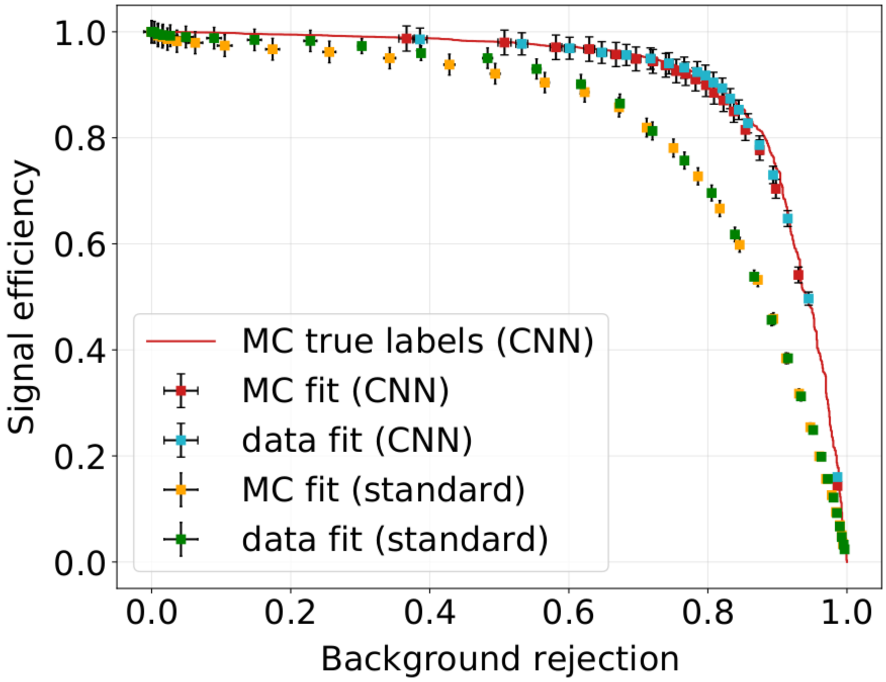

Figure 4.13.: ROC curves for the signal and background classification. The *classical* analysis is represented with green (data) and yellow (MC) dots, while the DNN one is plotted with blue (data) and red (MC) dots. The result can be compared with the MC true labels (red line), i.e., the classification based on the actual knowledge of the type of event generated with MC. Figure from [260].

reverse the diffusion happening during the electron cloud drift and electroluminescence production. The repercussion of the application of the deconvolution yields a background acceptance of (3.7 ± 0.7) % for a signal efficiency of (56.6 ± 1.6) %, applying the classical approach. Fig. 4.14 shows an example of a two-blob candidate track versus a single electron one after deconvolution. Further details in [227].

Background estimation

Following the objectives of the detector, the background has been carefully scrutinized. That resulted in two analyses being published: the first one estimating the incidence of the radon-induced contaminations and their impact in the next generation (see Sec. 7.2) and the other one measuring the different radiogenic backgrounds and their impact on both the two neutrino and neutrinoless mode (see Sec. 7.3). They can be found here [214, 261].

Beyond the published results, there has been an enormous effort towards the evaluation of the other sources, such as muons from the cosmic rays. More detail in Chapter 7.

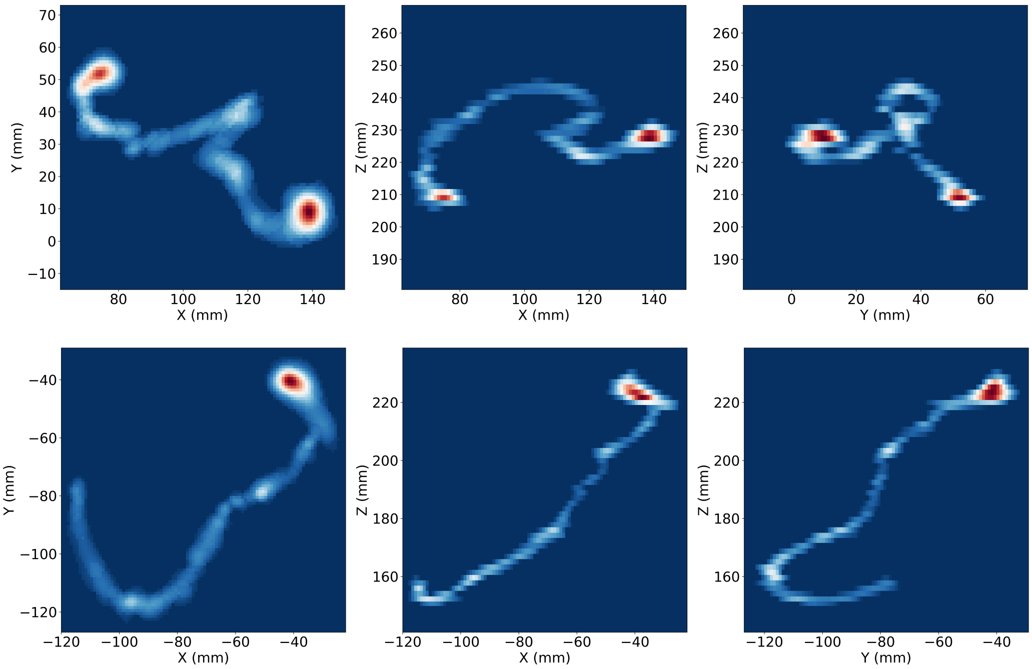

Figure 4.14.: Richarson-Lucy deconvolution result over a two-electron track candidate (top three projections) and a single electron candidate track (bottom three projections. Figure extracted from [227].

Double beta decay measurement

The experience earned in the background studies is a crucial part of the success of the $2\nu\beta\beta$ measurement. The possibility of acquiring data with the enriched and depleted Xe independently opens the possibility of using a novel background subtraction technique, displayed in Fig. 4.15. This represents the first demonstration of a feasible strategy of background-model-independent neutrinoless double beta decay searches. Finally, a half-life of $2.34^{+0.80}_{-0.46}\ (stat)\ ^{+0.30}_{-0.17}\ (sys)\ 10^{21}$ yr is reported. Meanwhile, using a more traditional background-model-dependent spectra fit (analog to the background one), it is found to be $2.14^{+0.65}_{-0.38}\ (stat)\ ^{+0.46}_{-0.26}\ (sys)\ 10^{21}$ yr. The complete analysis may be found in [262].

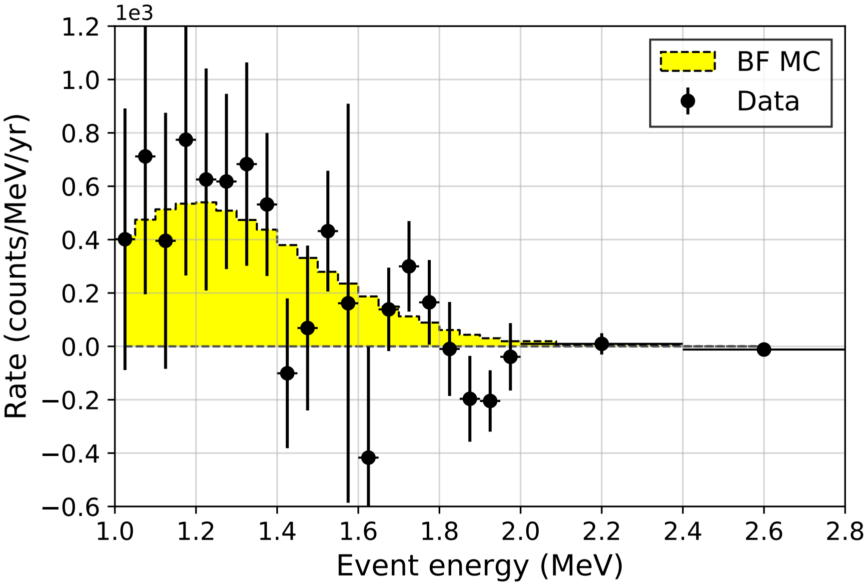

Figure 4.15.: Background-subtraction $2\nu\beta\beta$ fit. The background subtracted data (black dots) are superimposed to the best-fit MC (yellow histogram). Figure extracted from [262].

5

NEXT data reconstruction and simulation

Data coming from the detector must be processed in order to make it human-understandable and facilitate the posterior analysis. In addition, a fundamental piece for comprehending the real data is the simulation campaign. MonteCarlo (MC) simulations allow predicting the outcomes and study more profoundly all the effects individually that, otherwise, are convoluted in the detector performance. This chapter provides a brief overview of the reconstruction chain followed in the experiment, the simulation tools available, and the software framework developed within the collaboration the signal processing.

5.1 Reconstruction chain

The processing software aims to transform the raw data output by the detector electronics into a higher level and more meaningful structures that allow the several types of posterior analysis. This is also the case for the MC simulation outputs, as explained in Sec. 5.2. The following section will present a brief overview of the data processing chain. For a more thoughtful review, check [263].

5.1.1 Obtaining raw waveforms

Raw waveforms (`RWFs`) are the lowest level data that enters the reconstruction chain. They consist, basically, of a time-ordered signal amplitude measured in ADC counts (Figs. 5.1 and 5.3). Each sensor has its own waveform for every event. The `RWFs` are defined by two parameters: the total length and the size of the time interval used to sample the amplitude (sampling time). As mentioned in Sec. 4.1, the EP samples are at a rate of 25 ns, whereas the TP uses a sapling rate of 1 μs. Therefore, for any event, the outcome is a list of 12 PMT `RWFs` and a list of 1792 SiPM `RWFs`.

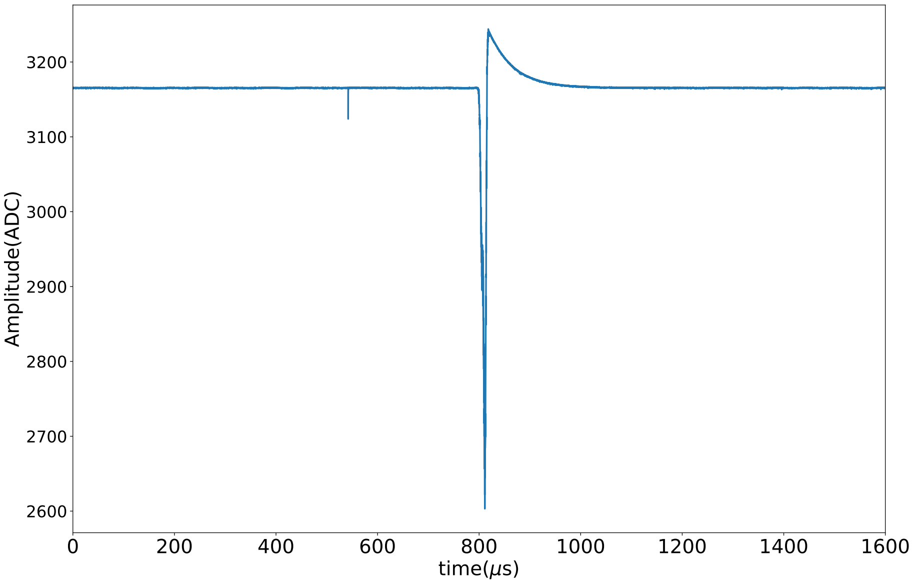

Figure 5.1.: Typical raw PMT waveform of a high-energy electron track from a calibration run. Both the S1 (left) and S2 (right) peaks are evident. The PMT electronic configuration causes a swing in the response.

They are produced from binary data, once decoded by a routine launched during the data taking (DECO), and stored directly in `hdf5` files using the PYTABLES module.

5.1.2 PMap production

Looking at Fig. 5.1, it is patent that the information along the waveform is concentrated in a specific region of it, while the rest holds no meaningful data. Thus, for simplicity and better data management, the next step should identify the correspondent peaks, slice the `RWF`, and eliminate the useless sections. In addition, at this step, the separate `RWF`s for each sensor need to be matched and combined into a single object. Here comes the `PMap` idea. A `PMap` is a collection of all the peaks in the set of waveforms of a given event.

The production of `PMap`s consists of three main stages:

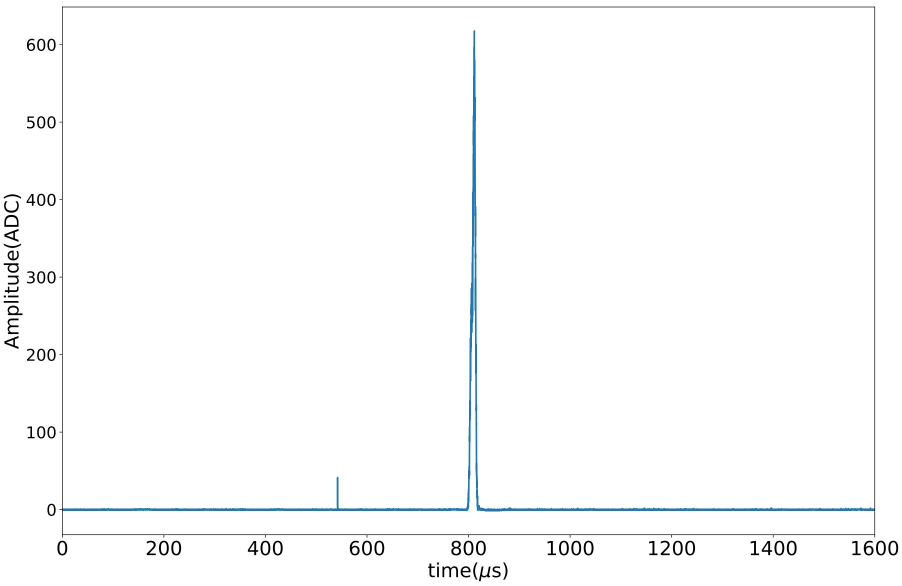

Figure 5.2.: Deconvoluted PMT waveform of Fig. 5.1. Now, the CWF is positive-defined and the baseline is set to zero.

Baseline subtraction and deconvolution

Because of the PMTs electronics configuration, the signal is not the actual output of the sensors but is derivative [248], as the one in Fig.5.1 manifests. Also, patent in that image, the baseline is far from zero.

Therefore, the first action is bringing the baseline back to zero. In order to do so, the average value of the entire waveform is subtracted. The reason this works is twofold. On the one hand, the output signal is characterized by having a total area equal to none. On the other hand, the intrinsic noise associated with PMTs is known to be gaussian. Thus, the waveform deviations above and below de baseline cancel out, and a simple subtraction is enough to remove it.

Regarding the recovery of the actual output, it is accomplished using a deconvolution algorithm (BLR) that is able to reverse the effect of the electronics. It is a delicate process, and the procedure must be carefully tuned since the signal area determines the event's energy. However, the computed impact of it in the final resolution has been quantified to lie under the 0.3 % FWHM for long signals, below the contribution of the Fano factor.

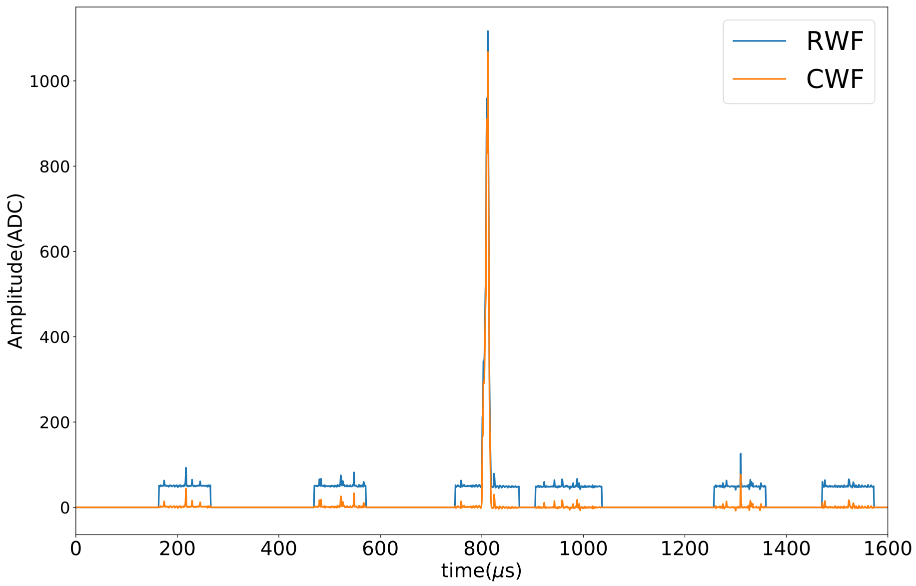

Figure 5.3.: Typical SiPM raw waveform and corrected waveform from the same event of Fig. 5.1. Note how the RWF has already been treated by the zero suppression (see Sec. 4.1.7), and large portions of the signal (away from the peaks) have been set to zero. Also, note that since the S1 signal is so weak, the SiPMs are not able to detect it.

The BLR algorithm transforms each PMT outcome individually to produce the Corrected Waveforms (`CWFs`). Fig 5.2 displays the same event of Fig 5.1 once the BLR is applied and Fig. 5.4 for various kinds of events.

Concerning the SiPM `RWFs`, they do not suffer from signal distortion, so the process is more straightforward: the only procedure is the baseline restoration. Since the waveforms are now positively defined, they cannot be reduced by the average but by the mode instead. In the same way as the PMT case, the baseline is computed and subtracted on an event-by-event basis and for each sensor individually. Fig 5.3 shows the raw and corrected cases for a SiPM signal example.

Waveform calibration

Every sensor, although manufactured in a controlled manner, has a specific variability in the response. Hence, the gain obtained is different for each one and should be corrected. In order to do so, periodic simulations measure the single photoelectron spectrum of each detector using the opposite plane's blue LED (see Sec. 4.1.1),

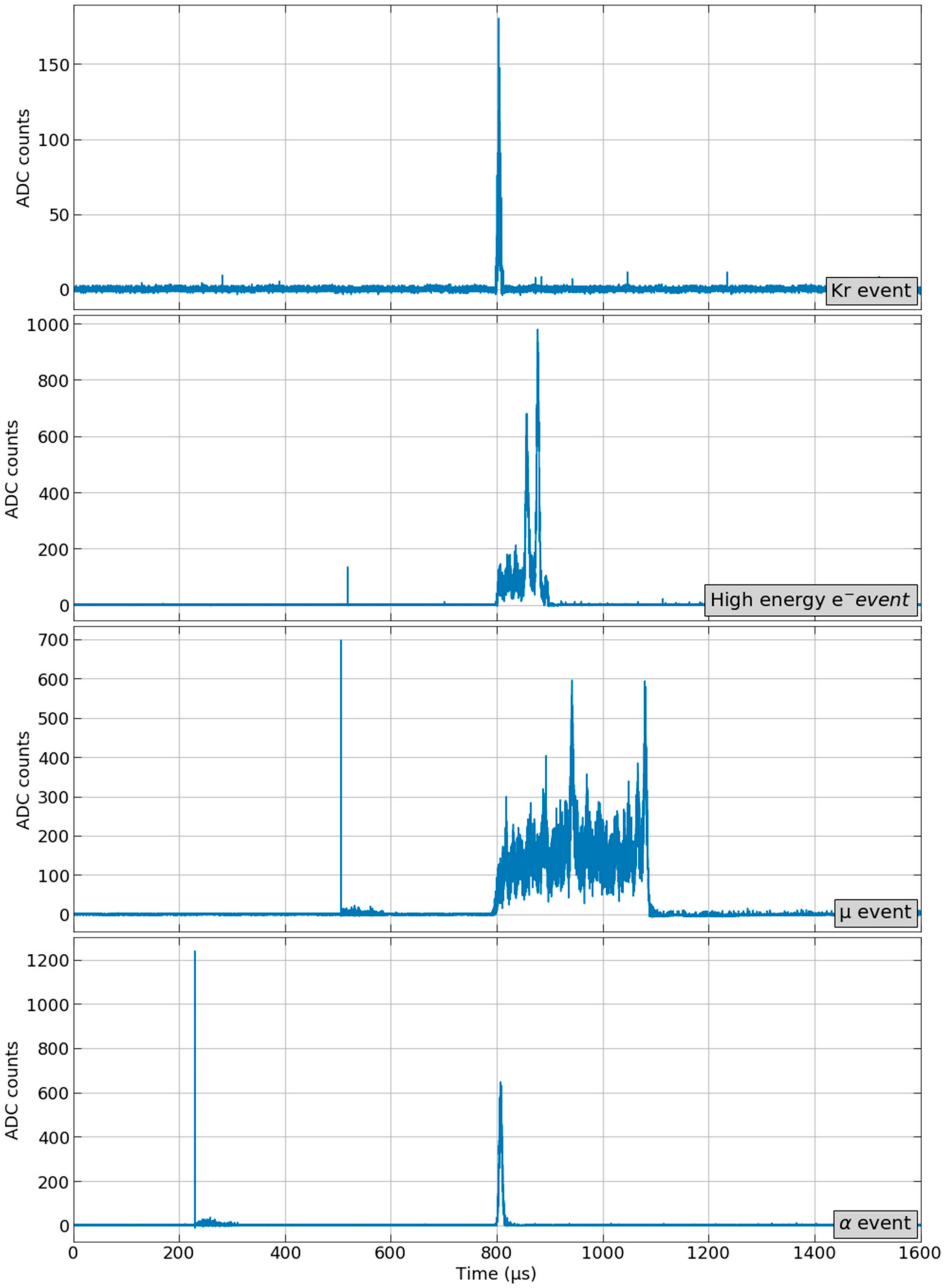

Figure 5.4.: Typical CWF for different event kinds. Figure from [257]. Note how the S1 (left and narrow peak) and the S2 (right and extended one) signals vary significantly depending on the particle interacting in the gas. Kr events leave almost no scintillation light, and the electroluminescence light is tiny. In the case of a high-energy electron, the S1 is now small but clear, and the S2 emits more light. The muon event, on the contrary, is a much more extended track (crossing the detector) but leaving a constant but small amount of energy (it behaves like a MIP), which reflects into a high S1 and a very spread S2. Finally, an alpha particle is a really energetic and concentrated event (usually saturating the PMTs), and thus the S1 is very high, and the S2 is narrow (the total energy is not that high since the alpha data are taken in dedicated runs with dedicated conditions, see Chapter 8). Figure from [257].

which emits short light pulses in regular intervals. The calibration factor translates the ACD counts into photoelectrons, a much more relevant quantity.

Therefore, the `CWFs`, both PMTs and SiPMs ones, are scaled by the calibration factor to produce a set of Calibrated Corrected Waveforms (`CCWFs`).

Peak finding and waveform slicing

The last step is to accurately identify the peaks present in the waveform and select the region to slice it and remove the rest of the signal. This is a sensitive process since it directly impacts the energy determination and many posterior analysis cuts.

In order to increase the signal-to-noise ratio (SNR), the individual PMT waveforms are combined (adding them). Assuming each sensor's noise is comparable and given its Gaussian behavior, and since the signal improves linearly, the SNR improves as the square root of the number of sensors added.

The algorithm responsible for the peak finding runs with two different configurations, one for S1-like signals and the other for S2-like ones. The reason for that is the significant disparity in phenomenology among both types. Therefore, the program scans the waveform to find the peaks above a given threshold (`thr_sum`), different for each signal and event-type. Additionally, a set of handy parameters to distinguish between them are the width, height, and area under the peak.[1] Lastly, in order to avoid splitting the peaks due to fluctuations around the limit, a buffer time (`stride`) is defined and, if they happen to fall within the stride time, they are considered the same peak.

Since the S1s are too small, only the PMTs are sensitive to them, and therefore, once they are identified, the regions are selected and stored.

On the other hand, S2s are recorded in both planes. However, now the waveforms from each one have different sample rates. Thus, PMT waveforms have to be rebinned to match the $1\,\mu$s of the TP. In addition, since the light emission occurs very close to the SiPM, the response is very localized in the plane, so just a few of them have actual information. Besides, the SiPMs suffer from the dark counts from thermal emission (patent in Fig. 5.3, where they are also above the threshold for the zero suppression procedure). Therefore, both effects are mitigated, asking for two conditions: that the signal is higher than a specific value (`thr_sipm`) and the overall integrated signal in the simps is above a given amount (`thr_sipm_s2`). The

---

[1] The final values for the search vary not only for the type of signal but also for the kind of event under study, given that their particularities differ depending on that, as displayed in Fig. 5.4.

former removes the waveform sections with no valuable information, whereas the latter rejects the whole individual SiPM data, considering this particular sensor has no actual signal at all. Both cuts allow a data reduction of an order of factor 100.

Finally, once the PMT's resampling and the SiPM's cleaning and selection are made, all the waveforms are matched, the `PMap` production is finished, and they are stored. Thus, `PMaps` are the final part of the waveform processing and starting point of the reconstruction methods.

5.1.3 Point-like events production

The production of point-like events is the condensation of the whole spatial information of an event into a single location in space (x, y, z) and a energy. It is especially helpful for very low-energy events (and alpha particles) since the energy deposit occurs in a tiny region in space. Nevertheless, they can be applied to perform a first view or rough estimations for all kinds of data. In addition to the position and energy, the method provides a set of convenient parameters to describe the peaks: their width (time duration above the threshold), height (maximum amplitude of the peak), time (time of the sample of the maximum amplitude), energy (integral of the PMT summed waveform under the peak), and charge (just for S2 peaks, the integral of the SiPM summed waveform).[2]

To extract the (x, y) coordinates, the SiPMs above a threshold have their signal integrated (thus, only the total charge per peak is considered), and both the positions and their standard deviations are computed via a barycenter algorithm. It consists, basically, of an average of the SiPMs position weighted by the charge each one had detected.

On the other hand, the z position is determined in two steps: first, the drift time is computed by the difference between the S2 and S1 time; second, the actual axial length can be calculated knowing the drift velocity.[3] The standard deviation of the z position is computed using a weighted average. Considering that the waveforms might have several S1s and S2s, the process of computing the z coordinate is run for every possible S1-S2 combination.[4]

---

[2] In general, throughout the present work, energy will be referred to the integrated measurement of the EP, whereas charge will be referred to the integrated signal in the TP, either of a specific peak or the whole event (summing all the peaks of the event).

[3] The quantification of the drift velocity can be performed by knowing the electric drift field and pressure. However, a more sensible and data-driven approach can be followed by determining the cathode position at the end of the z-distribution of the events (more detail in Chapter 6).

[4] This is not much of a problem since the event is characterized by a unique `event_number` that can be used to filter multiple-peaks events away.

Together with the peak parameters, the method also provides a set of other handle variables in order to characterize the event via the S2 features: `Nsipm` (number of SiPMs with signal above the threshold), the `event_number` (an integer identifying each event unambiguously), and the timestamp of the event.

The NEXT's chosen structure for the final data is the Data Summary Tape (DST), a typical format in the high-energy physics community. In this case, since they are meant for krypton-like events (point-like), they are known in the collaboration as `kdsts`.

5.1.4 Extended events production

Hits extraction

The aim of reconstructing the topology of the events relies profoundly on the reconstruction process. In contrast to the point-like procedure, the information from the sensors is now arranged into a collection of 3D objects called hits. A hit is a point in space with specific energy (and charge) deposit (see Fig 5.5).

After the possible rebinning of the S2 signals (typically to $2\,\mu$s), the first step consists of *slicing* the peaks. This means that the peak waveform is cut for each temporal (i.e., z) bin, and each slice is used to produce a set of (x, y) coordinates for that given time bin. The z is trivially computed by the difference between the times of the slice and the S1. Regarding the (x, y) reconstruction, it depends on the algorithm selected to perform the task. The ones the collaboration have been using more intensely are the one hit per slice (collapse all the (x, y) information per time bin into a single point using, for instance, the barycenter algorithm), one hit per SiPM (basically yields a point for every SiPM above a certain threshold, keeping the (x, y) position of the sensor as the location of each hit), and corona (an iterative algorithm that is able to find multiple energy deposits in a slice, given they are sufficiently separated, more detail in [263]). If there is more than one hit in a slice, the energy of the bin is divided for each one proportionally to their charges, whereas, if no hit is reconstructed, all energy is transferred to the nearest slice from the same S2 peak.

Following the scheme from the point-like data, the hits DSTs are known as `hdsts`.

Corrected hits

In the next stage, the energy of each hit is corrected to equalize the response across the detector (see Chapter 6), taking into account the geometric variations in the light response, the effect of the attachment along the electron cloud drift, the potential variation of the response that can change along the run time, and the minor residual corrections that might remain. In this step, the z coordinate is computed using the drift velocity provided[5] and the energy is converted from photoelectrons (pe) to electronvolts. This hit-by-hit correction leads to the production of the so-called corrected hits or `chits`.

Topology reconstruction

The final phase is the track reconstruction and the topology information extraction. The process in order to obtain tracks from hits involves some steps: grouping the hits belonging to all the possible tracks of the events, sorting the hits, and finding the extremes (the blobs).

The method of grouping relies on a connectivity criterium. First of all, the active volume is divided into fixed-size 3D pixels (voxels), where every voxel has a total energy equal to the sum of the hits falling inside and the given position in space. Then, an algorithm (known as Breadth First Search) separates the voxels not sharing a side or corner into separate sets (i.e., tracks in the event). In addition, the algorithm identifies each set's end-points. The extremes are defined as the pair voxels of each track with the greatest distance along the track between them, where the distance between any pair of voxels is the minimum is the shortest path along the track that connects them [117]. While the maximum size of the voxel is fixed, they can vary on an event-by-event basis according to the track spatial distribution, avoiding the possibility of having voxels with only one hit on the borders. An example of voxelization can be found in Fig. 5.5.

Regarding the blob position, instead of considering the center of the voxel, it is recomputed using the barycenter of the hits that fall inside that extreme voxel. Then, the blob is defined as the collection of hits that fall within a certain cartesian distance from the blob position previously calculated (thus, within a sphere of that radius centered on the reconstructed extreme position) restricted to those in voxels that are a radius-discance away along the track from the blob position (with some

---

[5] Up to this step, the z coordinate is taken directly as the time difference in μs, i.e., as if the drift velocity is 1 mm /μs

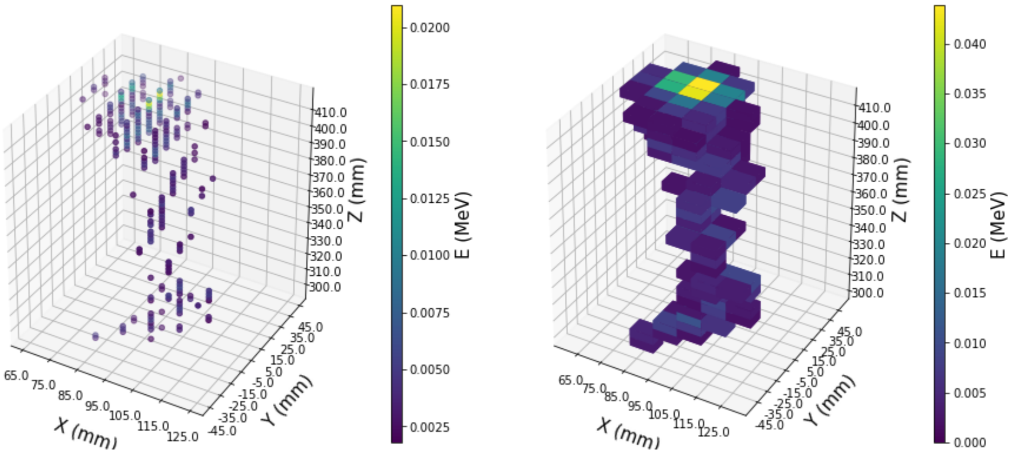

Figure 5.5.: Example of reconstructed hits and the later voxelization of a background MC event. Figure from [260].

tolerance), and its energy is the sum of all the hits included. Also, the blobs are denoted as `blob1` and `blob2` for the most and least energetic one, respectively.

Therefore, at this stage, not only the tracks are now satisfactorily reconstructed, but the principal information regarding their features is extracted: the number of tracks, hits, and voxels per event; the voxel size; the blobs positions and their energies; the mean position of the track and the maximum and minimum coordinate in each direction; and the total amount of energy shared by both blobs.[6] This final product is denoted as `tracks`.

Deconvolution

A more recent approach in the reconstruction applies the algorithm characterized in [227], known as Richardson-Lucy (RL), as an intermediate step in the chain. The method starts from hits and produces a new set of ones resulting from deconvolution, the so-called deconvoluted hits or `dhits`.

The essential inputs for the deconvolution are the Point Spread Functions (PSFs), which describe the system's effects on a point-like light source. They can be obtained directly from the ^{83m}Kr events. It takes the data from different z ranges and constructs PSFs combining the EL and the transversal diffusion distortions (in order to account for both effects at once).

---

[6] If the blob positions are closer than the blob radius, there are hits falling in both. Therefore, the overlapped energy takes into account the total energy shared by them.

The PSF enters the process that, for every z-slice separately (they are considered to be independent), tries to find iteratively the light source arrangement that matches the data better. Once the iteration is done, the energy is then assigned to the deconvoluted hits proportionally to their charge. Given the fineness of the procedure, the input hits have a lower cut than the ones used for the classical reconstruction. Therefore, two sets of hits are produced in the chain: the low threshold and the high threshold for deconvolution and classical analysis, respectively.

Finally, once the `dhits` are obtained, the step of the track reconstruction explained in the previous section is applied to them. The outcome is known as `dtracks`, to be distinguished from the ones without deconvolution.

5.2 Detector simulation

The simulation task is divided into three main distinctive pieces with their specific set of purposes: track simulation, electrons and light propagation, and detector simulation. There is also a pseudo reconstruction mode that allows fast emulation of the full simulation chain.

5.2.1 Event generation: NEXUS

NEXUS (NEXT Utility for Simulation) is a custom-made simulation tool, GEANT4-based [264], whose aim is to replicate the interaction of particles inside the chamber, considering the complete set of conditions occurring in the detector.

GEANT4 divides the process into four principal sections, a scheme that NEXUS inherits:

Detector geometry Defines the different volumes. Their dimensions, materials, placement, and characteristics are carefully detailed.

Physics list the collection of libraries comprising the physic phenomenology taken into consideration in the simulation.

Event generation The initial conditions of every event: number and type of particles, their positions (in any place of the implemented geometry), and their initial three-momenta.

User actions The series of operations defined by the user in order to retrieve data of interest throughout the simulation, as the trajectories and interactions of the particles of the events.

A user-defined macro fine gathers all the parameters involved in the simulation and the processes defined above.

The first stage of the process consists of the propagation of the primary particles and their effect in the detector: a set of initial particles is placed in a particular location of the detector geometry with a certain momentum. Their propagation and interactions are simulated following the set of physic models provided, and, once they get to the active volume (if they do), the energy deposits are stored as track hits and written to the output file.[7]

The final phase of the process computes the scintillation light emission (S1), and the secondary electrons drift. On the one hand, the individual scintillation photons propagation across the chamber are tracked (and the trajectory can be saved for additional analysis). The photons that reach the sensors (only PMTs for the S1 signal case) are incorporated in a time histogram representing the zero-suppressed detector waveform, with a configurable bin (i.e., sample rate). On the other hand, the secondary are drifted by the electric field and diffused along the path until they reach the EL region. There, the emission of the EL light takes place, and, as well as the previous scintillation process, each individual EL photon propagation is tracked. However, in this case, both the PMTs and SiPMs waveform are filled.

This last part of the simulation very time-consuming (up to hours for an event in the $\beta\beta$ region). Therefore, the NEXUS process can be asked to perform just the first steps concerning the particles propagation (known as *fast-mode* configuration) or all of the following light and electron drift (the so-called *full-mode* configuration).

For an exhaustive and meticulous review of the NEXUS simulation tool, see [265].

---

[7] For instance, a double beta decaying nucleus in the active volume can be a primary particle that, in its *propagation*, decays emitting two electrons; or a beta-decaying nucleus in a particular position in the surrounding material, stationery, that decays and produces a nuclear chain and several beta and gamma radiations that, subsequentially, undergo other processes and yield additional particles; or even a muon crossing the detector interacting with the gas and producing spallation neutrons, that can thermalize and cause additional processes.

5.2.2 Detector simulation: DETSIM

Since the track simulation is fairly rapid, but the light propagation exceeds the reasonable computation time, the chain has been divided into both processes, and the second one is treated from a new perspective. In addition, some of the computations performed, although correct, have been discovered to be unnecessary as they are accurately described using knowledge about the physical mechanisms. For instance, individually tracking and drifting all the electrons can be nicely substituted by an effective Gaussian diffusion. Also, the light emission only depends on the emission point since the materials and sensors are fixed; thus, the amount of light that reaches any point can be parametrized.

Therefore, a new and independent simulation stage is introduced to take the output of the fast-mode configuration of NEXUS and carry the posterior detector response, finally yielding the sensor waveforms: DETSIM (Detector Simulation). The different modules are based on the numerical models of the physical phenomena they are simulating:

- Ionization electrons: Starting from the NEXUS energy deposits (that are created for every mm traveled by the ionizing particle), they can be translated into the expected number of secondary electrons, N_i, by taking Eq. 3.3. Thus, the actual number of electrons can be obtained by sampling a Poisson distribution with $\lambda = N_i$, and their location is set to the very same as the original energy deposit placement.

- Electron drift to the EL region: The transport of electrons is affected by the longitudinal (z axis) and transverse (x-y plane) diffusions. Both of them have been experimentally determined for a broad range of chamber conditions (see [226]) and can be modeled as a gaussian spreading governed by the diffusion coefficients acting as the standard deviation. Hence, each electron (x, y) position and arrival time is obtained by sampling those gaussian distributions.

- Light emission and detection: There are two signals to simulate, the S1 and S2. Both of them can be characterized by the emission point by computing the probabilities in each sensor from any position, building a detection probability model for the detector. This estimate, multiplied by the gain (Eq. 3.11), yields the expected average number of photons in every detector, N_a. Then, the final number of photons measured by each sensor is extracted from a Poisson sampling with $\lambda = N_a$.

The outcome from the simulation procedure is, as well as from the NEXUS full-mode, is a set of zero-suppressed time histograms (thus, waveforms) for every sensor.

For a more detailed review, particularly concerning the light parametrization, check [263].

5.2.3 Electronics effects replication

The concluding step for the MC data processing is reproducing the effects of the acquisition electronics.

On the one hand, the PMTs waveforms have the most severe transformation. First, a baseline number of ADC is added based on the actual waveforms (extracted in calibration runs). In addition, the noise is computed. It is known to be gaussian; therefore, a Gaussian is sampled and summed to the baseline for each entry in the waveform. Later, the measured gain for each sensor is applied to convert the signal from photoelectrons (the output of the simulation) to ADC (the actual unit from the sensor). However, that conversion implies the inclusion of the charge fluctuations. The avalanche method inside PMTs is also gaussian; thus, the final convention is performed by sampling a gaussian distribution centered in the *true*[8] number of electrons and a variance scaled from the standard deviation in 1-photoelectron signals, extracted in calibration. Once translated into ADC, the last step is emulating the effects of the Front End electronics, that is, reversing the BLR procedure explained in Sec. 5.1.2.

On the other hand, the SiPMs are more straightforward to prepare. Analogously, the initial step is adding the ADC baseline extracted from calibration runs. Then, the noise is added. In this case, the noise is not gaussian but follows the so-called dark noise PDFs, which account for the spurious counts coming from the eventual electron-hole production in the semiconductor sensor at a finite temperature. Finally, the PDFs are sampled in order to add the noise, and the *true* waveform is translated to ADC following the same procedure previously sketched.

From now on, MC data mimics the actual data completely. Therefore, the further reconstruction chain explained in Sec. 5.1 is applied in complete analogy to detector data.

---

[8] Hereafter, when referring to *true* data, it means the actual MC value before a given transformation.

5.2.4 Pseudoreconstruction: FANAL

Bearing in mind the time-consuming task the simulation and reconstruction implies, it occasionally is impractical and limits the capabilities of some studies. This encouraged the development of the fast-analysis (FANAL) module that performs a pseudo-reconstruction mimicking the complete processing chain.

FANAL starts with the NEXUS fast-configuration output and does no signal nor detector simulation. Instead, the known effects such as diffusion, attachment, and energy resolution are emulated over the *true* information. The typical flow of the module starts with the energy smearing: given the desired resolution, the energy fluctuates following a gaussian with a sigma equal to the resolution. Later, the energy depositions are voxelized, analogously to the procedure mentioned in Sec. 5.1.4. The voxel size is chosen to match the expected diffusion, so the step considers this spreading naturally. Last, the same reconstruction algorithm (the BFS) performs the track information extraction. The final pseudo-reconstructed tracks can be subject to the same cuts applied to data but those related to S1 or S2 features.

A full description and characterization of the procedure can be found in [265, 266].

5.3 Software framework

The complexity of the set of tasks required in simulation and reconstruction endorses the creation of a framework that unifies and simplifies the collective efforts. Traditionally, the collaboration had a software assemblage in C++ [267] and ROOT-based [268] used, for instance, in the analysis of NEXT-DEMO data. However, prior to the experience of NEW, it became patent that the former scheme implied a significant imbalance between the input essay and the outcome. As a result, implementing new code was slow; revisiting it was hard, and there was no test suit ensuring the permanent well-behavior of the code. In addition, the *bus factor* was one or below.[9]

For this reason, a brand new software framework has been developed within the collaboration, based on PYTHON3 [270], and most of the processing chain migrated to the new paradigm. Nevertheless, not all the code is adapted to the new paradigm

---

[9] Bus factor [269] is a helpful concept accounting for the number of people with some degree of expertise and information about a particular piece of code, algorithm, procedure, etc. It is informally defined as the number of people who have to get hit by a bus in order to freeze the project. In general, the desired bus number on a project would be as high as possible.

since either it is planned to but not ready yet or is not worth it in terms of efficiency and performance.

This section will briefly describe the software state performing the processing and simulation chain previously described in the present chapter and summarized in Fig. 5.6.

5.3.1 ART

ART [271] is an event-processing framework for experimental particle physics developed in Fermilab as a shared suite for the experiments hosted by the lab. The environment is written in C++ and asks for the code to be also in that language. Additionaly, it naturally incorporates the ROOT and GEANT4 libraries.

Initially, the totality of the NEXT software was integrated into the ART framework. However, with the later migration, just a couple of modules remained, such as the decoder (DECO, see 5.1.1), and DETSIM. Eventually, as it is now, only the later component stills depend on the framework (red diamond in Fig. 5.6) since the other was built into independent libraries. Notwithstanding, there is an active campaign among the collaboration to dispense with this remaining dependency and incorporate it inside the current state-of-the-art framework.

5.3.2 Standalone libraries

NEXUS and GEANT4 are major pieces of code remaining in C++. On the one hand, NEXUS depends strongly on GEANT4, making it hard and meaningless to translate. On the other hand, DECO works online with data taking. Therefore, it requires a high and robust performance, making C++ the right choice. As mentioned in the previous section, DECO is a former ART-based module. However, with the paradigm migration, it became an independent library and it is planned to remain as such.

Additionally, FANAL also works as an independent library, primarily written in C++ and PYTHON.

These independent libraries are denoted in Fig. 5.6 as white (FANAL and DECO) and black (NEXUS) diamonds.

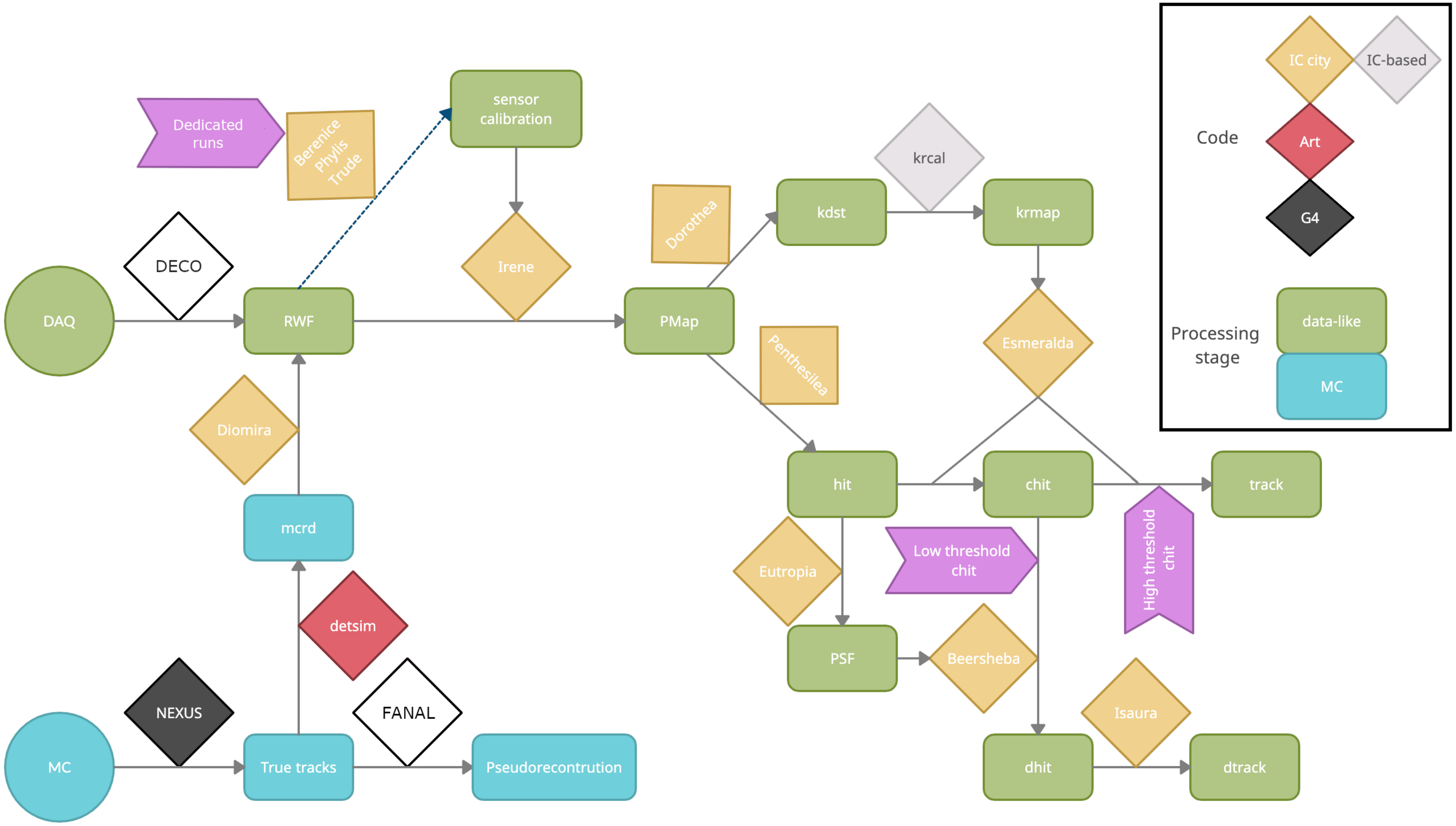

Figure 5.6.: Chart summarizing the whole reconstruction and simulation chain. The rounded rectangles represent the different processing stages, and the diamonds represent the piece of code performing the transformation. More detail across the chapter.

5.3.3 Invisible Cities

The core of the processing software is the so-called Invisible Cities[10] (IC) framework. It is almost entirely written in PYTHON3 and built around the ANACONDA suite. Besides, it does not interact with ROOT (often criticized for its lack of compatibility and memory management) but relies on solutions available in standard libraries.

The major advantages of the migration are that the language now is more user-friendly, easy-to-learn, widely spread, and with an extensive community behind it. Additionally, in contrast with the previous framework, IC comprises an extensive testing suite that ensures the behavior of the entire chain and prevents any significant modification that may affect the outcome. Finally, the code is well documented both by the implementation comments and the test suite.

IC code is open under the git paradigm here [272]. The git features facilitate testing any piece of code prior to the merge in the master branch and ensure the external revision (by a person not involved in that code contribution). The latter helps twofold. On the one hand, it improves the readability and performance of the code, the good practices, and an external point of view inside the enhancement. On the other hand, it is a constructive approach to increase the bus factor familiarizing another person in the code's inner aspects.

Fig.5.6 includes a summary of the entire IC-related reconstruction chain. The yellow diamonds represent so-called *cities*, the essential components of the software. There are, currently, eight cities in charge of processing data (as decribed in Sec. 5.1) and three devoted to the extraction of the calibration parameters. DIOMIRA transforms the MC waveforms into data-like `RWF`s. IRENE takes the `RWF`s and extracts the `PMap`s from them. Later, the process bifurcates in DOROTHEA, producing the `kDST`s (see 5.1.3), and PENTHESILEA, producing the `hits` (see 5.1.4). Now, another division happens. ESMERALDA, on the one hand, takes the `hits` and produces both the `chits` and tracks.[11] On the other hand, EUTROPIA uses the `hits` to create the PSFs. BEERSHEBA then, applying the PSFs, deconvolutes the `chits`[12] to get `dhits`. A final step by ISAURA performs a topologic reconstruction to create `dtracks`. Besides, the calibration cities act on devoted runs to produce the essential parameters to both reconstruct and simulate: PHYLLIS for the PMT calibration, BERENICE for the SiPM dark noise, and TRUDE for the calibration data of the SiPMs.

---

[10] The name stands for the Italo Calvino book Invisible Cities. The nomenclature for the inner components also refers to the book.

[11] The track reconstruction performed in ESMERALDA is based on the chits after a relatively high charge threshold is applied.

[12] On the contrary, for the deconvolution step, a lower threshold in the charge of the `hits` is applied.

A careful and exhaustive review of the IC framework may be found in [263].

6

Low energy calibration and continuous monitoring

The interesting events can occur at any place in the active volume, as well as the background ones. Ideally, the response must be independent of the emission point since the interesting event features, such as its energy and blob characteristics, do not have any spatial or temporal variability. However, in the process of data collection, several phenomena may affect the expected behavior of the measured signal and make fundamental the development of a correction strategy to recover the homogeneity and time stability of the chamber. In order to address the issue, a scheme with three stages has been implemented.

The first one is the sensor calibration. The different devices in the detector change their response because of the slightly varying conditions, apparatus aging, and eventual damages. Thus, as sketched in Sec. 4.2, dedicated runs are frequently scheduled in order to keep track and equalize the sensor signals. More details can be found in [232].

The second step is correcting the effects that arise when the light and secondary electrons propagate through the chamber. The EL light emission occurs in a very short region in the drift direction and, thus, only depends on the transverse positions (x, y). That transfer position varies the amount of light that the PMTs (placed right on the other extreme of the detector, check Fig. 3.1) see directly and reflected, involving the optical properties of the materials in the chamber (mainly PTFE). On the other hand, the secondary electrons drifting causes them to spread through all directions, but this is not a significant problem since it does not imply any charge loss. Additionally, the transverse diffusion is well under the fiducial volume selection implying no border effects either. Notwithstanding, the presence of electronegative impurities that capture the electrons is a troublesome problem. Even though there is an active and permanent campaign to reduce them, such as continuous gas cleaning, they can not be altogether removed, mainly due to the continual outgassing, but controlled under a safe concentration level. Consequently, electrons are lost during drift, and the effect depends strongly on the axial direction (the more gas traversed, the more electrons captured). Actually, the effect is known to be accurately modeled by an exponential behavior.

Hence, the chamber's response must be determined in order to be corrected for both effects, ideally by having a precise map of the signal in the whole volume. Here enters the perfect solution: $^{83m}\mathrm{Kr}$ decay. $^{83m}\mathrm{Kr}$ is a metastable state that lives for 4 h and decays via two consecutive internal conversions (indistinguishable), yielding a total of 41.5 keV in an electron point-like deposition. In addition, since Kr is gas, it can be dissolved in the active volume resulting in a complete coverage.

Consequently, obtaining a reasonable amount of Kr data, it is possible to parametrize the geometric (x, y) and lifetime (z) distortions in the energy measurement and correct them, as explained in detail in Sec. 6.1.3.

Lastly, when dealing with long signals (as high energy electron tracks), there may be some residual effects arising that ought to be addressed and characterized via a high energy calibration program. For instance, in [154], some slight dependency with the track length along the z direction was reported. It is adequately identified and accordingly corrected.

In the present section, the procedure and results of the low energy calibration will be presented. In addition, it will also cover the implementation of the continuous monitoring of the chamber status using $^{83m}\mathrm{Kr}$.

6.1 $^{83m}\mathrm{Kr}$ as a source for the low energy calibration

6.1.1 Events production

The isomeric state of the $^{83m}\mathrm{Kr}$ nucleus occurs naturally as an intermediate state in the $^{83}\mathrm{Rb}$ electron capture (ε) decay in approximately 80 % of the events. After a half-life of 1.83 h, the isomer decays via an internal conversion, radiating two consecutive electrons of 32.1 keV and 9.4 keV with a time difference of $\sim$0.1 μs [273]. However, due to the tiny time distance, they cannot be resolved and are detected as a single event deposition. The resulting ground state is stable. A depiction of the $^{83}\mathrm{Rb}$ decay and all the possibilities are displayed in Fig. 6.1, with a detailed look into the isomeric state decay.

In order to introduce the isomer in the gas system, a dedicated section stores small zeolite balls. The resulting Kr nuclei emanate from the zeolite and enter the gas flow.

Concerning the acquisition, the rate must be controlled since the DAQ is not designed for enormous rates. Additionally, although the possibility of the double

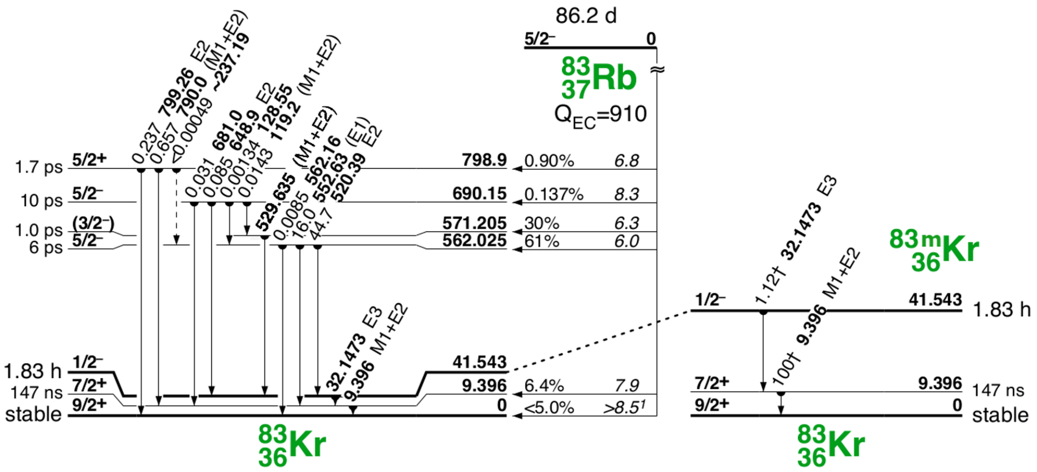

Figure 6.1.: $^{83}\mathrm{Rb}$ to $^{83}\mathrm{Kr}$ decay scheme (left) and zoom into the isomer decay (right). Each energy level is labeled with its half-life, spin-parity, and energy. Gamma decays are noted with their intensity, energy, and electromagnetic multipolarity. The different electron captures transitions present their probability and $\log ft$ values. Figure adapted from [274].

trigger is in hand for the calibration, a large rate may cause inefficiencies in keeping the events of interest. Therefore, the limit for adequate DAQ performance was determined to be 10 Hz. In contrast, the rate of events inside the chamber is $\sim$100 Hz.

The event measurement and posterior processing of the events is well described in the previous chapter. Note that, given they are point-like sources, the outcome is the so-called `kdst` (see Sec. 5.1.3 and Fig. 5.6).

Finally, it is important to remark two excellent features of the Kr. First, the infusion of the gas (and potential impurities) inside the chamber has been seen not to represent any troublesome source of background, especially electrons in the energy region of interest of $^{136}\mathrm{Xe}$ double beta decay processes. On the other hand, despite the fact that the Kr is dissolved in the Xe, it is easily removable via the cryorecovery procedure, given the significant difference in condensation and freezing temperatures between both gases.

6.1.2 Correction method

Following the previous discussion, the present method aims to rectify both the geometrical and attachment repercussions in the energy determination of the events.

For the case of the attachment, it is reasonable to assume that the electron cloud would encounter a uniform distribution of impurities in its propagation, and the number of trapped is proportional to the number of electrons in the cloud. Therefore, the charge loss can be parameterized as:

$$\frac{dq}{dt} = -\lambda q, \tag{6.1}$$

where q is the total charge of the cloud, t is the drift time,[1] and λ is the proportionality constant. Solving the differential equation, one gets the expected exponential behavior:

$$q = q_0 e^{-t/\tau}, \tag{6.2}$$

where q_0 is the initial charge at $t = 0$ and $\tau = \lambda^{-1}$ is the so-called lifetime.

However, the chamber is not entirely homogeneous due to deficiencies in the gas flow, causing the entering clean gas does not diffuse equally or virtual leaks. Therefore the lifetime can have local domains where it is constant but, in general, present a spatial dependence. Moreover, it is known that the impact over the z axis is not dramatic and can be taken as an effective value for the whole chamber along that direction, as depicted in Fig. 6.2. It shows the average residuals as a function of the drift time. The average is obtained after binning the (x, y) plane and fitting the events falling in each bin to the Eq. 6.2, then the individual residual[2] for each bin is computed, and finally, all of them are averaged.

Regarding the geometric corrections, they are meant to equalize the response across the EL, caused by EL imperfections, different solid angles for light collection, light reflection imperfections, border effects, and other minor phenomena. Since the S2 light is generated at a fixed z position, the only dependencies expected are in (x, y). Therefore, the final correction function is:

$$E_{\mathrm{C}} = \omega(x, y) e^{-t/\tau(x,y)} E_r, \tag{6.3}$$

where E_{C} stands for the corrected energy, E_r for the raw one, ω accounts for the geometric corrections, and τ reflects the potential (x, y) variation.

---

[1] Note that here, and hereafter, t and z are used indistinctly (remember, they only differ by the drift velocity). This, although it is kind of sloppy, does not cause any inconsistency. However, when extracting the lifetime factor, the suitable variable to do so is t, and the reason is that the conversion from time to axial length is performed once the correction map is computed and the drift velocity is estimated, much after the lifetime determination.

[2] The residuals are defined as

$$r_z = \frac{E - f(t)}{\sigma},$$

where E are the raw data points, $f(t)$ is the fitting function (Eq.6.2), and σ is the standard deviation.

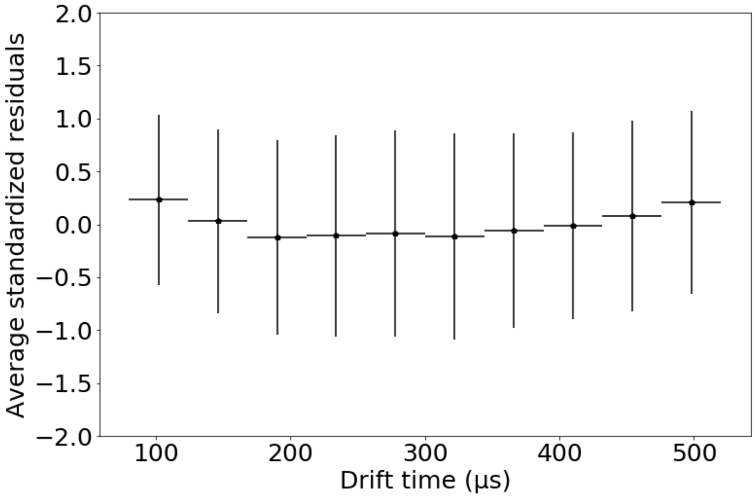

Figure 6.2.: Average electron lifetime residuals (R_z) as a function of the drift time. Given the small deviation from 0, it is safe to take an effective lifetime along the axial direction. Figure from [222].

Finally, by comparing Eqs. 6.2 and 6.3, it is patent that both correction factors (τ and ω) can be determined at once, performing an exponential fit.

In addition, another possible source of perturbation of the energy measurements is the variation of the overall scale within a particular run-taking period (the variations from run to run are not a problem since they can be easily corrected by a common normalization), as depicted in Fig. 6.3. Even though those variations happen all the time (the energy yield tends to increase over time, see Fig. 6.3), they are more dramatic just after a spark inside the chamber. In order to correct this difficulty, the energy yield evolution along the data taking is monitored and recorded (see Sec. 6.1.3) and can be later equalized.

6.1.3 Kr maps computation

Ideally, examining Eq. 6.3, one would hope to find a complete description of τ and ω. Unfortunately, an analytic computation is not feasible due to the complexity of the light propagation inside the chamber and the lack of knowledge of the gas flow inside the chamber. Those reasons, added to the imperfections inside the chamber and finite computing power, also prevents the possibility of an MC-driven calculation. Consequently, they have to be extracted via data analysis.

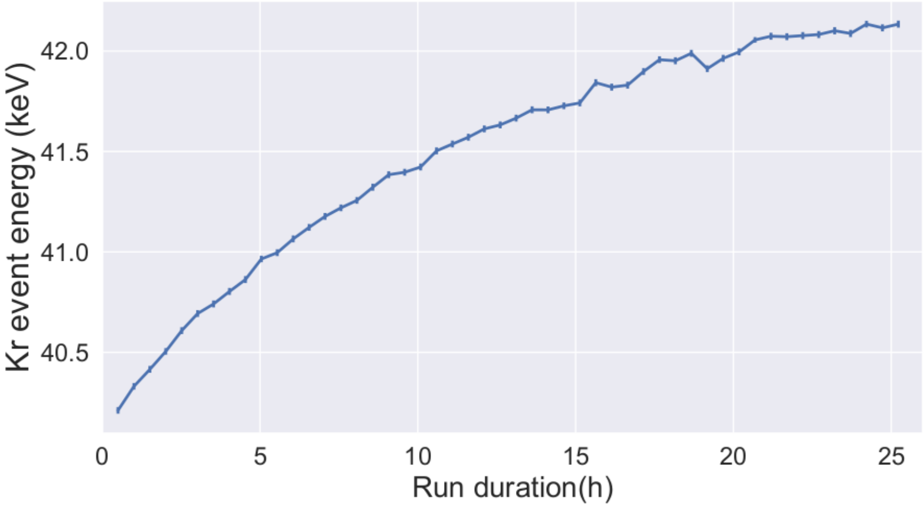

Figure 6.3.: Light yield evolution within a individual run duration. In order to stress the possible variation, a run with a significant change has been selected (a few hours after a spark). In general, they are stable and usually compatible with a flat line.

Moreover, the determination of the correction factors with arbitrary precision is not achievable (mainly limited by the chamber conditions and the amount and quality of the recorded data). Hence, for practical reasons, the transverse plane has to be binned (generally using square-shaped ones), and then, the events falling in each bin are fitted to extract both factors. A couple of examples of the fit are depicted in Fig 6.4, also showing the different lifetimes obtained in two separated regions of the plane. The collection of all the binned parameters is designated as a *correction map*. There are two kinds of maps, the so-called energy maps, the one gathering the energy at the origin (corresponding to the q_0 in Eq. 6.2), and the lifetime maps, collecting the different τ across the plane.

The procedure to create such maps has been refined and upgraded since the first attempts, described in [222], but the overall idea is identical. The code is framed as an independent package, called KrCalib, depending on the IC framework tools (see Fig. 5.6), and it is of public access in here [275]. Fig. 6.5 summarizes the map production chain that goes as follows:

Data selection

To start with, the data selection is described, which aims to obtain a mostly pure sample of $^{83m}\mathrm{Kr}$ events.

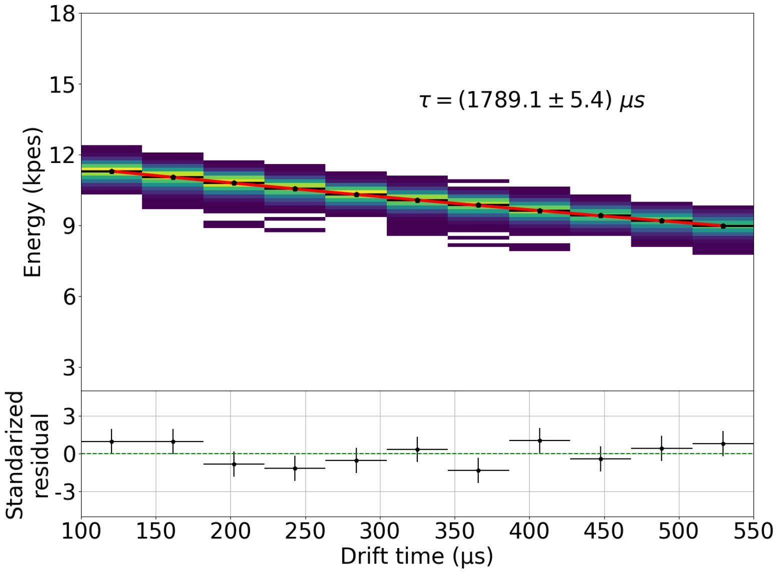

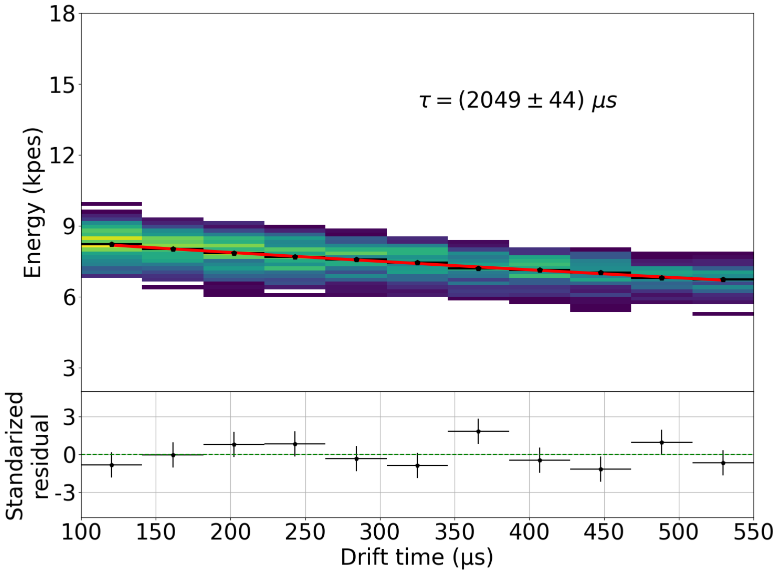

Figure 6.4.: Exponential fits to the energy of $^{83m}\mathrm{Kr}$ events as a function of the drift time in two regions of the tranverse plane. Both images show the distribution of the energy in a 2D histogram (color indicates the number of events), the energy average value for each drift time bin (black dots), the best fit curve (red line), and the residuals for the fit (inferior panel). The top figure represents the events falling in the bin defined by $x \in [0, 50]$ mm and $y \in [0, 50]$ mm, where the lifetime result is $\tau = (1789.1 \pm 5.4)\,\mu\mathrm{s}$ with a $\chi^2/\mathrm{ndof} = 0.9$. On the other hand, the bottom one represents the region $x \in [120, 150]$ mm and $y \in [120, 150]$ mm, where the lifetime result is $\tau = (2049 \pm 44)\,\mu\mathrm{s}$ with a $\chi^2/\mathrm{ndof} = 1$. It is also patent the different energies at the origin, being much greater in the central bin than in the more exterior one. Figure from [222]

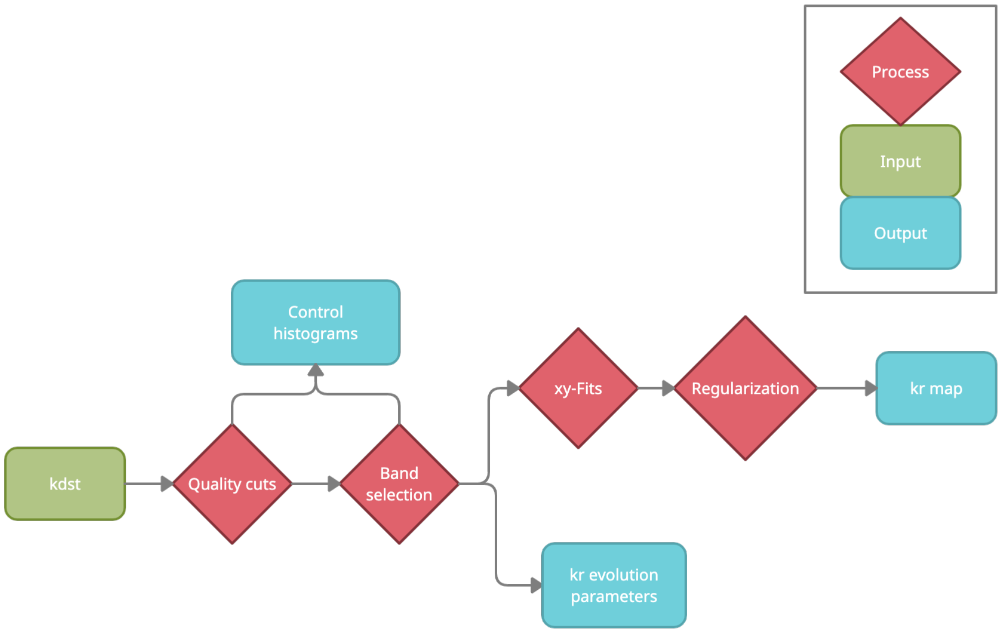

Figure 6.5.: Chart summarizing the map production chain. The rounded rectangles represent the input and output, and the diamonds represent the transformations performed to data. More detail in the text.

First, a soft set of cuts ensuring the events make sense (for instance, they are required to be inside the active volume) is applied. Then, a quick check concerning the rate over the run and the event distribution in the z direction takes place. This step yields a warning if any unusual value.

Second, a collection of cuts is performed to the input kdst to remove incorrectly reconstructed events:

- Only one S1.
- Only one S2.
- Energy band selection. To ensure a more pure Kr population, a band following the axial behavior is performed. First, the geometry factors are roughly corrected using a bootstrap map, and the whole chamber data is employed for a general lifetime determination.[3] Then, taking a user-defined tolerance, the band selects the candidate events, as depicted in Fig. 6.6.

---

[3] The band selection varies from run to run since, although the bootstrap map is the same, there is no assumption regarding the q_0 and τ. Both parameters are extracted only from the data.

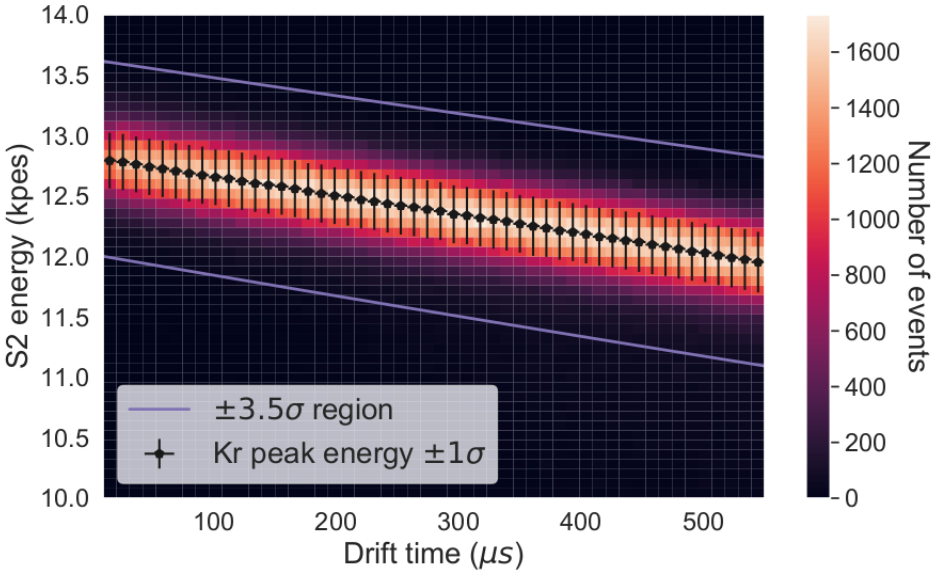

Figure 6.6.: Band selection example. The plot shows a 2D histogram of the S2 energy (with the geometric correction applied) as a function of the drift time, where the color of each bin represents the number of events falling in that bin. On top of the histogram, the energy average for each drift time bin is represented by the black points, and the violet bands delimit the accepted area for the Kr events.

Finally, a new check is done to the rate and z distribution. In addition, the efficiencies of the cuts are also compared to nominal values. Again, if any unusual value appears, the code yields a warning alert. Both check stages produce control histograms to monitor the map creation and data quality. Fig. 6.7 shows the typical distributions along the z axis and on the xy plane after all the selections have been applied.

Map computation

In this stage, the processing forks in two branches, the first one creating and processing the correction maps.

The Kr events are grouped into xy bins. Then, for every bin, the z-distribution of the events is fitted in order to extract the lifetime and energy at the origin (see Eq. 6.2). The fits are considered valid if their χ^2 falls into a reasonable range (defined by the user). Those bins where the fit has failed have to be treated and filled with a meaningful value in the so-called regularization procedure. Several regularization methods are available, such as replacing the unsuccessful bins with the mean of all the others, a regional mean just considering the neighbors, and an interpolation

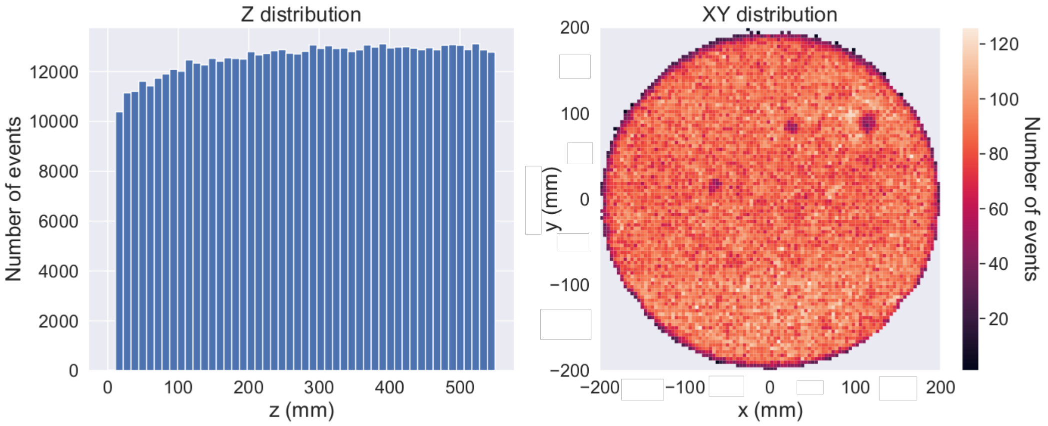

Figure 6.7.: Typical distributions along the z axis (left) and on the xy plane (right). Regarding the z distribution, although the distribution of the Kr is expected to be homogeneous across the chamber, the further from the EP the S1 emission point is, the broader it gets and the less solid angle for the PMTs. Hence, the efficiency of detecting Kr signals at low z is known to decrease. The transverse plane one shows good homogeneity except for the three dark spots that match the position of tree SiPMs known not to respond.

scheme to recover the values. Notwithstanding, it was found that the replacement by the whole plane mean works fine within the porpuses of the maps. Nevertheless, other more detailed studies may require more sophisticated algorithms. Now, the maps are in the final form, and an uncertainty map is provided for both energy and lifetime, accounting for the fit errors in each variable and bin.

An example of a energy and lifetime maps produced with the code can be found in Fig. 6.8.

Kr parameter evolution

On the other hand, the run is divided into several sub-run periods (generally 30 min long[4]). For each time bin, a set of parameters are extracted in order to track the evolution of the Kr in the chamber. Those parameters are (with its uncertainty): the mean of the energy at the origin and lifetime,[5] the S1 and S2 mean peak with, height, and integral, the integral of the charge in the SiPMs just for the S2 peak, the number of SiPMs with signal, the x and y RMS, the peak resolution, and the drift velocity. The peak resolution is extracted by performing a Gaussian fit of the events once all the corrections are applied. Then, the σ of the Gaussian is converted into

---

[4] In an everyday basis, runs are approximately all 24 h long.

[5] For each time bin, a map is computed (without the regularization).

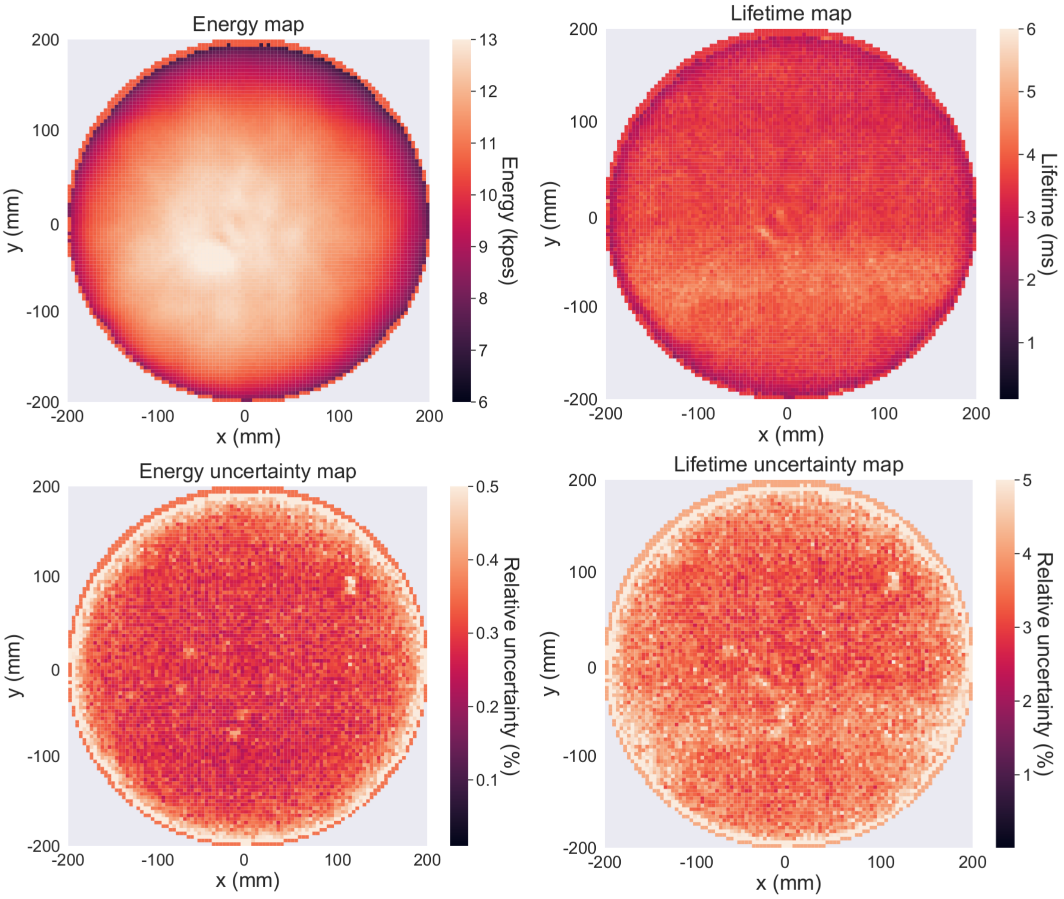

Figure 6.8.: Example of an energy (top left), lifetime (top right), energy uncertainty (bottom left), and lifetime uncertainty (bottom right) maps. The energy map shows a smooth behavior throughout the entire plane. Notwithstanding, the map presents a slight displacement towards the bottom left part of the plane. This dislocation has been consistent since the beginning of the Kr analysis period and may be due to a tiny deviation of the quartz plane, causing the EL planes to be not entirely parallel, so the electric field is not constant across the plane presenting the gradient displayed in the figure. With respect to the lifetime map, it also exhibits a uniform response apart from the bottom horizontal band. The high lifetime band is created, most certainly, because of the flow behavior of the gas inside the chamber. In fact, it is known that this pattern varies with time and has been correlated to changes in the way the gas enters the detector (more on that in Sec. 6.2.3). Concerning the uncertainties, the energy ones are well under 0.5 % while the lifetime ones are a bit higher, but under 5 %. For all maps, the outermost ring of bins is noticeably different. Those bins are where the fit failed cause of a lack of events (note that those coincide with empty spots on Fig. 6.7), and the regularization process fills the content with the average value for each map.

%FWHM, the standard resolution unit for the collaboration (and most of the field). The conversion between the FWHM and the standard deviation, σ, is

$$\text{FWHM} = 2.355\sigma. \tag{6.4}$$

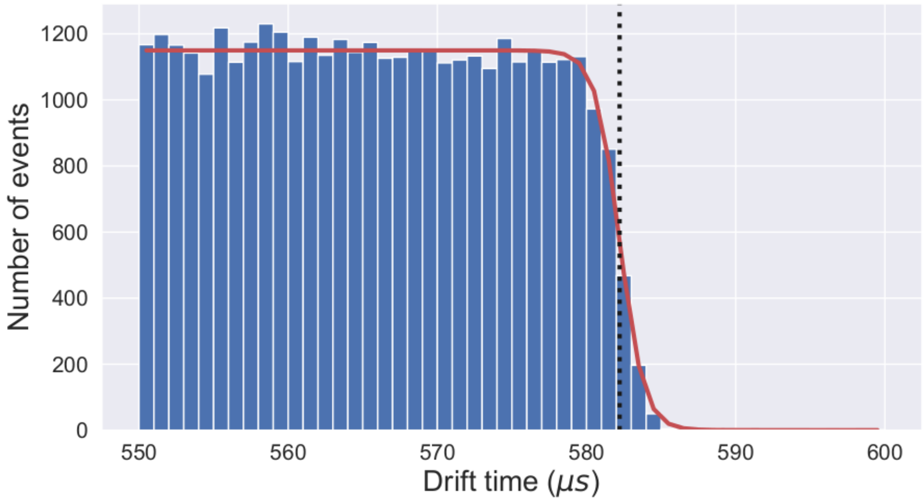

Figure 6.9.: Plot displaying the cathode time of arrival. The blue histogram represents the drift time distribution of the events in the chamber, the red line shows the best fit value for the sigmoid function in Eq. 6.5, and the black dotted line accounts for the computed t_{cath} from the fit results.

Finally, the drift velocity is estimated by finding the end of the z distribution (i.e., the actual chamber limit, the cathode). In order to determine the chamber boundary, the z distribution is fitted to a logistic function

$$f(t) = \frac{\alpha}{1 + e^{-\beta(t - t_{\text{cath}})}} + C, \tag{6.5}$$

where the only relevant parameter is t_{cath}, that represents the midpoint of the function (accounting for the time it took to the electrons in the cathode to arrive the EL region), α is the máximum of the function, β is the *steepness*, and C is an overall constant. Since the cathode position is known (and fixed), the drift velocity can be easily computed now. Fig. 6.9 displays an example of the drift velocity determination fit.

An example reporting the impact of the correction procedure is displayed in Fig. 6.10. when applied to Kr data and in Fig. 6.11., which reports the effect on high-energy electron events.

6.2 Chamber monitoring

At this point, it is manifest that $^{83m}\mathrm{Kr}$ energy depositions are an excellent tool for detector calibration. In addition, it also becomes clear that, beyond calibration, Kr

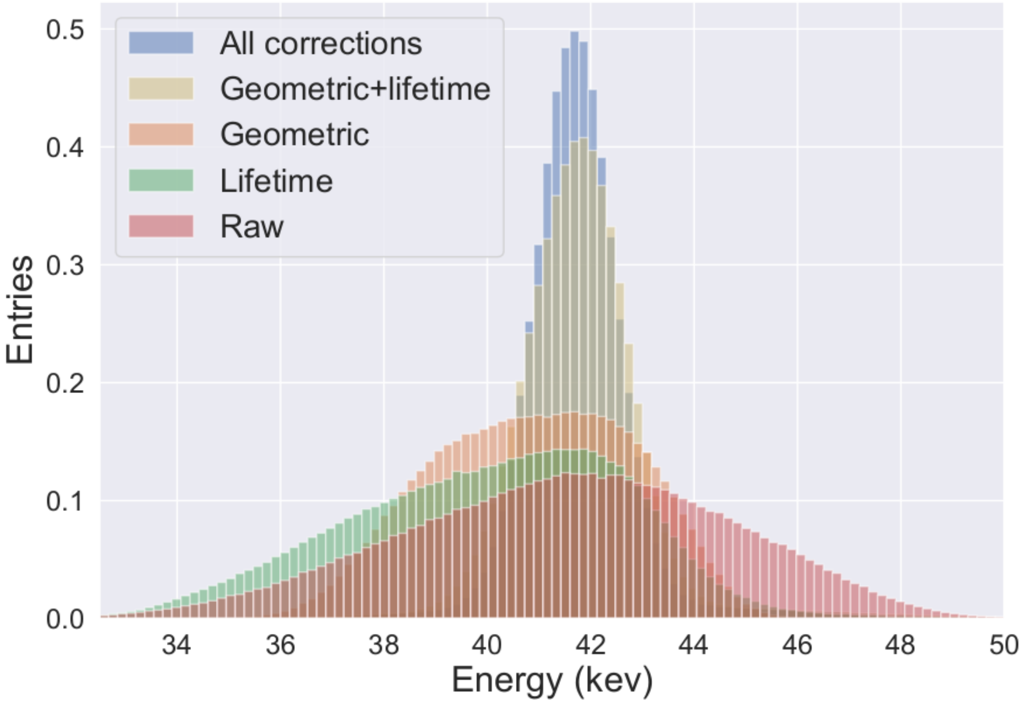

Figure 6.10.: Example of the impact of the correction procedure to $^{83m}\mathrm{Kr}$ data. The histograms are unit-area normalized, and each one represents a different set of corrections applied. The red line shows the raw data;[6] the green only removing lifetime distortion; the orange only taking into account the geometrical variations; the mustard shows both geometrical and lifetime corrections employed; and, finally, the blue curve presents the whole set of corrections extracted from the maps, i.e., lifetime, geometric, and energy yield variation within the run period. For the purpose of accentuating the influence of the time variation equalization, a run with a more prominent contrast has been selected (the one presented in Fig. 6.3). The resolution achieved for the whole set is $(4.571 \pm 0.019)\,\%$ FWHM at 41.5 keV

is a direct probe of the status of the interior of the detector in real-time, providing information about the stability of the chamber and valuable data in order to equalize the time variations happening during the run periods. Therefore, the Kr-dedicated paradigm the collaboration followed during Run II has been rethought. Making use of the double trigger configuration possibilities (see Sec. 4.1.7), it was decided to turn into a continous Kr event recording for Run IV and the subsequent ones.

Furthermore, the possibility of continually acquiring Kr data opens the door to use it as an additional tool for the constant monitoring of the quality of the data-taking and an excellent smoking gun finding issues in the detector.

---

[6] Here, and hereafter, *raw data* will refer to the energy measurement after the sensor calibration but before the application of the maps.

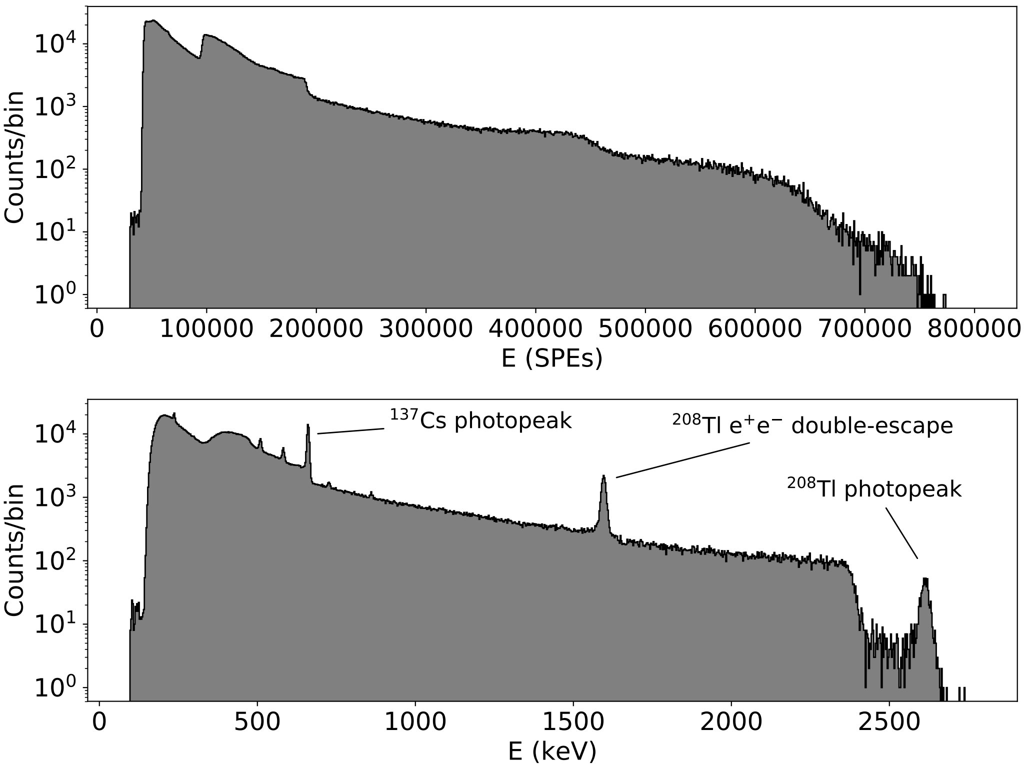

Figure 6.11.: Example of the impact of the correction procedure on high-energy electron tracks from a calibration run. The top plot displays the raw energy measurement, while the bottom one shows the spectrum after the whole set of corrections. In addition to the corrections, the peaks indicated in the image incorporate another correction step accounting for the axial effect present in long tracks [154], although it just narrows them, it does not change the spectrum any further, and only affect those peaks. The calibration campaign includes two isotopes: ^{232}Th and ^{137}Cs. Besides the signaled peaks at 662 keV [276] (^{137}Cs photopeal) and at 1593 keV and 2614 keV [277](^{208}Tl double escape and photopeak, respectively), the spectrum also presents lines at 236 keV (from ^{212}Pb decay), 511 keV (from e^+e^- annihilation, with contribution from ^{208}Tl decay), 583 keV (from ^{208}Tl decay), 727 keV (from ^{212}Bi decay)), and 860 keV (from ^{208}Tl) [277, 278]. The bottom figure has been extracted from [154]

6.2.1 Map evolution

The ability to recollect Kr events allows the long-term characterization of the detector and the quality of the data recorded. On the one hand, it has shown remarkable stability in the chamber conditions, as well as the precise impact the small changes in the configuration have. On the other hand, the quality of the data taking allows discarding those runs, or fractions, that do not match the minimum standard set of conditions for the posterior analysis, especially concerning the low background and double beta campaigns.

In the first place, the foremost concern regards the stability of the maps and their evolution in time.

On the one hand, the energy map has been immutable during the different run periods. In fact, besides being visually identical (see Appendix A.1), they are also statistically alike. Fig. 6.12 shows the former point by comparing all the maps produced since Run IVc among the ones of the same sub-run and also comparing all the different periods among them. The comparison is performed by computing the standard deviation of the distribution of the ratio (bin per bin) of both maps. It is patent that, besides the double peak structures, the whole data set standard deviation is well under 0.01, which has to be compared with the typical statistical uncertainty arising from the map production (of the level of 0.1–1 %, see Fig. 6.8).[7] Hence, the variation from one map to another is compatible with the expected statistical fluctuations of their computation.

The stability of the energy map ensures that the bootstrap method adopted for the map computation (Sec. 6.1.3) is valid. Moreover, it demonstrates that maps from other runs can be applied to correct an unrelated data set or even combine a set of energy maps in order to gain statistical significance.

On the other hand, unfortunately, the lifetime map situation is not that smooth. It has been seen that small changes in the chamber conditions may trigger dramatic variations in the features of the lifetime distribution across the chamber (see Appendix A.2). Notwithstanding, the lack of a detailed understanding of the gas flow patterns inside the detectors and the enormous computation resources that simulating it takes, the knowledge about how the external changes affect the actual behavior on the interior is limited, and the best approach is to monitor it closely, both for correction and study of the gas system performance.

Additionally, it also implies that, unlike the geometric corrections, lifetime ones are not interchangeable (at least not for runs taken in a considerable time interval). Hence, being able to improve the data selection of Kr candidates is mandatory in order to gain statistical significance (since the trigger rate is already around its maximum for the accurate efficiency of the high energy, trg2, data collection, see Sec. 4.1.7).

---

[7] Taking a look into the impact of the systematic uncertainties in the final resolution of the peak, it is determined to be around 1–10 % [222]. Thus, the variations on the maps between runs are also below the effects of the systematics.

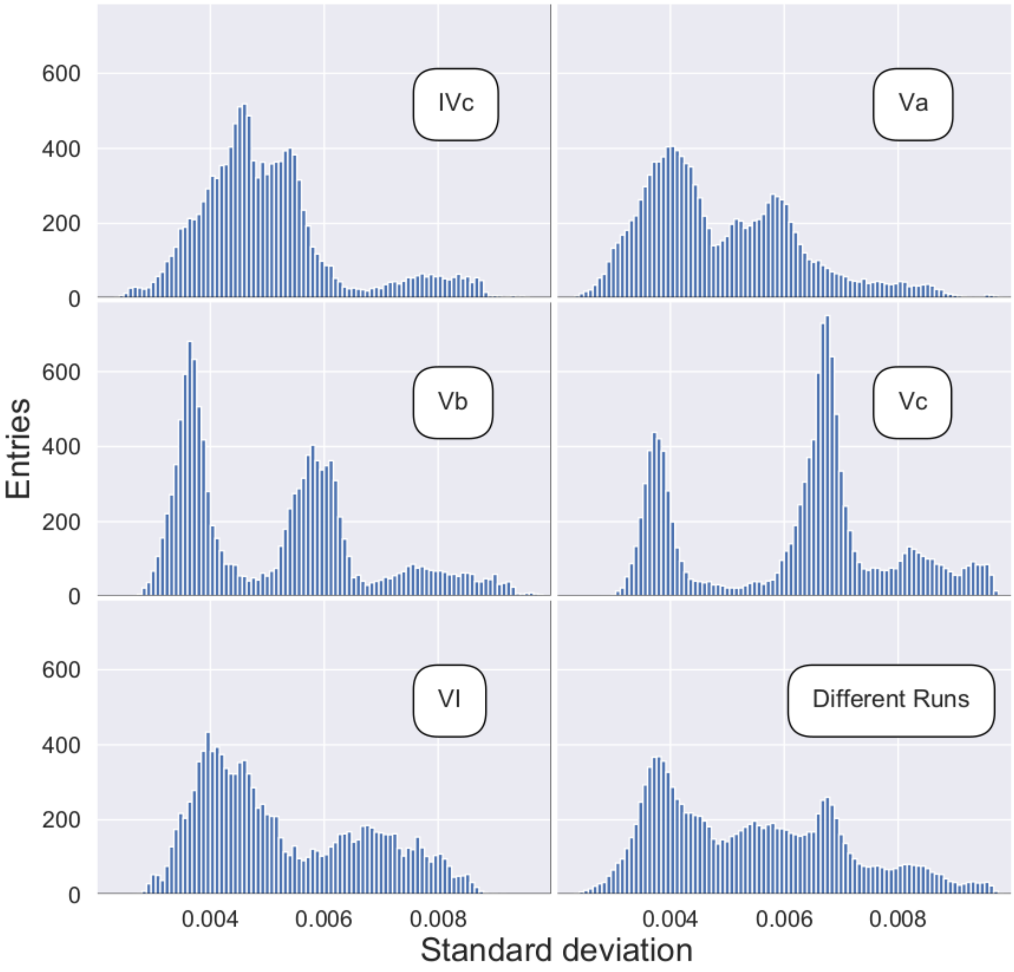

Figure 6.12.: Variance of the bin-per-bin ratio of the energy map among different runs. For each pair of runs, the ratio among them is computed for each bin. Then, the gaussian distribution is fitted to extract the variance. The results are separated depending on the runs computed: if they belong to the same run period, they enter each divided histogram, whereas if not, they enter the *Different Runs* category.

6.2.2 Individual run monitoring

One significant effort within the collaboration since the beginning of the NEXT-White operations was developing a monitoring scheme that would allow any person involved (not necessarily an expert on the detector) be able to run the independently ordinary operations and control the status of the machine safely and independently. The idea of using ^{83m}Kr events to perform part of that monitoring goes back to the period of dedicated runs during Run II, but it crystallized in its more mature and helpful form at the start of Run IV, in June 2018.

While the automatic processing transforms the raw data into the final high-level structures (see Fig. 5.6), a notebook takes the appearing `kdsts` and analyzes the file, generating a set of handy plots for the shifter.[8] Among them, those reporting the S1 patterns and the lifetime are the most useful.

S1 light collection is susceptible to any change in the trigger efficiency. Thus, the distribution of the number of S1s per event and its mean energy should stay constant, and, if not, the proper actions must be taken.

On the other hand, the lifetime value and its evolution along the run indicate the status of the gas inside the chamber and may indicate sudden pollution that must be considered, both given by virtual leaks or actual impurities entering the detector.

In addition to the real-time checking, once the run is finished (typically, the data acquisition is 24h long) and all the `kdsts` are produced, the map production (described in Sec. 6.1.3) starts. As mentioned before, the framework yields some monitoring plots regarding the quality of the process (see Fig. 6.13). Those plots include the selection efficiencies for the various cut, the rate before and after the selection, and the distribution of the events overall the chamber. They are uploaded with the rest of the control outputs for the shifter consideration.

6.2.3 Long-term monitoring

Along the lines of the map evolution and stability previously discussed, the collection of parameters extracted in the map production also provides a look into the long-term evolution of the chamber conditions and helps to make informed decisions about the desirable changes in the detector.

Among them, the most valuable piece of information comes from the average light yield and lifetime.[9]

The light yield is computed as the average for the energy map (note that the energy map content is the expected light yield from a $^{83m}\mathrm{Kr}$ event at $z = 0$, see Eq. 6.2). This parameter accounts for all the different effects on the chamber, especially for the EL field. In fact, the features standing out the most are the various spark incidents that implied restoration of the fields and the recovery time for the field

---

[8] This is not the only piece of monitoring that the shifter has available. In fact, both the `RWF` and `pmaps` outputs (see Fig. 5.6) are also analyzed and presented for the shifter supervision.

[9] Since the others are known to be stable (see 6.13) and nicely follow the changes in the detector pressure, temperature, or fields configuration. Therefore, they are more useful for spotting irregularities on a particular set of runs than studying the chamber evolution.

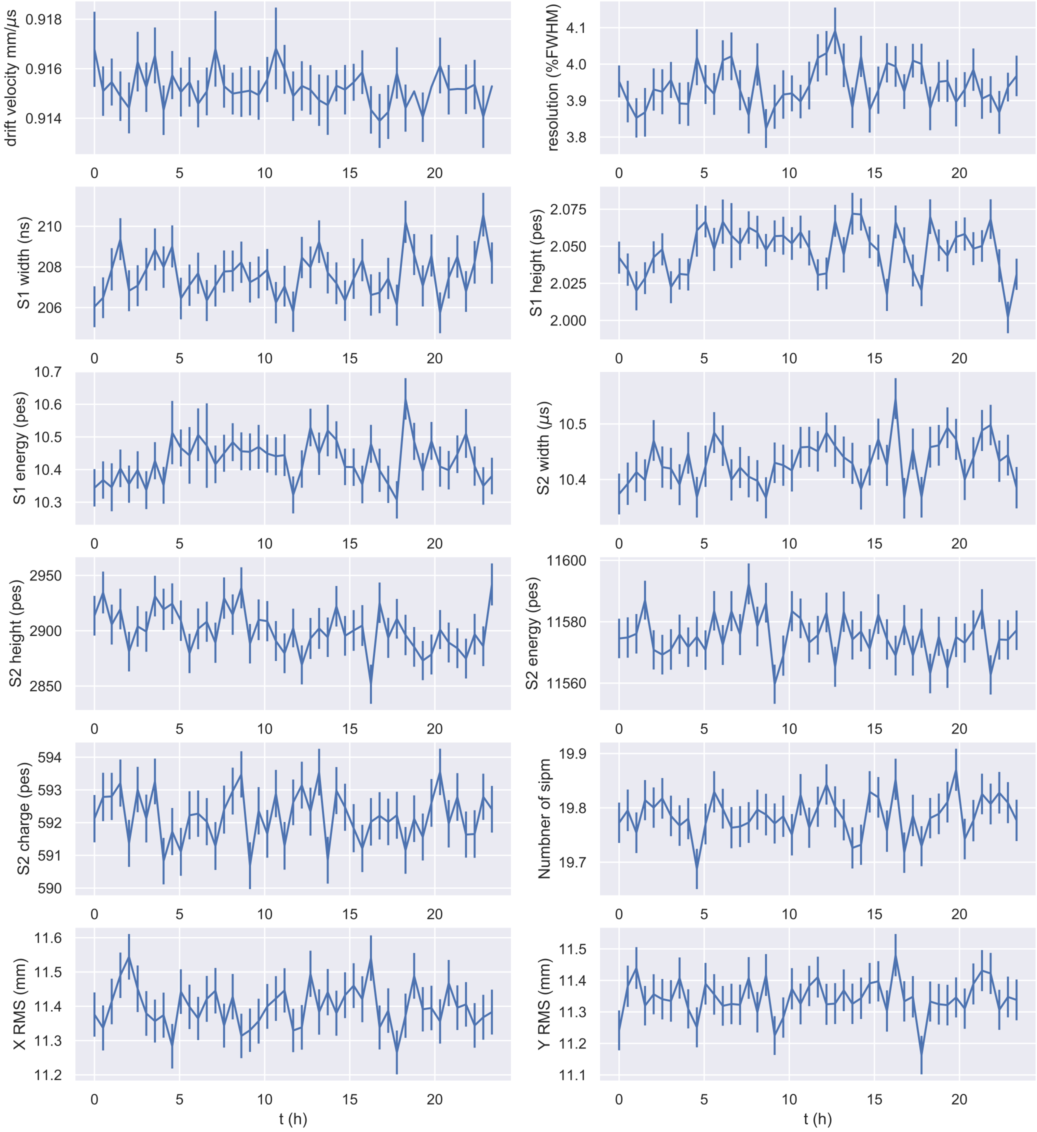

Figure 6.13.: Monitoring plots for a typical run (8004) showing the relevant parameters computed from Kr data for 30' slices: the drift velocity, resolution of the Kr peak, S1 and S2 widths, heights and energies, S2 charge, the number of SiPM triggered per Kr event, and the x and y RMS. All of them show a very steady behavior.

reach the operational conditions. Additionally, the light yield shows a slight rising tendency across all the data taking periods, probably due to the slight pressure loss occurring during regular operations. A detailed summary of the performance of the light yield throughout Runs IV, V, and VI is displayed in Fig. 6.14.

The lifetime is also computed as an average for the lifetime map. Even though this rough determination does not reflect the nuances of the distribution but an

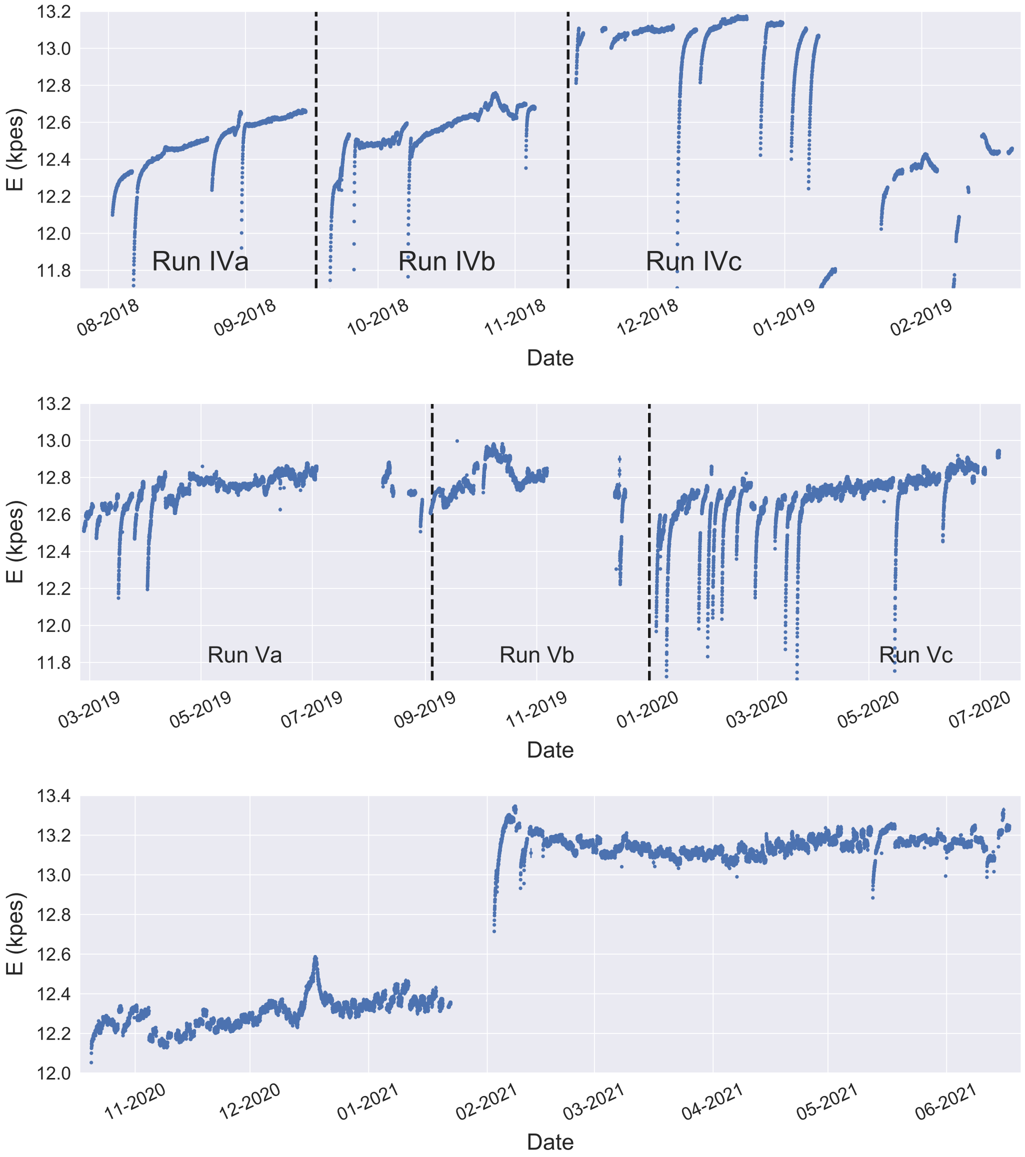

Figure 6.14.: Performance of the light yield throughout Runs IV (top), V (middle), and VI (bottom) and their corresponding subperiods.The dramatic ramps all over the plots correspond to occasions when the high voltage system has been switched on (in general due to sparks) and show the time period it takes for the high fields in the chamber to stabilize. Other temporal bumps are correlated to temperature and pressure changes in the system. One last significant fact that is immediately spotted is the sudden change in the middle of Run VI. Additionally, it seems that the increasing trend disappears after it. This alteration happened after some usual tests and the reason is yet to be understood.

overall scale, it is still helpful to follow the general status of the gas, leaving a more detailed understanding of the evolution for dedicated analysis.

Fig. 6.15 summarizes the evolution of the lifetime for the principal periods (Runs IV, V, and VI). The principal outcome after a brief look at it is the excellent improvement form around 2 ms in Run IV (even lower, < 1 ms, at the beginning of Run II) to more than 13 ms at the end of the operations in Run VI. The significant variations present in the evolution have their origin in multiple factors that might affect the gas, gas system and gas flow. Specifically, the principal events have been correlated to major problems in the laboratory cooling system causing the gas to heat, as depicted in Fig. 6.16. Another hint pointing towards this influence of the laboratory temperature is how the variability decreased significantly after the installation of the inner castle and the radon abatement system (right before Run IVc and Run IVb, respectively, see Table 4.1). Both enhancements help to isolate the detector from the possible ambient temperature changes.

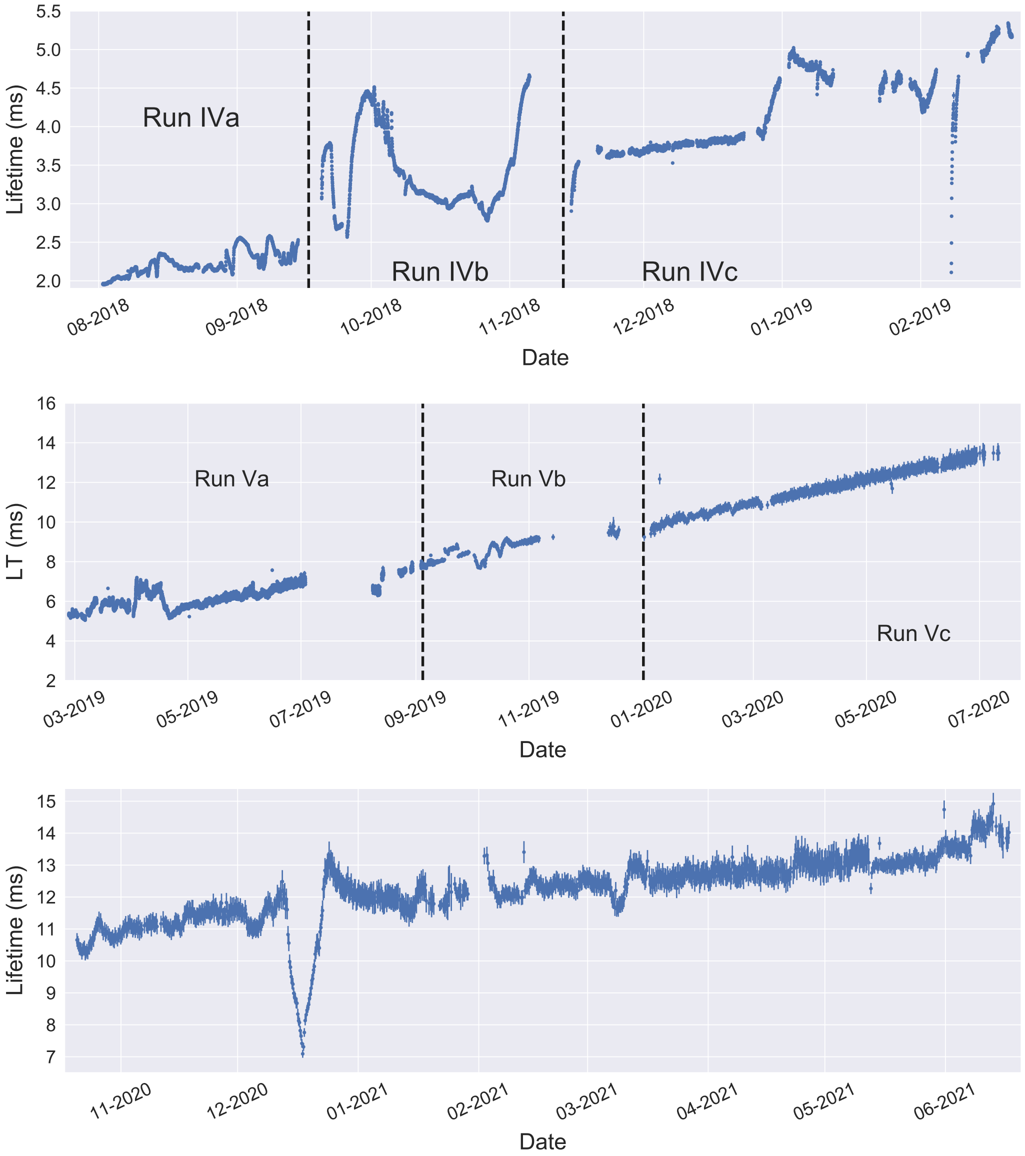

Figure 6.15.: Performance of the lifetime throughout Runs IV (top), V (middle), and VI (bottom) and their corresponding subperiods. The several bumps are correlated with episodes where the temperature in the hall hosting the experiment had increased because of the air cooling system malfunctioning, as shown in Fig. 6.16. In fact, it is remarkable how the variability decreased significantly after the installation of the inner castle and the radon abatement system, right before the starting of Run VIc (see Table 4.1). Finally, the graphs manifest a correlation between the lifetime measurement and its uncertainty. This is related to the fact that the higher the lifetime, the flatter the z coordinate effect. Thus, the fit reflects the fact that the parameter space for the possible lifetimes broadens the higher value it has (the chamber is $\sim 0.5\,\mu$s; therefore, lifetimes much greater than that become gradually more difficult to determine accurately).

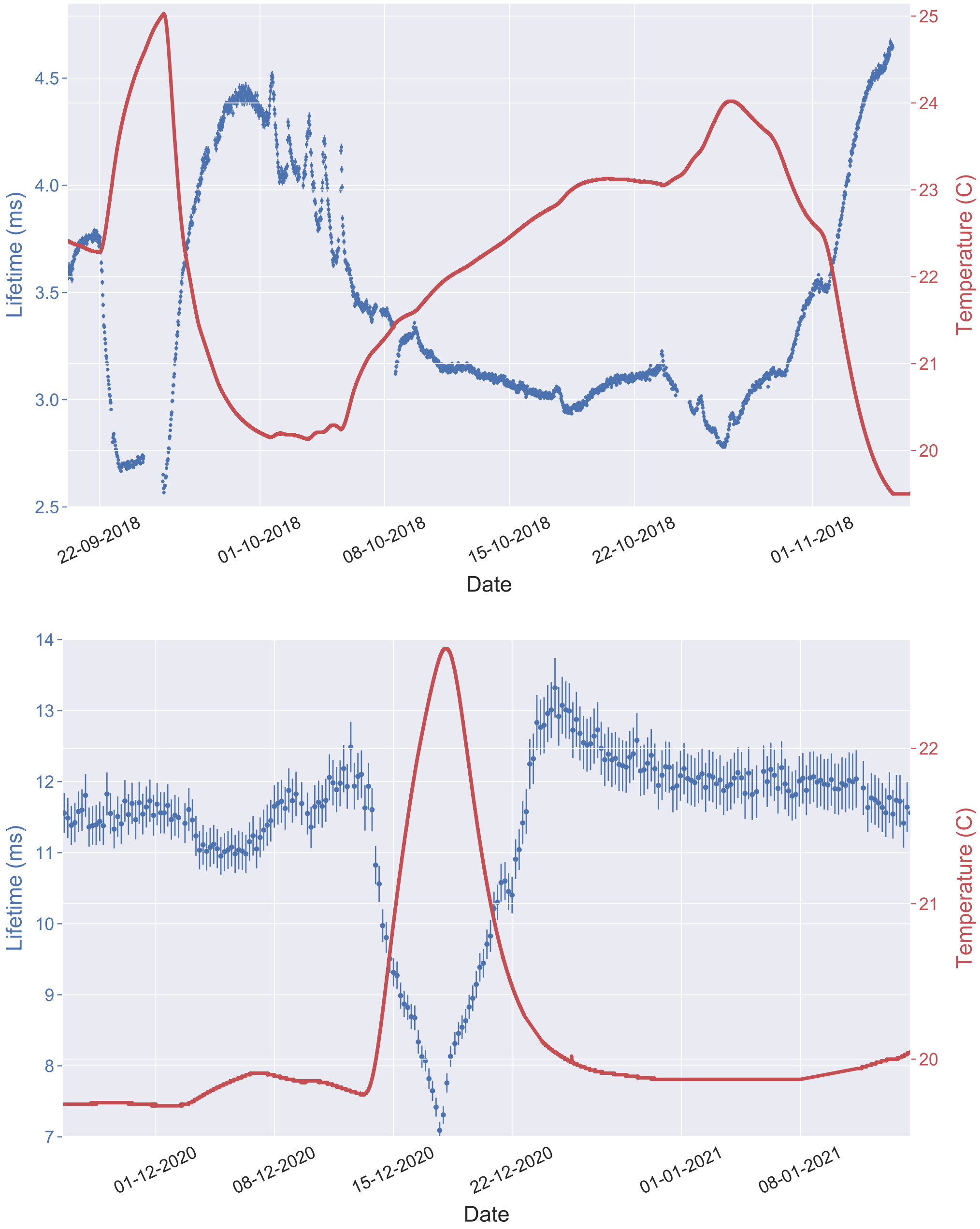

Figure 6.16.: Detail of the lifetime evolution (blue dots) during Runs IVb (top figure) and the beginning of Run VI (bottom figure), and the temperature (red line) of the gas inside the vessel during those periods, where an abrupt change in the lifetime evolution is detected. Certainly, the temperature variations of the gas, driven by the variations in the laboratory conditions, affect the system behavior. This is due to the increasing of the outgassing rate of the various materials with the temperature [279].

7

Sources of backgrounds for the NEXT experiment

The background is one of the fundamental pieces of any experiment aiming to search for the $0\nu\beta\beta$. Nevertheless, building a detector with no unwanted events of any kind is virtually impossible. Hence, the best one can do is attempting to reduce it as much as possible throughout the different stages of design and construction under levels compatible with the scope of the detector. The strategy to reduce it depends dramatically on the nature of the source, and the solutions are diverse and take place in different stages. The remaining background has to be characterized in order to decrease its effect on the physics campaign. In fact, the various backgrounds affect in different ways, depending on the intended study.

Throughout the present chapter, the principal sources of background will be presented. In addition, their impact on the various physics cases will be assessed.

7.1 Classification

In general, there are two mechanisms for the backgrounds to be harmful in the detector:

Beta decays (thus electron emission). Since the mean free path for the electrons in the detector materials is very short, the only contribution for this kind has to come from isotopes on the surface of the elements facing the active volume or from the active volume itself.

Gamma decays High energy gamma events entering the active volume may interact with the gas via the available processes (photoelectric, Compton, and pair production), yielding electron events. Gamma rays have considerable penetration powers, permeating the different materials and reaching the active volume. Although some isotopes will also be discussed, the crucial threats come from ^{208}Tl and ^{214}Bi for the $0\nu\beta\beta$ (both have gamma lines very close to the ROI,[1] at 2614 keV [277] and 2477 keV [280], respectively), and ^{40}K and

---

[1] $Q_{\beta\beta}$ =(2457.83 ± 0.37) keV [92]

$^{60}\mathrm{Co}$ for the $2\nu\beta\beta$ case (due to their predominance in all kind of materials and broad Compton spectrum range).

It is also worth mentioning that other events consisting of charged particles crossing the detector (muons, for instance) are also detected. However, since they are easily distinguishable from electron-like ones and can be vetoed, they do not constitute a severe troublesome.

Regarding the origin of the background, there are two principal natural sources, plus a man-made one:

Natural decay chains They come from elements present at the Earth formation, originated in the various stellar nucleosynthesis processes. Nowadays, the chains are considered to start on a long-lived isotope (in secular equilibrium) and undergo several decays until they reach a stable one. There are four[2] possible series known by the long-lived isotope are thorium ($4n$), neptunium ($4n+1$), radium ($4n+2$), and actinium ($4n+3$), all of them depicted in Fig. 7.1; however, the $4n+1$ one is already almost gone. Lighter elements generally have lifetimes low enough to not be explained by any decay from the original Earth's constituents (although one notable exception is $^{40}\mathrm{K}$, of interest in this work).

Cosmic rays Light elements are short-lived, so they must be created on Earth. The cosmic rays, high energy particles (mainly protons and light nuclei) originated in the sun or other astrophysical scenarios outside the solar system, enter the atmosphere and produce large cascades of secondary particles. A typical direct outcome is light isotopes, and, in addition, the neutrons yielded as byproducts and by byproducts interaction can activate stable elements.

Nuclear testing The last category are those fission products that appeared after 1945 and the nuclear weapon tests and releases. Although they are primarily short-lived elements, the time passed since their production is not enough for them to have decayed.

The backgrounds considered for the NEXT experiment are distributed in three categories[3] for their analysis: radon-induced, radiogenic, and cosmogenic.

---

[2] Since the dominant decay mechanisms are beta (that does not change the mass number) and alpha (that changes it in four units), only four principal branches are traditionally contemplated. Nevertheless, those are not the only available processes, and other more exotic ramifications may very rarely occur.

[3] The categories are somewhat arbitrary. The chosen ones reflect the reduction strategies.

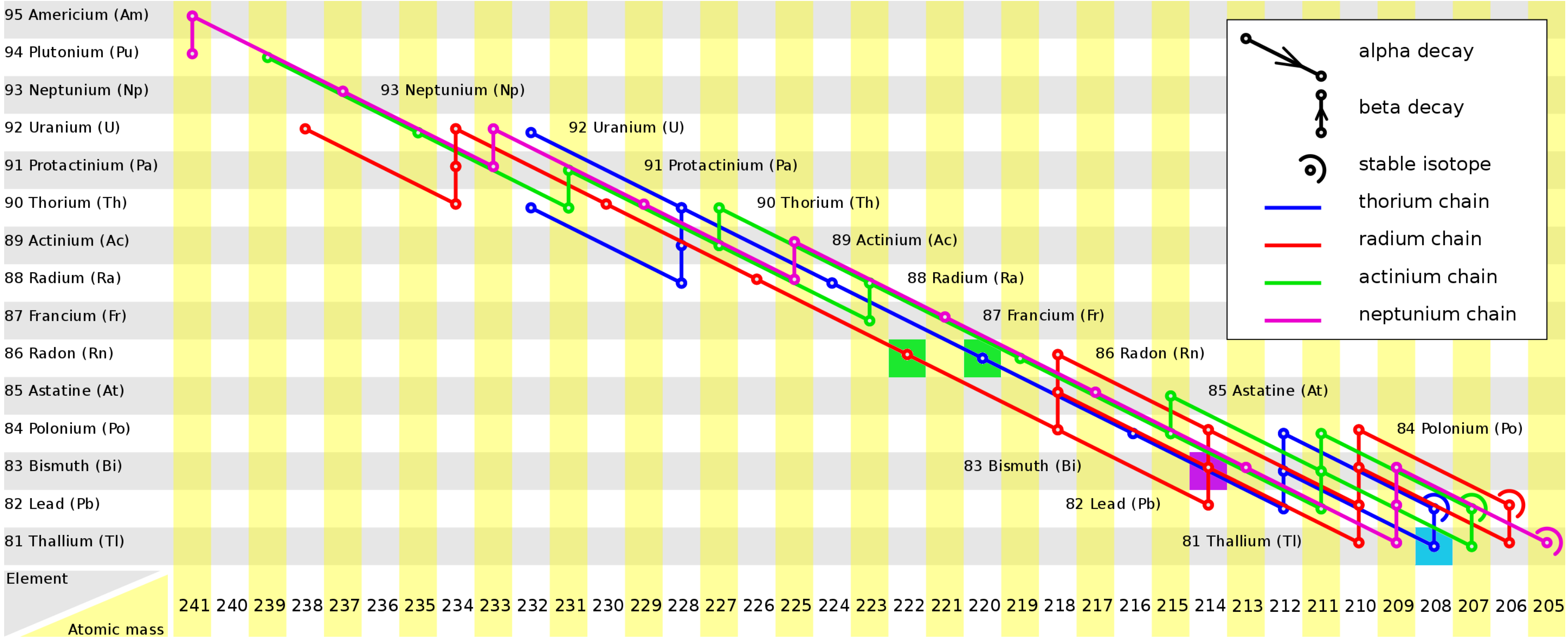

Figure 7.1.: Principal ramifications of the four natural decay chains: thorium (blue), neptunium (pink), radium or uranium (red), and actinium (green). The isotopes of interest in the background studies are highlithed in green (^{222}Rn and ^{220}Rn), purple (^{214}Bi), and cyan (^{208}Tl). Figure adapted from [281].

7.2 Radon-induced

Radon is a radioactive noble gas produced as an intermediate state in the natural decay series. From Fig. 7.1, one can see that there are mainly four radon isotopes involved in the main branches of the decay chains but, due to the very short lifetimes of $^{218}\mathrm{Rn}$ and $^{219}\mathrm{Rn}$, the troublesome isotopes are $^{222}\mathrm{Rn}$ and $^{220}\mathrm{Rn}$. Notwithstanding, only the former one was found to be of real danger (being the only present inside the detector, see Chapter 8).

Since it is gaseous, it can be present all around the detector (airborne) as well as inside the gas system (internal), and its distributions are homogeneous in all the gas (or fluid) volumes. Both are troublesome, but the impacts are pretty different.

Concerning the removal, radon gas has an advantage that no other background has: it can be removed via active filtration with various absorbers and techniques [282, 283, 284].

7.2.1 Airborn

Every material around the detector emanates radon, and since it is a noble gas, it diffuses and gets to a homogeneous spatial distribution, even entering the space between the vessel and the shielding castles (see Sec. 4.1.6 and Fig. 4.9b). Hence, the presence of such events introduces a source of unattenuated gammas inside the chamber (just the vessel and the copper bricks are left to shield the active volume).

Notwithstanding, as aforementioned, radon can be reduced via air filtration. Luckily, since the beginning of the Run IVb, the LSC provided the experiment with a supply of radon-free air, injected inside the outer lead castle. Fig. 7.2 shows the radon abatement system (RAS) by ATEKO installed in the laboratory and the pipes providing clear air, placed on the roof of the outer lead castle.

Regarding the impact of the RAS, Fig. 7.3a depicts the correlation between the event rate measured in the detector with the radon activity measured in the hall hosting the detector, prior to its installation. The linear fit predicts a fiducial rate of (3.97 ± 0.46) mHz in the absence of external radon, which is confirmed by the rate measurement after the beginning of the radon-free air supply, shown in Fig. 7.3b. Therefore, that confirms the RAS is successfully working and leading to an ideal airborne-radon-free situation.

Figure 7.2.: Radon abatement system by ATEKO installed in Hall A of the LSC (left) and detail of the pipes supplying the radon-free air inside the outer castle (right).

7.2.2 Internal

The circumstances regarding the internal radon emanation are notably different from the airborne one, and the reason is twofold. On the one hand, the events may occur inside the active volume, thus having no possible shielding against them. On the other hand, the daughters of the radon are produced in a charged state. Hence, in the presence of the drift field of the detector, they concentrate on the cathode, creating a highly contaminated area in contact with the gas (and again, with no shielding).

The internal radon may originate from the emanation either by the different components of the detector or through air leaks from the surroundings. This implies that parts such as the gas system (outside the castle volume), which is virtually harmless for the other backgrounds, can become a concern for this scenario.

Consequently, a dedicated campaign has been carried scrutinizing the activity of the radon-induced backgrounds in the chamber for NEXT-white, as well as a careful estimation of the results for the next generation of detectors. The studies show that the source is not of particular trouble, neither for this nor NEXT-100 physics case, as the radiogenic sources overpass the expected rate by two orders of magnitude in NEXT-White (regarding the $2\nu\beta\beta$ analysis) and at least one order of magnitude for the pessimistic scenario in NEXT-100 (regarding the $0\nu\beta\beta$ analysis). A detailed report on this can be found in Chapter 8.

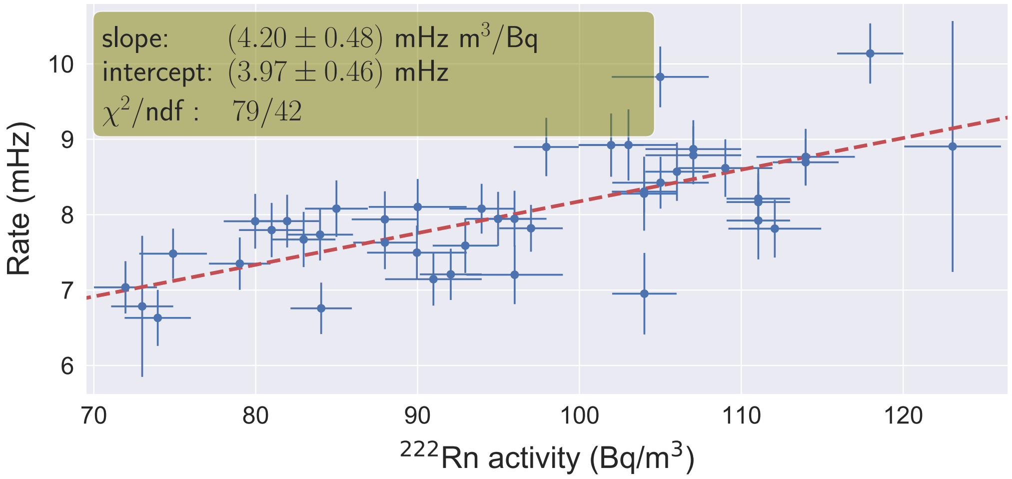

(a)

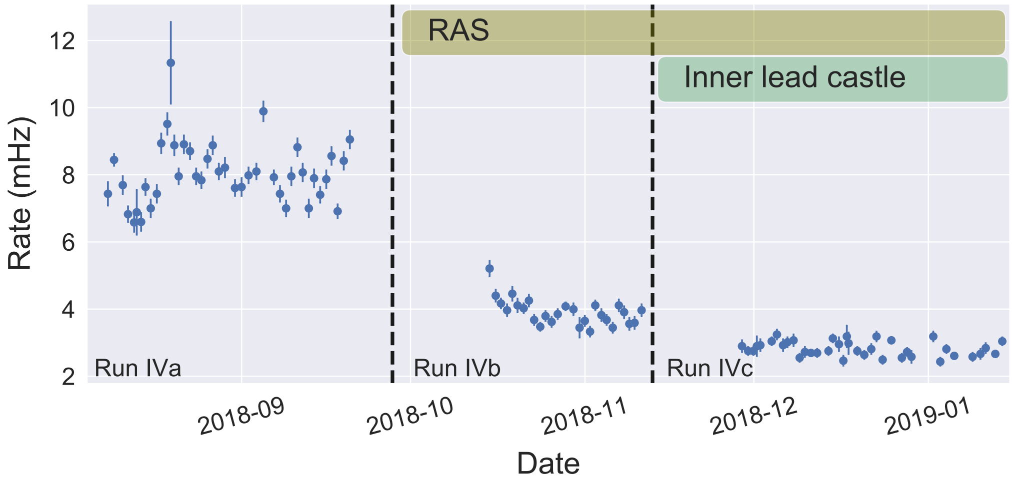

(b)

Figure 7.3.: a: Fiducial background rate as a function of the airborne-radon activity. A linear fit is over-imposed, showing a rate of (3.97 ± 0.46) mHz in the absence of airborne radon. b: Fiducial background rate as a function of the calendar day for the whole Run IV period and the main changes between subruns.

7.3 Radiogenic

Radiogenic backgrounds refer to events originating from radioactive decays of the impurities present in all the detector materials and elements surrounding it (including the laboratory's walls). The principal strategy against them is the passive shielding by the two lead castle structures, isolating the chamber of the external contributions. Notwithstanding, the detector remains a possible background source, partially mitigated by the inner copper shielding (see Sec. 4.1 for more detail on the detector construction). In order to palliate the various contributions, an exhaustive campaign of screening has to be carried for every single piece intended to be part of the final machine, and once the impact is evaluated, it may be accepted (or rejected) for the final design. This process is meticulous and affects the technological approaches that the detector can achieve since sometimes it happens that the commercial and standard solution is not suitable for the project, and other non-optimal or custom-made proposals have to arise.

Among all the enormous possible isotopes that may affect, four are causing a severe concern for the physics scenario. The rest of the candidates either do not have an energy window harming the searches, or their contribution is overwhelmed by the considered ones. Two of them are of special concern for the $0\nu\beta\beta$ physics case:

- The $^{214}\mathrm{Bi}$ beta decay into $^{214}\mathrm{Po}$ has a considerable population of high energy gammas (up to ~3.3 MeV) [280]. However, their intensities are almost negligible and therefore of no concern. There is, still, a gamma with an intensity high enough –(1.545 ± 0.011) %–, located at (2447.69 ± 0.03) keV, right below the ROI for $0\nu\beta\beta$, overlapping it, even at energy resolutions as good as 0.5 % FWHM.

- The case of the $^{208}\mathrm{Tl}$ decay into $^{208}\mathrm{Pb}$ is different. The dominant gamma line –(99.754 ± 0.004) %– lies at (2614.511 ± 0.010) keV [277] and is not actually an issue due to the detector's excellent energy resolution. However, several effects such as bremsstrahlung, double Compton interactions close to each other, or small energy losses can generate events from the photopeak populating the ROI.

On the other hand, the two remaining isotopes impact only the $2\nu\beta\beta$ searches. The $^{40}\mathrm{K}$ electron capture into $^{40}\mathrm{Ar}$ produces a gamma of (1460.820 ± 0.005) keV [285] and the $^{60}\mathrm{Co}$ beta decay into $^{60}\mathrm{Ni}$ yields two gammas at (1173.228 ± 0.003) keV and (1332.492 ± 0.004) keV [286]. Both the various gamma lines and their correspondent Compton spectra dominate inside the energy region of the $2\nu\beta\beta$ spectrum. In addition, also the $^{214}\mathrm{Bi}$ and $^{208}\mathrm{Tl}$ Compton spectra and lower energy gammas enter and interfere in the ROI for the two-neutrino mode.

A more profound characterization of the radiogenic backgrounds and their impact on the $2\nu\beta\beta$ search can be found in Chapter 9.

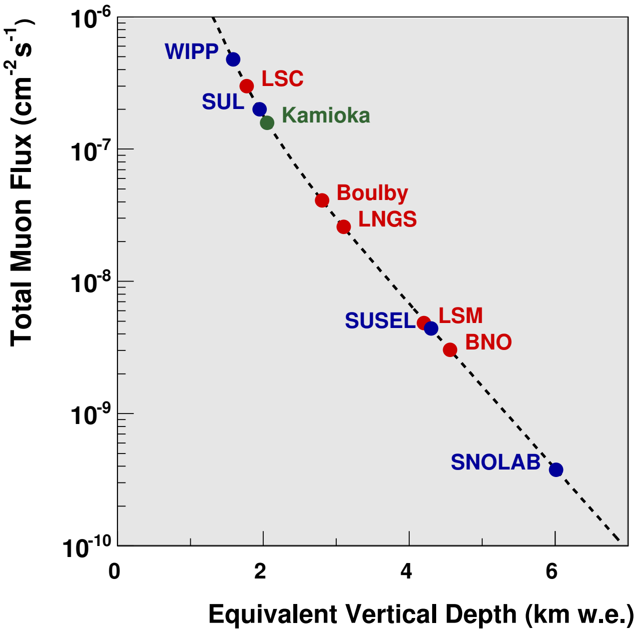

Figure 7.4.: Total muon flux as a function of the vertical depth of different underground laboratories around the world. The depth is expressed in terms of kilometers of water equivalent, a standard unit that removes the effect of the variable rock profiles attenuation into the equivalent length of water needed to reach it. The color of the laboratory name indicates the location: blue for America, red for Europe, and green for Asia. Figure extracted from [59].

7.4 Cosmogenic

The cosmogenic contribution is the reason that forces the experiments aiming to get virtually zero background rates to operate underground and requires a substantial effort by the experiments [287, 288, 289].

7.4.1 Muons

Muons have an enormous penetration power,[4] and, even underneath bast masses of rock, they can be detected at the laboratory. Fig. 7.4 depicts the expected muon flux as a function of the depth for various underground laboratories. The measured muon flux for the Hall A (where NEXT-White is located) of the LSC is $(5.26 \pm 0.21) \cdot 10^{-7}\,\mathrm{cm}^{-2}\mathrm{s}^{-1}$ [291].

---

[4] Neutrinos have even greater penetration power. Notwithstanding, due to the tiny interaction cross-section, they do not represent any significant concern for the upcoming generation of $0\nu\beta\beta$ experiments [290].

Muons do not represent a threat themselves. Their passage through the detector can be easily removed by topology reconstruction or, if needed, an active muon veto can help get rid of such kinds of events [233]. Unfortunately, muon can interact with the different materials in different forms, producing electromagnetic and hadronic showers, spallation products, muon-capture products, or even muon decay products. Among them, the most troublesome byproduct are neutrons

7.4.2 Neutrons

In addition to muon-originated events, neutrons can also be generated from other processes not involving muons, such as nuclear fissions in the natural chains and (α, n) or $(n, 2n)$ reactions. Those are even more problematic since they cannot be correlated with any muon (thus, there is no possible veto[5]). The total measured neutron flux for the Hall A of the LSC is $(1.38 \pm 0.14) \cdot 10^{-5}\,\mathrm{cm}^{-2}\mathrm{s}^{-1}$ [292, 293].

Neutrons may be captured by a nucleus and produce an unstable isotope, the so-called neutron activation, especially for intermediate-Z materials (Cu and Fe, for instance, which represent a considerable fraction of the detector) [32]. The neutron capture can produce a background via two processes. On the one hand, the activation itself is usually accompanied by a prompt gamma emission[6] that can interact in the active volume [294]. On the other hand, the unstable isotope decay may yield beta and gamma particles in the active volume.

Although most of the possible isotopes are negligible for the experiment physics case, it is necessary to study and keep under control the potential backgrounds produced by neutron activation. The potential threats can be divided into two categories: the activation of the materials surrounding the active volume and the activation of the gas itself.

Materials activation

Regarding the first category, the detector component can be activated either when being manipulated at ground level or once inside the underground lab. The former situation is mitigated by storing the material underground for the longest time possible, maneuvering them, and building the detector underground. In this manner, the

---

[5] In a lucky situation, unstable nuclei may happen to have a lifetime short enough to be vetoed via the detection of the original muon, causing a dead-time in the data taking.

[6] ${}^{A}\mathrm{X}\ (n,\gamma)^{A+1}\mathrm{X}$

potentially unstable isotopes are left with enough time to decay into safe elements.[7] Unfortunately, some may possess long lifetimes and still be present even after the waiting time (yet, the long lifetime also makes them have low activity and, therefore, less harmful). The latter can be mitigated via shielding, either active (a muon veto or detecting the prompt gammas from the neutron capture) or passive shielding (placing layers of neutron moderators and adsorbers, typically water or plastics).

It is crucial to identify all the potential sources of activation, which implies a detailed campaign studying the detector materials, the feasible activations, and their impact on the physical chases of the detector. This still-on-going effort within the collaboration led to spotting a list of probable isotopes, among them: $^{64,66}\mathrm{Cu}$, $^{2}\mathrm{H}$, $^{55,57,58,59}\mathrm{Fe}$, $^{116}\mathrm{In}$, $^{205,207,208,209}\mathrm{Pb}$, and traces of other elements.

Gas activation

Concerning the activation of the gas, if neutrons reach the active volume, they can be captured by the xenon nuclei present, producing other isotopes. This process is particularly delicate since there is no strategy to shield the decay products (beta electrons), and the only possibility is the correlation with the potential initial muon (if the event happens to originate from a muon event and it is detected). The potential products of the activation depend on the isotopic composition of the gas that, in the case of the enriched gas (of interest for the physics program), is predominantly– (90.4 ± 0.9) %– composed of $^{136}\mathrm{Xe}$. The rest is dominated by $^{134}\mathrm{Xe}$ and the other isotopes rapidly decrease in importance the lighter they are up to traces of $^{129}\mathrm{Xe}$. Therefore, the only unstable nuclei archivable via activation are $^{137}\mathrm{Xe}$ and, more residually, $^{133}\mathrm{Xe}$ and $^{135}\mathrm{Xe}$.

The latters[8] are of no particular concern since their production is significantly suppressed by the minor presence of the parent nuclei, and the low Q_β represent no real problem for the $0\nu\beta\beta$ search (and not much for the $2\nu\beta\beta$ one either). However, they might play a more relevant role when scaling the detector in mass, especially when dealing with the depleted Xe gas in terms of the background characterization studies.

---

[7] Actually, one precious item for the shielding is materials rescued from shipwrecks since a large amount of water shielded them from cosmic radiation [295]. For instance, the Roman lead bricks used for CUORE's shielding [131], or CDMS remains from an 18th-century vessel in France [296].

[8] $^{133}\mathrm{Xe}$ $Q_\beta = (427.4 \pm 2.4)$ keV $T_{1/2} = (5.2475 \pm 0.0005)$ d [297]
$^{135}\mathrm{Xe}$ $Q_\beta = (1165 \pm 4)$ keV $T_{1/2} = (9.14 \pm 0.02)$ h [298]

Notwithstanding, the case of the $^{137}\mathrm{Xe}$ is pretty different.[9] Given the predominant presence of the parent isotope (even larger as the detector program scales up in size), it may be produced in a considerable amount. Unfortunately, the Q_β is much higher than $Q_{\beta\beta}$ for $^{136}\mathrm{Xe}$, allowing the beta electrons to populate the ROI. Additionally, the lifetime is relatively large, and the event cannot be vetoed if correlated with a muon interaction. It is also the case for the daughter,[10] but its low Q_β and long lifetime discard any threat.

Alternatively, for the Xe isotope scenario, an additional approach can be considered on top of the already discussed ones. Preliminary studies have shown that small amounts of $^{3}\mathrm{He}$, even of 0.1 %, can reduce the neutron-capture rate of the $^{137}\mathrm{Xe}$ by one order of magnitude [113]. Additionally, He has shown to be an excellent choice when aiming to reduce diffusion [229]. The downside is that, apart from the shortage and its elevated prize [299], He is a troublesome gas when in contact with PMTs, deteriorating their performance [300]. Providentially, this obstacle may resolve naturally for future generations of detectors when the sensors will be replaced for other lower-radioactivity ones (see Sec. 3.2.5 for further information).

---

[9] $^{137}\mathrm{Xe}$ Q_β = (4173 ± 7) keV $T_{1/2}$ =(3.818 ± 0.013) min [276]

[10] $^{137}\mathrm{Cs}$ Q_β = (1175.63 ± 0.17) keV $T_{1/2}$ =(30.08 ± 0.09) y [276]

8

Internal radon activity in NEXT-White and its implications in the $\beta\beta$ searches

Radon gas is an identified problem for experiments intending very low background rates [301, 302]. Its ability to emanate from every material and diffuse throughout all the detector systems makes it a real danger. In addition, since it is a gas, if the lifetime is long enough, it reaches a homogeneous distribution in the active volume, and the daughter nuclei (usually in a charged state after the decay) may be driven towards the cathode, where they accumulate. Among all the various isotopes, only one of them, living more than a few seconds, is of particular concern: $^{222}\mathrm{Rn}$.

Furthermore, the subsequent isotopes of the decay chain of $^{222}\mathrm{Rn}$ (Fig. 8.1) includes the aforementioned problematic $^{214}\mathrm{Bi}$. Since the decay times in the chain are long enough, the different charged intermediate charged states can reach the cathode, becoming a hot emitting spot of gammas and beta electrons entering the $0\nu\beta\beta$ ROI. Luckily, the $^{214}\mathrm{Bi}$ and $^{214}\mathrm{Po}$ decay may occur in such a way that both steps are detected (due to the tiny lifetime of $^{214}\mathrm{Po}$). If so, those events can be safely rejected (typically effective for $>$50% of the cases [302, 303]).

Consequently, although some effects could be mitigated up to a certain level, it is mandatory to reduce the source of background as much as possible as it will become the dominant background source in future large-scale xenon detectors [301].

This chapter will review the presence of Rn in the detector and the resulting activity, the impact of the beta radiation from $^{214}\mathrm{Bi}$ following the $^{222}\mathrm{Rn}$ event, and the implication for the $2\nu\beta\beta$ and $0\nu\beta\beta$ campaigns in NEXT-White and NEXT-100, respectively. It is based on the analysis already reported in [214].

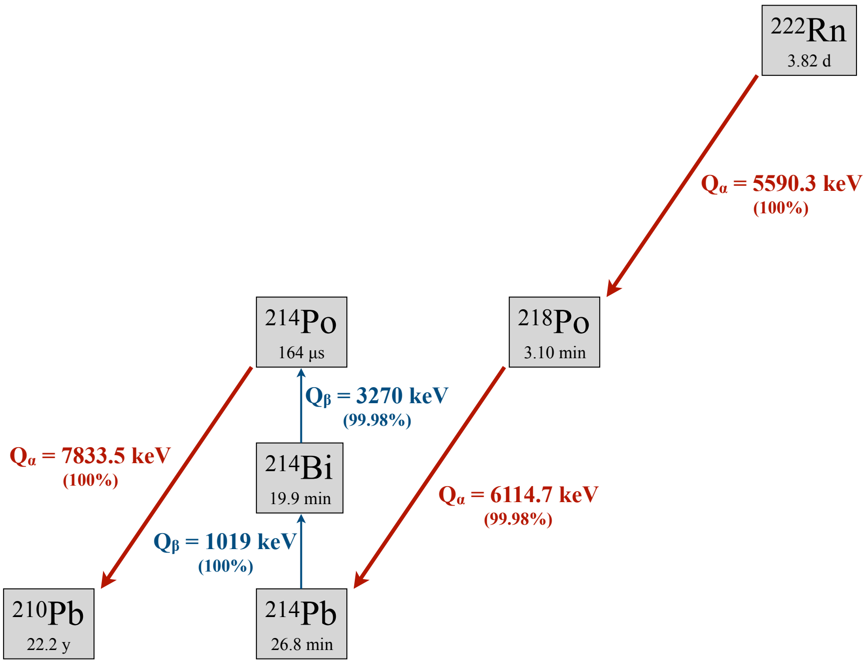

Figure 8.1.: Detail of the uranium (or radium) natural decay chain (depicting the most dominant branches, see Fig. 7.1) regarding the ^{222}Rn progeny up to the relatively long-living ^{210}Pb. The lifetimes, Q-values, and branching fractions are extracted from [280, 304, 305].

8.1 Characterization of the alpha decays

The first step in the characterization of the Rn and its progeny impact in the NEXT program is determining the activity of the parent nucleous itself. In order to do so, it is crucial to measure the ^{222}Rd decay directly in the chamber, which happens a 100% of the time via an alpha process into ^{218}Po [304].

8.1.1 Event selection

The alpha particle, although it has clear features and is easy to identify, saturates the PMTs under the typical operation conditions (more specifically, the gain) for the electron searches. Hence, in order to accurately measure the energy of that kind of event, the electric field conditions of the chamber must be adapted, and dedicated data takings have to be contemplated. Those data takings took place during the Run II (see Sec. 4.2) and were divided into three periods, depending on the operations

Period	Duration (s)	Pressure (bar)	ΔV_{drift} (kV)	ΔV_{EL} (kV)	Lifetime (μs)
A1	257 184	7.05–7.08	18.9	3.1	220–294
A2	105 622	6.85–6.88	19.2–20.0	2.8	409–595
A3	38 927	7.21	21.0	2.8	1061–1084

Table 8.1.: Data-taking periods for the alpha-dedicated runs and their main features. The voltage differences correspond to the drift and EL regions voltage drops.

of the cold getter. The cold getters, although they are fast and efficient in removing electronegative impurities, are a known source of radon gas [306]. Therefore, during the initial setup for each data-taking phase, they are employed to improve the gas quality quickly and later switch off (running only through the cold getter), providing enough time for the added contamination to decay. Luckily, even though they are troublesome for regular operations, this source of radon is in handy for the $^{222}\mathrm{Rn}$ studies.

The three subperiods, given their different nature, were used in different parts of the analysis. The first one (A1) took place before the cold getter activation. Thus, it is ideal for estimating the intrinsic $^{222}\mathrm{Rn}$ activity. The second period (A2) followed the first operation with the getter. During this stage, a series of short runs were recorded in order to monitor the chamber (very similar to the Kr,[1] described in Chapter 6) and check the decreasing of the activity of the $^{222}\mathrm{Rn}$ injected by the getter. Lastly, the third period (A3) happened shortly after another operation with the cold getter. In this case, the statistics can be applied to correlate the $^{222}\mathrm{Rn}$-induced alpha activity within the active volume with the rate of $^{214}\mathrm{Bi}$ electrons from the cathode. All the three stages main features are summarized in Table 8.1.

The voltage difference in the EL region had been empirically selected to avoid the aforementioned PMT saturation. Considering the EL thickness (6 mm) and pressures, the reduced field during the runs was E_{EL}/P =0.65–0.73 kV/(cm bar), in coincidence with the values found in the literature for the secondary scintillation threshold in pure xenon at 10 bar [221]. The EL gain is very sensitive to the reduced field when operating in near-threshold conditions.

---

[1] Alpha particles are also pointlike energy deposition that can be used to estimate the lifetime of the chamber. Since the fields must adapt to avoid PMT saturation, they are not helpful for extracting the geometric map.

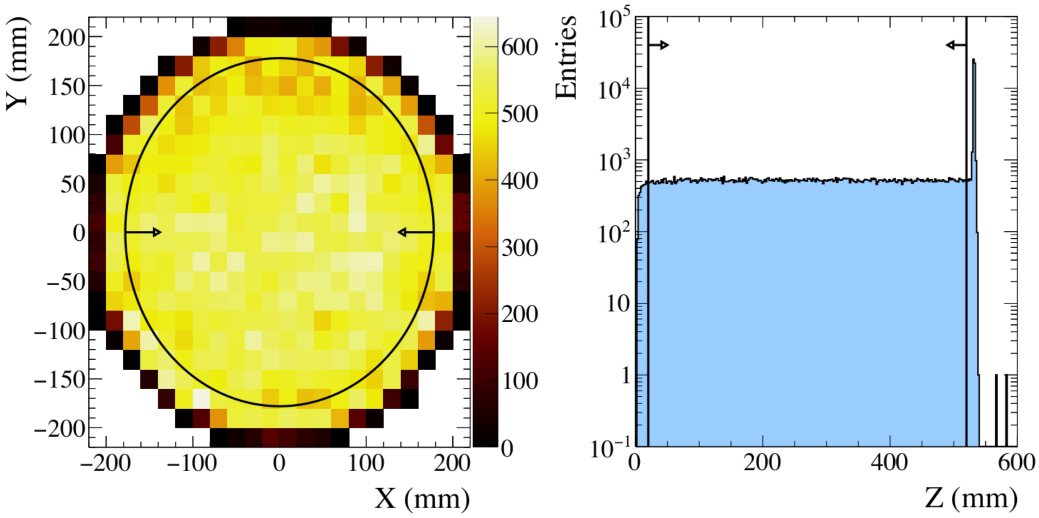

Figure 8.2.: Spatial distribution of alpha candidate events. Left: distribution in the (X,Y) plane where the color indicates the number of entries. Right: z distribution in logarithmic scale. The solid black lines and arrows indicate the region used for the fiducial selection.

Similarly, the drift voltage was selected to maintain a stable drift velocity, with a drift field range of E_{drift} =0.36–0.39 kV/cm. The drift velocity can be easily extracted by considering the alpha events produced right in the cathode position (see Fig. 8.2), likewise in the Kr case, and found to be 0.95–0.97 mm/μs.

Regarding the event reconstruction, the alpha events had been processed through the standard reconstruction, explained in detail in Chapter 5, from the raw data up to `kdsts`. This is again justified by the fact that alpha particles with 5.5 MeV have a continuous slowing down approximation range of 3.5 mm at 7 bar [307].

The selection of the alpha-candidate events was performed in two steps. The first is the selection of the characteristics of the alpha S1s and S2s based on the peak charge, width, and start time during the processing, in concordance with the previous experience in NEXT-DEMO [308] (the most relevant selection parameters can be found in Appendix B). Later, for the so-called *inclusive* sample, the events are required to have one and only one S1 and S2. The spatial distribution is homogeneous within the entire volume (see Fig. 8.2) except the outermost bins in XY (R>198 mm) and the events yielded from the cathode plate (z=530.3 mm). The excess of cathode alphas is produced from the accreted radon progeny and its subsequent decays from there. They represent up to a 20–24 % of the total inclusive alpha sample.

The trigger rate evolution for the inclusive sample is depicted in Fig. 8.3a. Focusing on the A2 period since it spans 15 days of data taking (in comparison with a couple of days of duration of the other two), a detailed view is depicted in Fig. 8.4. The image shows two curves: the raw DAQ rate, i.e., the actual recorded rate, in blue circles, and the corrected rate in red squares. Since the maximum accepted trigger rate is 15 Hz (the so-called trigger mask), the DAQ cannot acquire any event during a 1/15 s period after a trigger. Therefore, knowing the average trigger rate for each run, it is possible to estimate the actual DAQ efficiency and consequently account for the effect and correct the actual rate, as represented in the plot.

An exponential fit to the corrected rate of the A2 period can be performed, yielding a half-life of $T_{1/2}$=(3.822 $\pm$ 0.013) d. This result is in very well agreement with the $^{222}\mathrm{Rn}$ half-life found in the literature, $T_{1/2}$=(3.8222 $\pm$ 0.0009) d [304]. The accordance between those values indicates that, indeed, the alpha particles are induced by $^{222}\mathrm{Rn}$ and its progeny.[2]

8.1.2 Radon activity

The indication of the $^{222}\mathrm{Rn}$ chain dominant presence in the detector is not sufficient to disentangle the relative contribution of each alpha-emitter isotope ($^{222}\mathrm{Rn}$, $^{218}\mathrm{Po}$, and $^{210}\mathrm{Po}$, see Fig. 8.1). Additionally, it does not discard the existence of other second-order alpha sources in the chamber (for instance, the aforementioned $^{220}\mathrm{Rn}$ and its progeny). Therefore, a spectroscopic analysis is required to address those issues.

In order to avoid border effects and miss-reconstruction, the alpha candidates are required to be detected at least 20 mm away from the edges: $z \in$ (20, 520) mm and $r <$ 178 mm . This is the so-called fiducial sample, which includes about 54 % of the candidates and corresponds to a 2.0 kg fiducial mass.

Following the previous analysis, the energy estimator is defined in four steps:

1. The lifetime effect is corrected. Similar to the Kr case (see Chapter 6, the z distribution of alpha events suffers the attachment of secondary electrons on their way to the anode. Therefore, a universal correction factor is computed using Eq. 6.2, and the respose is recovered. Regarding the S1, the non-perfect detector reflectivity distorts the signal that is also parametrized and corrected, separately for S1 and S2.

---

[2] Given the great difference in half-lives of the daughters of $^{222}\mathrm{Rn}$ until $^{210}\mathrm{Pb}$, they are in secular equilibrium. Thus, the dominant decay rate is the Rn's itself.

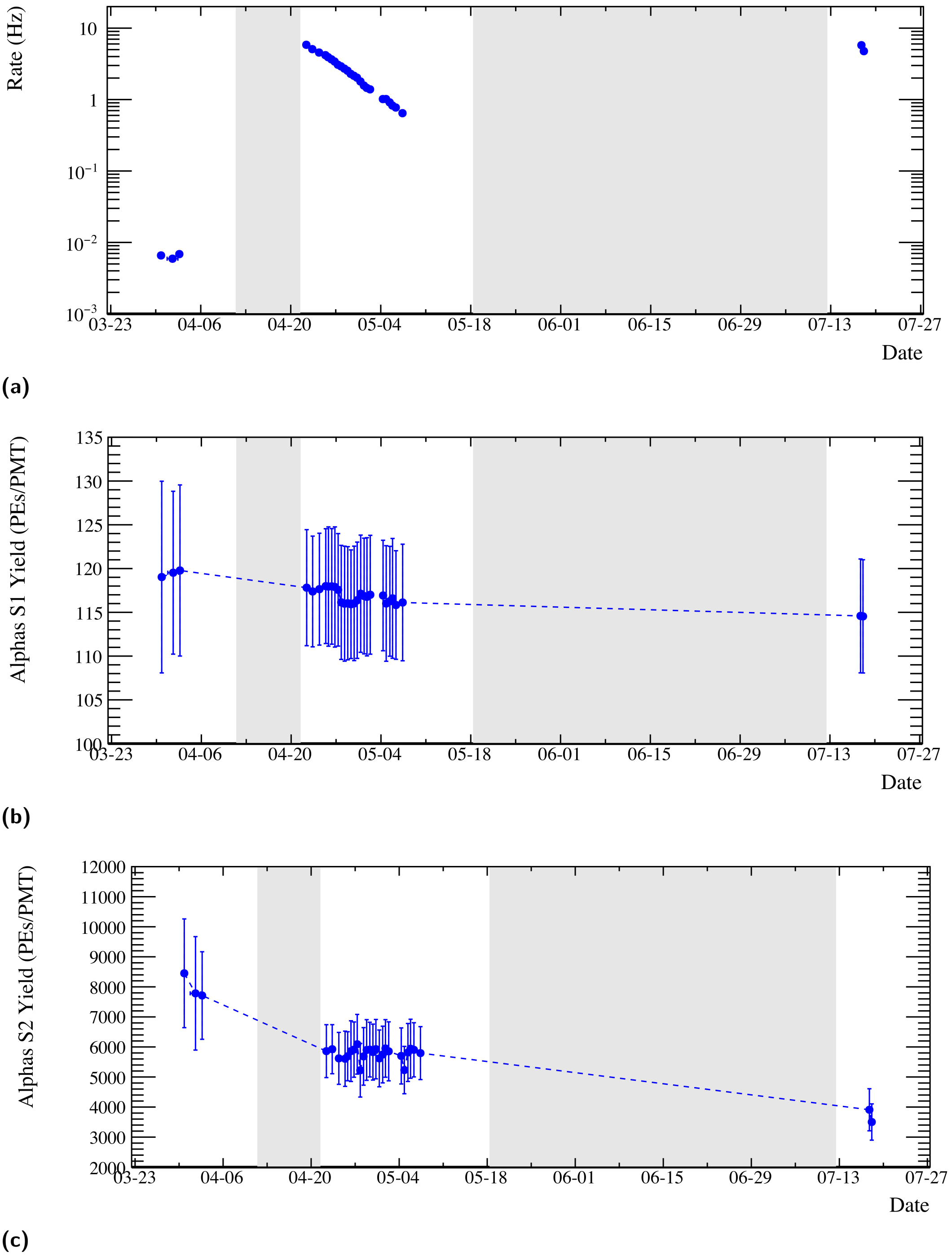

Figure 8.3.: Rate of the inclusive sample (a), S1 yield (b), and S2 yield (c), both for the fiducial sample, evolution during the three data-taking periods (A1-3). The shaded areas correspond to the operation time of the cold getter. For the yields, the data points and the error bars represent the mean and RMS of the z-corrected distributions, respectively.

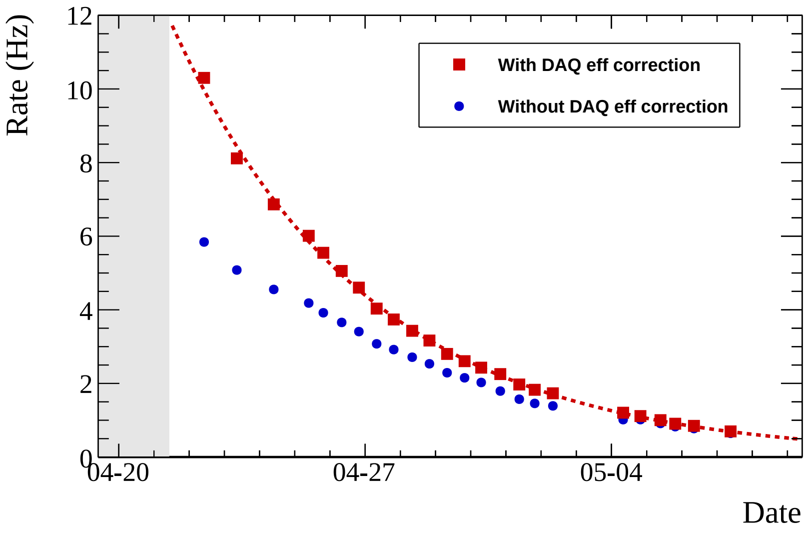

Figure 8.4.: Radon decay evolution during period A2, with (red squares) and without (blue circles) DAQ efficiency correction. The red dashed line represents the exponential fit to the corrected data.

2. The geometric inhomogeneities are removed. Again, analogously to the procedure developed in Chapter 6, the different response across the XY plane is computed and corrected.

3. It is time to mitigate the recombination fluctuations. Unlike the electron tracks in gas, alpha particle events deposit a significant amount of energy in a very tiny volume, so the drift field is not enough to prevent the secondary electrons from recombining with the Xe ions and producing more light (the same happens for all kind of event in liquid Xe detectors, see Section 3.1.2). Thus, there is an anticorrelation between light (S1) and electron (S2) signals that can be taken into account in order to improve energy resolution. Therefore, an estimator is defined as:

$$E = \lambda \left(N_1 + N_2/\eta \right), \tag{8.1}$$

where λ is an overall conversion factor, N_1 and N_2 are the corrected S1 and S2 signals, respectively, and η is a weight factor to rescale the ionization yield component. In this step, the η is computed by finding the optimal value: the one that maximizes the energy resolution for the $^{222}\mathrm{Rn}$ peak.

4. Lastly, the overall scale, λ, is computed as the conversion factor from PEs per PMTs to keV. In order to extract it, the $^{222}\mathrm{Rn}$ alpha energy is aligned with the literature value.

In addition to the above-mentioned scheme, the compatibility among runs has to be assessed to check if a global set of parameters can be found. In the case of the S1 signals, the yield depends softly on the pressure and, given the relatively small change (around 5 % for all the alpha dedicated runs), the variation is expected to be negligible. This agrees with the measured stability of the S1 signal, within a 4 %, as shown in Fig. 8.3b. In contrast, the dependence of the S2 yield is expected to be much more dramatic, given the near-to-EL-threshold conditions of operation to the reduced field (E/P). This is patent in Fig. 8.3c, where the S2 decrease is about a factor 2, although it is relatively stable within the three subperiods. Therefore, the λ factor in Eq. 8.1 must be computed of each period separately.

Fig. 8.5 presents the anticorrelation for scintillation and ionization light for alpha events. In contrast, Fig. 8.6 shows the energy estimator (for simplicity, from now on, denoted just by energy) for the A1 and A3 periods of low and high radon activity, respectively. A Gaussian fit is performed for every peak in both spectra. The three distributions correspond with the alphas events from $^{222}\mathrm{Rn}$ ((5590.4 ± 0.3) keV [304]), $^{218}\mathrm{Po}$ ((6114.75 ± 0.09) keV [280]) and $^{214}\mathrm{Po}$ ((7833.46 ± 0.06) keV [305]),[3] although the later is only visible in the high activity run.

	$^{222}\mathrm{Rn}$ (events)	$^{218}\mathrm{Po}$ (events)	$^{214}\mathrm{Po}$ (events)	$^{222}\mathrm{Rn}$ activity (Bq/m^3)
A1	487 ± 28	154 ± 21	-	$(38.1 \pm 2.2)\cdot 10^{-3}$
A3	$(7.28 \pm 0.03)\cdot 10^{4}$	$(2.32 \pm 0.02)\cdot 10^{4}$	$(1.09 \pm 0.11)\cdot 10^{2}$	37.56 ± 0.14

Table 8.2.: Fitted yields and specific $^{222}\mathrm{Rn}$ activity in the fiducial volume during run periods A1 and A3. The activity is expressed per volume, considering a fiducial volume of $\sim$0.05 m^3.

The results of the fit are presented in Table 8.2 and depicted in Figs. 8.6. It is noticeable the enormous difference between the activities for both periods. This fact is easily explainable since the A3 data was taken only six days after the operation of the cold getter, while the A1 is considered to only account for the intrinsic radon emanation of the normal operations.

The first one, and more straightforward, is the estimation of the $^{222}\mathrm{Rn}$ activity. After a quantification of the possible sources of inefficiency and background

---

[3] It is important to notice that the reported energy is the Q-value of the decay instead of the kinetic energy of the alpha particle. This is due to the ability of the detector to measure the nuclear recoil.

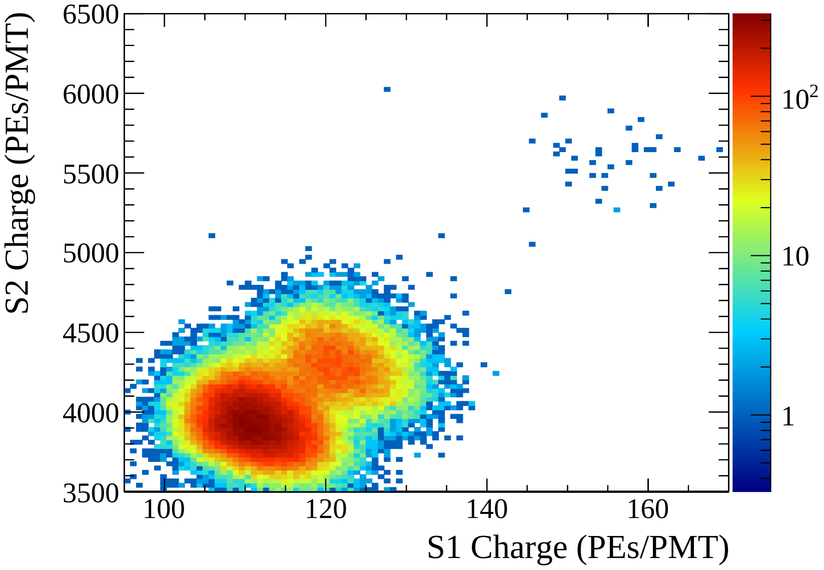

Figure 8.5.: Corrected S2 yield versus corrected S1 yield for A3 period data. The three alpha populations are clearly distinguishable, two on the bottom left quadrant and the few events in the top right one. It is also patent the anticorrelation between scintillation and ionization for alphas, in correspondence with the liquid xenon case (Fig. 3.2).

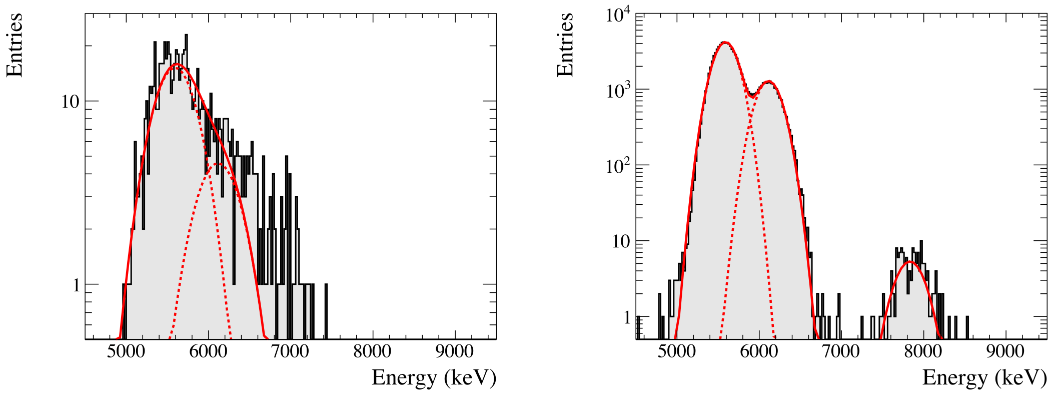

Figure 8.6.: Energy distribution for fiducial alphas during run periods A1 (left) and A3 (right). The dashed red curves represent the individual gaussian contributions from each alpha line (^{222}Rn, ^{218}Po, and ^{214}Po), and the solid red line accounts for the total fit function applied to the histograms. For the low rate scenario (A1), only the ^{222}Rn and ^{218}Po contributions are present, while for the high rate period, the three peaks are considered.

contamination in the fiducial yield measurement during A1, the overall systematic uncertainty in the activity measurement is estimated to be 16% (possibly dominated by energy miss-reconstruction effects and event reconstruction inefficiencies). Therefore, the definitive reported activity for the ^{222}Rn during the low activity period (A1) is $38.1 \pm 2.2(stat) \pm 5.9(sys)$ mBq/m^3.

Another important one concerns the presence of $^{220}\mathrm{Rn}$ in the system.[4] In principle, the A3 data suggest the null presence of such isotope in the chamber, and its presence is estimated to represent a $\sim 10^{-3}$ fraction compared to the $^{222}\mathrm{Rn}$ activity. However, the situation in A1 is not that clear. The fit model does not describe data accurately, and there is a ∼17 % of unaccounted alpha events. They could be justified due to alpha energy reconstruction biases and poor energy resolution effects, with no need to include other significant alpha emitters beyond the already considered isotopes. Another interpretation would be that this excess around the 6–7 MeV region is caused by sub-dominant contributions from the $^{220}\mathrm{Rn}$ chain, explaining the mentioned data excess. As a summary, although no definitive statement about the presence of $^{220}\mathrm{Rn}$ can be made, it is patent that the prevailing contribution to the alpha rate production is caused by $^{222}\mathrm{Rn}$ and its progeny, also during A1.

Finally, another interesting outcome refers to ion mobility. In order to do so, it is mandatory to examine two production ratios, the $^{218}\mathrm{Po}$ to $^{222}\mathrm{Rn}$ and the $^{214}\mathrm{Po}$ to $^{218}\mathrm{Po}$, taking into account that the branching fractions chain shown in Fig. 8.1 are, essentially, 100%.

The former ratio during A3 is (31.92 ± 0.25) % (the ratio from A1 is compatible with that, within errors). The alpha particle may kick out some electrons, leaving the daughter in a charged state, having time enough (see Fig. 8.1) to migrate towards the cathode and decay there. In contrast, it may well be that during the drift, some ions get neutralized via recombination. Neutral atoms will tend to stop drifting. In order to prove that, it has been seen that the $^{218}\mathrm{Po}$ fiducial alpha decay candidates in the 6.1–6.6 MeV region have a uniform distribution. However, it is impossible to disentangle whether those decays come from a neutral daughter or a recombined one, although it shows that most of the cases involved charged $^{218}\mathrm{Po}$, up to (68.08 ± 0.25) %, as one would expect for a gaseous detector [310]. In contrast, liquid xenon behaves quite differently due to the high electron-ion recombination, in line with the ratio of (50.3 ± 3.0) % reported by EXO collaboration [311].

On the other hand, the former ratio regarding the Po isotopes during the A3 period (the only one where there is any evidence of the presence of $^{214}\mathrm{Po}$) has been determined to be (0.47 ± 0.05) %. Hence, due to the very short lifetime of $^{214}\mathrm{Po}$, this ratio can be used to extract the fraction of $^{214}\mathrm{Bi}$ produced in an ionized form from $^{214}\mathrm{Pb}$. The ratio between $^{218}\mathrm{Po}$ and $^{214}\mathrm{Po}$ is directly dependent on the fraction of neutral $^{214}\mathrm{Pb}$ and $^{214}\mathrm{Bi}$ originated in the subsequent decays. For the first alpha

---

[4] The main alpha emitters in the $^{220}\mathrm{Rn}$ chain are expected to be $^{220}\mathrm{Rn}$ ((6404.67 ± 0.10) keV [309]) and its daughter $^{216}\mathrm{Po}$ ((6906.4 ± 0.5) keV) [278].

decay (from $^{218}\mathrm{Po}$ to $^{214}\mathrm{Pb}$), it is safe to assume the same ratio already computed, given the similar energy range. Thus, the ratio can be approximated by [311]:

$$\frac{N\left(^{214}\mathrm{Po}\right)}{N\left(^{218}\mathrm{Po}\right)} \simeq \left(1 - f_{^{214}\mathrm{Bi}}\right)\left(1 - f_{^{214}\mathrm{Pb}}\right), \tag{8.2}$$

where $f_{^{214}\mathrm{Bi}}$ and $f_{^{214}\mathrm{Pb}}$ are the fractions of charged $^{214}\mathrm{Bi}$ and $^{214}\mathrm{Pb}$ produced in the respective decays.

Solving the Eq. 8.2 for the only unknown variable yields a fraction of charged $^{214}\mathrm{Bi}$ of $(98.53 \pm 0.25)\,\%$. Again, when compared to the same value computed for liquid xenon [311], $(76.4 \pm 5.7)\,\%$, the more significant recombination for the liquid phase seems to account for the difference. Additionally, the disparity between the fraction of events into charged states for the alpha and beta decays can be again owed to the dissimilar recombination behavior observed for the processes.

Therefore, there are two principal conclusions regarding ion mobility in gaseous xenon. The first one, of importance in this work, is that it is reasonable to expect that the entire of the radon-induced $^{214}\mathrm{Bi}$ events originate from the cathode position. The second one is that the almost 100 % fraction of charged daughters in beta decay events in gaseous xenon suggests a similar behavior of the Ba^{2+}, daughter of $^{136}\mathrm{Xe}$. If confirmed by future measurements, it will strongly encourage the R&D program towards the effective tagging of the Ba^{2+} (see Sec. 3.2.5).

8.2 Cathode electrons

Now it is time to evaluate the incidence that the radon-induced electrons have in the physics program of NEXT. In particular, the only really concerning isotope in the chain is the $^{214}\mathrm{Bi}$, since it presents a gamma line that enters the $0\nu\beta\beta$ ROI (see Chapter 7). With that purpose, two dedicated data-taking periods have been considered. The first one (E1) happened during a high $^{222}\mathrm{Rn}$ activity since the cold getter had been turned off for 5 days (right after the A3 dedicated alpha run). The second (E2) one corresponds to data taken 21-22 days after the getter was turned off. The main features are described in Table 8.3.

Regarding the reconstruction, it is almost analogous to the alpha runs. However, electron events cannot be considered pointlike energy deposition and, therefore, they follow the reconstruction chain up to `tracks` (see Chapter 5 for more details). The events are required to present one and only one S1 and S2, hence suppressing contamination, especially Bi-Po delayed coincidences. In addition, in order to avoid

Period	Duration (s)	Pressure (bar)	ΔV_{drift} (kV)	ΔV_{EL} (kV)	Lifetime (μs)
E1	55 203	7.20	21.0	7.0	1089–1130
E2	78 639	7.19	21.0	7.0	1289–1365

Table 8.3.: Data-taking periods for the electron-dedicated runs and their main features. The voltage differences correspond to the drift and EL regions voltage drops.

alpha-like events, the S1 yield is required to be lower than 82 PEs/PMT (see Fig. 8.3b).

Now concerning the energy reconstruction, it is relevant to notice that the energy estimation relies on the S2 signal only, unlike the alpha case. However, the method differs slightly from the procedure explained in the early chapters, mainly for two reasons. The first one is that the continuous Kr monitoring was not in place already for this data-taking period. Therefore, the lifetime and XY corrections rely on a Kr map extracted from a dedicated run two weeks prior to E1. The other one is that the final energy conversion from PEs to keV is performed by aligning the double scape peak from ^{208}Tl's 2.6 MeV gamma emission, from a $^{228}\mathrm{Th}$ calibration source in a dedicated run.

Fig. 8.7 presents the electron-like event rate for both periods as a function of z. For extended events, the z position is defined as the charge-weighted average over the time slices of the track. The image shows a noticeable decrease in the cathode events as the radon content in the system reduces. On the other hand, the rate for the region far from the cathode shows a good agreement between the periods, suggesting that those electrons have no relation with radon.

In addition, a typical topology for a high-energy (>1.5 MeV electron event originating in the cathode is depicted in Fig. 8.8, produced with a Maximum Likelihood Expectation Maximization algorithm, described in [312]. The pattern illustrated matches the expected behavior of an electron track (Sec. 3.1.4), an erratic path due to the multiple scattering, and two different sections: an initial MIP section with a propagation more straight and a second section entirely dominated by multiple scattering showing a curling path where it deposits the Bragg peak energy (the so-called blob). In addition, the track clearly depicts its origin in the cathode plane.

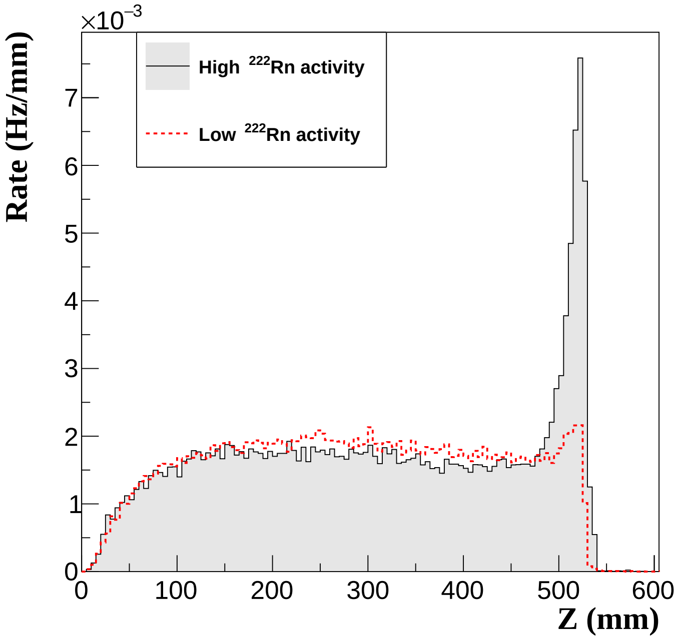

Figure 8.7.: Radon-induced electron rate as a function of z for the high rate (solid black and filled histogram) and low rate (dashed red line) periods.

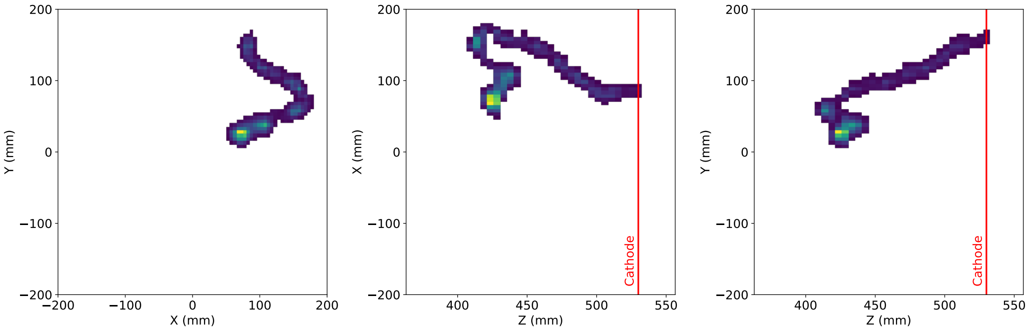

Figure 8.8.: High-energy (>1.5 MeV) electron event originating in the cathode. The three projections xy (left), zx (center), and zy (right) match the expected behavior of an electron track (Sec. 3.1.4).

A sample of cathode electrons is now prepared in order to study its energy and spatial distributions and compare it with the MC expectations. The requirement for the electron to be considered as a cathode-originated event is to present a $z_{\text{max}}>520\,\text{mm}$, where z_{max} is the greatest z position of all the slices belonging to the event. The distribution and rate of the Rn-induced electrons can be obtained by subtracting the cathode electron sample in E2 from the corresponding sample collected in E1. In this subtraction, it is taken into account the residual radon activity induced by the cold getter, still present during E2, by considering the time difference between both data-takings and the $^{222}\mathrm{Rn}$ half-life. Besides, the correction of the DAQ mask effect on the rate is applied. Additionally, a last issue must be assessed. Since the search for S1s is performed only before the S2 that triggers the event (i.e., the first half of the waveform), delayed Bi-Po events where the second decay happens half a buffer time after the trigger have not a second S1 reconstructed, as one would anticipate (and therefore are not rejected by the one and only one S1 cut). The fraction of such events has been quantified to be 5 %. Considering all this, the measured rate for radon-induced cathode electrons is (0.096 ± 0.003) Hz.

The MC production to contrast the results was obtained by generating, using the NEXUS software, 10^7 events of $^{214}\mathrm{Bi}$ decays at 7.2 bar from the cathode plane (z) and uniformly distributed across it (x and y). For completeness, due to the short lifetime of $^{214}\mathrm{Po}$, its decay is also simulated according to the proper half-life time distribution. The production was processed via the full simulation chain (i.e., through DETSIM and DIOMIRA) to produce RWFs. From there, the same procedure afore-explained was applied to data and MC up to `tracks`. For the MC normalization, it has been estimated using the radon measurement from the A3 period. The volume now includes all the relevant parts of the detector from which a $^{222}\mathrm{Rn}$ decay product can reach the cathode plate, i.e., all the active and the buffer gas volumes of the apparatus. The normalization also takes into account the DAQ inefficiency correction and the 1.0 day average time difference between A3 and E1 runs. As a result, the estimated live-time[5] for the initial events is (20.5 ± 5.0) days. The large error emerges from the uncertainty in the actual volume relevant for the $^{222}\mathrm{Rn}$ to be considered for the calculation.

Consequently, from the MC simulation and the normalization derived from the alpha results, the expected rate of radon-induced electrons in the cathode is (0.142 ± 0.028) Hz. This expectation agrees with the data measurement within errors. Essentially, this agreement shows that $^{222}\mathrm{Rn}$-induced alpha production in the fiducial volume is consistent with the $^{214}\mathrm{Bi}$-induced electron production rate from the cathode at $1.6\,\sigma$. Therefore, alpha data has been demonstrated to be a valuable tool to understand that kind of background source in NEXT.

Regarding the z and E distribution of data and MC for cathode electrons, they are displayed in Fig. 8.9, where both rates are absolutely normalized. The z distribution depicts a peak around the cathode, asymmetric towards low z values (this is due to the extent of electron tracks in the active volume and the definition of the z coordinate as the charge-weighted average of all the slices of the event). On the other hand, the energy spectrum shows a featureless and monotonically

---

[5] Live-time accounts for the actual time that the detector is taking data, once removed the dead time.

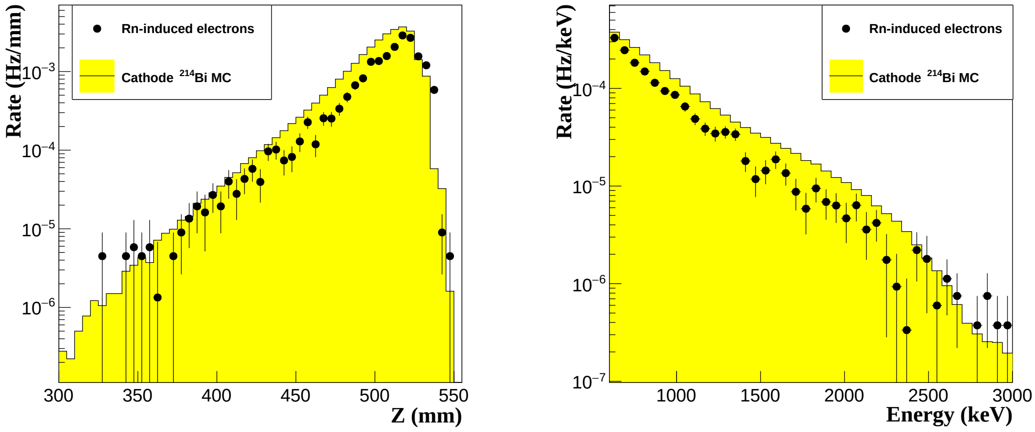

Figure 8.9.: Radon-induced electrons from cathode (black dots) superimposed to the MC expectation (yellow histogram), as a function of the reconstructed energy (left) and the z coordinate (right).

decreasing distribution. This absence of peaks originates from the selection applied. When a fiducial selection is applied (for instance, see Fig. 6.11), the only events surviving the cuts are beta electrons originating in the active volume and gamma lines interacting in it. Notwithstanding, the selection implemented here enhances the presence of electrons tracks starting on the edge of the chamber (the only gamma interaction entering should be produced within the last 2 cm of the chamber, which is a 2 % of the active volume). Thus, the spectrum represents beta decay characteristics, as expected. Since the runs took place with the outer lead castle open, variations in the ambient background between E1 and E2 periods may account for some distortions in the data, especially in the 1.4–1.7 MeV range. In particular, a variation between periods of 9 % in the total background rate in the fiducial volume has been observed.

Nevertheless, the differences between data and MC are not expected to significantly impact the extrapolations for the NEXT-100 detector reported in the next section.

8.3 Monte-Carlo study of radon-induced backgrounds for the $\beta\beta$ searches

This last section will be devoted to the study of the impact that the radon-induced contaminations have on the NEXT physics program, both for NEXT-White ($2\nu\beta\beta$)

Detector	NEXT-White	NEXT-100
Maximum drift length (m)	0.530	1.300
Active region diameter (m)	0.396	1.070
Active gas volume (m^3)	0.065	1.169
Total (active + buffer) gas volume (m^3)	0.081	1.286
Surface in contact with total gas volume (m^2)	1.068	6.606
Gas pressure (bar)	7.2–15	15
Xenon mass in active volume (kg)	2.6–5.6	100.5

Table 8.4.: Comparison of NEXT-White and NEXT-100 detector geometries, and adopted/-planned run configurations.

and NEXT-100 ($0\nu\beta\beta$) cases. A review regarding the characteristics of the detectors may be found in Chapter 4 and Sec. 3.2.4 respectively. Additionally, for the clarity of the discussion along this section, the main features for the detectors are summarized in Tab. 8.4.

8.3.1 Implications on the two-neutrino measurement in NEXT-White

For the NEXUS step (Sec. 5.2.1), a total of 10^7 events of ^{214}Bi decay have been generated from the cathode at 15 bar.[6] Only NEXUS events with deposited energy >600 keV are stored for further processing. The simulation configuration is the same as for the 7.2 bar MC used in the previous section. The same processing chain and quality cuts are applied now, with the exception of the ones regarding the S1. S1 peaks as wide as 1 μs are allowed, and no upper limits on the S1 amplitude or charge are placed. The S1 peak finding conditions have been relaxed to efficiently reconstruct cathode alpha S1s so that events with both an electron-like s1 and an alpha-like S1 can be rejected. For the final $2\nu\beta\beta$ candidate selection, the following cuts are considered:

1 S1 and 1 S2: Only events with one S1 peak and one S2 peak are kept.

Non-zero active volume hits: It is possible to have events where all hits are reconstructed for z >530.3 mm, that is outside the active volume boundaries. This unphysical situation can occur in ^{214}Bi-^{214}Po delayed coincidences, where the

---

[6] Nominal pressure of NEXT-White detector.

reconstructed S1 originates from the electron and the reconstructed S2 from the time-delayed alpha particle. Such events are rejected in order to suppress all alpha particle activity.

Fiducial radius: Events are required to satisfy R_{max} <178 mm, where the maximum radial position is obtained from the entire collection of reconstructed hits in the event. In other words, no reconstructed hits within 20 mm from the active volume boundaries are allowed in the barrel region.

Fiducial z position: Events are required to satisfy Z_{min} >20 mm and z_{max} <512 mm, where the minimum and maximum z positions are extracted from the entire collection of reconstructed hits in the event. That means that no reconstructed hits within 20 mm from the active volume boundaries are allowed in the two end-cap regions.

Single track: Once the tracks are reconstructed using the BFS algorithm with a 10 mm voxel size (see Sec. 5.1.4), only events with a single reconstructed track are kept.

Blob cut: Energy *blob* candidates are built around the two track extremes. For each track extreme, if an energy greater than 300 keV within a radius of 15 mm is found, the extreme is considered to be a valid blob candidate. Events without two valid blob candidates are rejected.

Energy ROI: The event energy E_{reco} is obtained by summing the hit charges after correcting for detector non-uniformities in response and after applying an energy scale factor to convert PEs into keV. Only events within the energy region of interest (ROI), defined in the $2\nu\beta\beta$ case to be E_{reco} >700 keV, are retained.

In addition to the aforementioned full MC production, there was also a parallel analysis performed with FANAL pseudo reconstruction tool (see Sec. 5.2.4), assuming a 0.5 % FWHM resolution at $Q_{\beta\beta}$ and a voxel size of 15 mm. The reason for this is twofold. On the one hand, it is a helpful way to implement a crosscheck for the full analysis result. On the other hand, it is also mandatory to understand the behavior of the pseudo reconstruction for the NEXT-100 case, where fanal is the only practical solution since the full chain was not yet fully refined. The scheme for the selection is analogous to the full simulation with the exception of the cuts regarding S1 and S2. Since fanal does no step concerning waveforms, those selections are meaningless, especially the one and only one S1 and S2.

Selection	Full analysis	Fast analysis
None	1	
Min. deposited energy	$(1.536 \pm 0.001) \cdot 10^{-1}$	
1 S1 and 1 S2	$(1.141 \pm 0.001) \cdot 10^{-1}$	N/A
Non-zero active volume hits	$(1.130 \pm 0.001) \cdot 10^{-1}$	$(1.500 \pm 0.001) \cdot 10^{-1}$
Fiducial radius	$(8.166 \pm 0.009) \cdot 10^{-2}$	$(1.069 \pm 0.001) \cdot 10^{-1}$
Fiducial z position	$(5.757 \pm 0.024) \cdot 10^{-3}$	$(2.813 \pm 0.017) \cdot 10^{-3}$
Single track	$(5.092 \pm 0.024) \cdot 10^{-3}$	$(1.713 \pm 0.013) \cdot 10^{-3}$
Blob cut	$(9.396 \pm 0.097) \cdot 10^{-4}$	$(7.664 \pm 0.088) \cdot 10^{-4}$
Energy ROI	$(8.622 \pm 0.093) \cdot 10^{-4}$	$(3.001 \pm 0.055) \cdot 10^{-4}$

Table 8.5.: Cumulative efficiencies through the various event selection criteria for $2\nu\beta\beta$ searches in NEXT-White. The uncertainties are statistical only.

Table 8.5 provides the cumulative efficiencies (i.e., all of them refer to the total number of events generated) for all the cuts mentioned above for both simulations. After all cuts, the background acceptance for the full analysis of the $2\nu\beta\beta$ is 8.622 ± 0.093. In contrast, FANAL result is around 3 times higher, as expected for a more idealized simulation and analysis.

In order to estimate the radon-induced background arising from those results, the rate from the low activity alpha run, $(38.1 \pm 6.3)\,\mathrm{mBq/m^3}$, and the ultimate efficiency in Table 8.5,$(8.622 \pm 0.093) \cdot 10^{-4}$. As well as the cathode-electron case, the $^{222}\mathrm{Rn}$ is assumed to present a uniform concentration across the chamber, including the active volume and buffer. The estimated radon-induced background rate for events above 0.7 MeV is (85 ± 14) counts / yr, or equivalently $(2.69 \pm 0.44) \cdot 10^{-3}$ mHz. Contrasting this rate with the measured radiogenic[7] rate for events above 1 MeV passing all the $2\nu\beta\beta$ selection cuts, (0.248 ± 0.010) mHz [261], the radon-induced contribution is, at least, two orders of magnitude smaller. Therefore, it is safe to assume it is negligible within the NEXT-White physics program.

Regarding the compatibility among the two simulations, although the final efficiency is not entirely harmonious, the overall features of the spectra seem to agree excellently. Fig. 8.10 depicts the distributions, unit-area normalized, along

---

[7] As a reminder from Chapter 7, radiogenic backgrounds refer to events originating from radioactive decays of the impurities present in all materials. In this case, more specifically, the expected contributors are $^{40}\mathrm{K}$, $^{60}\mathrm{Co}$, $^{208}\mathrm{Tl}$, and $^{214}\mathrm{Bi}$.

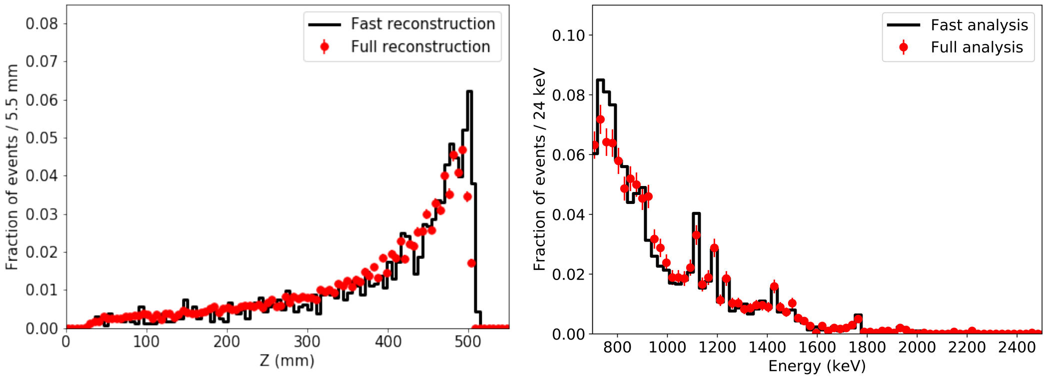

Figure 8.10.: Distributions of average z position (left) and reconstructed event energy (right) for all the events passing the $2\nu\beta\beta$ selection (explained in the text) for cathode ^{214}Bi simulated decays at 15 bar in NEXT-White. Fast analysis (FANAL) is depicted with black histograms and the full analysis with red dots. All the curves are unit normalized.

z and E for the two simulations for all the events passing all the $2\nu\beta\beta$ selection, showing the accordance. As well as the cathode electron case, the z distribution peaks around the cathode plate position. On the other hand, the energy distribution is somewhat different from the cathode electron's since it depicts a typical gamma line spectrum. There are several visible gammas, the full energy depositions at 768, 1120, 1238 and 1764 keV, and the double-escape peaks at 1182 and 1426 keV from the 2204 and 2448 keV gamma-ray lines, respectively [280].

8.3.2 Implications on the neutrinoless measurement in NEXT-100

In this case, the NEXUS step comprises a total of 10^8 events fo ^{214}Bi generated at 15 bar. Since the physics program of interest here is the $0\nu\beta\beta$, the requirement for the minimum energy deposit in the chamber for the initial stage is set to 2.3 MeV.

However, as anticipated in the previous section, the full analysis chain was not thoroughly developed or optimized to deal with the NEXT-100 processing at the time of this study. Hence, the remaining option is to proceed via the fast analysis approach. The whole process chain and selections are similar with two significant exceptions: the aforementioned initial cut in the NEXUS output and the definition of the ROI region. Because of the features of the $0\nu\beta\beta$ decay, being a monoenergetic peak at 2458 keV, the energy region is selected accordingly to be $E_{\text{reco}} \in$(2453, 2475) keV (22 keV wide), an asymmetric region (accounting for the presence of the ^{214}Bi peak) following the work in [237]. The efficiencies per cut are presented in Table 8.6.

Selection	Fast analysis
None	1
Min. deposited energy	$(1.593 \pm 0.001) \cdot 10^{-2}$
1 S1 and 1 S2	N/A
Non-zero active volume hits	$(1.417 \pm 0.001) \cdot 10^{-2}$
Fiducial radius	$(1.207 \pm 0.001) \cdot 10^{-2}$
Fiducial z position	$(8.029 \pm 0.028) \cdot 10^{-4}$
Single track	$(4.453 \pm 0.021) \cdot 10^{-4}$
Blob cut	$(9.528 \pm 0.098) \cdot 10^{-5}$
Energy ROI	$(4 \pm 2) \cdot 10^{-8}$

Table 8.6.: Cumulative efficiencies through the various event selection criteria for $0\nu\beta\beta$ searches in NEXT-100. The uncertainties are statistical only.

It is patent how the much more strict selection cuts (mainly the ROI one) yield a total efficiency four orders of magnitude smaller than the $2\nu\beta\beta$ case in NEXT-White, presented in Table 8.5. The rest of the selections behave similarly, with compatible individual efficiencies.

In order to translate this result into a background rate, first, for a more conservative approach, the ratio between the fast and full efficiencies for the NEXT-White case is considered, resulting in an inferred efficiency of about $1.1 \cdot 10^{7}$ (i.e., this implies a sort of rough estimation of what the result for a full analysis for the NEXT-100 data would be). Then, when extrapolating the results from the alpha rate computed in Sec. 8.1.2, there are two approaches. This is due to the lack of identification of the primary source of $^{222}\mathrm{Rn}$.

The first assumes that the dominant contributor to radon presence in the chamber is the gas system emanations, thus external to the vessel. Given that the same gas system is foreseen for both detectors' operations, the total radon activity in the chamber would result to be the same. This results in an expected $^{214}\mathrm{Bi}$ rate of $(9.8 \pm 1.6) \cdot 10^{4}$ counts/yr.

The second suspects that the dominant contribution arises from the inner detector components, thus by the chamber's surfaces emanations. In this scenario, the contribution is supposed to increase linearly with the total surface of the detector exposed to the gas. Unlikely, this would imply a factor 6 more background for

Scenario	Total ^{214}Bi activity from cathode (counts/yr)	Background acceptance	$0\nu\beta\beta$ background rate (counts/yr)
Optimistic	$(9.8 \pm 1.6) \cdot 10^{4}$	$(4 \pm 2) \cdot 10^{-8}$	$(3.9 \pm 2.1) \cdot 10^{-3}$
Pessimistic	$(6.1 \pm 1.0) \cdot 10^{5}$	$(1.1 \pm 0.5) \cdot 10^{-7}$	0.07 ± 0.03

Table 8.7.: Radon-induced background rates expected for the $0\nu\beta\beta$ selection in NEXT-100 under different assumptions.The optimistic scenario assumes the radon to emanate from the gas system, being, therefore, the same as in the case of NEXT-White, while the efficiency is the fast analysis result presented in Table 8.6. While the pessimist one assumes the radon background to escalate with the detector inner surface area, and the efficiency is estimated for the case of a full reconstruction chain. See details in the text.

the NEXT-100 case when compared to NEWXT-White's (see Table 8.4). Thus, the predicted rate is $(6.1 \pm 1.0) \cdot 10^{6}$ counts/yr.

Therefore, by combining the two possible efficiency estimators and the two approaches for extrapolating the $^{222}\mathrm{Rn}$ presence for NEXT-100, it is possible to build two scenarios for the final incidence of this background on the $0\nu\beta\beta$ searches. The so-called pessimistic scenario assumes the worst predictions for both the lower limit on $^{214}\mathrm{Bi}$ activities extrapolation and the full-like efficiency in an attempt to provide a very conservative result, a kind of worst-case possible. On the other hand, the optimistic approach assumes the upper limits on $^{214}\mathrm{Bi}$ activities extrapolation and the fast analysis efficiency.

Even though the optimistic scenario is not based on a full reconstruction and reconstruction analysis, it is not an unrealistic estimate. In fact, it can be a fair approximation of the best possible background rejection performance when applied novel techniques such as deconvolution [227] and DNN classification algorithms [260], as well as potential detector upgrades.

The results for both outlines are summarized in Table 8.7. Those numbers ought to be compared with the estimation from the radioactive contribution, expected to be at the level of $4 \cdot 10^{-4}$ counts/keV· kg· yr, or in this case,[8] ~1 counts/yr [237]. Therefore, even at the most adverse conditions, the prediction for the radon-induced backgrounds remains one order of magnitude slower than the dominant source and possibly much more negligible. In summary, the conclusion is that radon-induced backgrounds will occur at a tolerable level for the NEXT-100 physics campaign.

---

[8] A 22 keV-wide energy window and 90 kg of $^{136}\mathrm{Xe}$.

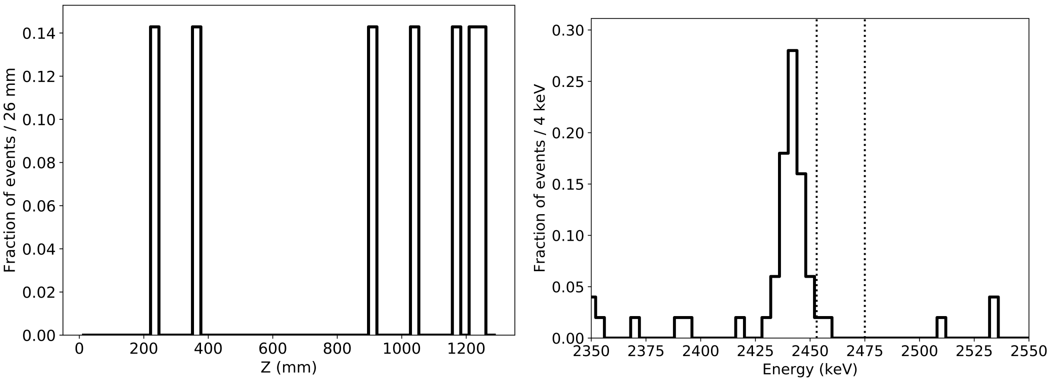

Figure 8.11.: Distributions of average z position (left) and reconstructed event energy (right) for all the events passing the $0\nu\beta\beta$ selection, except the ROI one, for cathode ^{214}Bi simulated decays at 15 bar in NEXT-100. All the curves are unit normalized.

Notwithstanding, for the future ton-scale detector program, it is expected to become a more serious issue, and, eventually, an active filtration system to mitigate radon emanation might be considered by the NEXT Collaboration.

Figure 8.11 presents the unit-area normalized distributions for the z and E variables. Both distributions include all the selection cuts for the $0\nu\beta\beta$, except for the ROI one. This is done to highlight the importance of the ^{214}Bi gamma line at 2448 keV, right next to the ^{136}Xe $Q_{\beta\beta}$, and even at an ideal resolution, entering the ROI. On the other hand, the z distribution shows a tendency for these events to happen near the cathode position, which can be an additional tool for their identification.

9

Radiogenic background activity in NEXT-White and implications in the $\beta\beta$ searches

The radioactive impurities contained in all kinds of materials represent the dominant background for any experiment aiming for very rare events [302, 313, 314, 315]. The final ability to pursue such searches depends dramatically on reducing, mitigating, and characterizing potentially harmful isotopes.

The reducing strategy lies in searching for the most radiopure materials to be used in the detector construction. That implies the screening of every single piece planned to be used in order to assess the potential usage (depending on the final position within the machine, different tolerance levels are considered). The screening process must be meticulous and detailed, but, unfortunately, there are no completely radioactive-free materials.

The second strategy, mitigation, attempts to shield the active volume from the remaining activity passively. In order to achieve that, a set of thick layers are placed in the way of incoming gammas, the two lead castles, and the inner copper shield (see Sec. 4.1.6 for more detail).

Finally, the potential gammas reaching the gas need to be quantified and described, attempting to deduce their origin and source. Those results can be extrapolated for the $2\nu\beta\beta$ dedicated Run V because the principal operation conditions are kept the same (e.g., the gas pressure and TPC voltages).

The analysis is based on an intense and dedicated MC campaign, the Run IV low background data, and dedicated high-energy calibration data taken along the Run IV period.

This chapter will present the data selection, the MC background model and its comparison with the actual measurements, and, finally, a brief discussion about the extrapolation of those results in the $\beta\beta$ analysis.

9.1 Background Model

The background model of the experiment refers to the a priori set of expectations built to estimate the potential background level, sources, and their implications for the various physics programs. It gathers information for all kinds of backgrounds (explained in detail in Chapter 7). Notwithstanding, since both the radon-induced and cosmogenic inputs are subdominant and each contribution must be considered separately, this chapter will focus only on the study of radiogenic ones. Therefore, from now on, the background model will refer only to the radiogenic component, unless otherwise specified.

It represents a fundamental tool in order to understand the physics potential and the ultimate background index for a given stage of the program. In addition, it is a handy instrument to evaluate the detector construction (i.e., the materials of use for every constituent, assessing its viability) and new strategies for background reduction (both via the implementation of further passive shielding systems and the development or refinement of algorithms for rejecting the noise).

The construction of the background model lies in two central constituents: the materials screening and the efficiencies computation.

9.1.1 Components activity assessment

A material screening and selection process for NEXT components has been underway for several years, with a dedicated team, both to inform the experimental design and to help construct a realistic background model. The goal is to determine the activity levels regarding the most crucial isotope chains[1] using gamma-ray spectroscopy with ultralow background High Purity germanium (Ge) detectors, and complementary techniques.[2] After an extensive campaign, the results have shed light on the contamination of the materials used in the shielding, pressure vessel, electroluminescence and high voltage components, and energy and tracking readout planes.

Due to the limited capacity of the germanium detector and the finite time for the task, only small batches for each tested item can be screened. Thus, the model has an

---

[1] As a reminder from Chapter 7, the isotopes considered from a radiogenic point of view are ^{40}K and ^{60}Co regarding the $2\nu\beta\beta$ analysis and ^{208}Tl and ^{214}Bi concerning the $0\nu\beta\beta$ searches.

[2] Serving as additional support for the standard technique, ICP-MS (inductively coupled plasma mass spectrometry) and GDMS (glow discharge mass spectrometry) were also used. However, they are not sensitive to the isotopes of interest but to the upper part of the decay chain, and secular equilibrium must be assumed.

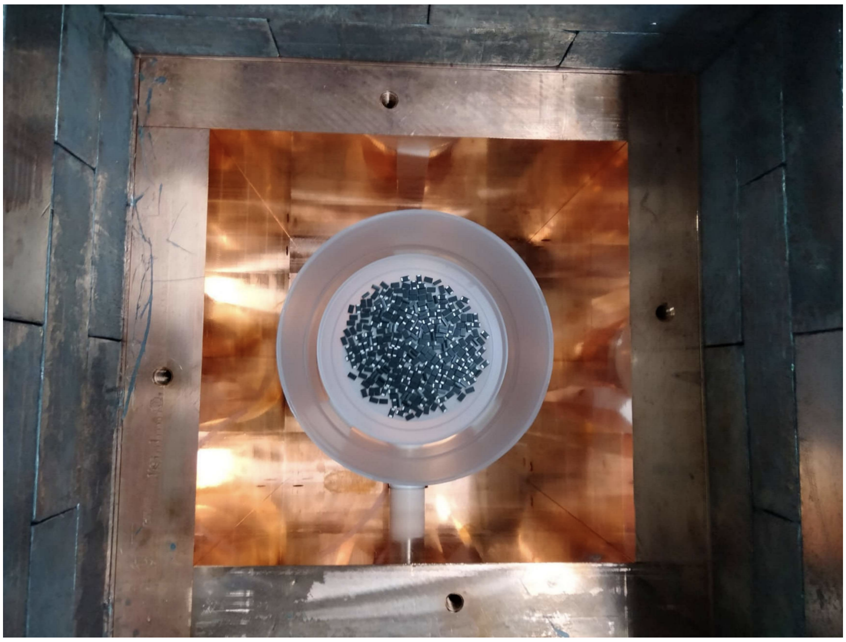

Figure 9.1.: Example of a sample analyzed at the Radiopurity Service of the LSC for NEXT. In this case, the screened items are capacitors to be used in the PMT bases of NEXT-100, and the specific detector is the *Anayet*.

implicit assumption that the examined material behaves as a whole like the sample provided for the analysis. On other occasions, the complete system can undergo the process altogether (e.g., the SiPMs and PMTs, and other small components). An example of a set of elements to be tested in the HPGe detectors can be found in Fig. 9.1. Additionally, an instance of a typical spectrum from a screening measurement is depicted in Fig. 9.2.

Finally, due to the unavoidable ambient background, the HPGe may find no evidence for some isotopes in some cases. If possible, the material was processed via complementary methods in order to determine the activities accurately. If not, a 95 % CL upper limit is set. For most elements, the upper limit is enough for a safe determination of their viability; others require a literature exploration, e.g., the case of the quartz used for the anode.

In consequence, a set of components constituting the machine is considered, accounting for their material composition following the detector designs. Therefore, it is possible to assess the expected activity for each component once the forming materials have been screened, scaling accordingly to reproduce its actual presence. In addition, a contribution from the radon-induced ^{214}Bi decays from the cathode is also acknowledged, in compliance with the results presented in the previous chapter.

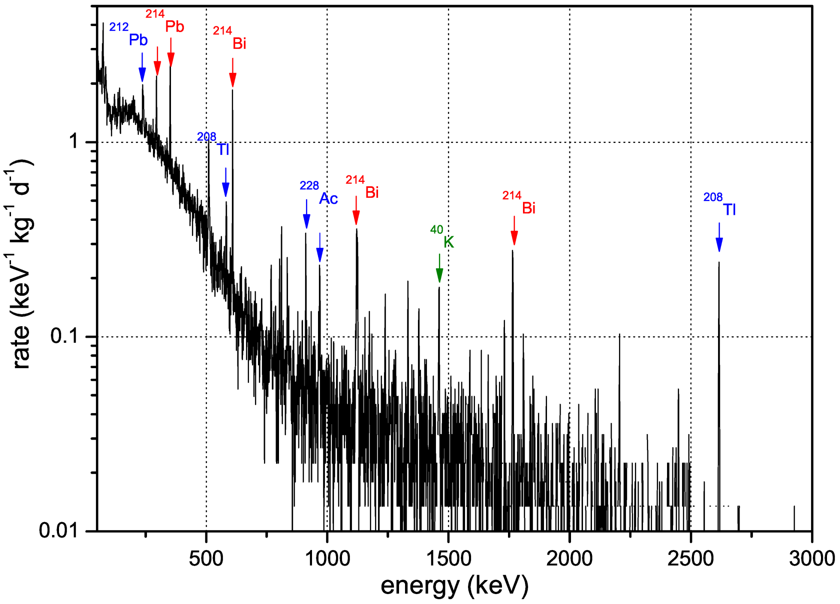

Figure 9.2.: Example of a recorded energy spectrum from a screening measurement lasting 38 days by the *Oroel* HPGe detector at LSC for NEXT. The main gammas from the uranium (red), thorium (blue), and ^{40}K (green) chains are marked. Figure from [316].

Moreover, also the contribution from the $^{136}\mathrm{Xe}\ 2\nu\beta\beta$ is reflected once determined that the fraction of $^{136}\mathrm{Xe}$ in the depleted gas is $(2.6 \pm 0.2)\,\%$.

A more comprehensive review of the methods and the results can be found in the set of publications by the collaboration regarding the radiopurity assessment campaign [250, 316, 317, 318, 319, 320, 321]. Additionally, a Table presenting the activities in NEXT-White can be found in Appendix C.[3]

9.1.2 Efficiencies estimation

The second cornerstone in the background model building is the estimation of the number of events that deposit energy in the active volume for each component and isotope, denoted as the efficiency. I.e., this efficiency represents a translation between the activity measurement covered in the previous section and the actual impact in the detector.

---

[3] The table is a minor updated version of the exact assumptions for this work. However, the changes are minimal, and the conclusions drawn are still the same. The most significant difference is the addition of the tracking frames volume to describe stainless steel frames supporting anode plate and gate mesh, representing ∼1 % of the total expected rate.

The strategy for the appraisal draws upon simulations. The detection efficiency is therefore defined as the number of radioactive decays depositing at least 400 keV in the detector active volume divided by the total number of radioactive decays. In order to compute the efficiency, a NEXUS (see Sec. 5.2.1) production is conducted for each component (the same ones defined in the previous step) and isotope. The components are carefully modeled as GEANT4 volumes, taking into account the designs and materials implicated. A total of 22 volumes are contemplated, resulting in a total of 84 background sources.[4]

The simulation is performed using the geometry and characteristics of Run IVc (thus, including the ILC, see Sec. 4.1.6), and a pressure of 10.1 bar. A total of 10^{11} NEXUS events have been generated, of which around $1.5 \cdot 10^6$ survived the minimum deposit energy requirement and continued the processing, corresponding to an exposure of 5.48 year. The results (available in the Appendix C) show the expected behavior, where the outermost components, as the lead castle, have efficiencies around 10^{-8}–10^{-5}, whereas the elements exposed to the gas have efficiencies raging 10^{-2}–$5 \cdot 10^{-1}$.

9.1.3 EVENT MIXER

The last piece in the background model construction is the EVENT MIXER algorithm. It combines the measured activities and the estimated efficiencies in order to produce a realistic expectation for the background behavior in the detector. In short, it computes the expected rate of events for a given exposure for each volume and isotope. Then randomly selects n events for each isotope-volume pair, where n follows a Poisson distribution which average is the expected rate.

The output of the EVENT MIXER is then propagated through the standard software chain explained in Chapter 5, including the electronic simulation (DETSIM and DIOMIRA) and the event reconstruction (IC up to `tracks`).

Fig.9.3 shows the model expectations for the energy and average axial position distributions for the NEXUS events passing the minimum energy threshold. Regarding the energy distributions per isotope, it is patent the role that the ^{40}K and ^{60}Co have for mid and low energies (up to their photopeaks at 1461 keV [285] and 1332 keV [286], respectively), and, in contrast, the high energy regime is dominated by the ^{208}Tl and ^{214}Bi. In contrast, the distribution per volume categories show

---

[4] 20 GEANT4 volumes include the four isotopes (a total of 80 sources), another volume includes only 2 isotopes, plus the contribution from the radon-induced ^{214}Bi in the cathode, and the $2\nu\beta\beta$ signal for a total of 84 sources.

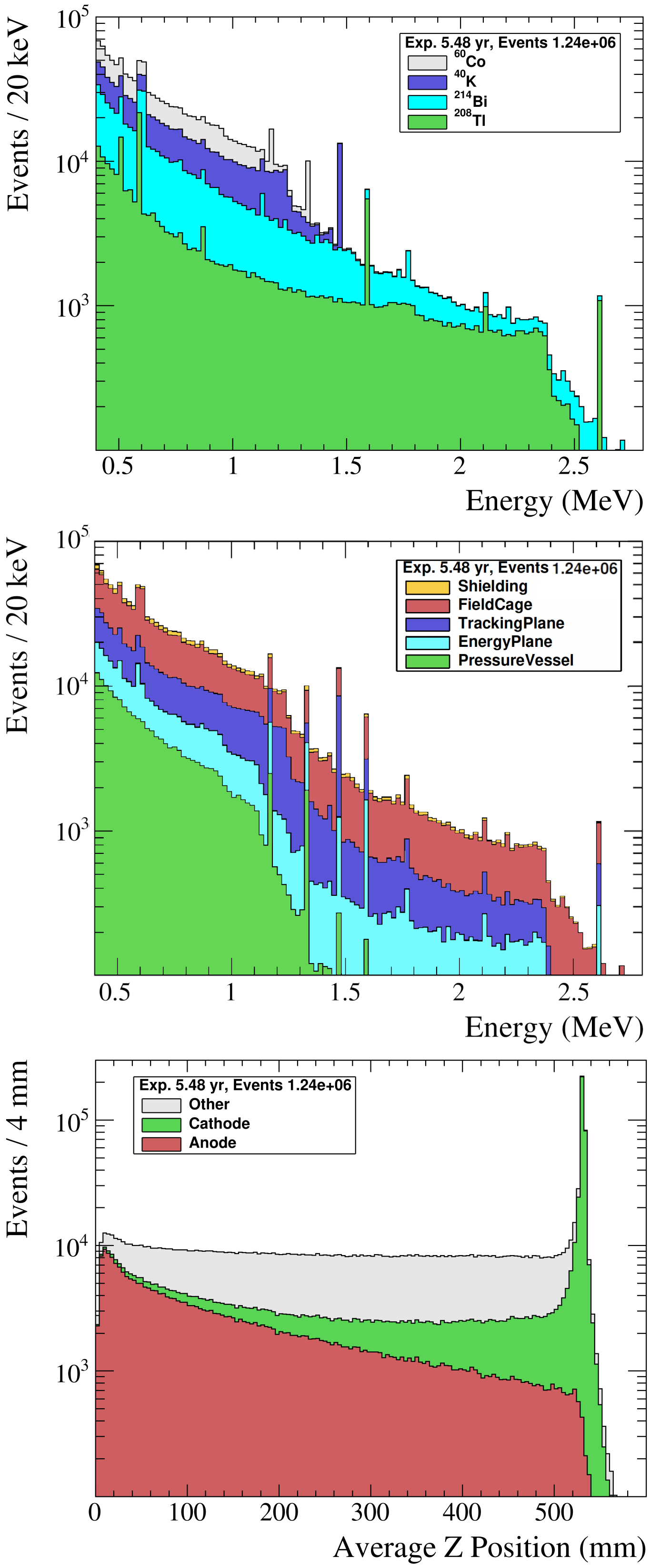

Figure 9.3.: Distributions of the background model expectations for the events fulfilling the NEXUS minimum deposited energy requirement of 400 keV in the active volume. The stacked histograms depict the energy distribution separated by the isotope (top) and volume (middle) contributions and the average z position distribution classified by the fit volume type (see Fig.9.7).

that there is no dominant isotope in any section. However, it is patent the low contribution at high energies from the vessel, as well as the almost negligible impact of the shielding sections. The z distribution certainly depicts the advantage of the fit region definitions (see Fig.9.7 as all of them show a distinct profile: the "Anode" peaks at low drift and rapidly decreases; the "Cathode" is the opposite, peaking at the cathode position and quickly fading towards low z; last, the "Other" present a more flat behavior, although they also present a small peak around the cathode position.

9.2 Background characterization

It is time to contrast the background model to the measured data. This is not only helping to validate the model itself but also sheds light on the actual contributions to the total background by making use of the energy and topologic information of the events. Additionally, this comparison allows a better understanding of the expectation for the $^{136}\mathrm{Xe}$ campaign.

This section will focus on the fit performed to Run IVc data in order to disentangle the contributions. It will cover the data preparation, fit description, and results.

9.2.1 Data preparation

Processing and selection

The data incorporated for the fit include all the Run IVc. It has been processed following the steps described in Chapter 5, from the binary DAQ output to `tracks`. A set of cuts ensure a minimum quality in the S1 and S2 properties. In addition, there is a veto against alpha events based on the amplitude of the S1 signals (see Fig. 8.6).

Analogously with the alpha-electron analysis, the so-called inclusive sample is defined by requiring all the events to have one and only one S1 and S2. Moreover, the fiducial selection also rejects any event that presents any reconstructed hit within 20 mm of the detector edges. This last cut eliminates all the beta events occurring in the detector's walls, reducing the background significantly. Therefore, the only remaining background is expected to be induced by gamma interactions in the fiducial volume.

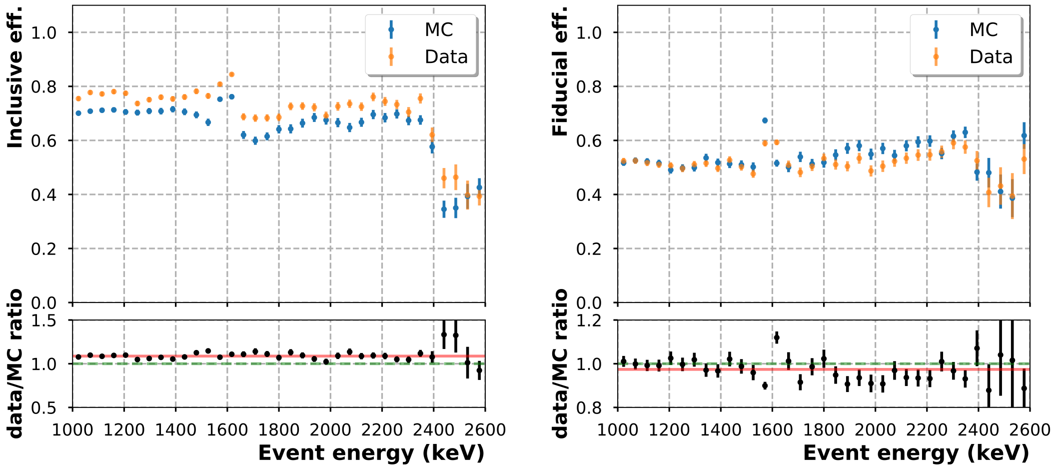

Figure 9.4.: Efficiency of inclusive (left) and fiducial (right) selection as a function of the event energy for data (orange) and MC (blue). The lower panel show the ratio between data and MC for each selection, fited to a horizontal line (i.e., a constant).

The efficiency[5] for the selections has been evaluated using calibration runs, where a source of ^{228}Th is placed in the calibration port at the top of the vessel (see [259] for further detail). This source provides a large sample of ^{208}Tl candidate events, 42 788 of them fulfill the >1 MeV energy requirement, prior to the inclusive selection. In parallel, an MC sample of 40 523 ^{208}Tl events has been produced, for comparison proposes. Both calibration and MC data were processed strictly as the background (with the obvious exception of the EVENT MIXER step).

Fig. 9.4 presents the efficiencies of the inclusive and fiducial selection for them as a function of the event energy. The first observation would be the fair agreement of the behavior with the energy. Also, the peak in efficiency observed around 1.6 MeV matches the position of the ^{208}Tl double escape peak. This increase is therefore expected since the double electron tracks[6] are shorter than the single-electron ones. Thus, they tend to be more likely fully contained in the detector and reconstructed as a unique S2. The drop around 2.4 MeV is owed to multi-Compton events from the ^{208}Tl gamma.

The relative inclusive and fiducial efficiencies are, for data, (74.8 ± 0.2) % and (52.5 ± 0.3) %, respectively, whereas for MC, they are (68.5 ± 0.2) % and (53.7 ± 0.3) %. Hence, there is some tension between data and MC regarding

---

[5] The efficiency is defined as the number of events passing the selection over the total number of events.

[6] Technically, the double escape event consists of an electron-positron pair, but the effect in the track length is general to any electron-like pair.

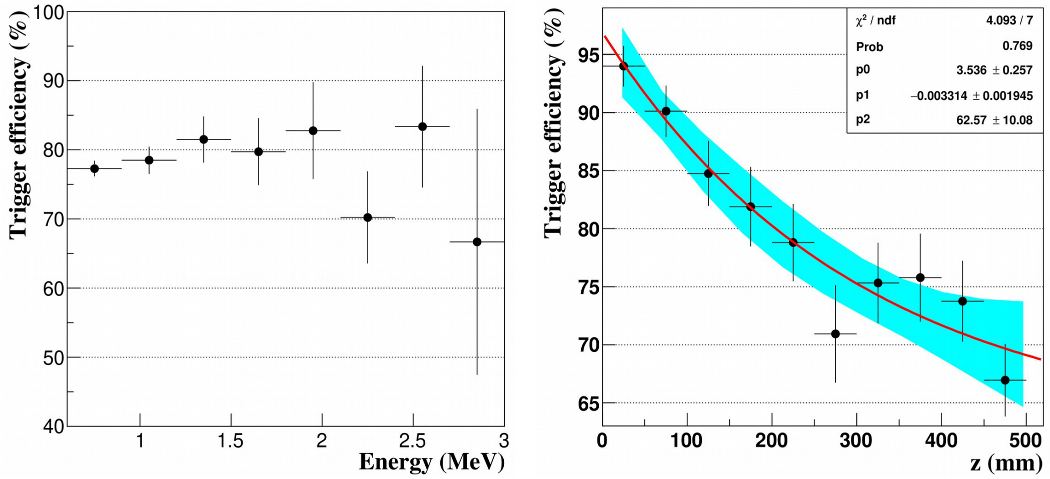

Figure 9.5.: Trigger efficiency as a function of the event energy (left) and average z position (right). The z distribution presents a fit (red line) superimposed and its 67 % coverage band.

the reconstruction stage. This discordance is taken into account when comparing the background samples in data and MC. In order to do so, the background expectations are re-scaled according to the best-fit of data and MC efficiency ratios in Fig. 9.4, and the uncertainty in the ratios is propagated when extracting low-background expectations after the fiducial selection.

Trigger efficiency correction

Dedicated trigger studies showed a bias of the acquisition due to the time coincidence window between the two PMTs in use ($0.1\,\mu$s).This small window affected events differently depending on the drift position, creating a tendency to reject more events the larger the z (attributable to diffusion).

Even though the bias is corrected for the Run V and subsequents, it must be considered for the accurate evaluation of the background data. A trigger efficiency of $(75 \pm 1)\,\%$ ($(74 \pm 2)\,\%$) has been computed for the inclusive (fiducial) sample of background events. Fig. 9.5 depicts the trigger efficiency as a function of the energy of the event and its average z position. It shows a flat response regarding the energy; however, as anticipated, it exhibits a significant variation along the drift direction.

In order to account for the effect, a heuristic model is proposed:

$$z_{\text{bias}} = \left(e^{\alpha-\beta\cdot x} + c\right) \cdot \frac{\tau}{100}, \tag{9.1}$$

where α $=3.54 \pm 0.26$, β $=(3.3 \pm 1.9) \cdot 10^{-3}\,\mathrm{mm}^{-1}$, c $=67 \pm 10$, $\tau = 0.9476$ accounts the trigger deadtime, and the 100 factor translates the percentage into per-unit.

An unpleasant side-effect of the bias is the loss in the characterization power of the z since the distant features get somewhat reduced. Notwithstanding, as demonstrated later, there is still discrimination power that allows the better characterization of the background sources.

Energy scale and resolution

The next stage in the data preparation refers to the energy, both for data and MC.

Sec. 5.1.4 explains that when the hits are corrected by the Kr map information, there is a conversion from photoelectrons to electronvolts. This energy scale is acceptable for the posterior steps in the processing, but, unfortunately, it is not accurate enough for the analysis. This is mainly due to the fact that the Kr map is only providing a single translation point at very low energies and can miss effects that only appear at moderate and high energies. Therefore, an additional energy calibration is performed by extracting the conversion factors from a calibration run close to the background data-taking. The calibration sample presents the photopeak from $^{137}\mathrm{Cs}$ at (661.659 ± 0.003) keV [276] and the $^{208}\mathrm{Tl}$ photopeak at (2614.529 ± 0.010) keV [277] and its double-scape peak at (1592.531 ± 0.010) keV (see Fig. 6.11). Thus, a linear fit for the three peaks comparing the measured energy (i.e., the Kr energy scale) and the tabulated one provides a handy tool for the energy scale conversion.

Moreover, maybe owed to an idealized case in some aspects of the simulation assumptions, the energy resolution in MC is relatively better than in data. In order to palliate this difference, an ad-hoc gaussian energy-dependent smearing is applied to the MC to match with the data response.

Fig. 9.6 shows an example of the energy scale correction (left panel) and the different resolutions for data and MC (on the right panel). Both were obtained, as described earlier, with calibration data.

Volumes considered for the fit

Finally, the last consideration towards the fit is the volumes studied for the spatial information. Attempting to determine 22 volumes for the 4 isotopes is more than

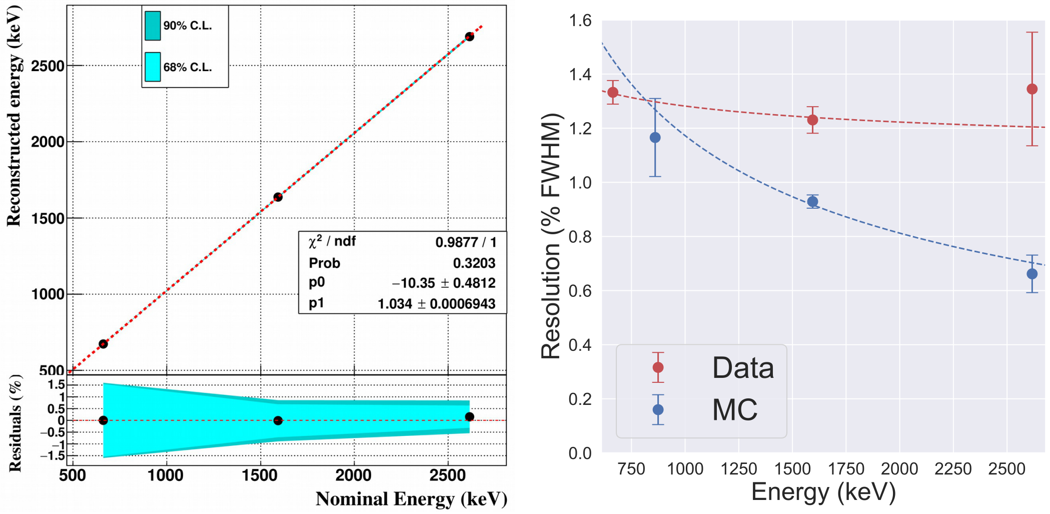

Figure 9.6.: Example of the extraction of the parameters for the energy alignment (left) and energy resolution (right). In the left image, the three peaks from the calibration (in order: ^{137}Cs photopeak, ^{208}Tl double escape peak, and ^{208}Tl photopeak) compare their measured energy (in the *Kr scale*) vs. the values found in the literature. A linear fit is superimposed (dashed line), both for the parameter determination and the demonstration of the linearity of the detector. The bottom panel shows the fit residuals, as well as the 68 %CL and 90 %CL bands. The right plot presents the resolution for the calibration runs in data (red) and MC (blue). The data peaks correspond with the aforementioned gamma lines while the MC has no ^{137}Cs simulated. In order to incorporate an extra peak, the ^{208}Tl's (860.557 ± 0.004) keV [277] is also considered. The fit for the $E^{-1/2}$ expected performance of resolution is superimposed (dashed line).

unreasonable. In order to still use the information in a more realistic approach, three regions are established. They are, as anticipated: "Anode," "Cathode," and "Other." The definition of the sections has been arranged regarding the position of the sources with respect to the chamber in the axial plane, as reflected in Fig. 9.7. The different profiles inside the active volume are exhibited in the bottom panel of Fig. 9.3.

9.2.2 Fit inputs

There are two considerations regarding the inputs for the fit: the variables to be examined and the samples to be incorporated.

The first and obvious variable is the event energy. Energy distributions are unique for every isotope, and, therefore, the presence of any background must be confirmed by the unambiguous detection of its energy spectrum. However, it does

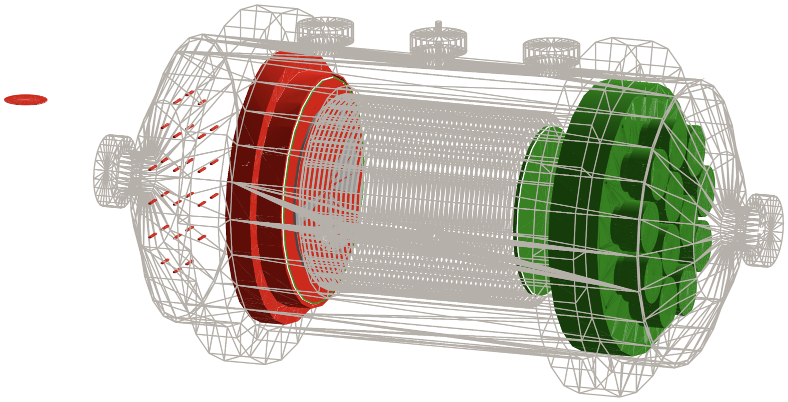

Figure 9.7.: Visualization of the GEANT4 volumes composing the NEXT-White inner-components geometry. The colored regions represent the classification considered for the fit: "Anode" (green), "Cathode (red), and "Other" (grey).

not provide any information concerning the origin of the event. Additionally, some of the spectra with less distinctive features are correlated, as $^{136}\mathrm{Xe}$ and $^{214}\mathrm{Bi}$ are.

In order to disentangle the origin and break the correlations, one option is adding more variables. The spatial details are a good possibility since they may provide additional information about the background source. For symmetry of the chamber, x and y can be summarized in a radial distance, $R = \sqrt{x^2 + y^2}$. Thus, there are two variables to take into account: z and R. Notwithstanding, looking at the distributions in Fig. 9.8, it is patent that their discrimination power is significantly different.

On the one hand, the R^2 distribution is featureless in both the origin of the event and the isotope generating it. In contrast, it presents a fine and expected flat distribution across the chamber for all the cases. On the other hand, the z distributions do vary regarding their originating region and also by the isotope,[7] being an additional tool for the fit.

Unfortunately, apart from the originating isotope and its implications in the energy range, the vast majority the backgrounds studied in this section represent the same type of event, single electrons.[8] Hence, there is no other feasible variable that can distinguish them since the same behavior is expected in their interaction in the gas. This is not the case for the $\beta\beta$ signals. The presence of two blobs allows

---

[7] Obviously, both observations are correlated since the contributions of each isotope for each region are different.

[8] There is a small and irreducible contribution of double electron-like events from the $^{208}\mathrm{Tl}$ double escape peak.

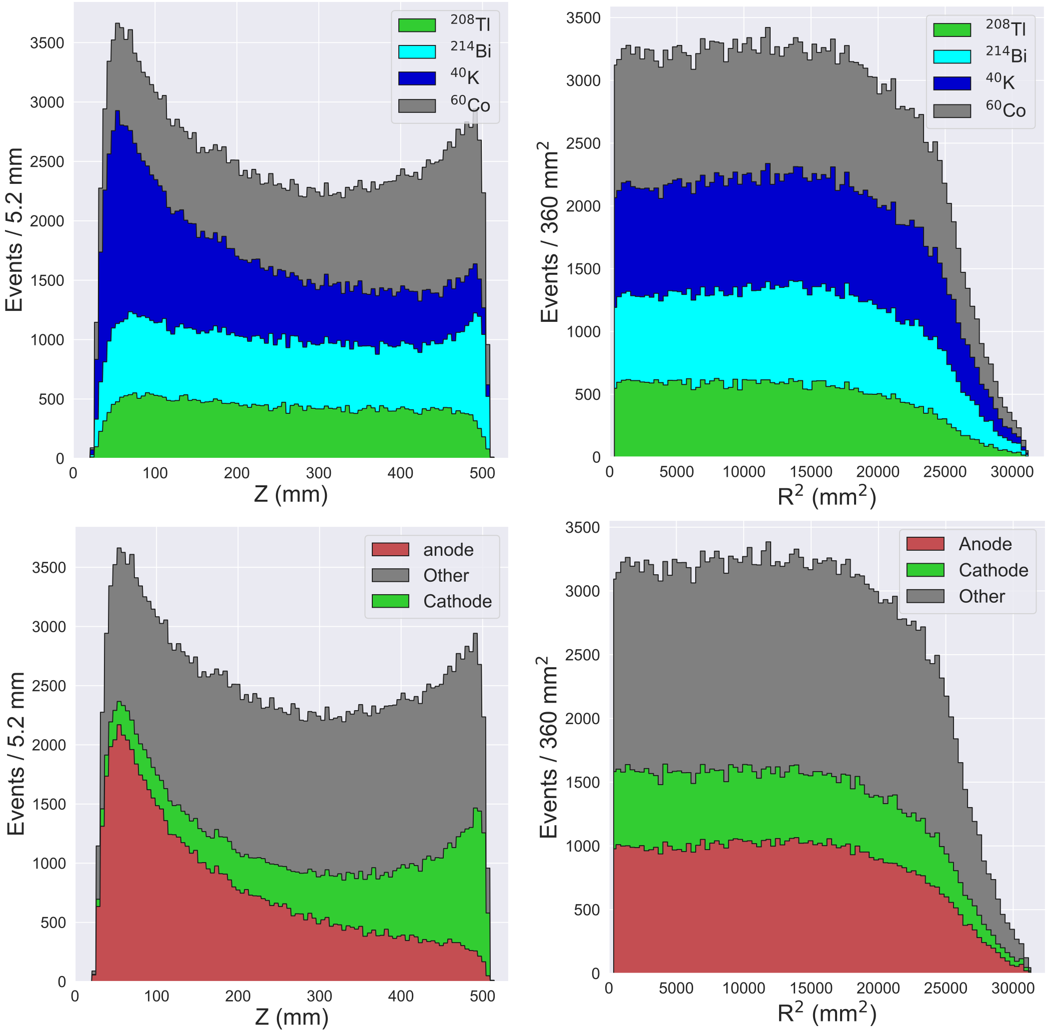

Figure 9.8.: R^2 and average z distributions of the MC candidates for the fit after the whole processing chain. The top row breaks the contributions of each variable per isotope, while the bottom one presents each fit volume contribution. The z distributions (left panels) show distinctive patterns for the various sources and origins. However, the R^2 ones (right panels) present featureless and flat distributions. It is important to notice that the z figures incorporate the trigger efficiency correction that, although smooths the cathode peak (in comparison with the lower panel in Fig.9.3), stills preserves a notable profile. Also, when comparing these distributions to the ones in Fig. 9.3, it is relevant to mention the different y axis scales, linear for the former case and logarithmic for the latter.

exploiting additional information from the events, such as the energy of the two blobs.[9]

Another different approach would be the incorporation of additional data samples, such as electrons coming from the detector boundaries. Unfortunately, the electron MC performance is not fully understood and does not match the data. A supplementary and more profound analysis is required in order to consider it for the fit. Nevertheless, it is a possibility when referring to the $\beta\beta$ analysis, where the events rejected from the $\beta\beta$ selection constitute an independent single electron sample.

In the case of the $\beta\beta$ analysis, another promising strategy is combining the enriched and depleted runs, thus providing another independent source that disentangles all the correlations if the background levels are compatible between both data-taking periods (thus, no additional background is found to play a role in the detector).

9.2.3 Fit description

As illustrated in the previous section, the fit takes into consideration the four isotopes and three effective volumes. Therefore, a total of 12 independent parameters must be extracted. The fit is performed in the 1–3 MeV energy range and 20–512 mm z range. The reason for setting the lower threshold in energy at 1 MeV is twofold. First, the cosmogenic activation products in the forms of long-living isotopes are known to contribute before that energy range. Second, the experience examining the behavior of the fit incorporating the low energy range has been observed to deteriorate the goodness-of-fit.

The fit consists of the maximization of a binned extended likelihood function. The likelihood method is defined, for a general case, as [322]:

$$\mathscr{L}(\boldsymbol{\theta}) = \prod_{i=1}^{N} f(n_i; \boldsymbol{\theta}), \tag{9.2}$$

where n_i are the statistical independent measured values (value of each bin); N is the number of values (number of bins); $\boldsymbol{\theta}$ are the parameters of the optimization, and f is the PDF each component follows. In this case, the fit parameters are the relative normalization of the 12 backgrounds with respect to the background

---

[9] Single electron events typically have only one blob that matches the criteria, while the other is a low energy track end. Thus, asking for the energy of this second blob provides information on the kind of track producing the event. See Sec. 3.1.4.

model expectation. For the case of binned likelihood, where the n_i is regarded as independet and following a Poisson distribution, the PDF can be expresed as [322]:

$$f_P(\boldsymbol{n};\boldsymbol{\theta}) = \prod_{i=1}^{N} \frac{\mu^{n_i}}{n_i!} e^{-\mu_i}, \tag{9.3}$$

where $\mu_i = \mu_i(\boldsymbol{\theta}) = E[x_i]$. This is equivalent to maximize the likelihood ratio

$$\lambda(\boldsymbol{\theta}) = \frac{f_P(\boldsymbol{n};\boldsymbol{\theta})}{f(\boldsymbol{n};\hat{\boldsymbol{\mu}})}, \tag{9.4}$$

where $f(\boldsymbol{n};\hat{\boldsymbol{\mu}})$ is the so-called saturated model, and the hat denotes the estimators for the variable. Although it may seem arbitrary, this new definition allows to connect and define the likelihood method to the general χ^2 statistics [323].

Generally, for computational effectiveness, it is more common to turn the products into sums by computing the logarithm. Along with the same lines, it is easier to find a minimum; therefore, instead of maximizing $\ln \mathscr{L}$, $-\ln \mathscr{L}$ is minimized. Finally, for a direct translation into p-values, a factor 2 is added. Applying these prescriptions, the final function to minimize is:

$$-2\ln\lambda(\boldsymbol{\theta}) = -2\sum_{i=0}^{N}\left[n_i \ln\left(\frac{n_i}{\mu_i(\boldsymbol{\theta})}\right) + \mu_i(\boldsymbol{\theta}) - n_i\right] = \chi^2_P. \tag{9.5}$$

The fit is applied to two distributions (E and z) that are assumed to be independent. Hence, they can be easily incorporated into the minimization as two independent λ:

$$-2\ln\lambda(\boldsymbol{\theta}) = -2\ln\lambda^E(\boldsymbol{\theta}) - 2\ln\lambda^z(\boldsymbol{\theta}), \tag{9.6}$$

where each λ^η is defined following Eq. 9.5.

As anticipated, in this case, the fit parameters are the relative normalization of the 12 backgrounds with respect to the background model expectation.

$$\theta_i = \frac{\text{rate}_i^{\text{data}}}{\text{rate}_i^{\text{MC}}}, \quad \text{where } i = (\text{isotope, volume}). \tag{9.7}$$

I.e., all the 12 parameters start with a value of 1, meaning the background model expectation is presumed to be accurate. The fit changes those values to reproduce data spectra, and the parameters can be interpreted as corrections needed for the background model to account for the actual data. Thus, the net effect of the fit is increasing or lowering each isotope and volume contribution as a whole but does

Isotope	θ	Rate (mHz)
^{40}K	0.76 ± 0.11	0.13 ± 0.02
^{60}Co	2.70 ± 0.22	0.23 ± 0.02
^{208}Tl	1.95 ± 0.15	0.27 ± 0.02
^{214}Bi	2.21 ± 0.37	0.22 ± 0.04
total	1.72 ± 0.04	0.85 ± 0.05
data	-	0.84 ± 0.02

Table 9.1.: Best-fit parameter results in terms of the normalization value (the direct fit output) and their translation to rate. The measured rate is also included for comparison purposes.

not affect the shape of the z and E distributions for the individual ingredients, just its overall rate.

In order to cross-check this critical result, two independent fitting codes have been independently developed following the abovementioned principles. They are both based on the same minimization strategy (MINOS from IMINUIT [324]), and yielded compatible results, as detailed in the next section.

9.2.4 Fit results

The fit results are depicted in Fig. 9.9. The final goodness-of-fit is $\chi^2/\text{ndof} = 1.07$ (p-value $= 0.29$), which indicates that the best-fit reproduces satisfactorily well the data energy and z patterns. Regarding the estimates for the parameters ($\boldsymbol{\theta}$), combined by isotope for clarity (taking into account the three volumes and their correlations) are summarized in Table 9.1.

Both the visual and objective parameters confirm that the fit reproduces the energy and z distributions features. In addition, the overall rate from all the contributions reflects the measured rate to better than a 2%. On the other hand, the nominal background model underestimates the final rate by a factor lower than two. In short, this implies a validation of the background model for NEXT-White in the 1–3 MeV, and therefore it can be safely used to assess the backgrounds for the double beta searches within the NEXT program.

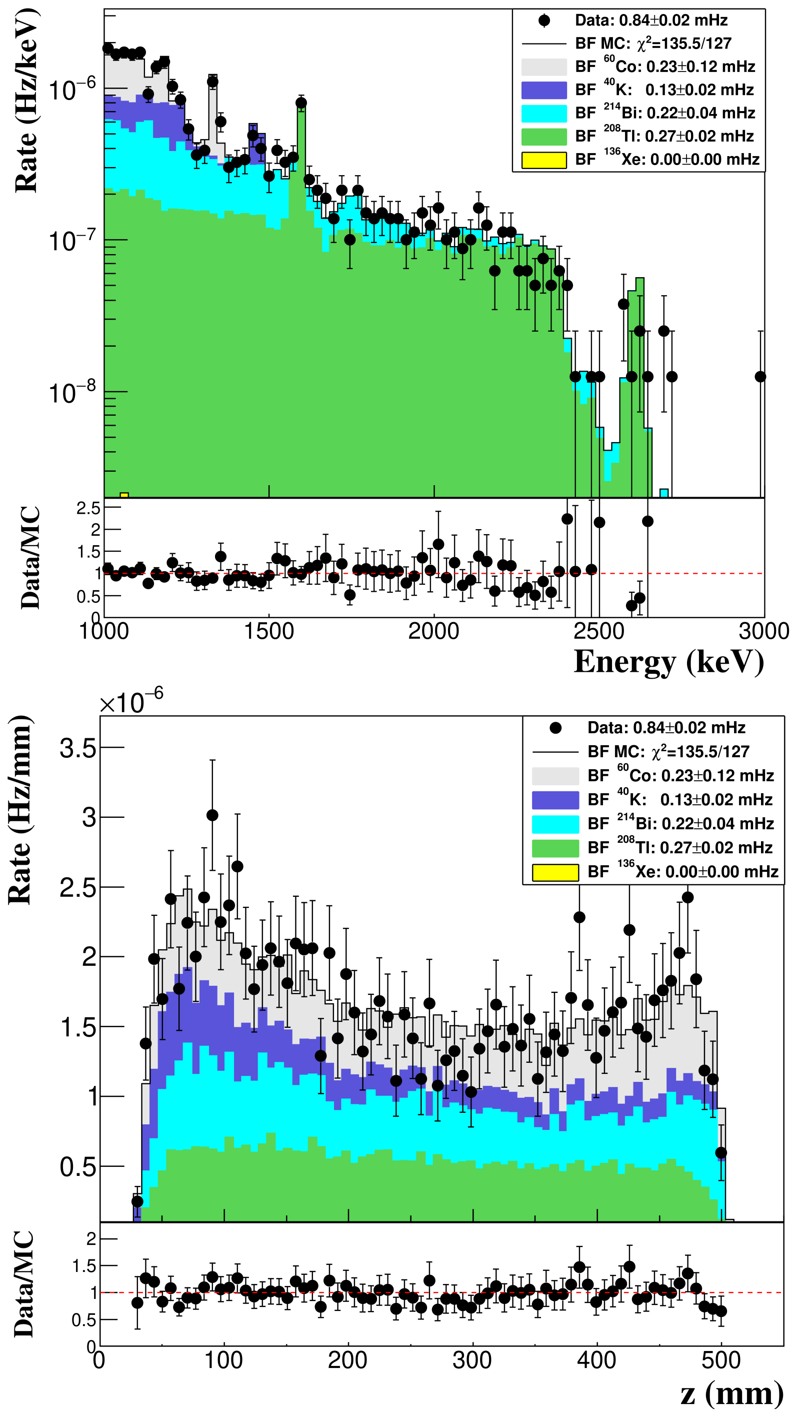

Figure 9.9.: Fit to background IVc data. Data (black dots) are confronted with the best-fit model expectation (solid black line). The different contributions to the model expectation are also displayed (as stacked histograms). The numerical results are obtained propagating the individual best-fit normalizations of the three effective volumes for every isotope.

Regarding the per volume contributions, the picture is not that precise. Fig.9.10 summarizes the corresponding results in terms of the normalization factors and their corresponding rates. It is possible to extract some information about the origin of the various sources.

The excess in the low z and energy regions is counterbalanced by huge normalization factors for the contributions coming from the "Anode" volume, mainly $^{60}\mathrm{Co}$, $^{214}\mathrm{Bi}$, and $^{208}\mathrm{Tl}$, with normalization factors of 17 ± 11, 7.7 ± 1.5, and 3.5 ± 1.6, respectively. Those considerable divergences from the nominal model may suggest an unaccounted background source around the anode region.

On the contrary, there are some contributions that the fit is not sensitive to and are set to zero, both in the "Other" volume. They are two possible interpretations of that. On the one hand, they may well be that the dominant contributions from the "Anode" and "Cathode" regions dominate the behavior of the isotopes, leaving the sub-dominant volume with lesser sensitivity. On the other hand, those contributions to the background model are mainly based on upper limits instead of central values. Thus, it is reasonable to assume those parameters' best-fit values result under the nominal expectations.

Concerning the cross-check code results, also present in Fig.9.10, it seems to match the published results within errors, following the principal trends. The only significant deviation refers to $^{214}\mathrm{Bi}$ value from the "Anode" and "Cathode" fit volumes. Nevertheless, those differences can be owed to the significant correlation between the parameters (see the correlation matrix and some selected plots in Appendix D) and slight variations in the data inputs. Hence, they are not especially worrisome, and both codes can be granted to be validated.

9.3 Implications for the $\beta\beta$ searches

Intending to evaluate the impact that the background would have in the physics campaign of the detector, it is time to exploit the topological information the technology provides. This information will focus on the blob energy estimation for the track, regarded as a fingerprint for a double beta event (see Sec. 3.1.4). The section will follow the previous attempts to characterize the topology of the events [116,117] while trying to optimize the selection. Besides, the foreseen impact on the $2\nu\beta\beta$ search will be presented.

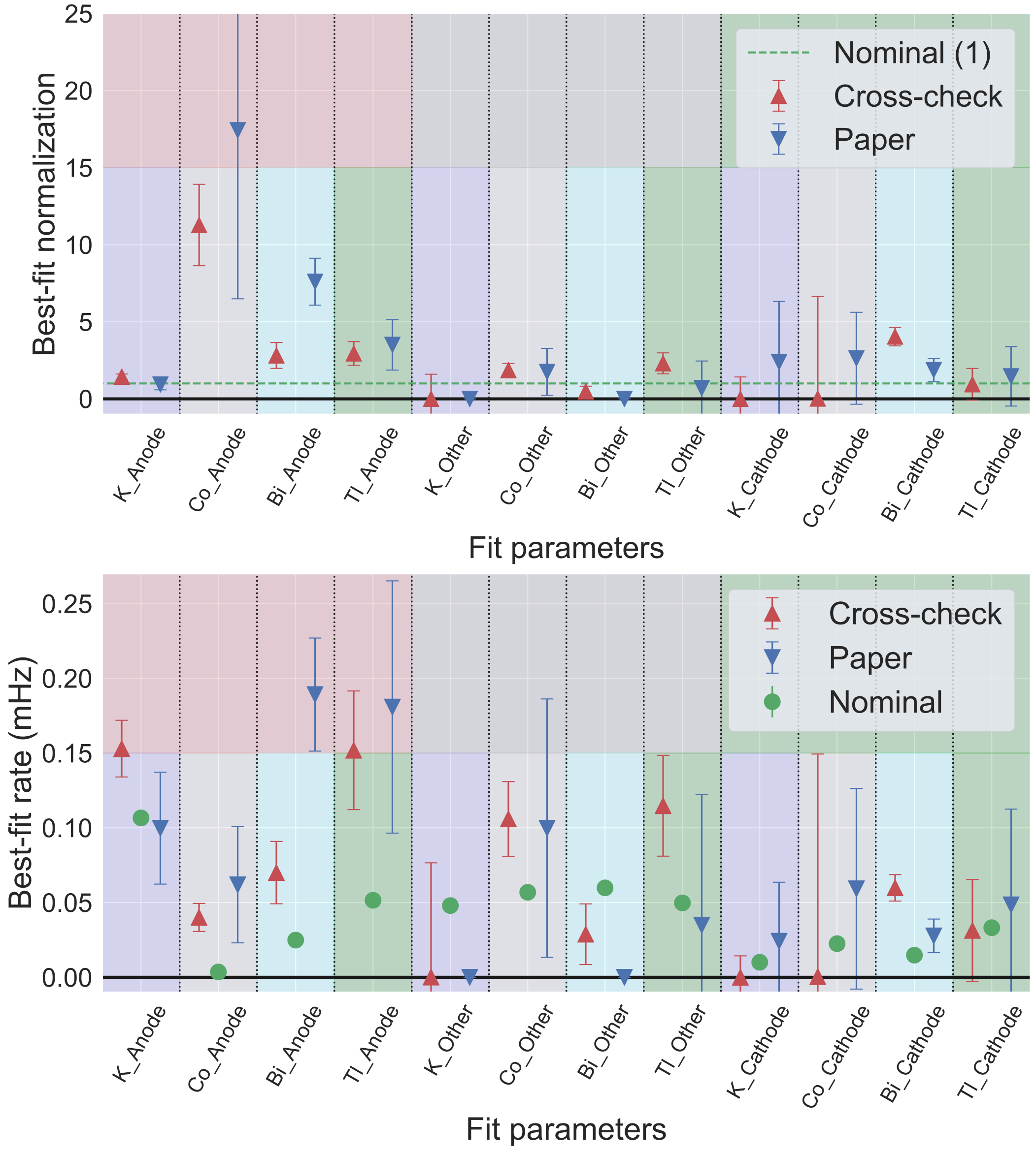

Figure 9.10.: Best-fit values for the individual normalizations considered in the background fit. The top image displays the direct scaling values for the four isotopes in the three fit volumes with respect to the nominal background model expectations (green dashed line). The bottom panel translates those results to rates, comparing them to the nominal expectations. The two codes' results are presented for contrasting purposes.The colors in the background follow the scheme for the fit volumes (top section) and isotope (bottom section), according to Figs. 9.7 and 9.8, respectively.

9.3.1 Topological selection

The track reconstruction follows the steps detailed in Sec. 5.1 up to `tracks`, with a blob radius set to 21 cm. Regarding the selection, three cuts are applied (on top of the already mentioned fiducial selection).

Single track cut

It is demanded that the event presents one and only one reconstructed continuous track. The efficiency (Fig. 9.11 top-left panel) shows the expected trend since as the track energy increases, so does the length and thereby the possibility of miss-reconstructing and fragmenting, resulting in a multi-track event, also raises.

Overlap cut

Given the large blob radius, some curvy or short tracks may present their blobs overlapping. This causes a faulty definition of the per blob energy when some hits are counted twice, once for each track extreme. Therefore, the blobs must not share any hits above 1 keV.

Regarding the efficiency (Fig. 9.11 top-right panel), it increases with the track length (since it is more probable the extremes of the track are more distant), i.e., with the energy of the event and stabilizes at 100 % at around 1.3 MeV. However, in this case, the MC does not accurately reproduce the data. The disagreement appears from the difference in track length between data and MC, being consistently shorter in the latter case. Notwithstanding, the effect can be described and therefore accounted for.

Blob energy cut

In order to tell single and double electrons apart, it is required that the least energetic blob (`blob2` by construction) integrates a total energy within the blob radius above some threshold, defined in terms of the track's energy. This threshold has been determined by maximizing the figure of merit.[10] The efficiency of the signal has

---

[10]

$$f.o.m. = \frac{\varepsilon_\mathrm{s}}{\varepsilon_\mathrm{b}^{1/2}}, \tag{9.8}$$

where ε_s and ε_b are the signal and background efficiencies for $2\nu\beta\beta$ events.

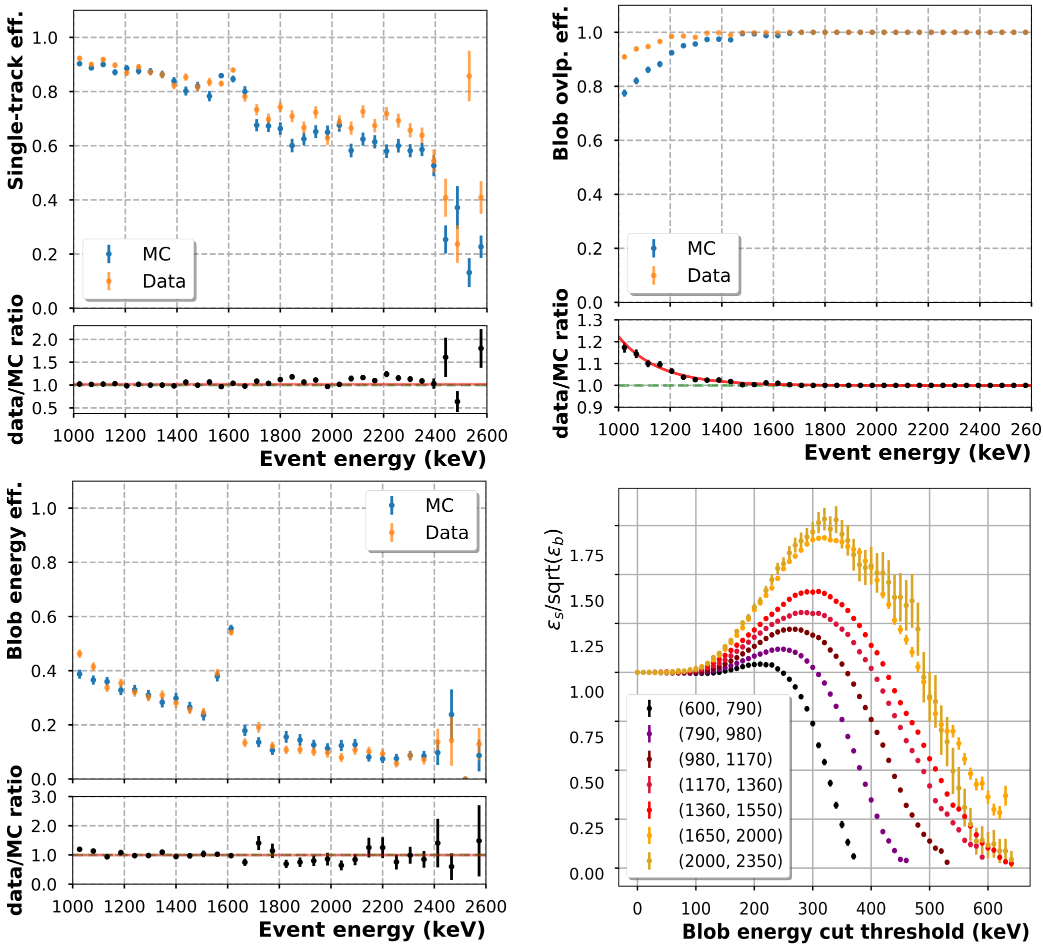

Figure 9.11.: Efficiencies for the various $\beta\beta$ selection cuts as a function of the event energy: single track (top left), blob overlap (top right), and blob energy (bottom left), for ^{208}Tl calibration data (orange) and MC (blue). The lower panels present the data and MC ratio fitted (red line) to a horizontal line for the single track and blob energy cuts and to an exponential plus a constant term for the overlap cut. The bottom right panel shows the optimization of the blob energy cut (i.e., the figure of merit) for different track energy ranges.

	Efficiencies (%)	
Cut	Data	MC
Single track	89.8 ± 0.2	87.4 ± 0.3
Overlap	98.3 ± 0.1	94.5 ± 0.2
Blob energy	29.3 ± 0.4	28.1 ± 0.4

Table 9.2.: Integrated efficiencies for the double beta topology selection cuts for $^{208}\mathrm{Tl}$ calibration data and MC.

been estimated using a $2\nu\beta\beta$ MC sample, while the background one arises from the background MC. In order to correct the track length discrepancy, the energy of the MC blobs has been corrected by a factor of (12.2 ± 0.6) % with respect to the data. The optimization, shown in the bottom right panel of Fig. 9.11, shows a higher threshold as the energy increases. To parametrize the trend for each energy range, an exponential is used.

Concerning efficiency (Fig. 9.11 bottom-left panel), it distinctly decreases as the energy increases. This is expected since both the energy deposited at the starting point of a single electron track decreases and the cut threshold rises. In addition, the MC is able to reproduce the trend correctly. Another good agreement between data and MC refers to the behavior in the vicinity of the double electron peak. The sharp efficiency increase corresponds to the presence of actual double electron events.

⁂

The integrated efficiencies have been computed for data and MC, and they are reported in Table 9.2. Complementary, Fig. 9.11 depicts the efficiencies as a function of the energy as well as the figure of merit for the blob energy cut.

9.3.2 Backgrounds in double beta decay searches

In an effort to evaluate the possibilities of the $\beta\beta$ campaign, all the previous results are incorporated. The selection cuts introduced in the previous section are applied to Run IVc data and MC background samples. In addition, the different contributions of the background model have been rescaled according to the fit results presented in

	Rate (mHz)	
Cut	Data	MC
Fiducial	0.84 ± 0.02	0.849 ± 0.002 $(stat)$$\pm$ 0.005 (sys)
Single track	0.743 ± 0.018	0.751 ± 0.002 $(stat)$$\pm$ 0.004 (sys)
Overlap	0.721 ± 0.017	0.721 ± 0.002 $(stat)$$\pm$ 0.018 (sys)
Blob energy	0.248 ± 0.010	0.246 ± 0.001 $(stat)$$\pm$ 0.008 (sys)

Table 9.3.: Background rates during Run-IVc for data and MC, for E>1 MeV after the application of the indicated topological cut.

Sec. 9.2.4, as well as the differences between data and MC, found in the selection process (see Fig. 9.11 data and MC ratios). The resulting rates are presented in Table 9.3.

The correspondence between the rates for the various cuts in data and MC validates the background model even after the topological selection. The background spectra after the topological cuts, depicted in Fig. 9.12, confirm the validation. They present an excellent agreement, despite the limited statistics.

$2\nu\beta\beta$ sensitivity

Once the application of the $\beta\beta$ selection is validated, it is possible to perform an estimation of the sensitivity of the NEXT-White detector to the $^{136}\mathrm{Xe}$'s two neutrino mode half-life. The conditions for the study are the ones in Run-V with enriched xenon at 10.1 bar pressure. The remaining set of conditions is kept the same as the Run-IVc operations. On the one hand, the $^{136}\mathrm{Xe}$ signal half-life is extracted from the literature to be $T_{1/2} = (2.165 \pm 0.061)$ yr [325]. On the other hand, the background expectations from the nominal background model are rescaled according to the results presented in Sec. 9.2.4, in order to match Run-IVc rates.

The study consists of scanning the sensitivity yielded by the fit for different exposures. For each considered exposure, 1000 toy experiments are generated according to the signal and background expectations.[11] Then, a maximum likelihood fit is performed to the energy spectrum only. The fit contemplates five parameters,

---

[11] The expected number of events for each exposure is taken as the mean of a Poisson distribution, and the different toy experiment yields are extracted by sampling those distributions.

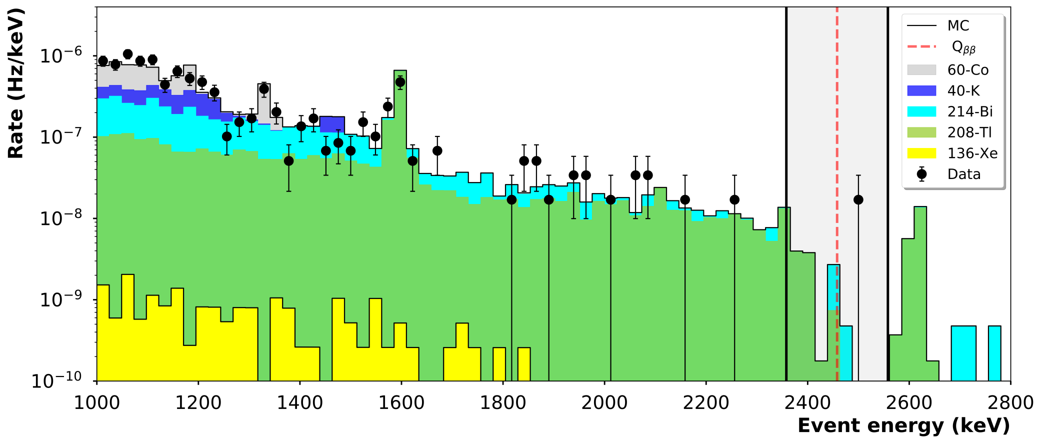

Figure 9.12.: Energy spectrum of the Run-IVc background sample after the $\beta\beta$ selection is applied for data (dots) and MC (bar histograms). A wide ROI window (grey band) is depicted around the $Q_{\beta\beta}$ ±100 keV, built for comparing data and MC expectations around the $Q_{\beta\beta}$ (vertical red dashed line).

the normalization factors[12] for the four background isotopes and the $2\nu\beta\beta$ signal. Later, the best-fit value and its error for the $\beta\beta$ signal are extracted from the fit, and a signal sensitivity is computed as the value/error ratio. In order to break the correlations present in the fit, especially between ^{214}Bi and ^{136}Xe parameters (see D, and in accordance with the expected procedure for the future Run-V analysis, the background fit results are incorporated into the likelihood, also considering the correlations among them, constraining the contributions from ^{40}K, ^{60}Co, ^{208}Tl, and ^{214}Bi, as [326]:

$$\ln \mathscr{L}(\boldsymbol{\theta}) = \ln \lambda(\boldsymbol{\theta}) + (\boldsymbol{\theta} - \tilde{\boldsymbol{\theta}})\Sigma^{-1}(\boldsymbol{\theta} - \tilde{\boldsymbol{\theta}}) \tag{9.9}$$

where $\ln \lambda(\boldsymbol{\theta})$ is defined in Eq. 9.5, $\tilde{\theta}$ denotes the fit results depicted in Sec. 9.2.4, and Σ is their covariance matrix.

The procedure is conducted on three data samples: one with only the fiducial selection applied, another incorporating the double beta selection described in the previous section, and the last sample trying to reproduce the deconvolution performance. The latter is computed applying a toy acceptance efficiency for data, and MC is extracted from the values achieved with the RL deconvolution in the $\beta\beta$ selection [262]. The selection is taken as flat and therefore is not expected to mimic the behavior of a real selected sample but an idealized version.

A fit is replicated for each sample, exposure volume, and toy experiment. The mean sensitivity is extracted from the average over the toy experiments and shown

---

[12] Analogously to the background fit, the normalization factors account for the nominal background model expectation.

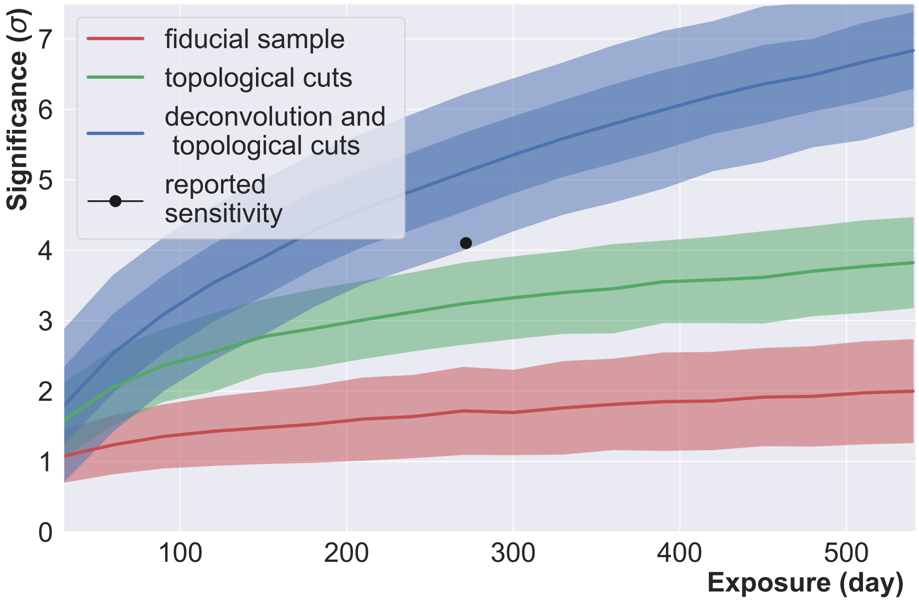

Figure 9.13.: Sensitivity to the $^{136}\mathrm{Xe}$ $2\nu\beta\beta$ signal in NEXT-White as a function of exposure, after fiducial cuts only (red), after the whole set of topological cuts (green), and a toy prediction of the effect of the convolution and the topological cuts (blue). Both the average sensitivities (solid lines) and the sensitivity standard deviations (shaded areas) are shown. The significance result from [262] (black dot) is incorporated for reference. A $2\,\sigma$ band is depicted for the deconvolution result to show the coverage of the actual measured value.

in solid lines in Fig. 9.13. Additionally, the bands represent the sensitivity standard deviation. Besides, the significance result from [262] is incorporated for reference. It is clear that the conventional set of cuts is able to improve the $\beta\beta$ selection significantly since, after a year of exposure, the significance is predicted to be only about $(1.8 \pm 0.6)\,\sigma$ for the fiducial selection and around $(3.5 \pm 0.6)\,\sigma$ for the topological one. Additionally, the deconvolution effect is patent and considerably would improve the capabilities of the detector, anticipating a significance around $(5.1 \pm 0.4)\,\sigma$ after a year of exposure.

Clearly, when compared with the measurement significance –4.1 σ after 271.6 days of exposure [262]– it manifests the idealized conditions for this sample. There are three significant differences to note between both quantities. The first one is the aforementioned simplification concerning the selection of the improved reconstruction, regarded as flat for all the energies, while the actual selection in the $2\nu\beta\beta$ analysis incorporates all the nuances. The second one is that the constraints of the background data are distinct in both cases: 37.9 d for Run-IV and 208.9 d for Run-VI. Last, the reported sensitivity considers the systematic effects, the prediction only the

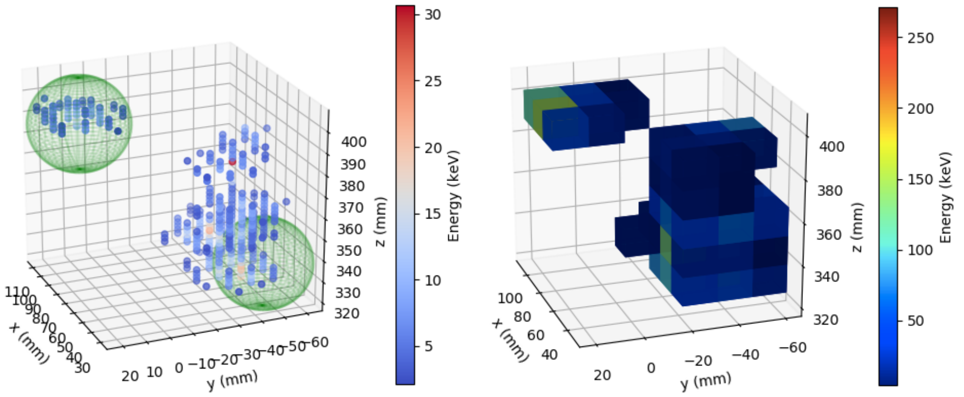

Figure 9.14.: Display of the Run-IVc event that passes the loose $0\nu\beta\beta$ selection cuts. Left panel: energy-corrected hits. Blobs are represented as green spheres. Right: voxelized track of the same event; in this case, all voxels are connected.

statistical uncertainties. Nevertheless, the reported sensitivity is still within the $2\,\sigma$ coverage range from the mean expectation.

Backgrounds in the $0\nu\beta\beta$ energy window

In order to assess the impact of the background in the $0\nu\beta\beta$ searches, and given the limited statistics after just 37.86 days of exposure, a relatively broad ROI is defined around ± 100 keV of the $Q_{\beta\beta}$ value (grey shaded area in Fig.9.12). This wide energy window is not representative of the 1 % FWHM resolution of the detector but provides a significant data/MC comparison and avoids the ^{208}Tl photopeak. Therefore, an additional requirement is added on top of the topological selection for the $0\nu\beta\beta$ *candidates*. The plot shows one data event entering the region, agreeing with an MC expectation of $0.75 \pm 0.12(stat) \pm 0.02(sys)$ events. This validates the background model even in the $0\nu\beta\beta$ ROI. Out of the background MC events passing the loose $0\nu\beta\beta$ cuts, 81 % correspond to ^{208}Tl decays and a corresponding 19 % ^{214}Bi decays. The Tl events come mostly from the anode (60 %) and the cathode (28 %) regions. On the other hand, the ^{214}Bi events originate a 80 % at the anode and a 20 % at the cathode. Concerning the fiducial sample, an average rejection factor of 16.8 ± 2.2 is obtained for the $0\nu\beta\beta$ selection in the entire energy range.

In addition, a visual examination of the data point entering the ROI shows that the event consists of two tracks wrongly reconstructed as a single one due to the voxel size of 15 mm used in the reconstruction, as depicted in Fig. 9.14. This suggests that improved reconstruction and novel classification techniques can play a supplemental role in reducing the background in the $0\nu\beta\beta$ campaigns.

Summary and conclusions

10

Neutrinos have been a gateway to giant paradigm shifts in the understanding of Particle Physics and still have some role to play in the decades to come. The recent discoveries of the neutrino flavor oscillation imply the rupture of one of the Standard Model (SM) of Particle Physics's main assumptions: neutrinos are no longer massless particles. Their mass opens the question of its origin, whether they follow the precepts for the rest of the fermions (i.e., they are Dirac fermions) or obey the Majorana mechanism (i.e., they are Majorana fermions). The potential Majorana nature of neutrinos could shed light on open questions in the field, such as the relatively low neutrino mass scale and the matter-antimatter asymmetry observed in the universe today. Among all the possible ways to discern neutrinos' true nature, the neutrinoless double beta decay is, currently, the most promising and developed technique.

Double beta decay with neutrino emission is a standard process allowed within the SM and has been observed for several nuclei. Notwithstanding, the neutrinoless mode is only possible if neutrinos present a Majorana nature. That motivated a profound activity since it was first proposed in 1939 that has gradually pushed the limits for the process in several different R&D approaches, up to the current leading experiments: GERDA for $^{76}\mathrm{Ge}$ and Kamland-Zen for $^{136}\mathrm{Xe}$. Furthermore, the field stands on the threshold of a new generation of experiments aiming to reach the tonne-scale mass.

The Neutrino Experiment with a Xenon TPC (NEXT) is a recent competitor in the pursuit of the $0\nu\beta\beta$ decay, but with really interesting features to contest. NEXT approach is based on a high-pressure gas-$^{136}\mathrm{Xe}$ time projecton chamber (TPC). It is an optical TPC where the ionization signal is detected as vacuum ultraviolet photons via a nearly noiseless amplification mechanism called electroluminescence (EL). The experiment proposes a novel technique for the detection, the SOFT concept, that consists of the separation of the energy and spatial information in two independent measurement planes. On the one hand, a plane of PMT's behind the cathode would collect the event's energy. On the other hand, a plane full of SiPMs very close to the anode would record the tracking information. The project is founded on a solid R&D program that has already proven some of the relevant challenges concerning the proof of concept, the excellent energy resolution, the background model, and the topological potentials.

The initial stage of the NEXT program (2009-2014) was devoted to the demonstration of the viability of the concept, with detectors of $\sim$1 kg of mass of Xe. The results in terms of the best energy resolution achieved for NEXT-DBDM and NEXT-DEMO were 1 % FWHM (0.5 % FWHM) and 1.62 % FWHM (0.74 % FWHM) at 662 keV and 511 keV (and the naive extrapolation to the $Q_{\beta\beta}$), respectively.

The next phase of the collaboration was the construction of the NEXT-White detector (2016-2021). This detector is a 1:2 scaled version of the NEXT-100 apparatus, with $\sim$ 5 Kg of Xe, and implements most of the projected technical solutions and materials. Besides, it is the first prototype built following radiopurity guidances, as well as the first running in an underground laboratory, the Laboratorio Subterraneo de Canfranc (LSC). The main goals of the apparatus are the validation of the concept in a large-scale detector, the assessment of the background model, and the measurement of the $2\nu\beta\beta$ mode half-life. In addition, it can serve as a testing bench for any update for future detectors.

First, concerning the monitoring (Chapter 6), $^{83m}\mathrm{Kr}$ internal transition electrons have shown to be an excellent tool for performing not only the geometric and lifetime corrections but also the continuous screening of the NEXT-White chamber conditions during 2017-2021. The existing procedure for dedicated $^{83m}\mathrm{Kr}$ data-takings devoted to the production of the energy and lifetime maps has been presented and updated. However, the possibility of a double trigger acquisition (one for the interesting events at high energy and the other with lower priority for the low energy ones) opens the opportunity of adapting the $^{83m}\mathrm{Kr}$ for continuous monitoring of the detector. This option has been explored, and the results exposed. The chamber has shown outstanding stability and smooth conditions during most of the operations, recovering nicely from any inconvenience such as sparks or laboratory temperature conditions. Furthermore, the energy maps have been shown to be almost invariant throughout all the NEXT-White functioning. On the contrary, lifetime maps seem to change in time, but the evolution appears to correlate with the gas flow patterns inside the active volume and has been observed to be correctable with sufficient accuracy via the production of a daily calibration map.

Low-background operations of the NEXT-White detector are a central piece of the program's success. Nevertheless, building a detector with no unwanted events of any kind is virtually impossible. Hence, the best one can do is attempt to reduce the background rate as much as possible throughout the different design and construction stages under levels compatible with the scope of the detector. The strategy to reduce it depends dramatically on the nature of the source, and the solutions are diverse and take place in different stages. The remaining background has to be characterized in order to decrease its effect on the physics campaign. This work explores two central pieces of background: radon-induced and radiogenic.

Radon gas is an identified problem for experiments aming for very low background rates (Chapter 8). Its ability to emanate from every material and diffuse throughout the detector systems makes it a real danger. In addition, since it is a gas, if the lifetime is long enough, it reaches a homogeneous distribution in the active volume. The daughter nuclei may be driven towards the cathode, where they accumulate. Among all the various isotopes, only one was found to be of particular concern: $^{222}\mathrm{Rn}$.

After a careful characterization of the alpha decays in the NEXT-White, the rate of $^{222}\mathrm{Rn}$ during the low radon activity data-taking is measured to be (38.1 ± 2.2 (stat) ± 5.9 (sys)) mBq/m^3. In addition, it was proven that this rate could explain the cathode-electron presence and rates. Therefore, the radon contamination in the physics of NEXT-White is negligible, and the computed rate can be applied to estimate the impact for the NEXT-100 campaign. A set of simulations have been carried out in this regard. The results are presented in a pessimistic and an optimistic projection. The former assumes the worst-case scenario where radon contributions escalate with the detector inner surface area, and the selection efficiency is performing conservatively, and the resulting rate is (0.07 ± 0.03) counts/yr. The latter considers the radon to emanate from the gas system, being, therefore, the same as in the case of NEXT-White and the reconstruction to perform favorably, yielding a rate of $(3.9 \pm 2.1) \cdot 10^{-3}$ counts/yr. When compared with the other sources of background, even at the most adverse conditions, the prediction for the radon-induced backgrounds remains one order of magnitude slower than the dominant source and possibly much more negligible. Hence, radon-induced backgrounds will occur at a tolerable level for the NEXT-100 physics program.

The radioactive impurities contained in all kinds of materials represent the dominant background for most experiments aiming for very rare events. Chapter 9 presents the data selection, the MC background model and its comparison with the actual measurements in NEXT-White, and a discussion about the extrapolation of those results in the $\beta\beta$ analysis. The analysis is based on an intense and dedicated MC campaign, the Run IV low background data ($\sim$ 40 days during 2018-2019), and dedicated high-energy calibration data taken along the Run IV period.

Meticulous screening of all the materials present in the detector, as well as an exhaustive campaign of simulations to assess the impact of the materials in their placement with respect to the active volume, led to the building of a background model. The predicted fiducial rate for events with an energy $E >$1 MeV is (0.489 ± 0.002 (stat) ± 0.0042 (sys)) mHz, while the measured one was (0.84 ± 0.02) mHz. Then, after data selection, a fit of the energy and z distributions of the low background data to the background model expectations provides a way to tune the background model and to yield some information regarding the contributions per isotope. The isotopes of interest are four: $^{40}\mathrm{K}$ and $^{60}\mathrm{Co}$, especially dominat in the $2\nu\beta\beta$ energy region, and $^{208}\mathrm{Tl}$ and $^{214}\mathrm{Bi}$ presenting gamma emissions in the vecinity of the $Q_{\beta\beta}$. The contributions per isotopes were found to be : $R_{^{40}\mathrm{K}} =$ 0.13 ± 0.02, $R_{^{60}\mathrm{Co}} =$ 0.23 ± 0.02, $R_{^{208}\mathrm{Tl}} =$ 0.27 ± 0.02, and $R_{^{214}\mathrm{Bi}} =$ 0.23 ± 0.02. Regarding spatial information, the most significant excess seems to come from the anode region.

In order to use those results to estimate the background in the $\beta\beta$ searches, a set of topological cuts have been applied: events must contain a single track and mimic the expected characteristics of a double electron track, that is the presence of two Bragg peaks (or *blobs*) per event at the electron stopping point positions. The background rate after the topological selection is (0.248 ± 0.010) mHz for data and the corresponding tuned MC expectation is (0.246 ± 0.001 (stat) ± 0.008 (sys)) mHz, showing excellent agreement. The best-fit background model has been used to estimate the sensitivity of NEXT-White to the $2\nu\beta\beta$ measurement, which is found to be between (3.5 ± 0.6) σ and (5.1 ± 0.4) σ after one year of NEXT-White operations with $^{136}\mathrm{Xe}$-enriched data. The sensitivity range refers to different choices of the topological reconstruction algorithms applied to the events: standard and improved (with deconvolution) for the lower and higher sensitivity number, respectively. This sensitivity is in good agreement with the sensitivity recently reported by the NEXT Collaboration of 4.1 σ.

Regarding the $0\nu\beta\beta$, the expected background in a wide 200 keV window around the $Q_{\beta\beta}$ of is (0.75 ± 0.12 (stat) ± 0.02 (sys)) events in 37.9 days, while 1 event is observed in data. Thus, the radiogenic background model tuned using $E >$ 1 MeV data is validated even in the higher-energy $0\nu\beta\beta$ range.

Currently, the collaboration is entirely devoted to the following stages of the program, starting with the construction and commissioning of NEXT-100 in 2022. NEXT-100 will contain up to $\sim$ 100 kg and will be competitive with the current sensitivities in the literature for the $0\nu\beta\beta$ half-life. The technological leap into the ton scale is also considered and under investigation, pushing the concepts and lessons learned and incorporating new ideas such as gas mixtures to reduce diffusion and barium tagging.

A

Kr maps evolution

The purpose of this section is to present a visual look at the map variation (or stability) displaying several maps from different periods. This is meant to complement the discussion in Sec. 6.2.3. The different Run periods are described in Tab. 4.1.

A.1 Energy maps

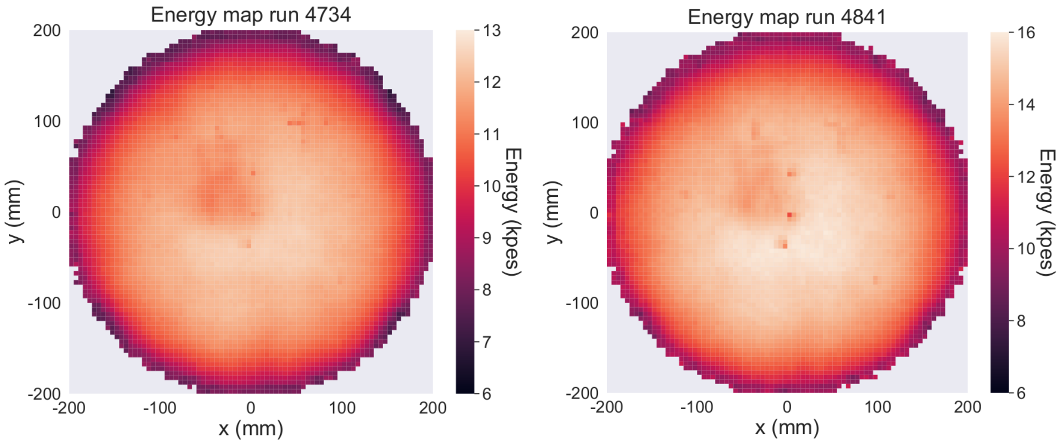

Figure A.1.: Runs 4734 (left) and 4841 (right) from Run IIa and IIb, respectively. It is patent the giant difference in the light yield between both runs, driven basically by the pressure increase. Their detailed analysis have been reported on [222].

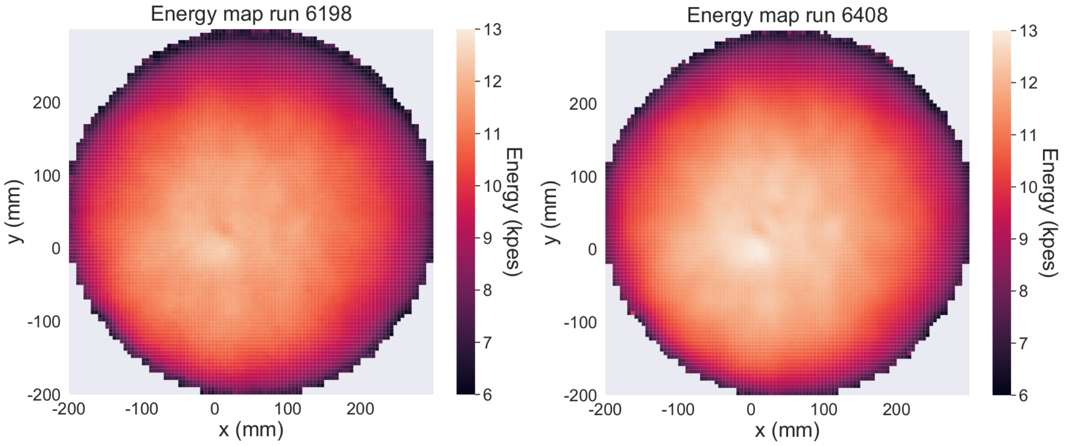

Figure A.2.: *(Continues on the next page).*

If the values allow it, the range for the maps will remain constant for a better comparison.

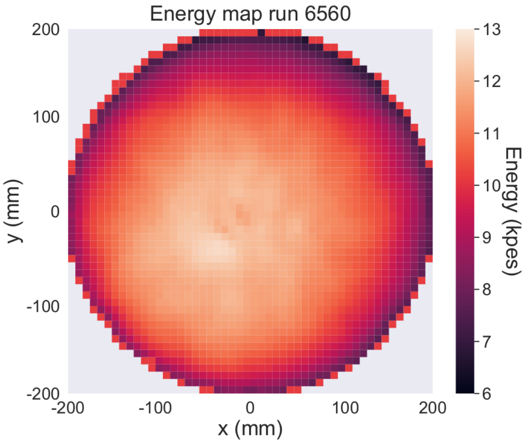

Figure A.2.: Maps of runs 6198 (top left, previous page), 6408 (top right, previous page), and 6560 (bottom) from Run IVa, IVb, and IVc, respectively.

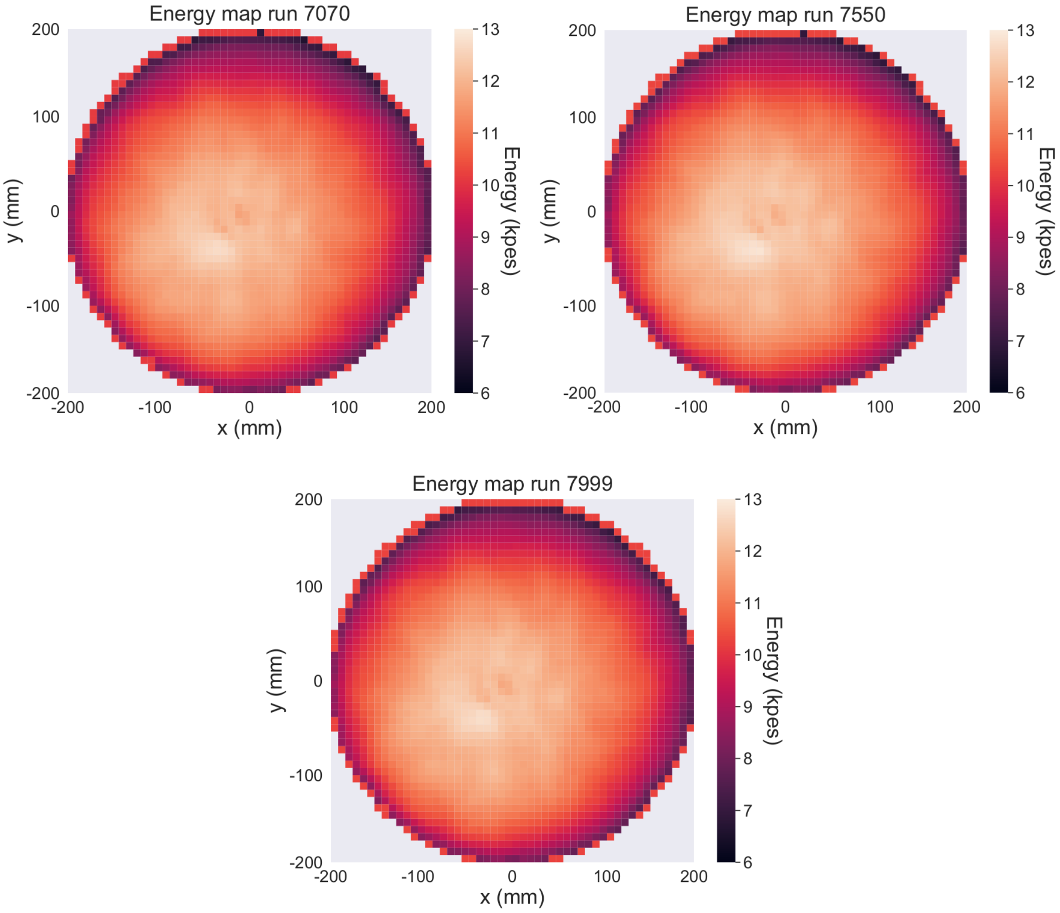

Figure A.3.: Maps of runs 7070 (top left), 7550 (top right), and 7999 (bottom) from Run Va, Vb, and Vc, respectively.

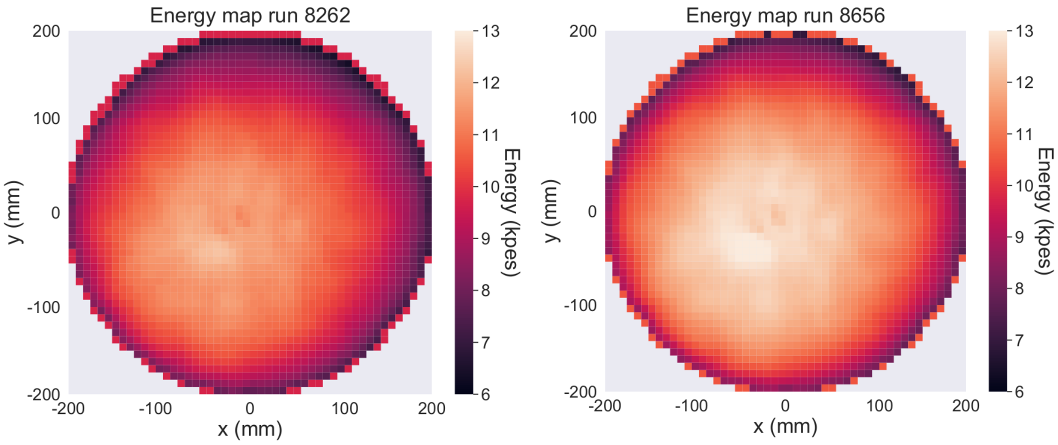

Figure A.4.: Maps of runs 8262 (left), and 8656 (right) from Run VI.

It is patent that energy maps are stable on time. The only noticeable change is between Run II and the posterior run periods, most probably due to the difference in the distribution of death SiPM, due to some operational works inside the chamber. Other than that, the overall structure seems identical, and the only remarkable variation is the general energy scale, which tends to increase over time.

A.2 Lifetime maps

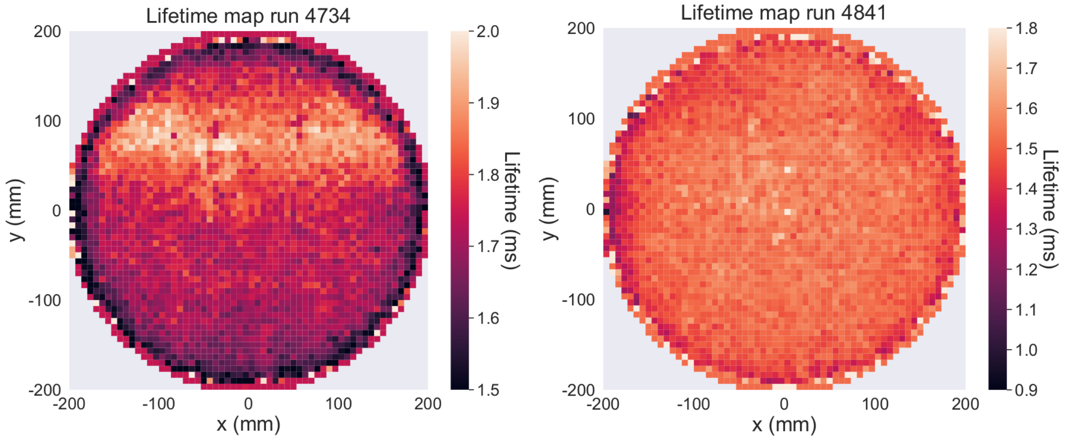

Figure A.5.: Runs 4734 (left) and 4841 (right) from Run IIa and IIb, respectively. It is patent the giant difference in the light yield between both runs, driven basically by the pressure increase. Their detailed analysis have been reported on [222].

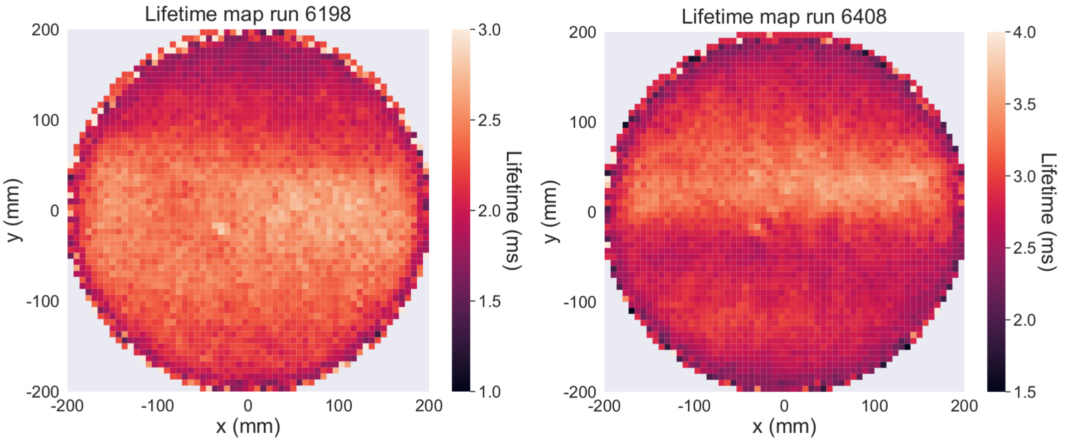

Figure A.6.: *(Continues on the next page)*.

Note that the range for the maps does not remain constant due to the considerable range of variation.

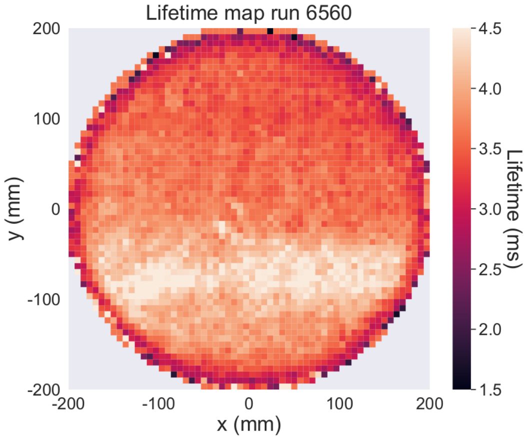

Figure A.6.: Maps of runs 6198 (top left, previous page), 6408 (top right, previous page), and 6560 (bottom) from Run IVa, IVb, and IVc, respectively.

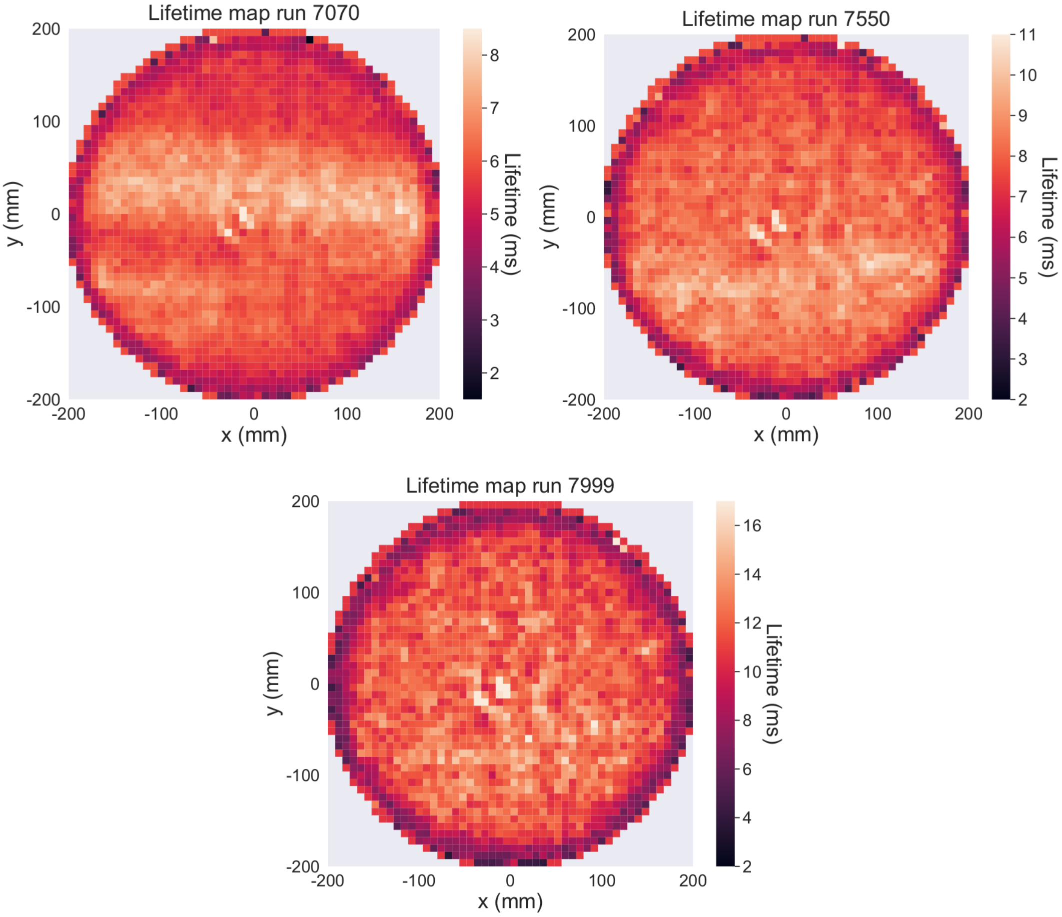

Figure A.7.: Maps of runs 7070 (top left), 7550 (top right), and 7999 (bottom) from Run Va, Vb, and Vc, respectively.

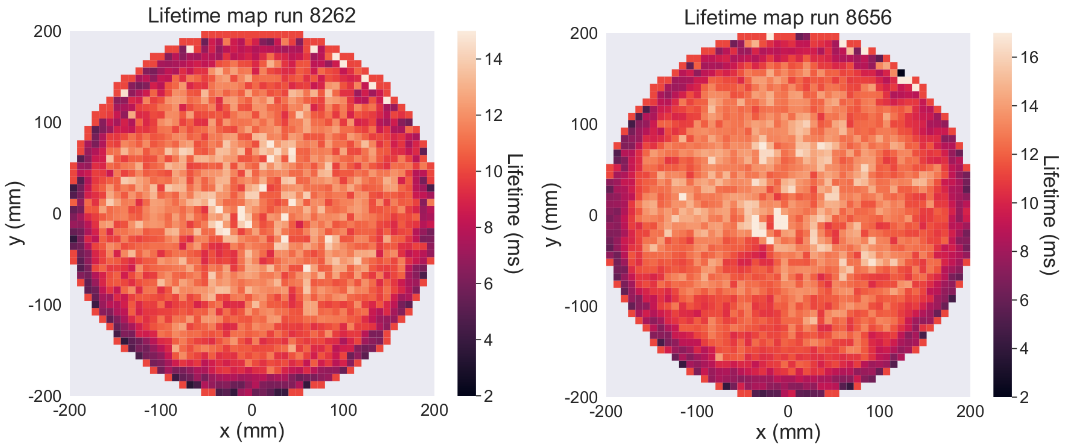

Figure A.8.: Maps of runs 8262 (left), and 8656 (right) from Run VI.

Unfortunately, the lifetime scenario is quite unalike of the energy map one. Even though there are periods where the distribution seems homogeneous, like, for instance, Run IIb (Fig. A.5, right) or all Run VI (Fig. A.8, it is frequent to find horizontal bands with a significantly high value for the lifetime. Those bands can widen, narrow, and change their position, and, in general, some hits indicate the correlation of the bands and their change to the gas flow patterns inside the chamber. For instance, it has been seen that a slight change in a flexible pipe inputting the gas in the detector impacted the lifetime value and its distribution dramatically across the plane.

B

Radon processing selection

This appendix will briefly depict the alpha candidate selection performed in the peaks, with the example of the distributions of a particular run (4517), although the selection values are general. The vertical lines and arrows show the peak selection cuts.

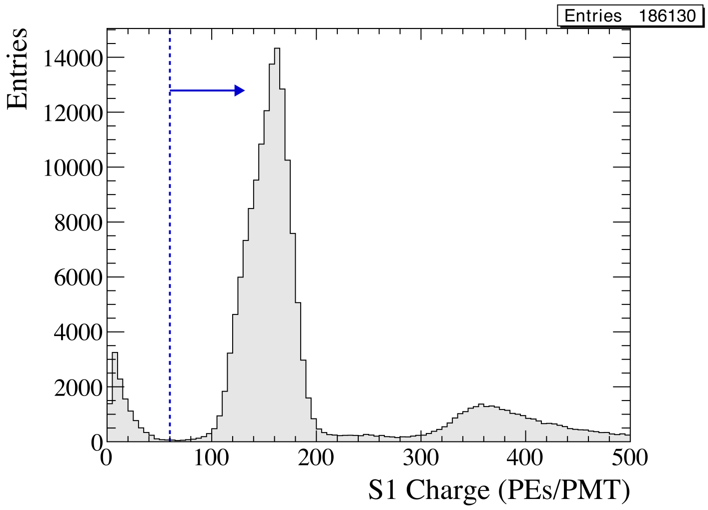

Figure B.1.: Seleccion of the S1 measured charge per PMT (i.e. the integral under the peak divided by the number of PMTs).

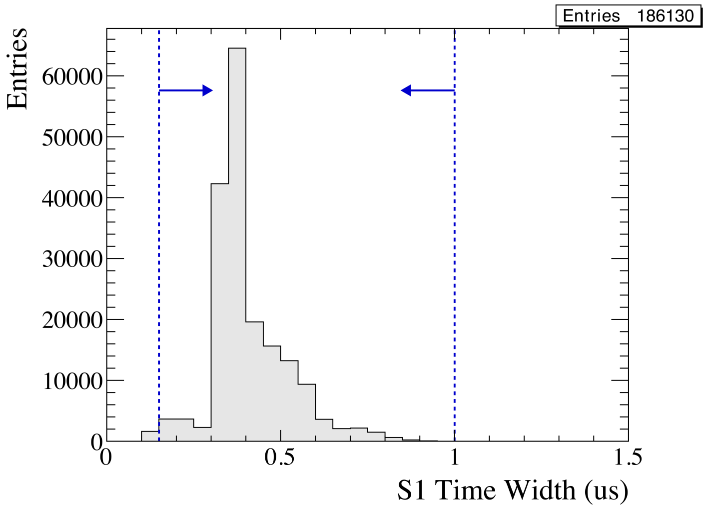

Figure B.2.: Selection of the S1 peak width.

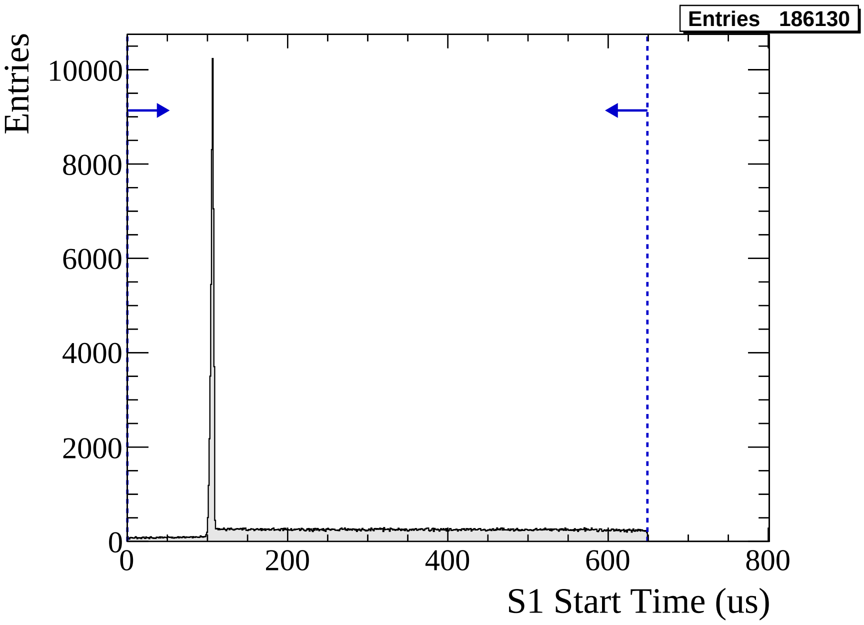

Figure B.3.: Selection of the S1 peak position in the waveform (see Chapter 5. The position is defined, in this ocasion, as the time of the first bin of the peak. The excess at ~100 μs corresponds to the events happening in the cathode plate, corresponding to those obseerved in Fig. 8.2.

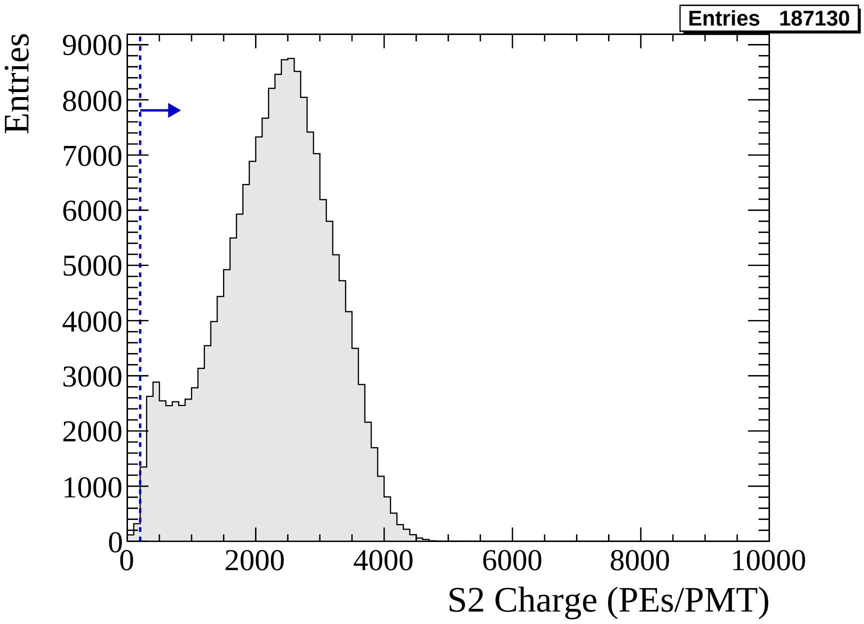

Figure B.4.: Seleccion of the S2 measured charge per PMT.

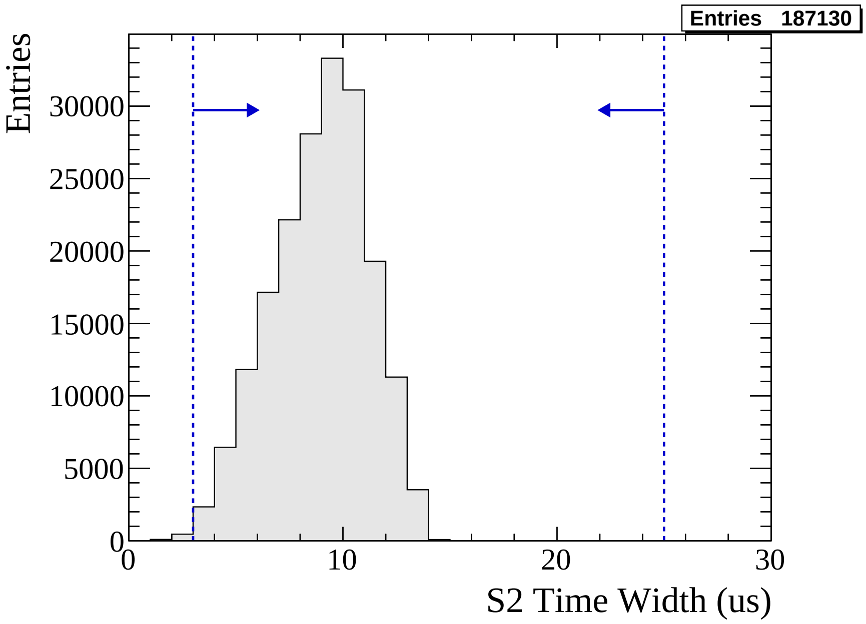

Figure B.5.: Selection of the S2 peak width.

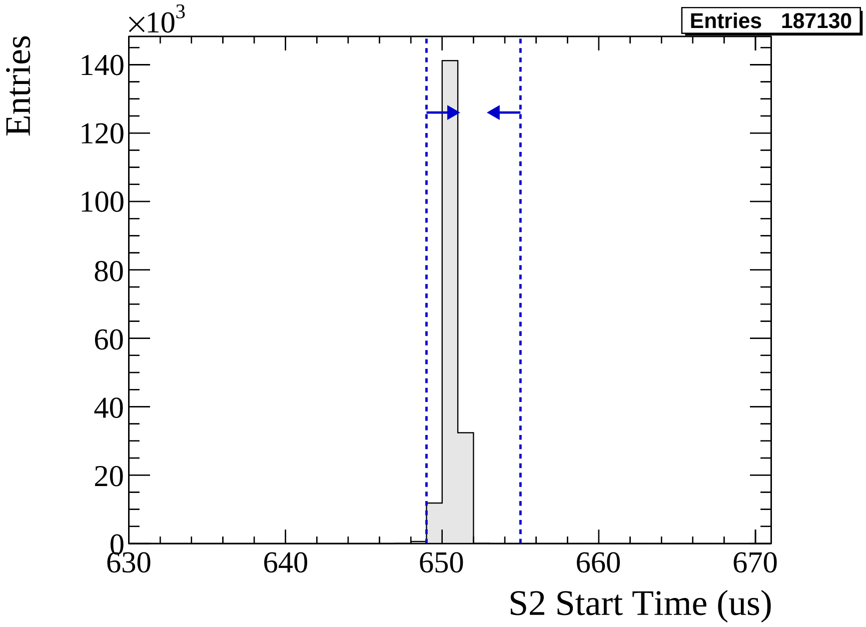

Figure B.6.: Selection of the S2 peak position in the waveform. Note that since the trigger is based on the S2 detection, the candidate peak is centered in the waveform.

C

Background Model Data

The aim of this section is to present the best understanding of the background model built by the Collaboration, following the discussion in Section 9.1.

The table presented is the result of the combination of two factors. The first one is the activity measurements provided by the radiopure team (in the A column) for each isotope of interest and every detector component. The input from the screenings is already translated into the expected activity for the detector components, taking into account the elements that constitute each component (thus, it is a sum of the activities of the composing elements weighted by their presence in the final piece). The second one is the efficiency (ε), defined as the number of radioactive decays depositing at least 400 keV in the detector active volume divided by the total number of radioactive decays. It is an MC-based estimation and assesses the actual impact that the background sources have in relation to their place within the detector (obviously, it is not the same if a noisy element is located outside any shielding layers or in direct contact with the gas in the active volume). Both quantities are then combined into the expected rate, which accounts for the assumed impact that each component and isotope has on the active volume.

As already commented, for some of the screenings, there is no evidence for the presence of some isotopes. In those cases, an upper limit is set (represented by "<" in the table). In the propagation of quantities, and for a more straightforward statement of their influence, only when an upper limit exceeds a 5 % of the final result, this outcome gets propagated and labeled as an upper limit.

System	G4 Volume	^{40}K			^{60}Co			^{208}Tl			^{214}Bi			Total
		A (mBq)	ε	rate (mHz)	A (mBq)	ε	rate (mHz)	A (mBq)	ε	rate (mHz)	A (mBq)	ε	rate (mHz)	rate (mHz)
Shielding and Structure	LC Steel	$<3.21 \cdot 10^{2}$	$3.95 \cdot 10^{-7}$	$<1.27 \cdot 10^{-4}$	$<4.17 \cdot 10^{1}$	$5.27 \cdot 10^{-6}$	$<2.20 \cdot 10^{-4}$	$<2.12 \cdot 10^{1}$	$1.10 \cdot 10^{-5}$	$<2.33 \cdot 10^{-4}$	$<6.99 \cdot 10^{2}$	$3.52 \cdot 10^{-6}$	$<2.46 \cdot 10^{-4}$	$<8.25 \cdot 10^{-4}$
	LC Structure	$2.41 \cdot 10^{5}$	$4.69 \cdot 10^{-8}$	$1.13 \cdot 10^{-2}$	$<8.19 \cdot 10^{2}$	$6.57 \cdot 10^{-7}$	$<5.38 \cdot 10^{-4}$	$6.81 \cdot 10^{3}$	$1.55 \cdot 10^{-6}$	$1.05 \cdot 10^{-2}$	$6.83 \cdot 10^{4}$	$3.87 \cdot 10^{-7}$	$2.64 \cdot 10^{-2}$	$4.88 \cdot 10^{-2}$
	LC Lead	$1.87 \cdot 10^{3}$	$1.07 \cdot 10^{-7}$	$2.02 \cdot 10^{-4}$	$<1.25 \cdot 10^{3}$	$1.16 \cdot 10^{-6}$	$<1.45 \cdot 10^{-3}$	$5.27 \cdot 10^{2}$	$3.46 \cdot 10^{-6}$	$1.83 \cdot 10^{-3}$	$5.46 \cdot 10^{3}$	$8.88 \cdot 10^{-7}$	$4.85 \cdot 10^{-3}$	$<8.32 \cdot 10^{-3}$
	ILC Lead	$6.37 \cdot 10^{2}$	$3.47 \cdot 10^{-6}$	$2.21 \cdot 10^{-3}$	$<4.25 \cdot 10^{2}$	$4.55 \cdot 10^{-5}$	$<1.93 \cdot 10^{-2}$	$1.80 \cdot 10^{2}$	$8.30 \cdot 10^{-5}$	$1.49 \cdot 10^{-2}$	$1.86 \cdot 10^{3}$	$2.69 \cdot 10^{-5}$	$5.00 \cdot 10^{-2}$	$<8.65 \cdot 10^{-2}$
	ILC Structure	-	-	-	-	-	-	$2.07 \cdot 10^{2}$	$2.25 \cdot 10^{-4}$	$4.67 \cdot 10^{-2}$	$1.26 \cdot 10^{2}$	$8.50 \cdot 10^{-5}$	$1.07 \cdot 10^{-2}$	$5.74 \cdot 10^{-2}$
	ICS	$3.81 \cdot 10^{1}$	$4.53 \cdot 10^{-4}$	$1.73 \cdot 10^{-2}$	$2.52 \cdot 10^{1}$	$7.69 \cdot 10^{-3}$	$1.94 \cdot 10^{-1}$	$2.65 \cdot 10^{-1}$	$8.27 \cdot 10^{-3}$	$2.19 \cdot 10^{-3}$	$7.75 \cdot 10^{0}$	$4.28 \cdot 10^{-3}$	$3.32 \cdot 10^{-3}$	$2.17 \cdot 10^{-1}$
	Pedestal	$<7.39 \cdot 10^{3}$	$3.62 \cdot 10^{-7}$	$<2.68 \cdot 10^{-3}$	$<1.00 \cdot 10^{3}$	$3.90 \cdot 10^{-6}$	$<3.90 \cdot 10^{-3}$	$<3.54 \cdot 10^{2}$	$1.33 \cdot 10^{-5}$	$<4.71 \cdot 10^{-3}$	$<4.83 \cdot 10^{2}$	$3.12 \cdot 10^{-6}$	$<1.51 \cdot 10^{-3}$	$<1.28 \cdot 10^{-2}$
Vessel		$<2.14 \cdot 10^{3}$	$2.64 \cdot 10^{-5}$	$<5.66 \cdot 10^{-2}$	$2.00 \cdot 10^{3}$	$3.83 \cdot 10^{-4}$	$7.67 \cdot 10^{-1}$	$<5.89 \cdot 10^{1}$	$5.53 \cdot 10^{-4}$	$<3.25 \cdot 10^{-2}$	$<3.64 \cdot 10^{2}$	$2.12 \cdot 10^{-4}$	$<7.70 \cdot 10^{-2}$	$<9.33 \cdot 10^{-1}$
Field Cage	Drift Tube	$<1.09 \cdot 10^{2}$	$9.58 \cdot 10^{-3}$	$<1.04 \cdot 10^{0}$	$<7.93 \cdot 10^{0}$	$4.63 \cdot 10^{-2}$	$<3.67 \cdot 10^{-1}$	$<1.28 \cdot 10^{0}$	$6.07 \cdot 10^{-2}$	$<7.77 \cdot 10^{-2}$	$<4.69 \cdot 10^{-1}$	$4.19 \cdot 10^{-2}$	$<1.97 \cdot 10^{-2}$	$<1.51 \cdot 10^{0}$
	HDPE Tube	$<8.41 \cdot 10^{1}$	$1.51 \cdot 10^{-3}$	$<1.27 \cdot 10^{-1}$	$<1.65 \cdot 10^{0}$	$<2.75 \cdot 10^{-2}$	$4.53 \cdot 10^{-2}$	$<1.55 \cdot 10^{0}$	$<2.94 \cdot 10^{-2}$	$4.56 \cdot 10^{-2}$	$<3.61 \cdot 10^{0}$	$1.64 \cdot 10^{-2}$.	$<5.92 \cdot 10^{-2}$	$<2.77 \cdot 10^{-1}$
EL	Anode Quartz	$<2.60 \cdot 10^{0}$	$1.08 \cdot 10^{-2}$	$<2.82 \cdot 10^{-2}$	$<4.32 \cdot 10^{-2}$	$3.55 \cdot 10^{-2}$	$<1.53 \cdot 10^{-3}$	$<1.62 \cdot 10^{0}$	$5.07 \cdot 10^{-2}$	$<8.21 \cdot 10^{-2}$	$<4.86 \cdot 10^{-1}$	$3.92 \cdot 10^{-2}$	$<1.90 \cdot 10^{-2}$	$<1.31 \cdot 10^{-1}$
	Tracking Frames	$<1.87 \cdot 10^{-1}$	$8.68 \cdot 10^{-4}$	$<1.62 \cdot 10^{-4}$	$5.71 \cdot 10^{0}$	$1.66 \cdot 10^{-2}$	$9.50 \cdot 10^{-2}$	$<8.94 \cdot 10^{-2}$	$1.78 \cdot 10^{-2}$	$<1.59 \cdot 10^{-3}$	$<9.54 \cdot 10^{-1}$	$9.57 \cdot 10^{-3}$	$<9.13 \cdot 10^{-3}$	$<1.06 \cdot 10^{-1}$
Cathode (Rn-induced)		-	-	-	-	-	-	-	-	-	$3.10 \cdot 10^{0}$	$6.52 \cdot 10^{-1}$	$2.02 \cdot 10^{0}$	$2.02 \cdot 10^{0}$
EP	Carrier Plate	$1.41 \cdot 10^{1}$	$1.59 \cdot 10^{-4}$	$2.24 \cdot 10^{-3}$	$8.84 \cdot 10^{0}$	$2.65 \cdot 10^{-3}$	$2.34 \cdot 10^{-2}$	$<1.32 \cdot 10^{-1}$	$2.81 \cdot 10^{-3}$	$<3.70 \cdot 10^{-4}$	$<3.71 \cdot 10^{-1}$	$1.48 \cdot 10^{-3}$	$<5.48 \cdot 10^{-4}$	$2.66 \cdot 10^{-2}$
	Enclosure Body	$3.05 \cdot 10^{0}$	$1.06 \cdot 10^{-4}$	$3.23 \cdot 10^{-4}$	$2.02 \cdot 10^{0}$	$1.75 \cdot 10^{-3}$	$3.54 \cdot 10^{-3}$	$2.12 \cdot 10^{-2}$	$1.84 \cdot 10^{-3}$	$3.90 \cdot 10^{-5}$	$6.20 \cdot 10^{-2}$	$8.94 \cdot 10^{-4}$	$5.54 \cdot 10^{-5}$	$3.95 \cdot 10^{-3}$
	Enclosure Window	$<1.20 \cdot 10^{1}$	$8.48 \cdot 10^{-4}$	$<1.02 \cdot 10^{-2}$	$3.55 \cdot 10^{0}$	$1.56 \cdot 10^{-2}$	$5.55 \cdot 10^{-2}$	$<1.58 \cdot 10^{0}$	$1.62 \cdot 10^{-2}$	$<2.56 \cdot 10^{-2}$	$<3.17 \cdot 10^{0}$	$9.23 \cdot 10^{-3}$	$<2.93 \cdot 10^{-2}$	$<1.21 \cdot 10^{-1}$
	Optical Pad	$<4.44 \cdot 10^{0}$	$8.00 \cdot 10^{-4}$	$<3.55 \cdot 10^{-3}$	$<1.16 \cdot 10^{-1}$	$1.46 \cdot 10^{-2}$	$<1.69 \cdot 10^{-3}$	$<1.66 \cdot 10^{-1}$	$1.58 \cdot 10^{-2}$	$<2.62 \cdot 10^{-3}$	$<5.65 \cdot 10^{-1}$	$8.67 \cdot 10^{-3}$	$<4.90 \cdot 10^{-3}$	$<1.28 \cdot 10^{-2}$
	PMT Base	$1.40 \cdot 10^{2}$	$1.96 \cdot 10^{-4}$	$2.75 \cdot 10^{-2}$	$<2.10 \cdot 10^{0}$	$3.43 \cdot 10^{-3}$	$<7.21 \cdot 10^{-3}$	$<1.07 \cdot 10^{1}$	$3.52 \cdot 10^{-3}$	$<3.76 \cdot 10^{-2}$	$<8.40 \cdot 10^{0}$	$1.92 \cdot 10^{-3}$	$<1.61 \cdot 10^{-2}$	$<8.84 \cdot 10^{-2}$
	PMT Body	$1.45 \cdot 10^{2}$	$4.73 \cdot 10^{-4}$	$6.86 \cdot 10^{-2}$	$4.56 \cdot 10^{1}$	$8.39 \cdot 10^{-3}$	$3.82 \cdot 10^{-1}$	$2.28 \cdot 10^{0}$	$8.56 \cdot 10^{-3}$	$1.95 \cdot 10^{-2}$	$4.20 \cdot 10^{0}$	$4.78 \cdot 10^{-3}$	$2.01 \cdot 10^{-2}$	$4.91 \cdot 10^{-1}$
TP	DB Plug	$9.46 \cdot 10^{1}$	$1.63 \cdot 10^{-5}$	$1.54 \cdot 10^{-3}$	$<8.40 \cdot 10^{-1}$	$2.25 \cdot 10^{-4}$	$<1.89 \cdot 10^{-4}$	$5.91 \cdot 10^{1}$	$3.63 \cdot 10^{-4}$	$2.14 \cdot 10^{-2}$	$7.73 \cdot 10^{1}$	$1.34 \cdot 10^{-4}$	$1.03 \cdot 10^{-2}$	$3.35 \cdot 10^{-2}$
	DB	$<4.07 \cdot 10^{2}$	$1.98 \cdot 10^{-3}$	$<8.06 \cdot 10^{-1}$	$<2.39 \cdot 10^{-1}$	$3.67 \cdot 10^{-2}$	$<8.78 \cdot 10^{-3}$	$<3.91 \cdot 10^{-1}$	$4.04 \cdot 10^{-2}$	$<1.58 \cdot 10^{-2}$	$<2.21 \cdot 10^{0}$	$2.32 \cdot 10^{-2}$	$<5.13 \cdot 10^{-2}$	$<8.82 \cdot 10^{-1}$
	Extra Vessel	$3.58 \cdot 10^{4}$	$3.92 \cdot 10^{-6}$	$1.40 \cdot 10^{-1}$	$<7.05 \cdot 10^{1}$	$5.49 \cdot 10^{-5}$	$<3.87 \cdot 10^{-3}$	$3.69 \cdot 10^{3}$	$9.56 \cdot 10^{-5}$	$3.53 \cdot 10^{-1}$	$8.22 \cdot 10^{3}$	$3.22 \cdot 10^{-5}$	$2.65 \cdot 10^{-1}$	$7.62 \cdot 10^{-1}$
	Support Plate	$1.88 \cdot 10^{1}$	$3.22 \cdot 10^{-4}$	$6.06 \cdot 10^{-3}$	$1.24 \cdot 10^{1}$	$5.47 \cdot 10^{-3}$	$6.78 \cdot 10^{-2}$	$1.31 \cdot 10^{-1}$	$6.22 \cdot 10^{-3}$	$8.14 \cdot 10^{-4}$	$3.82 \cdot 10^{-1}$	$2.98 \cdot 10^{-3}$	$1.14 \cdot 10^{-3}$	$7.58 \cdot 10^{-2}$
Total rate (mHz)		-		2.36	-		2.05	-		0.797	-		2.70	7.90

Table C.1.: Background model activities, efficiencies, and effective rate for each isotope and Geant4 volume.

D

Background Fit additional material

This section presents the details concerning the fits performed in Chapter 9

D.1 Pulls

This section shows the pulls aming to test the fit procedure.

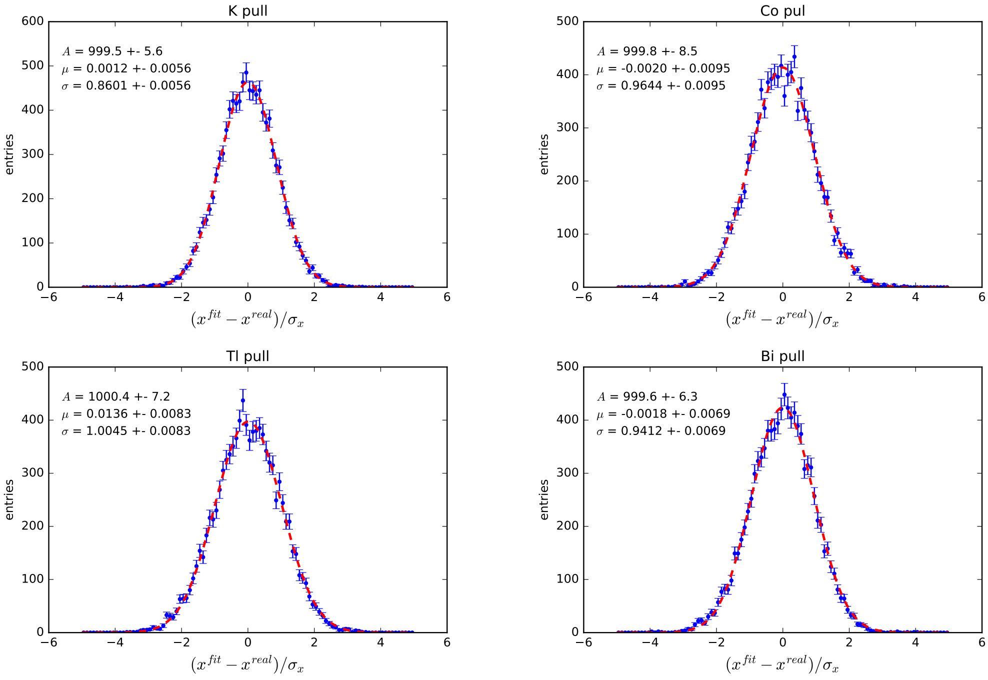

Figure D.1.: Pulls to test the fit algorithm.

The mean behaves as expected, tending to 0, while the sigma is slightly further from the desired value, most probably because of the high correlations present in the data.

D.2 Background Fit Correlations

This section shows the correlations in the background fit reported in Sec. 9.2.4.

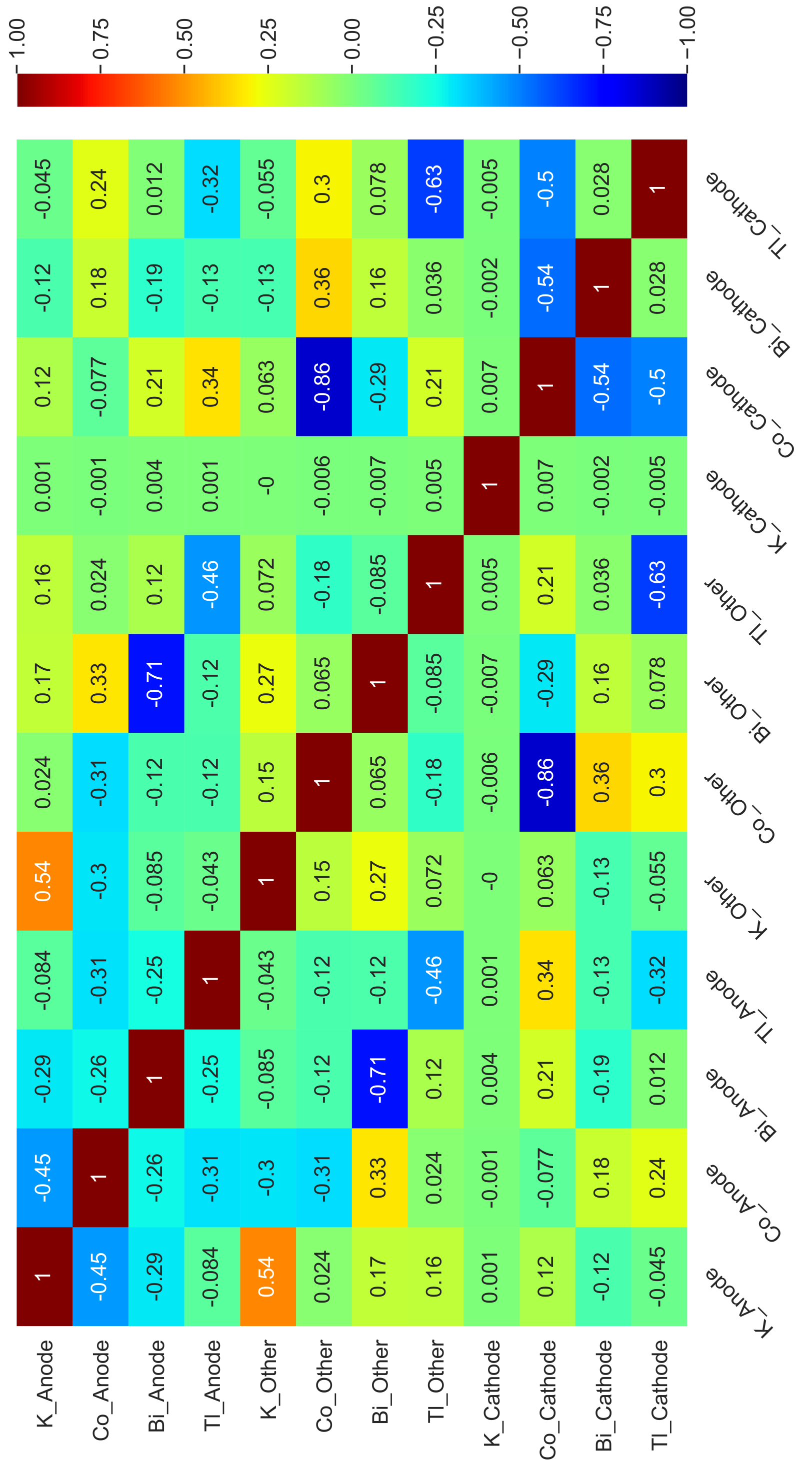

	K_Anode	Co_Anode	Bi_Anode	Tl_Anode	K_Other	Co_Other	Bi_Other	Tl_Other	K_Cathode	Co_Cathode	Bi_Cathode	Tl_Cathode
K_Anode	1	-0.45	-0.29	-0.084	0.54	0.024	0.17	0.16	0.001	0.12	-0.12	-0.045
Co_Anode	-0.45	1	-0.26	-0.31	-0.3	-0.31	0.33	0.024	-0.001	-0.077	0.18	0.24
Bi_Anode	-0.29	-0.26	1	-0.25	-0.085	-0.12	-0.71	0.12	0.004	0.21	-0.19	0.012
Tl_Anode	-0.084	-0.31	-0.25	1	-0.043	-0.12	-0.12	-0.46	0.001	0.34	-0.13	-0.32
K_Other	0.54	-0.3	-0.085	-0.043	1	0.15	0.27	0.072	-0	0.063	-0.13	-0.055
Co_Other	0.024	-0.31	-0.12	-0.12	0.15	1	0.065	-0.18	-0.006	-0.86	0.36	0.3
Bi_Other	0.17	0.33	-0.71	-0.12	0.27	0.065	1	-0.085	-0.007	-0.29	0.16	0.078
Tl_Other	0.16	0.024	0.12	-0.46	0.072	-0.18	-0.085	1	0.005	0.21	0.036	-0.63
K_Cathode	0.001	-0.001	0.004	0.001	-0	-0.006	-0.007	0.005	1	0.007	-0.002	-0.005
Co_Cathode	0.12	-0.077	0.21	0.34	0.063	-0.86	-0.29	0.21	0.007	1	-0.54	-0.5
Bi_Cathode	-0.12	0.18	-0.19	-0.13	-0.13	0.36	0.16	0.036	-0.002	-0.54	1	0.028
Tl_Cathode	-0.045	0.24	0.012	-0.32	-0.055	0.3	0.078	-0.63	-0.005	-0.5	0.028	1

Figure D.2.: Correlation matrix from the background fit parameters

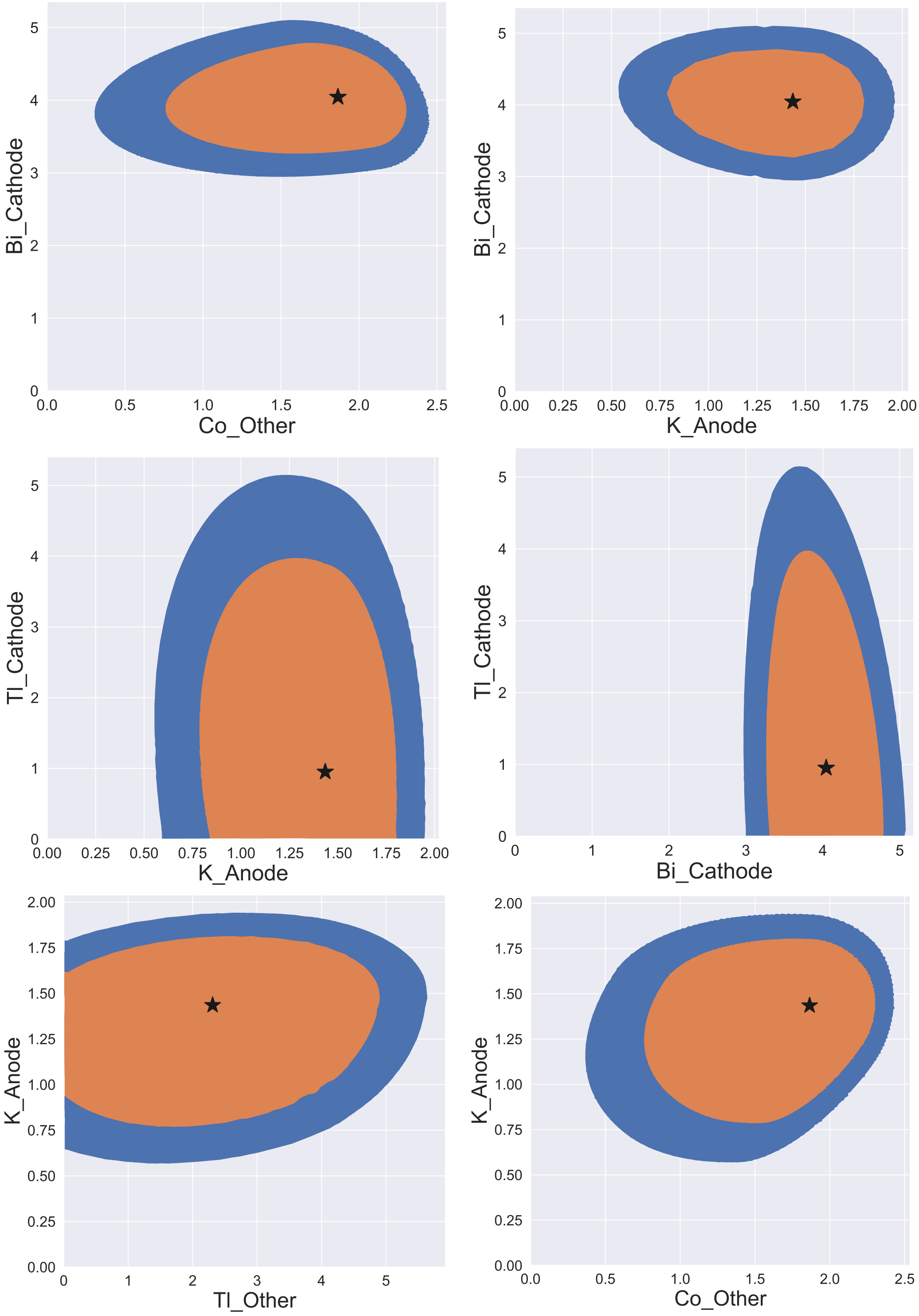

Figure D.3.: (Continues on the next page).

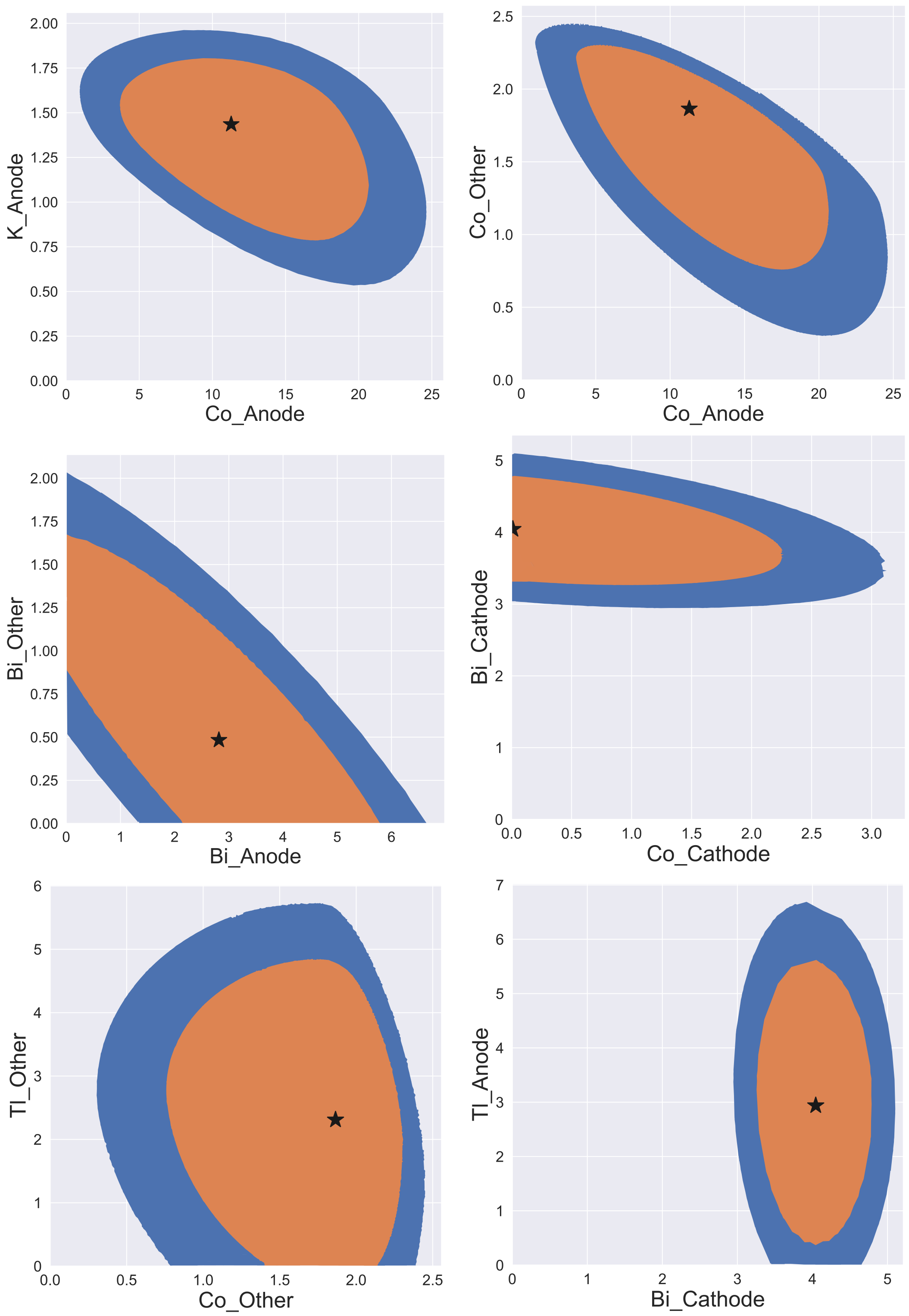

Figure D.3.: Example of some correlation curves from the background fit parameters. The orange (blue) areas represents the 68 % (90 %) CL region and the star denotes the best-fit value.

D.3 Correlations in the $\beta\beta$ fit estimation

This section shows the correlations in the $2\nu\beta\beta$ significance estimation, reported in Sec. 9.3.2.

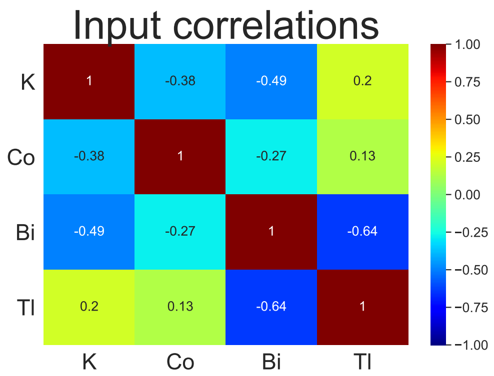

Figure D.4.: Correlation matrix from input to the $2\nu\beta\beta$ significance estimation (see Eq. 9.9).

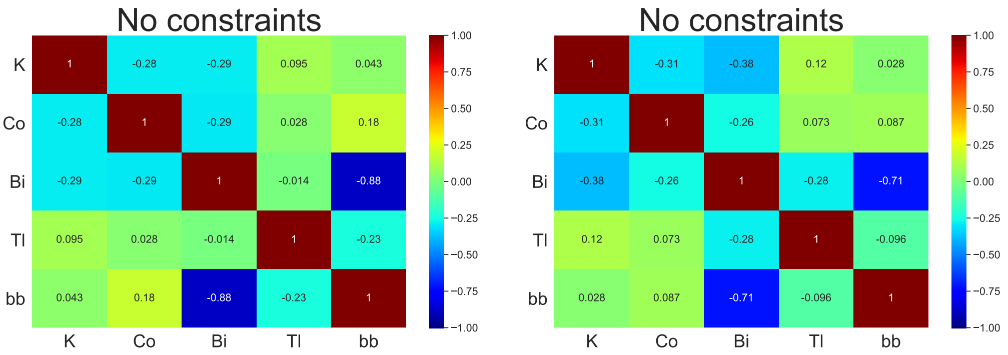

Figure D.5.: Correlation matrix from the output from the $2\nu\beta\beta$ significance estimation in the unconstrained and constrained scenarios.

It is patent that the constrained method does reduce the correlation in general. However, it does introduce some correlation among parameters that were not related, following the input correlation matrix. Still, the parameters with the constrained method tend to reproduce the input values more accurately, and the uncertainties are dramatically reduced, as shown in Fig.D.6.

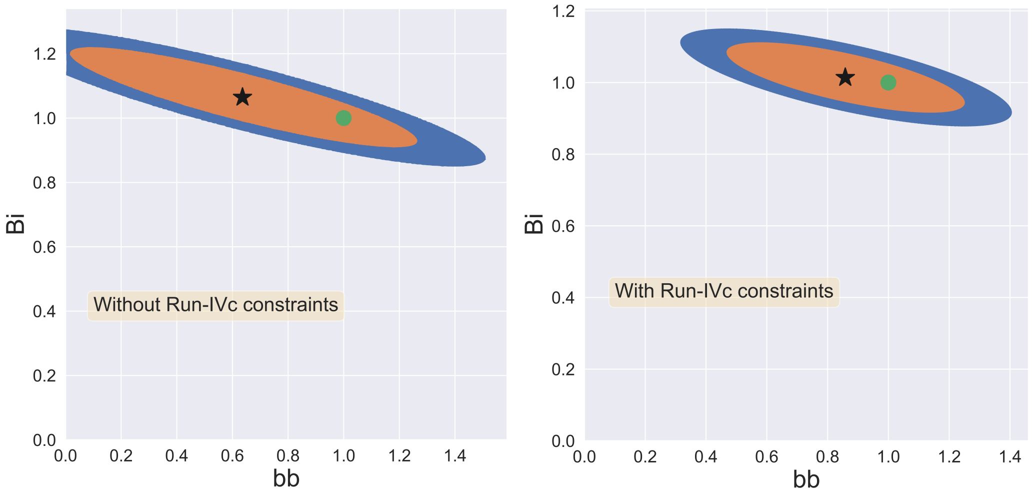

Figure D.6.: Correlation curves for $2\nu\beta\beta$ and ^{214}Bi from the output from the $2\nu\beta\beta$ significance estimation in the unconstrained and constrained scenarios. The orange (blue) areas represents the 68 % (90 %) CL region, the star denotes the best-fit value, and the green dot shows the true value.

Bibliography

[1] J. Chadwick, *Intensitätsverteilung im magnetischen Spectrum der β-Strahlen von radium B + C*, Verhandl. Dtsc. Phys. Ges. **16**, 383 (1914).

[2] C. Ellis and W. A. Wooster, *The average energy of disintegration of radium E*, Proc. R. Soc. Lond. A **117**, 108 (1927).

[3] W. Pauli, *Pauli letter collection, letter to gruppe der radioaktiven bei der gauvereins-tatung zu tübingen*, Physics Today 31, 9, 23 (1978), 1930.

[4] E. Fermi, *Tentativo di una Teoria Dei Raggi β*, Il Nuovo Cimento (1924-1942) **11**, 1 (2008).

[5] A. Pais, *Inward Bound Of Matter and Forces in the Physical World*, 1st ed. (Oxford University Press, 1986).

[6] G. Gamow and E. Teller, *Selection Rules for the β-Disintegration*, Phys. Rev. **49**, 895 (1936).

[7] S. L. Glashow, *Partial Symmetries of Weak Interactions*, Nucl. Phys. **22**, 579 (1961).

[8] S. Weinberg, *A Model of Leptons*, Phys. Rev. Lett. **19**, 1264 (1967).

[9] A. Salam, *Weak and Electromagnetic Interactions*, Conf. Proc. **C680519**, 367 (1968).

[10] H. Bethe and R. Peierrls, *The "Neutrino"*, Nature **133**, 532 (1934).

[11] B. Pontecorvo, *Inverse beta process*, Camb. Monogr. Part. Phys. Nucl. Phys. Cosmol. **1**, 25 (1991).

[12] B. Pontecorvo, *On a method of detection of free neutrinos. Report PD141.*, Chalk River (1946).

[13] H. R. Crane, *An Attempt to Observe the Absorption of Neutrinos*, Phys. Rev. **55**, 501 (1939).

[14] B. T. Cleveland *et al.*, *Measurement of the Solar Electron Neutrino Flux with the Homestake Chlorine Detector*, The Astrophysical Journal **496**, 505 (1998).

[15] **GNO** Collaboration, M. Altmann *et al.*, *Complete results for five years of GNO solar neutrino observations*, Phys. Lett. **B616**, 174 (2005), [arXiv:hep-ex/0504037].

[16] V. N. G., *The Russian-American gallium experiment SAGE*, Physics-Uspekhi **54**, 941 (2011).

[17] C. L. Cowan, F. Reines, F. B. Harrison, H. W. Kruse, and A. D. McGuire, *Detection of the Free Neutrino: a Confirmation*, Science **124**, 103 (1956), [arXiv:https://science.sciencemag.org/content/124/3212/103.full.pdf].

[18] F. Reines, C. L. Cowan, F. B. Harrison, A. D. McGuire, and H. W. Kruse, *Detection of the Free Antineutrino*, Phys. Rev. **117**, 159 (1960).

[19] P. Hernandez, *Neutrino Physics*, CERN Yellow Reports **5**, 85 (2016).

[20] R. Davis, Jr. and D. S. Harmer, *Attempt to observe the* $Cl^{37}(\bar{\nu}e^{-})Ar^{37}$ *reaction induced by reactor antineutrinos*, Bull. Am. Phys. Soc. **4**, 217 (1959).

[21] A. Bettini, *A Brief History of Neutrino*, Adv. Ser. Direct. High Energy Phys. **28**, 1 (2018).

[22] G. Feinberg, *Decays of the* μ *Meson in the Intermediate-Meson Theory*, Phys. Rev. **110**, 1482 (1958).

[23] **MEG** Collaboration, T. Mori, *Final Results of the MEG Experiment*, Nuovo Cim. C **39**, 325 (2017), [arXiv:1606.08168].

[24] B. Pontecorvo, *Electron and Muon Neutrinos*, Sov. Phys. JETP **10**, 1236 (1960), [Zh. Eksp. Teor. Fiz.37,1751(1959)].

[25] G. Danby *et al.*, *Observation of High-Energy Neutrino Reactions and the Existence of Two Kinds of Neutrinos*, Phys. Rev. Lett. **9**, 36 (1962).

[26] **DONUT** Collaboration, K. Kodama *et al.*, *Observation of tau neutrino interactions*, Physics Letters B **504**, 218 (2001).

[27] M. L., *pet projects, standard-model*, `https://github.com/mlubej/pet_projects/tree/master/standard-model`, 2020.

[28] R. Woodard, *How Far Are We from the Quantum Theory of Gravity?*, Rept. Prog. Phys. **72**, 126002 (2009), [arXiv:0907.4238].

[29] L. Canetti, M. Drewes, and M. Shaposhnikov, *Matter and antimatter in the universe*, New Journal of Physics **14**, 095012 (2012).

[30] A. Sakharov, *Violation of CP Invariance, C asymmetry, and baryon asymmetry of the universe*, Sov. Phys. Usp. **34**, 392 (1991).

[31] **LHCb** Collaboration, R. Aaij *et al.*, *Implications of LHCb measurements and future prospects*, Eur. Phys. J. C **73**, 2373 (2013), [arXiv:1208.3355].

[32] **Particle Data Group** Collaboration, P. Zyla *et al.*, *Review of Particle Physics*, PTEP **2020**, 083C01 (2020).

[33] G. 't Hooft, *Naturalness, chiral symmetry, and spontaneous chiral symmetry breaking*, NATO Sci. Ser. B **59**, 135 (1980).

[34] C. Csáki and P. Tanedo, *Beyond the Standard Model*, in *2013 European School of High-Energy Physics*, pp. 169–268, 2015, [arXiv:1602.04228].

[35] H. P. Nilles, *Supersymmetry, Supergravity and Particle Physics*, Phys. Rept. **110**, 1 (1984).

[36] **SNO** Collaboration, Q. Ahmad *et al.*, *Measurement of the rate of $\nu_e + d \rightarrow p + p + e^-$ interactions produced by ^8B solar neutrinos at the Sudbury Neutrino Observatory*, Phys. Rev. Lett. **87**, 071301 (2001), [arXiv:nucl-ex/0106015].

[37] **Super-Kamiokande** Collaboration, Y. Fukuda *et al.*, *Evidence for oscillation of atmospheric neutrinos*, Phys. Rev. Lett. **81**, 1562 (1998), [arXiv:hep-ex/9807003].

[38] **GALLEX** Collaboration, P. Anselmann *et al.*, *GALLEX results from the first 30 solar neutrino runs*, Phys. Lett. B **327**, 377 (1994).

[39] **SAGE** Collaboration, J. Abdurashitov *et al.*, *Results from SAGE*, Phys. Lett. B **328**, 234 (1994).

[40] **Super-Kamiokande** Collaboration, R. Wendell *et al.*, *Atmospheric neutrino oscillation analysis with sub-leading effects in Super-Kamiokande I, II, and III*, Phys. Rev. D **81**, 092004 (2010), [arXiv:1002.3471].

[41] B. Pontecorvo, *Mesonium and anti-mesonium*, Sov. Phys. JETP **6**, 429 (1957).

[42] B. Pontecorvo, *Inverse beta processes and nonconservation of lepton charge*, Sov. Phys. JETP **7**, 172 (1958).

[43] Z. Maki, M. Nakagawa, and S. Sakata, *Remarks on the Unified Model of Elementary Particles*, Progress of Theoretical Physics **28**, 870 (1962), [arXiv:https://academic.oup.com/ptp/article-pdf/28/5/870/5258750/28-5-870.pdf].

[44] S. Bilenky*Introduction to the Physics of Massive and Mixed Neutrinos* Vol. 947 (Springer, 2018).

[45] L. Wolfenstein, *Neutrino oscillations in matter,* Phys. Rev. D **17**, 2369 (1978).

[46] S. Mikheyev and A. Smirnov, *Resonance Amplification of Oscillations in Matter and Spectroscopy of Solar Neutrinos,* Sov. J. Nucl. Phys. **42**, 913 (1985).

[47] Stanco, L., *The next challenge for neutrinos: the mass ordering,* EPJ Web Conf. **164**, 01031 (2017).

[48] P. F. de Salas *et al.*, *2020 global reassessment of the neutrino oscillation picture,* JHEP **02**, 071 (2021), [arXiv:2006.11237].

[49] C. A. Ternes *et al.*, *Neutrino mass ordering at DUNE: An extra ν bonus,* Phys. Rev. D **100**, 093004 (2019), [arXiv:1905.03589].

[50] R. Dvornicky, K. Muto, F. Simkovic, and A. Faessler, *The absolute mass of neutrino and the first unique forbidden beta-decay of 187Re,* Phys. Rev. **C83**, 045502 (2011), [arXiv:1101.3413].

[51] A. B. McDonald, G. Drexlin, V. Hannen, S. Mertens, and C. Weinheimer, *Current Direct Neutrino Mass Experiments,* Advances in High Energy Physics **2013**, 293986 (2013).

[52] **KATRIN** Collaboration, M. Aker *et al.*, *Direct neutrino-mass measurement with sub-electronvolt sensitivity,* Nature Phys. **18**, 160 (2022).

[53] A. Giuliani, *Neutrino Physics with Low-Temperature Detectors,* Journal of Low Temperature Physics **167**, 991 (2012).

[54] A. De Rújula and M. Lusignoli, *Calorimetric measurements of 163holmium decay as tools to determine the electron neutrino mass,* Physics Letters B **118**, 429 (1982).

[55] T. J. Loredo and D. Q. Lamb, *Bayesian analysis of neutrinos observed from supernova SN 1987A,* Phys. Rev. D **65**, 063002 (2002).

[56] G. Pagliaroli, F. Rossi-Torres, and F. Vissani, *Neutrino mass bound in the standard scenario for supernova electronic antineutrino emission,* Astroparticle Physics **33**, 287 (2010).

[57] **Planck** Collaboration, Aghanim, N. *et al.*, *Planck 2018 results - VI. Cosmological parameters,* A&A **641**, A6 (2020).

[58] C. Giunti and C. W. Kim, *Fundamentals of Neutrino Physics and Astrophysics* (Oxford Scholarship, 2007).

[59] J. Gomez-Cadenas, J. Martin-Albo, M. Mezzetto, F. Monrabal, and M. Sorel, *The Search for neutrinoless double beta decay*, Riv. Nuovo Cim. **35**, 29 (2012), [arXiv:1109.5515].

[60] E. Majorana, *Teoria simmetrica dell'e del positrone*, Nuovo Cim. **14**, 171 (1937).

[61] S. Weinberg, *Baryon- and Lepton-Nonconserving Processes*, Phys. Rev. Lett. **43**, 1566 (1979).

[62] E. Ma, *Pathways to Naturally Small Neutrino Masses*, Phys. Rev. Lett. **81**, 1171 (1998).

[63] S. Centelles Chuliá, R. Srivastava, and J. Valle, *Seesaw roadmap to neutrino mass and dark matter*, Phys. Lett. B **781**, 122 (2018), [arXiv:1802.05722].

[64] S. Davidson, E. Nardi, and Y. Nir, *Leptogenesis*, Physics Reports **466**, 105 (2008).

[65] C. Dib, S. Gribanov, V.and Kovalenko, and I. Schmidt, *Lepton number violating processes and Majorana neutrinos*, Part. Nucl. Lett. **106**, 42 (2001), [arXiv:hep-ph/0011213].

[66] A. Atre, V. Barger, and T. Han, *Upper bounds on lepton-number violating processes*, Phys. Rev. D **71**, 113014 (2005).

[67] K. Zuber, *Effective Majorana neutrino masses and Delta(L) = 2 processes*, Prog. Part. Nucl. Phys. **48**, 223 (2002).

[68] **KamLAND-Zen** Collaboration, A. Gando *et al.*, *Search for Majorana Neutrinos Near the Inverted Mass Hierarchy Region with KamLAND-Zen*, Phys. Rev. Lett. **117**, 082503 (2016).

[69] **SINDRUM II** Collaboration, J. Kaulard *et al.*, *Improved limit on the branching ratio of mu- –> e+ conversion on titanium*, Phys. Lett. B **422**, 334 (1998).

[70] A. J. Long, C. Lunardini, and E. Sabancilar, *Detecting non-relativistic cosmic neutrinos by capture on tritium: phenomenology and physics potential*, Journal of Cosmology and Astroparticle Physics **2014**, 038 (2014).

[71] **PTOLEMY** Collaboration, M. Betti *et al.*, *Neutrino physics with the PTOLEMY project: active neutrino properties and the light sterile case*, JCAP **07**, 047 (2019), [arXiv:1902.05508].

[72] A. Faessler, R. Hodak, S. Kovalenko, and F. Simkovic, *Tritium and rhenium as a probe of cosmic neutrino background*, J. Phys. **G38**, 075202 (2011).

[73] S. Alekhin *et al.*, *A facility to search for hidden particles at the CERN SPS: the SHiP physics case*, Reports on Progress in Physics **79**, 124201 (2016).

[74] G. Hernández-Tomé, J. I. Illana, M. Masip, G. López Castro, and P. Roig, *Effects of heavy Majorana neutrinos on lepton flavor violating processes*, Phys. Rev. D **101**, 075020 (2020).

[75] A. Atre, T. Han, S. Pascoli, and B. Zhang, *The search for heavy Majorana neutrinos*, Journal of High Energy Physics **2009**, 030 (2009).

[76] F. del Aguila and J. Aguilar-Saavedra, *Distinguishing seesaw models at LHC with multi-lepton signals*, Nuclear Physics B **813**, 22 (2009).

[77] D. Alva, T. Han, and R. Ruiz, *Heavy Majorana neutrinos from $W\gamma$ fusion at hadron colliders*, JHEP **02**, 072 (2015), [arXiv:1411.7305].

[78] **LBNE** Collaboration, C. Adams *et al.*, *The Long-Baseline Neutrino Experiment: Exploring Fundamental Symmetries of the Universe*, in *Snowmass 2013: Workshop on Energy Frontier*, 2013, [arXiv:1307.7335].

[79] N. Kitazawa, N. Okada, and S. Sasaki, *Majorana neutrinos as the dark matters in the cold plus hot dark matter model*, Physics Letters B **380**, 324 (1996).

[80] M. Goeppert-Mayer, *Double Beta-Disintegration*, Phys. Rev. **48**, 512 (1935).

[81] M. G. Inghram and J. H. Reynolds, *Double Beta-Decay of* Te^{130}, Phys. Rev. **78**, 822 (1950).

[82] S. R. Elliott, A. A. Hahn, and M. K. Moe, *Direct evidence for two-neutrino double-beta decay in* $^{82}\mathrm{Se}$, Phys. Rev. Lett. **59**, 2020 (1987).

[83] A. Barabash, *Precise Half-Life Values for Two-Neutrino Double-β Decay: 2020 Review*, Universe **6**, 159 (2020), [arXiv:2009.14451].

[84] S. S. Ratkevich *et al.*, *Comparative study of the double-K-shell-vacancy production in single- and double-electron-capture decay*, Phys. Rev. C **96**, 065502 (2017).

[85] **XENON** Collaboration, E. Aprile *et al.*, *Observation of two-neutrino double electron capture in* ^{124}*Xe with XENON1T*, Nature **568**, 532 (2019), [arXiv:1904.11002].

[86] M. Pujol, B. Marty, P. Burnard, and P. Philippot, *Xenon in Archean barite: Weak decay of 130Ba, mass-dependent isotopic fractionation and implication for barite formation*, Geochimica et Cosmochimica Acta **73**, 6834 (2009).

[87] A. L. Turkevich, T. E. Economou, and G. A. Cowan, *Double-beta decay of* ^{238}U, Phys. Rev. Lett. **67**, 3211 (1991).

[88] W. H. Furry, *On Transition Probabilities in Double Beta-Disintegration*, Phys. Rev. **56**, 1184 (1939).

[89] J. Schechter and J. Valle, *Neutrinoless Double beta Decay in SU(2) x U(1) Theories*, Phys. Rev. D **25**, 2951 (1982).

[90] M. Duerr, M. Lindner, and A. Merle, *On the Quantitative Impact of the Schechter-Valle Theorem*, JHEP **06**, 091 (2011), [arXiv:1105.0901].

[91] F. T. Avignone, S. R. Elliott, and J. Engel, *Double beta decay, Majorana neutrinos, and neutrino mass*, Rev. Mod. Phys. **80**, 481 (2008).

[92] J. Kotila and F. Iachello, *Phase-space factors for double-*β *decay*, Phys. Rev. C **85**, 034316 (2012).

[93] F. Cappuzzello *et al.*, *The role of nuclear reactions in the problem of* $0\nu\beta\beta$*decay and the NUMEN project at INFN-LNS*, Journal of Physics: Conference Series **630**, 012018 (2015).

[94] M. Cavallaro *et al.*, *Measuring nuclear reaction cross sections to extract information on neutrinoless double beta decay*, Journal of Physics: Conference Series **966**, 012021 (2018).

[95] **GAMBIT Cosmology Workgroup** Collaboration, P. Stöcker *et al.*, *Strengthening the bound on the mass of the lightest neutrino with terrestrial and cosmological experiments*, Phys. Rev. D **103**, 123508 (2021), [arXiv:2009.03287].

[96] F. Vissani, *Signal of neutrinoless double beta decay, neutrino spectrum and oscillation scenarios.*, Journal of High Energy Physics **1999**, 022 (1999).

[97] M. Agostini, G. Benato, and J. A. Detwiler, *Discovery probability of next-generation neutrinoless double-*β *decay experiments*, Phys. Rev. D **96**, 053001 (2017).

[98] W. Rodejohann, *Neutrino-less Double Beta Decay and Particle Physics*, International Journal of Modern Physics E **20**, 1833 (2011), [arXiv:https://doi.org/10.1142/S0218301311020186].

[99] R. N. Mohapatra, *Limits on the Mass of the Right-handed Majorana Neutrino*, Phys. Rev. D **34**, 909 (1986).

[100] R. Mohapatra, *New Contributions to Neutrinoless Double beta Decay in Supersymmetric Theories*, Phys. Rev. D **34**, 3457 (1986).

[101] H. M. Georgi, S. L. Glashow, and S. Nussinov, *Unconventional Model of Neutrino Masses*, Nucl. Phys. B **193**, 297 (1981).

[102] G. J. Feldman and R. D. Cousins, *Unified approach to the classical statistical analysis of small signals*, Phys. Rev. D **57**, 3873 (1998).

[103] F. Avignone, G. King, and Y. Zdesenko, *Next generation double-beta decay experiments: Metrics for their evaluation*, New J. Phys. **7**, 6 (2005).

[104] J. Gómez-Cadenas and J. Martín-Albo, *Phenomenology of neutrinoless double beta decay*, PoS **GSSI14**, 004 (2015), [arXiv:1502.00581].

[105] J. Meija *et al.*, *Isotopic compositions of the elements 2013 (IUPAC Technical Report)*, Pure and Applied Chemistry **88**, 293 (01 Mar. 2016).

[106] G. Audi and A. Wapstra, *The 1993 atomic mass evaluation: (I) Atomic mass table*, Nuclear Physics A **565**, 1 (1993).

[107] J. Menendez, A. Poves, E. Caurier, and F. Nowacki, *Disassembling the Nuclear Matrix Elements of the Neutrinoless beta beta Decay*, Nucl. Phys. A **818**, 139 (2009), [arXiv:0801.3760].

[108] J. Suhonen and O. Civitarese, *Review of the properties of the 0 nu beta- beta- nuclear matrix elements*, J. Phys. G **39**, 124005 (2012).

[109] F. Šimkovic, V. Rodin, and P. Faessler, A.and Vogel, *$0\nu\beta\beta$ and $2\nu\beta\beta$ nuclear matrix elements, quasiparticle random-phase approximation, and isospin symmetry restoration*, Phys. Rev. C **87**, 045501 (2013), [arXiv:1302.1509].

[110] J. Barea, J. Kotila, and F. Iachello, *Nuclear matrix elements for double-β decay*, Phys. Rev. C **87**, 014315 (2013), [arXiv:1301.4203].

[111] N. López Vaquero, T. R. Rodríguez, and J. L. Egido, *Shape and pairing fluctuations effects on neutrinoless double beta decay nuclear matrix elements*, Phys. Rev. Lett. **111**, 142501 (2013), [arXiv:1401.0650].

[112] A. V. Tikhomirov, *Centrifugal enrichment of stable isotopes and modern physical experiments*, Czechoslovak Journal of Physics **50**, 577 (2000).

[113] **NEXT** Collaboration, L. Rogers *et al.*, *Mitigation of backgrounds from cosmogenic* ^{137}*Xe in xenon gas experiments using* ^{3}*He neutron capture*, J. Phys. G **47**, 075001 (2020), [arXiv:2001.11147].

[114] M. Agostini *et al.*, *Pulse shape discrimination for GERDA Phase I data*, Eur. Phys. J. C **73**, 2583 (2013), [arXiv:1307.2610].

[115] S. Z. and, *Pulse-shape discrimination techniques for the COBRA double beta-decay experiment at LNGS*, Journal of Physics: Conference Series **888**, 012076 (2017).

[116] **NEXT** Collaboration, P. Ferrario *et al.*, *First proof of topological signature in the high pressure xenon gas TPC with electroluminescence amplification for the NEXT experiment*, JHEP **01**, 104 (2016), [arXiv:1507.05902].

[117] **NEXT** Collaboration, P. Ferrario *et al.*, *Demonstration of the event identification capabilities of the NEXT-White detector*, JHEP **10**, 052 (2019), [arXiv:1905.13141].

[118] **EXO** Collaboration, S. Delaquis *et al.*, *Deep Neural Networks for Energy and Position Reconstruction in EXO-200*, JINST **13**, P08023 (2018), [arXiv:1804.09641].

[119] **LZ** Collaboration, D. Akerib *et al.*, *Projected sensitivity of the LUX-ZEPLIN experiment to the* $0\nu\beta\beta$ *decay of* ^{136}Xe, Phys. Rev. C **102**, 014602 (2020), [arXiv:1912.04248].

[120] **NEXT** Collaboration, A. D. McDonald *et al.*, *Demonstration of Single-Barium-Ion Sensitivity for Neutrinoless Double-Beta Decay Using Single-Molecule Fluorescence Imaging*, Phys. Rev. Lett. **120**, 132504 (2018).

[121] **nEXO** Collaboration, C. Chambers *et al.*, *Imaging individual barium atoms in solid xenon for barium tagging in nEXO*, Nature **569**, 203 (2019), [arXiv:1806.10694].

[122] C. S. Wu, E. Ambler, R. W. Hayward, D. D. Hoppes, and R. P. Hudson, *Experimental Test of Parity Conservation in Beta Decay*, Phys. Rev. **105**, 1413 (1957).

[123] V. Lyubimov, E. Novikov, V. Nozik, E. Tretyakov, and V. Kosik, *An Estimate of the electron-Neutrino Mass from the beta Spectrum of Tritium in the Valine Molecule*, Phys. Lett. B **94**, 266 (1980).

[124] H. Klapdor-Kleingrothaus, *The Heidelberg-Moscow double beta decay experiment with enriched Ge-76: First results*, Conf. Proc. C **910725V1**, 667 (1991).

[125] H. Klapdor-Kleingrothaus *et al.*, *Latest results from the Heidelberg-Moscow double beta decay experiment*, Eur. Phys. J. A **12**, 147 (2001), [arXiv:hep-ph/0103062].

[126] H. Klapdor-Kleingrothaus and I. Krivosheina, *The evidence for the observation of 0nu beta beta decay: The identification of 0nu beta beta events from the full spectra*, Mod. Phys. Lett. A **21**, 1547 (2006).

[127] H. Harney, *Reply to the comment on 'Evidence for neutrinoless double beta decay'*, (2001), [arXiv:hep-ph/0205293].

[128] C. Aalseth *et al.*, *Comment on 'Evidence for neutrinoless double beta decay'*, Mod. Phys. Lett. A **17**, 1475 (2002), [arXiv:hep-ex/0202018].

[129] **GERDA** Collaboration, M. Agostini *et al.*, *Improved Limit on Neutrinoless Double-β Decay of $^{76}\mathrm{Ge}$ from GERDA Phase II*, Phys. Rev. Lett. **120**, 132503 (2018).

[130] **KamLAND-Zen** Collaboration, A. Gando *et al.*, *Limit on Neutrinoless $\beta\beta$ Decay of ^{136}Xe from the First Phase of KamLAND-Zen and Comparison with the Positive Claim in ^{76}Ge*, Phys. Rev. Lett. **110**, 062502 (2013), [arXiv:1211.3863].

[131] **CUORE** Collaboration, C. Arnaboldi *et al.*, *CUORE: A Cryogenic underground observatory for rare events*, Nucl. Instrum. Meth. A **518**, 775 (2004), [arXiv:hep-ex/0212053].

[132] R. Arnold *et al.*, *Technical design and performance of the NEMO 3 detector*, Nucl. Instrum. Meth. A **536**, 79 (2005), [arXiv:physics/0402115].

[133] S. Umehara *et al.*, *Neutrino-less double-β decay of $^{48}\mathrm{Ca}$ studied by CaF_2(Eu) scintillators*, Phys. Rev. C **78**, 058501 (2008).

[134] **CUPID** Collaboration, O. Azzolini *et al.*, *Final result of CUPID-0 phase-I in the search for the ^{82}Se Neutrinoless Double-β Decay*, Phys. Rev. Lett. **123**, 032501 (2019), [arXiv:1906.05001].

[135] **NEMO-3** Collaboration, J. Argyriades *et al.*, *Measurement of the two neutrino double beta decay half-life of Zr-96 with the NEMO-3 detector*, Nucl. Phys. A **847**, 168 (2010), [arXiv:0906.2694].

[136] **CUPID** Collaboration, E. Armengaud *et al.*, *New Limit for Neutrinoless Double-Beta Decay of* ^{100}*Mo from the CUPID-Mo Experiment*, Phys. Rev. Lett. **126**, 181802 (2021), [arXiv:2011.13243].

[137] **NEMO-3** Collaboration, R. Arnold *et al.*, *Measurement of the* $2\nu\beta\beta$ *Decay Half-Life and Search for the* $0\nu\beta\beta$ *Decay of* ^{116}*Cd with the NEMO-3 Detector*, Phys. Rev. D **95**, 012007 (2017), [arXiv:1610.03226].

[138] **CUORE** Collaboration, D. Q. Adams *et al.*, *High sensitivity neutrinoless double-beta decay search with one tonne-year of CUORE data*, (2021), [arXiv:2104.06906].

[139] **KamLAND-Zen** Collaboration, S. Abe *et al.*, *First Search for the Majorana Nature of Neutrinos in the Inverted Mass Ordering Region with KamLAND-Zen*, (2022), [arXiv:2203.02139].

[140] **NEMO-3** Collaboration, R. Arnold *et al.*, *Measurement of the* $2\nu\beta\beta$ *decay half-life of* ^{150}*Nd and a search for 0*$\nu\beta\beta$ *decay processes with the full exposure from the NEMO-3 detector*, Phys. Rev. D **94**, 072003 (2016), [arXiv:1606.08494].

[141] M. J. Dolinski, A. W. Poon, and W. Rodejohann, *Neutrinoless Double-Beta Decay: Status and Prospects*, Annual Review of Nuclear and Particle Science **69**, 219 (2019), [arXiv:https://doi.org/10.1146/annurev-nucl-101918-023407].

[142] A. B. McDonald, A. Giuliani, and A. Poves, *Neutrinoless Double-Beta Decay*, Advances in High Energy Physics **2012**, 857016 (2012).

[143] **GERDA** Collaboration, K. Ackermann *et al.*, *The GERDA experiment for the search of* $0\nu\beta\beta$ *decay in* ^{76}*Ge*, Eur. Phys. J. C **73**, 2330 (2013), [arXiv:1212.4067].

[144] **Majorana** Collaboration, S. Alvis *et al.*, *A Search for Neutrinoless Double-Beta Decay in* ^{76}*Ge with 26 kg-yr of Exposure from the MAJORANA DEMONSTRATOR*, Phys. Rev. C **100**, 025501 (2019), [arXiv:1902.02299].

[145] **LEGEND** Collaboration, N. Abgrall *et al.*, *The Large Enriched Germanium Experiment for Neutrinoless Double Beta Decay (LEGEND)*, AIP Conf. Proc. **1894**, 020027 (2017), [arXiv:1709.01980].

[146] D. Adams *et al.*, *CUORE: The first bolometric experiment at the ton scale for the search for neutrino-less double beta decay*, Nucl. Instrum. Meth. A **958**, 162440 (2020).

[147] D. Artusa *et al.*, *The LUCIFER/CUPID-0 demonstrator: searching for the neutrinoless double-beta decay with Zn^{82}Se scintillating bolometers*, J. Phys. Conf. Ser. **888**, 012077 (2017).

[148] **AMoRE** Collaboration, M. H. Lee, *AMoRE: A search for neutrinoless double-beta decay of 100Mo using low-temperature molybdenum-containing crystal detectors*, JINST **15**, C08010 (2020), [arXiv:2005.05567].

[149] **CROSS** Collaboration, A. Zolotarova, *The CROSS experiment: search for $0\nu2\beta$ decay with surface sensitive bolometers*, J. Phys. Conf. Ser. **1468**, 012147 (2020).

[150] **KamLAND-Zen** Collaboration, A. Gando *et al.*, *Search for Majorana Neutrinos near the Inverted Mass Hierarchy Region with KamLAND-Zen*, Phys. Rev. Lett. **117**, 082503 (2016), [arXiv:1605.02889], [Addendum: Phys.Rev.Lett. 117, 109903 (2016)].

[151] **SNO+** Collaboration, S. Andringa *et al.*, *Current Status and Future Prospects of the SNO+ Experiment*, Adv. High Energy Phys. **2016**, 6194250 (2016), [arXiv:1508.05759].

[152] Y. Fukuda, T. Gunji, S. Moriyama, and I. Ogawa, *Development of a liquid scintillator containing a zirconium β-keto ester complex for the ZICOS experiment*, Nucl. Part. Phys. Proc. **273-275**, 2615 (2016).

[153] **EXO-200** Collaboration, G. Anton *et al.*, *Measurement of the scintillation and ionization response of liquid xenon at MeV energies in the EXO-200 experiment*, Phys. Rev. C **101**, 065501 (2020), [arXiv:1908.04128].

[154] **NEXT** Collaboration, J. Renner *et al.*, *Energy calibration of the NEXT-White detector with 1% resolution near $Q_{\beta\beta}$ of^{136}Xe*, JHEP **10**, 230 (2019), [arXiv:1905.13110].

[155] S. Wang, *PandaX-III high pressure xenon TPC for Neutrinoless Double Beta Decay search*, Nucl. Instrum. Meth. A **958**, 162439 (2020).

[156] **AXEL** Collaboration, S. Ban, *AXEL : High pressure Xe gas TPC for neutrinoless double-beta decay search*, J. Phys. Conf. Ser. **1468**, 012207 (2020).

[157] A. Jeremie, *The SuperNEMO demonstrator double beta experiment*, Nucl. Instrum. Meth. A **958**, 162115 (2020).

[158] D. Poda and A. Giuliani, *Low background techniques in bolometers for double-beta decay search*, Int. J. Mod. Phys. A **32**, 1743012 (2017), [arXiv:1711.01075].

[159] **CUORE** Collaboration, D. Artusa *et al.*, *Searching for neutrinoless double-beta decay of ^{130}Te with CUORE*, Adv. High Energy Phys. **2015**, 879871 (2015), [arXiv:1402.6072].

[160] **CUORE** Collaboration, D. Chiesa, *The CUORE experiment at LNGS*, in *18th Lomonosov Conference on Elementary Particle Physics*, pp. 90–93, 2019, [arXiv:1712.07995].

[161] **CUORE** Collaboration, D. Adams *et al.*, *Improved Limit on Neutrinoless Double-Beta Decay in ^{130}Te with CUORE*, Phys. Rev. Lett. **124**, 122501 (2020), [arXiv:1912.10966].

[162] **CUORE** Collaboration, C. Alduino *et al.*, *CUORE sensitivity to $0\nu\beta\beta$ decay*, Eur. Phys. J. C **77**, 532 (2017), [arXiv:1705.10816].

[163] **GERDA** Collaboration, C. M. Cattadori, *Double beta decay searches by semi-conductor detectors*, J. Phys. Conf. Ser. **136**, 022033 (2008).

[164] **COBRA** Collaboration, J. Ebert *et al.*, *The COBRA demonstrator at the LNGS underground laboratory*, Nucl. Instrum. Meth. A **807**, 114 (2016), [arXiv:1507.08177].

[165] A. Chavarria, C. Galbiati, X. Li, and J. Rowlands, *A high-resolution CMOS imaging detector for the search of neutrinoless double β decay in ^{82}Se*, JINST **12**, P03022 (2017), [arXiv:1609.03887].

[166] **GERDA** Collaboration, M. Agostini *et al.*, *Upgrade for Phase II of the Gerda experiment*, Eur. Phys. J. C **78**, 388 (2018), [arXiv:1711.01452].

[167] **GERDA** Collaboration, M. Agostini *et al.*, *Results on Neutrinoless Double-β Decay of ^{76}Ge from Phase I of the GERDA Experiment*, Phys. Rev. Lett. **111**, 122503 (2013), [arXiv:1307.4720].

[168] **GERDA** Collaboration, M. Agostini *et al.*, *Final Results of GERDA on the Search for Neutrinoless Double-β Decay*, Phys. Rev. Lett. **125**, 252502 (2020), [arXiv:2009.06079].

[169] A. Domula *et al.*, *Pulse shape discrimination performance of Inverted Coaxial Ge detectors*, Nucl. Instrum. Meth. A **891**, 106 (2018), [arXiv:1711.01433].

[170] **KamLAND-Zen** Collaboration, A. Gando *et al.*, *Measurement of the double-β decay half-life of ^{136}Xe with the KamLAND-Zen experiment*, Phys. Rev. C **85**, 045504 (2012), [arXiv:1201.4664].

[171] R. Raghavan, *New approach to the search for neutrinoless double beta decay*, Phys. Rev. Lett. **72**, 1411 (1994).

[172] J. Caravaca *et al.*, *Experiment to demonstrate separation of Cherenkov and scintillation signals*, Phys. Rev. C **95**, 055801 (2017), [arXiv:1610.02029].

[173] J. Gruszko *et al.*, *Detecting Cherenkov light from 1–2 MeV electrons in linear alkylbenzene*, JINST **14**, P02005 (2019), [arXiv:1811.11144].

[174] I. Ostrovskiy and K. O'Sullivan, *Search for neutrinoless double beta decay*, Mod. Phys. Lett. A **31**, 1630017 (2016), [arXiv:1605.00631], [Erratum: Mod.Phys.Lett.A 31, 1692004 (2016)].

[175] **KamLAND-Zen** Collaboration, H. Ozaki and A. Takeuchi, *Upgrade of the KamLAND-Zen mini-balloon and future prospects*, Nucl. Instrum. Meth. **A**, 162353 (2019).

[176] J. N. Marx and D. R. Nygren, *The Time Projection Chamber*, Phys. Today **31N10**, 46 (1978).

[177] **NEXT** Collaboration, V. Alvarez *et al.*, *Near-Intrinsic Energy Resolution for 30 to 662 keV Gamma Rays in a High Pressure Xenon Electroluminescent TPC*, Nucl. Instrum. Meth. A **708**, 101 (2013), [arXiv:1211.4474].

[178] **XENON** Collaboration, J. Naganoma, *The XENON dark matter search experiment*, JINST **11**, C02048 (2016).

[179] **LUX** Collaboration, D. Akerib *et al.*, *The Large Underground Xenon (LUX) Experiment*, Nucl. Instrum. Meth. A **704**, 111 (2013), [arXiv:1211.3788].

[180] **DARWIN** Collaboration, F. Agostini *et al.*, *Sensitivity of the DARWIN observatory to the neutrinoless double beta decay of ^{136}Xe*, Eur. Phys. J. C **80**, 808 (2020), [arXiv:2003.13407].

[181] M. Sorel, *Xenon TPCs for Double Beta Decay Searches*, in *Prospects in Neutrino Physics*, 2019, [arXiv:1904.06349].

[182] J. J. Gomez-Cadenas, F. Monrabal Capilla, and P. Ferrario, *High Pressure Gas Xenon TPCs for Double Beta Decay Searches*, Front. in Phys. **7**, 51 (2019), [arXiv:1903.02435].

[183] **KamLAND-Zen** Collaboration, M. Auger *et al.*, *The EXO-200 detector, part I: Detector design and construction*, JINST **7**, P05010 (2012), [arXiv:1202.2192].

[184] **EXO-200** Collaboration, J. Albert *et al.*, *Search for Majorana neutrinos with the first two years of EXO-200 data*, Nature **510**, 229 (2014), [arXiv:1402.6956].

[185] **EXO-200** Collaboration, G. Anton *et al.*, *Search for Neutrinoless Double-β Decay with the Complete EXO-200 Dataset*, Phys. Rev. Lett. **123**, 161802 (2019), [arXiv:1906.02723].

[186] **CUPID** Collaboration, M. Pavan, *CUPID: CUORE Upgrade with Particle IDentification*, J. Phys. Conf. Ser. **1468**, 012210 (2020).

[187] **LEGEND** Collaboration, A. J. Zsigmond, *LEGEND: The future of neutrinoless double-beta decay search with germanium detectors*, J. Phys. Conf. Ser. **1468**, 012111 (2020).

[188] **LEGEND** Collaboration, N. Abgrall *et al.*, *The Large Enriched Germanium Experiment for Neutrinoless $\beta\beta$ Decay: LEGEND-1000 Preconceptual Design Report*, (2021), [arXiv:2107.11462].

[189] R. Nakamura, H. Sambonsugi, K. Shiraishi, and Y. Wada, *Research and development toward KamLAND2-Zen*, J. Phys. Conf. Ser. **1468**, 012256 (2020).

[190] **SNO+** Collaboration, E. Leming, *SNO+: Current Results and Future Prospects*, PoS **NOW2018**, 027 (2019).

[191] **nEXO** Collaboration, J. Albert *et al.*, *Sensitivity and Discovery Potential of nEXO to Neutrinoless Double Beta Decay*, Phys. Rev. C **97**, 065503 (2018), [arXiv:1710.05075].

[192] **NEXT** Collaboration, V. Alvarez *et al.*, *Initial results of NEXT-DEMO, a large-scale prototype of the NEXT-100 experiment*, JINST **8**, P04002 (2013), [arXiv:1211.4838].

[193] D. Nygren, *High-pressure xenon gas electroluminescent TPC for 0nu beta beta-decay search*, Nucl. Instrum. Meth. A **603**, 337 (2009).

[194] **NEXT** Collaboration, V. Alvarez *et al.*, *The NEXT-100 experiment for neutrinoless double beta decay searches (Conceptual Design Report)*, (2011), [arXiv:1106.3630].

[195] U. Fano, *Ionization Yield of Radiations. 2. The Fluctuations of the Number of Ions*, Phys. Rev. **72**, 26 (1947).

[196] S. J. C. do Carmo, F. I. G. M. Borges, F. L. R. Vinagre, and C. A. N. Conde, *Experimental Study of the w-Values and Fano Factors of Gaseous Xenon and Ar-Xe Mixtures for X-Rays*, IEEE Transactions on Nuclear Science **55**, 2637 (2008).

[197] E. De Lima, M. Salete, S. Leite, M. Alves, and A. Policarpo, *Fano factors of rare gases and their mixtures*, Nuclear Instruments and Methods in Physics Research **192**, 575 (1982).

[198] N. Ishida, J. Kikuchi, T. Doke, and M. Kase, *Fano factor in xenon*, Phys. Rev. A **46**, 1676 (1992).

[199] G. Alkhazov, A. Komar, and A. Vorob'ev, *Ionization fluctuations and resolution of ionization chambers and semiconductor detectors*, Nuclear Instruments and Methods **48**, 1 (1967).

[200] T. H. V. T. Dias *et al.*, *Xenon-neon gas proportional scintillation counters: Experimental and simulation results*, Journal of Applied Physics **85**, 6303 (1999), [arXiv:https://doi.org/10.1063/1.370131].

[201] **EXO-200** Collaboration, E. Conti *et al.*, *Correlated fluctuations between luminescence and ionization in liquid xenon*, Phys. Rev. B **68**, 054201 (2003), [arXiv:hep-ex/0303008].

[202] E. Aprile *et al.*, *Simultaneous measurement of ionization and scintillation from nuclear recoils in liquid xenon as target for a dark matter experiment*, Phys. Rev. Lett. **97**, 081302 (2006), [arXiv:astro-ph/0601552].

[203] T. Doke, A. Hitachi, S. Kubota, A. Nakamoto, and T. Takahashi, *Estimation of Fano factors in liquid argon, krypton, xenon and xenon-doped liquid argon*, Nucl. Instrum. Meth. **134**, 353 (1976).

[204] E. Aprile and T. Doke, *Liquid Xenon Detectors for Particle Physics and Astrophysics*, Rev. Mod. Phys. **82**, 2053 (2010), [arXiv:0910.4956].

[205] E. Aprile, A. E. Bolotnikov, A. L. Bolozdynya, and T. Doke, *Noble Gas Detectors* (Wiley, 2008).

[206] **EXO-200** Collaboration, M. Auger *et al.*, *Search for Neutrinoless Double-Beta Decay in ^{136}Xe with EXO-200*, Phys. Rev. Lett. **109**, 032505 (2012), [arXiv:1205.5608].

[207] A. Bolotnikov and B. Ramsey, *The spectroscopic properties of high-pressure xenon*, Nuclear Instruments and Methods in Physics Research Section A: Accelerators, Spectrometers, Detectors and Associated Equipment **396**, 360 (1997).

[208] G. Knoll, *Radiation Detection and Measurement (4th ed.)* (John Wiley, Hoboken, NJ, 2010).

[209] **NEXT** Collaboration, L. Serra *et al.*, *An improved measurement of electron-ion recombination in high-pressure xenon gas*, JINST **10**, P03025 (2015), [arXiv:1412.3573].

[210] C. A. N. Conde, A. J. P. L. Policarpo, and M. A. F. Alves, *Gas Proportional Scintillation Counter with Xenon and Xenon Mixtures*, IEEE Transactions on Nuclear Science **15**, 84 (1968).

[211] K. N. Pushkin *et al.*, *A scintillation response and an ionization yield in pure xenon and mixtures of it with methane*, Instruments and Experimental Techniques **49**, 489 (2006).

[212] **NEXT** Collaboration, C. Henriques *et al.*, *Secondary scintillation yield of xenon with sub-percent levels of CO_2 additive for rare-event detection*, Phys. Lett. B **773**, 663 (2017), [arXiv:1704.01623].

[213] T. H. V. T. Dias *et al.*, *Full-energy absorption of x-ray energies near the Xe L- and K-photoionization thresholds in xenon gas detectors: Simulation and experimental results*, Journal of Applied Physics **82**, 2742 (1997), [arXiv:https://doi.org/10.1063/1.366105].

[214] **NEXT** Collaboration, P. Novella *et al.*, *Measurement of radon-induced backgrounds in the NEXT double beta decay experiment*, JHEP **10**, 112 (2018), [arXiv:1804.00471].

[215] Dougsim, *Visualisation of discrete Townsend avalanches in a proportional counter*, `https://commons.wikimedia.org/wiki/File:Proportional_counter_avalanches.jpg`, 2012, [accessed 01-August-2020].

[216] J. Miyamoto and G. Knoll, *The statistics of avalanche electrons in micro-strip and micro-gap gas chambers*, Nuclear Instruments and Methods in Physics

Research Section A: Accelerators, Spectrometers, Detectors and Associated Equipment **399**, 85 (1997).

[217] P. J. B. M. Rachinhas, T. H. V. T. Dias, A. D. Stauffer, F. P. Santos, and C. A. N. Conde, *Energy resolution of xenon proportional counters: Monte Carlo simulation and experimental results*, IEEE Transactions on Nuclear Science **43**, 2399 (1996).

[218] **NEXT** Collaboration, V. Álvarez *et al.*, *Characterization of a medium size Xe/TMA TPC instrumented with microbulk Micromegas, using low-energy γ-rays*, JINST **9**, C04015 (2014), [arXiv:1311.3535].

[219] C. M. B. Monteiro, L. M. P. Fernandes, and J. M. F. dos Santos, *Detection of VUV Light with Avalanche Photodiodes,* in *Photodiodes*, edited by J.-W. Shi, chap. 11, IntechOpen, Rijeka, 2011.

[220] G. Charpak, H. N. Ngoc, and A. Policarpo, *Neutral radiation detection and localization*, (1981).

[221] C. Oliveira *et al.*, *Energy Resolution studies for NEXT*, JINST **6**, P05007 (2011), [arXiv:1105.2954].

[222] **NEXT** Collaboration, G. Martínez-Lema *et al.*, *Calibration of the NEXT-White detector using 83mKr decays,* Journal of Instrumentation **13**, P10014 (2018), [arXiv:1804.01780].

[223] L. Landau, *On the energy loss of fast particles by ionization*, J. Phys. (USSR) **8**, 201 (1944).

[224] P. Sigmund, *Particle Penetration and Radiation Effects: penetration of atomic and molecular ions* (Springer, 2016).

[225] G. R. Lynch and O. I. Dahl, *Approximations to multiple Coulomb scattering*, Nucl. Instrum. Meth. B **58**, 6 (1991).

[226] **NEXT** Collaboration, A. Simón *et al.*, *Electron drift properties in high pressure gaseous xenon,* JINST **13**, P07013 (2018), [arXiv:1804.01680].

[227] **NEXT** Collaboration, A. Simón *et al.*, *Boosting background suppression in the NEXT experiment through Richardson-Lucy deconvolution*, JHEP **21**, 146 (2020), [arXiv:2102.11931].

[228] C. D. R. Azevedo *et al.*, *Microscopic simulation of xenon-based optical TPCs in the presence of molecular additives,* Nucl. Instrum. Meth. A **877**, 157 (2018), [arXiv:1705.09481].

[229] **NEXT** Collaboration, R. Felkai *et al.*, *Helium–Xenon mixtures to improve the topological signature in high pressure gas xenon TPCs,* Nucl. Instrum. Meth. A **905**, 82 (2018), [arXiv:1710.05600].

[230] **NEXT** Collaboration, A. F. M. Fernandes *et al.*, *Low-diffusion Xe-He gas mixtures for rare-event detection: Electroluminescence Yield,* JHEP **04**, 034 (2020), [arXiv:1906.03984].

[231] **NEXT** Collaboration, F. Granena *et al.*, *NEXT, a HPGXe TPC for neutrinoless double beta decay searches,* (2009), [arXiv:0907.4054].

[232] M. N. Guinot, *Calibration and background model of the NEW detector at the LSC,* PhD thesis, Universitat de València, 2017.

[233] **NEXT** Collaboration, V. Álvarez *et al.*, *Operation and first results of the NEXT-DEMO prototype using a silicon photomultiplier tracking array*, JINST **8**, P09011 (2013), [arXiv:1306.0471].

[234] **NEXT** Collaboration, D. Lorca *et al.*, *Characterisation of NEXT-DEMO using xenon* K_α *X-rays*, JINST **9**, P10007 (2014), [arXiv:1407.3966].

[235] **NEXT** Collaboration, V. Álvarez *et al.*, *NEXT-100 Technical Design Report (TDR): Executive Summary*, JINST **7**, T06001 (2012), [arXiv:1202.0721].

[236] J. Benlloch-Rodríguez, *The NEXT experiment: DAQ, backgrounds and medical applications*, PhD thesis, Universitat de València, 2020.

[237] **NEXT** Collaboration, J. Martín-Albo *et al.*, *Sensitivity of NEXT-100 to Neutrinoless Double Beta Decay*, JHEP **05**, 159 (2016), [arXiv:1511.09246].

[238] **NEXT** Collaboration, C. Adams *et al.*, *Sensitivity of a tonne-scale NEXT detector for neutrinoless double-beta decay searches*, Journal of High Energy Physics **2021**, 164 (2021).

[239] J. J. Gomez-Cadenas, *Status and prospects of the NEXT experiment for neutrinoless double beta decay searches,* in *54th Rencontres de Moriond on Electroweak Interactions and Unified Theories*, pp. 201–206, 2019, [arXiv:1906.01743].

[240] E. Bainglass, B. J. P. Jones, F. W. Foss, M. N. Huda, and D. R. Nygren, *Mobility and Clustering of Barium Ions and Dications in High Pressure Xenon Gas*, Phys. Rev. A **97**, 062509 (2018), [arXiv:1804.01169].

[241] **NEXT** Collaboration, K. Woodruff *et al.*, *Radio frequency and DC high voltage breakdown of high pressure helium, argon, and xenon,* JINST **15**, P04022 (2020), [arXiv:1909.05860].

[242] B. J. P. Jones, A. D. McDonald, and D. R. Nygren, *Single Molecule Fluorescence Imaging as a Technique for Barium Tagging in Neutrinoless Double Beta Decay*, JINST **11**, P12011 (2016), [arXiv:1609.04019].

[243] P. Thapa *et al.*, *Barium Chemosensors with Dry-Phase Fluorescence for Neutrinoless Double Beta Decay*, Sci. Rep. **9**, 15097 (2019), [arXiv:1904.05901].

[244] I. Rivilla *et al.*, *Towards a background-free neutrinoless double beta decay experiment based on a fluorescent bicolor sensor*, (2019), [arXiv:1909.02782].

[245] I. Rivilla *et al.*, *Fluorescent bicolour sensor for low-background neutrinoless double β decay experiments*, Nature **583**, 48 (2020).

[246] **NEXT** Collaboration, F. Monrabal *et al.*, *The Next White (NEW) Detector*, JINST **13**, P12010 (2018), [arXiv:1804.02409].

[247] B. Rebel *et al.*, *High voltage in noble liquids for high energy physics*, Journal of Instrumentation **9**, T08004 (2014).

[248] V. Álvarez *et al.*, *The electronics of the energy plane of the NEXT-White detector*, Nuclear Instruments and Methods in Physics Research Section A: Accelerators, Spectrometers, Detectors and Associated Equipment **917**, 68 (2019).

[249] J. Rodriguez *et al.*, *Mass production automated test system for the NEXT SiPM tracking plane*, in *2012 IEEE Nuclear Science Symposium and Medical Imaging Conference and 19th Workshop on Room-Temperature Semiconductor X-ray and Gamma-ray Detectors*, 2012.

[250] **NEXT** Collaboration, S. Cebrián *et al.*, *Radiopurity assessment of the tracking readout for the NEXT double beta decay experiment*, JINST **10**, P05006 (2015), [arXiv:1411.1433].

[251] J. Rodríguez, J. Toledo, R. Esteve, D. Lorca, and F. Monrabal, *The front-end electronics for the 1.8-kchannel SiPM tracking plane in the NEW detector*, JINST **10**, C01025 (2015).

[252] J. R. Samaniego, *Study and design of the front-end and readout electronics for the tracking plane in the NEXT experiment*, PhD thesis, Universitat Politècnica de València, 2017.

[253] **NEXT** Collaboration, L. Serra *et al.*, *An improved measurement of electron-ion recombination in high-pressure xenon gas*, JINST **10**, P03025 (2015), [arXiv:1412.3573].

[254] **ALICE** Collaboration, F. Carena *et al.*, *The ALICE data acquisition system*, Nucl. Instrum. Meth. A **741**, 130 (2014).

[255] S. Martoiu, H. Muller, A. Tarazona, and J. Toledo, *Development of the scalable readout system for micro-pattern gas detectors and other applications*, JINST **8**, C03015 (2013).

[256] J. Toledo *et al.*, *The Front-End Concentrator card for the RD51 Scalable Readout System*, JINST **6**, C11028 (2011).

[257] R. E. Bosch *et al.*, *The Event Detection System in the NEXT-White Detector*, Sensors **21**, 673 (2021).

[258] R. Esteve *et al.*, *The trigger system in the NEXT-DEMO detector*, JINST **7**, C12001 (2012).

[259] **NEXT** Collaboration, J. Renner *et al.*, *Initial results on energy resolution of the NEXT-White detector*, JINST **13**, P10020 (2018), [arXiv:1808.01804].

[260] **NEXT** Collaboration, M. Kekic *et al.*, *Demonstration of background rejection using deep convolutional neural networks in the NEXT experiment*, JHEP **01**, 189 (2021), [arXiv:2009.10783].

[261] **NEXT** Collaboration, P. Novella *et al.*, *Radiogenic Backgrounds in the NEXT Double Beta Decay Experiment*, JHEP **10**, 051 (2019), [arXiv:1905.13625].

[262] **NEXT** Collaboration, P. Novella *et al.*, *Measurement of the Xe136 two-neutrino double-β-decay half-life via direct background subtraction in NEXT*, Phys. Rev. C **105**, 055501 (2022), [arXiv:2111.11091].

[263] G. M. Lema, *Low-energy calibration, reconstruction software and light-collection efficiency parametrization of the NEXT-White detector*, PhD thesis, Universidade de Santiago de Compostela, 2018.

[264] **GEANT4** Collaboration, S. Agostinelli *et al.*, *GEANT4–a simulation toolkit*, Nucl. Instrum. Meth. A **506**, 250 (2003).

[265] J. Martín-Albo, *The NEXT experiment for neutrinoless double beta decay searches*, PhD thesis, Universitat de València, 2015.

[266] J. M. Vidal, *The NEXT path to neutrino inverse hierarchy*, PhD thesis, Universidade de Santiago de Compostela, 2018.

[267] ISO, *ISO/IEC 14882:2003: Programming languages — C++* (pub-ISO, 2003).

[268] R. Brun and F. Rademakers, *ROOT: An object oriented data analysis framework*, Nucl. Instrum. Meth. A **389**, 81 (1997).

[269] J. Coplien and N. Harrison, *Organizational Patterns of Agile Software Development* (Pearson Prentice Hall, 2005).

[270] G. Van Rossum and F. L. Drake, *Python 3 Reference Manual* (CreateSpace, Scotts Valley, CA, 2009).

[271] C. Green *et al.*, *The Art Framework*, J. Phys. Conf. Ser. **396**, 022020 (2012).

[272] N. Collaboration, *Invisible Cities*, `https://github.com/next-exp/IC`, 2021.

[273] E.a.Mccutchan, *Nucl. Data Sheets*, 125,201 (2015).

[274] R. Firestone, C. Baglin, and S. Chu, *Table of Isotopes: 1999 Update*, A Wiley-Interscience publication No. v. 4 (Wiley, 1999).

[275] N. Collaboration, *krcalib*, `https://github.com/next-exp/ICAROS/tree/master/krcal`, 2021.

[276] E. Browne and J.K.Tuli, *Nucl. Data Sheets*, 108, 2173 (2007).

[277] M. Martin, *Nucl. Data Sheets*, 108,1583 (2007).

[278] K. Auranen and E. A. Mccutchan, *Nucl. Data Sheets*, 168, 117 (2020).

[279] J. Strong, *Procedures in experimental physics* (Journal of the American Pharmaceutical Association, NewYork, 1945).

[280] S. Zhu and E. A. Mccutchan, *Nucl. Data Sheets*, 175,1 (2021).

[281] Johantheghost, *A diagram illustrating the radioactive decay chains of the non-synthetic elements*, `https://en.wikipedia.org/wiki/Decay_chain#/media/File:Radioactive_decay_chains_diagram.svg`, 2006, [accessed 01-July-2021].

[282] M. Wojcik, G. Zuzel, and H. Simgen, *Review of high-sensitivity Radon studies*, Int. J. Mod. Phys. A **32**, 1743004 (2017).

[283] G. Benato *et al.*, *Radon mitigation during the installation of the CUORE $0\nu\beta\beta$ decay detector*, JINST **13**, P01010 (2018), [arXiv:1711.07936].

[284] J. Benziger *et al.*, *The Scintillator Purification System for the Borexino Solar Neutrino Detector*, Nucl. Instrum. Meth. A **587**, 277 (2008), [arXiv:0709.1503].

[285] J. Chen, *Nucl. Data Sheets*, 140, 1 (2017).

[286] J. T. E. Browne, *Nucl. Data Sheets*, 114, 1849 (2013).

[287] **XENON100** Collaboration, E. Aprile *et al.*, *The neutron background of the XENON100 dark matter search experiment*, J. Phys. G **40**, 115201 (2013), [arXiv:1306.2303].

[288] **EXO-200** Collaboration, J. B. Albert *et al.*, *Cosmogenic Backgrounds to $0\nu\beta\beta$ in EXO-200*, JCAP **04**, 029 (2016), [arXiv:1512.06835].

[289] K. L. Freund, *Muonic background in the GERDA neutrinoless $\beta\beta$ experiment*, PhD thesis, Tubingen U., 2014.

[290] S. R. Elliott and H. Ejiri, *Solar Neutrinos as Background to Neutrinoless Double-beta Decay Experiments*, AIP Conf. Proc. **1894**, 020008 (2017), [arXiv:1708.00927].

[291] W. H. Trzaska *et al.*, *Cosmic-ray muon flux at Canfranc Underground Laboratory*, Eur. Phys. J. C **79**, 721 (2019), [arXiv:1902.00868].

[292] D. Jordan *et al.*, *Measurement of the neutron background at the Canfranc Underground Laboratory LSC*, Astropart. Phys. **42**, 1 (2013), [Erratum: Astropart.Phys. 118, 102372 (2020)].

[293] S. E. A. Orrigo *et al.*, *Measurement of the neutron flux at the Canfranc Underground Laboratory with HENSA*, in *17th International Conference on Topics in Astroparticle and Underground Physics*, 2021, [arXiv:2111.09202].

[294] R. B. Firestone *et al.*, *The Evaluated Gamma-ray Activation File (EGAF)*, AIP Conf. Proc. **769**, 219 (2005).

[295] A. Alessandrello *et al.*, *Measurements of internal radioactive contamination in samples of Roman lead to be used in experiments on rare events*, Nucl. Instrum. Meth. B **142**, 163 (1998).

[296] **CDMS** Collaboration, D. S. Akerib *et al.*, *Exclusion limits on the WIMP-nucleon cross section from the first run of the Cryogenic Dark Matter Search in the Soudan Underground Laboratory*, Phys. Rev. D **72**, 052009 (2005).

[297] A. Y.L.Khazov and F.G.Kondev, *Nucl. Data Sheets*, 112, 855 (2011).

[298] A. B. Singh and Y.L.Khazov, *Nucl. Data Sheets*, 109, 517 (2008).

[299] D. Shea and D. Morgan, *The Helium-3 Shortage: Supply, Demand, and Options for Congress*, Congressional Research Service , R41419 (2011).

[300] J. R. Incandela *et al.*, *THE PERFORMANCE OF PHOTOMULTIPLIERS EXPOSED TO HELIUM*, Nucl. Instrum. Meth. A **269**, 237 (1988).

[301] N. Rupp, *Radon background in liquid xenon detectors*, JINST **13**, C02001 (2018), [arXiv:1712.07471].

[302] J. B. Albert *et al.*, *Investigation of radioactivity-induced backgrounds in EXO-200*, Phys. Rev. C **92**, 015503 (2015), [arXiv:1503.06241].

[303] **XENON** Collaboration, E. Aprile *et al.*, *Intrinsic backgrounds from Rn and Kr in the XENON100 experiment*, Eur. Phys. J. C **78**, 132 (2018), [arXiv:1708.03617].

[304] B. Singh *et al.*, *Nucl. Data Sheets*, 160, 405 (2019).

[305] M. S. Basunia, *Nucl. Data Sheets*, 121, 561 (2014).

[306] **ArDM** Collaboration, J. Calvo *et al.*, *Commissioning of the ArDM experiment at the Canfranc underground laboratory: first steps towards a tonne-scale liquid argon time projection chamber for Dark Matter searches*, JCAP **03**, 003 (2017), [arXiv:1612.06375].

[307] M. Berger, J. Coursey, M. Zucker, and J. Chang, *ESTAR, PSTAR, and ASTAR: Computer Programs for Calculating Stopping-Power and Range Tables for Electrons, Protons, and Helium Ions (version 2.0.1)*, http://physics.nist.gov/Star, 2017.

[308] **NEXT** Collaboration, V. Alvarez *et al.*, *Ionization and scintillation response of high-pressure xenon gas to alpha particles*, JINST **8**, P05025 (2013), [arXiv:1211.4508].

[309] S. C. Wu, *Nucl. Data Sheets*, 108, 1057 (2007).

[310] **NEMO** Collaboration, J. Argyriades *et al.*, *Measurement of the background in the NEMO 3 double beta decay experiment*, Nucl. Instrum. Meth. A **606**, 449 (2009), [arXiv:0903.2277].

[311] **EXO-200** Collaboration, J. B. Albert *et al.*, *Measurements of the ion fraction and mobility of α- and β-decay products in liquid xenon using the EXO-200 detector*, Phys. Rev. C **92**, 045504 (2015), [arXiv:1506.00317].

[312] **NEXT** Collaboration, A. Simón *et al.*, *Application and performance of an ML-EM algorithm in NEXT*, JINST **12**, P08009 (2017), [arXiv:1705.10270].

[313] **GERDA** Collaboration, M. Agostini *et al.*, *The background in the $0\nu\beta\beta$ experiment GERDA*, Eur. Phys. J. C **74**, 2764 (2014), [arXiv:1306.5084].

[314] D. S. Akerib *et al.*, *Radiogenic and Muon-Induced Backgrounds in the LUX Dark Matter Detector*, Astropart. Phys. **62**, 33 (2015), [arXiv:1403.1299].

[315] J. Amare *et al.*, *Analysis of backgrounds for the ANAIS-112 dark matter experiment*, Eur. Phys. J. C **79**, 412 (2019), [arXiv:1812.01377].

[316] V. Alvarez *et al.*, *Radiopurity control in the NEXT-100 double beta decay experiment: procedures and initial measurements*, JINST **8**, T01002 (2013), [arXiv:1211.3961].

[317] V. Álvarez *et al.*, *Radiopurity control in the NEXT-100 double beta decay experiment*, AIP Conf. Proc. **1549**, 46 (2013).

[318] P. J. Pérez, *The NEXT-100 experiment for Neutrino-less Double Beta decay: Main features, Results from Prototypes and Radiopurity issues..*, PoS **EPS-HEP2013**, 528 (2013).

[319] **NEXT** Collaboration, T. Dafni *et al.*, *Results of the material screening program of the NEXT experiment*, Nucl. Part. Phys. Proc. **273-275**, 2666 (2016), [arXiv:1411.1222].

[320] S. Cebrián *et al.*, *Radon and material radiopurity assessment for the NEXT double beta decay experiment*, AIP Conf. Proc. **1672**, 060002 (2015), [arXiv:1505.07052].

[321] J. P. Pérez, *Radioactive Contamination in Neutrino Experimental Physics: the Cases of NEXT and Super-Kamiokande Experiments*, PhD thesis, Universidad Autónoma de Madrid, 2017.

[322] O. Behnke and L. Moneta, *Parameter Estimation* (John Wiley & Sons, Ltd), chap. 2, pp. 27–73, [arXiv:https://onlinelibrary.wiley.com/doi/pdf/10.1002/9783527653416.ch2].

[323] S. Baker and R. D. Cousins, *Clarification of the Use of Chi Square and Likelihood Functions in Fits to Histograms*, Nucl. Instrum. Meth. **221**, 437 (1984).

[324] H. Dembinski and P. O. et al., *scikit-hep/iminuit*, (2020).

[325] **EXO-200** Collaboration, J. Albert *et al.*, *Improved measurement of the $2\nu\beta\beta$ half-life of ^{136}Xe with the EXO-200 detector*, Phys. Rev. C **89**, 015502 (2014), [arXiv:1306.6106].

[326] T. Chu, J. Zhu, and H. Wang, *Penalized maximum likelihood estimation and variable selection in geostatistics*, The Annals of Statistics **39** (2011).

[327] Bill Watterson, *Final Calvin and Hobbes*, 1995, [Picture in the acknowledgements].

[328] Fermilab, *Bubble chamber showing muon neutrino traces*, 1978, [Image in the cover].